Sampling Error and Environmental Noises in Passive Microwave Rainfall Retrieval From Space

by

Qihang Li

B. S., Water Resources Engineering
Tsinghua University, 1984

M. S., Civil Engineering
University of Tokyo, 1990

Submitted to the Department of Civil and Environmental Engineering
in Partial Fulfillment of the Requirements for the Degree of
Doctor of Philosophy

at the
MASSACHUSETTS INSTITUTE OF TECHNOLOGY
February 1996

Signature of Author .....
Department of Civil and Environmental Engineering
January 12, 1996

Certified by .....
Rafael L. Bras
Bacardi and Stockholm Water Foundations Professor
Thesis Supervisor

Accepted by .....
Joseph M. Sussman
Chairman, Departmental Committee on Graduate Students

Sampling Error and Environmental Noises in Passive Microwave Rainfall Retrieval From Space

by

Qihang Li

Submitted to the Department of Civil and Environmental Engineering
on January 12, 1996, in partial fulfillment of the
requirements for the degree of
Doctor of Philosophy

Abstract

This study investigates the sampling error and the measuring error associated with space-borne rainfall measurement. On the sampling error issue, we have analyzed Darwin rainfall data in terms of the mean, variance, and auto-correlation of area-averaged rain rate, and their diurnal variation. Compared with the well-studied GATE data, Darwin rainfall has larger coefficient of variation (CV), faster reduction of CV with increasing area size, weaker temporal correlation, and a strong diurnal cycle and intermittence. Stationary and non-stationary models have been used to quantify the sampling errors. The non-stationary model shows that the sampling error is generally sensitive to the starting sampling time. Sampling experiments using observed data also show such sensitivity. At the small areas for which data are available for both Darwin and GATE, the sampling error is expected to be larger for Darwin due to its larger CV. On the measuring error issue, we have focused on the effects of wind and non-precipitating clouds on the upwelling brightness temperature (T_B) from the ocean surface. A model is developed to relate T_B to the fractional coverage of rain, f, within a FOV. The critical parameter of the model, $T_{B,min}$, which is the threshold brightness temperature for the presence of rain, depends on the strength of the storm. The strength of the storm can be characterized by the fraction of the FOVs within a large area that have T_B higher than 240 °K, which is readily obtained from satellite data alone. The instantaneous FOV rain rate R can then be obtained through the $f \sim R$ relationship which is empirically derived using radar data. A new algorithm has been proposed based on the $T_B \sim f$ and $f \sim R$ relationship. Application of the new algorithm and two existing ones to some storms has shown the ability of our model to remove the bias caused by the non-rain effects.

Thesis Supervisor: Rafael L. Bras
Title: Bacardi and Stockholm Water Foundations Professor

Acknowledgments

While I am writing this section and reflecting on the recent past, I suddenly realize how much I have been changed during my MIT years. The change has occurred as a result of being influenced by many brilliant people, particularly the individual members of my thesis committee. Professor Rafael Bras, my advisor, is my model of excellence both academically and in everyday life. He has demonstrated, through everything he did, big and small, the importance of having a large picture of what you are doing, taking initiative, acting promptly, working hard, and attending to details. I thank you for so dramatically improving my view of the world. Professor Daniele Veneziano provided most timely guidance on technical issues during my research. I appreciate the numerous discussions, many occurred in late Friday afternoons, concerning all aspects of the research, including interpreting model results and preparing manuscripts. Thank you for your generous help and friendship. Professor Dara Entekhabi helped me tremendously by providing important literature and suggesting solutions to many fundamental issues encountered during the research. Professor Elfatih Eltahir has always been enthusiastic and involved closely with my research. I appreciate your many helpful discussions and suggestions which have motivated me to do more and improved the quality of the research. I thank you all.

Thanks are also due to Dr. Earle Williams for his help during the many months I was working on the radar data at MIT radar laboratory, and for interesting discussions on radar meteorology.

I would like to thank Elaine Healy and Karen Joss for their everyday help, without which I would have been years behind schedule.

I am most indebted to my wife, Lili, who has sacrificed so much and provided the most support to me, while taking good care of our son, Darwin, and daughter, Gina, and attempting to keep up with her own program of study at the University of Massachusetts. Your existence, together with Darwin and Gina, reminds me of what the most important things in life are.

Finally, thanks are due to the sponsors, National Science Foundation and National Aeronautics and Space Administration, which supported this research under grants ATM-9020832 and NAG5-1615.

Contents

List of Figures

List of Tables

Chapter 1

Introduction

1.1 Background

Information about the spatial and temporal distribution of rainfall over the globe is very important in several ways. The latent heat released by the condensation of water vapor into liquid water during the precipitation process is a major energy source that drives the atmospheric circulation. Most of the global precipitation occurs in the tropics, and the released latent heat is subsequently transported polewards, partially balancing the radiation deficit at high latitude. The variability in rainfall amount can have a major impact on the global energy budget and hence the climate variability. Rainfall provides fresh water input to the ocean, which affects the ocean circulation by altering the surface layer salinity. Over the land, besides being an input to all hydrologic processes, rainfall controls the state of the biosphere.

Traditionally, rainfall has been measured overland with raingage networks. In remote parts of the continent, rainfall information is rare. Over the ocean rainfall information is essentially not available. Therefore, oceanic rainfall information has been derived using indirect methods, normally for climatological

purposes. One such indirect method, based on the concept proposed by Sawyer (1952) and further refined by Tucker (1961) using data from the British Isles, relates measured rainfall amounts at land stations to the "current weather" reported in the synoptic weather observations from these stations. These relationships are then applied to ship reports in order to estimate oceanic rainfall. Reed and Elliott (1973) used this method to derive precipitation estimates for the North Pacific from weather observations reported by ships.

The potential of observations from satellite in the visible, infrared (IR), and microwave wavelengths for rainfall estimation has been evident for some time. Satellite-based rainfall retrieval algorithms fall into two major categories: those using visible/IR imagery and those using microwave radiometer measurements. The first category relies on the fact that rainfall is nearly always associated with clouds of some type, and that higher and/or thicker clouds appear to be associated with heavier or more frequent rainfall. This is a relatively indirect method because it does not measure the rain directly. On the other hand, the second category, the one using microwave measurements, is more direct in that it is based on observations of the radiative effects of precipitation-sized hydrometeors.

Radiation in the Visible/IR channels have been related to rainfall information in numerous studies. For example, Kilonsky and Ramage (1976) used the frequency of highly reflective clouds (HRC) in visible polar-orbiter imagery as an index of monthly rainfall in the tropical Pacific. The reasoning behind their study was that, because most rainfall in the tropics is caused by organized convection, rainfall might be estimated from once-a-day satellite observations of relatively large-scale convective activity. They defined HRC subjectively as the assemblage of areas of bright cloudiness with a radius equal to or greater

than 2° of latitude. Raingages on islands less than 30 meters in height were selected to be correlated with the HRC totals. A total of 820 station-months of rainfall measured between May 1971 and April 1973 were plotted against the monthly HRC totals at the exact geographic positions of the respective stations. A correlation of 0.75 was found significant at the 1% level. Garcia (1981) used Kilonsky and Ramage's method to make rainfall estimates for the GARP Atlantic Tropical Experiment (GATE) study area. He then compared these results with high-resolution geostationary satellite IR-based rainfall estimates derived by the Griffith-Woodley method (Woodley et al., 1980), and found that for the entire GATE period (27 June through 20 September 1974) there was a 0.92 correlation between the two methods. Both these procedures yielded rainfall volume estimates that were within 15% of the ship radar estimates.

Microwave techniques observe directly the radiative effects of precipitation-sized hydrometeors and thus should be more accurate than Visible/IR techniques in producing instantaneous rain rate estimates. Passive microwave radiation to space is controlled by three processes: emission, absorption, and scattering. These processes depend upon the properties of the earth's surface, atmospheric constituents and hydrometeors (water droplets and ice crystals). Over the oceans, the emissivity from the water surface is low (approximately 0.4–0.5 for calm water surfaces), providing a cold background. The high brightness temperature of rain drops is a strong signal over this cold background, which can be quantitatively related to the rain rate.

The importance of and the need for the space-born measurement of rainfall have been recognized by the atmospheric and hydrologic community. The Tropical Rainfall Measuring Mission (TRMM) is a joint US-Japan program to measure the tropical rainfall using a low-altitude, low-inclination satellite.

The satellite, which is scheduled to be launched in 1997, will carry microwave radiometers and active radars for the sole purpose of measuring rainfall. The rainfall products resulting from TRMM will greatly improve our understanding of the large-scale space-time variability of rainfall and its relation to climate change.

Space-born microwave rainfall estimates have two sources of error. Here we call them sampling error and measurement error. The sampling error arises from the fact that orbiting satellites observe a given part on earth at discrete times. The measurement error is caused by the imperfect algorithms used to convert the measured brightness temperature to surface rain rate. The quantification and reduction of these errors are important to make programs such as TRMM successful. A number of studies have tried to estimate the sampling error of the TRMM satellite. These studies have mainly depended on GATE (GARP Atlantic Tropical Experiment) radar rainfall data. As rainfall statistics vary from place to place, it is necessary to study data sets from other parts of the tropics. Numerous algorithms exist to estimate oceanic rainfall from observations of microwave radiation. These algorithms are based on theories of radiative transfer through raining clouds and use sophisticated cloud models. Most of them have ignored the variability in the underlying surface condition and other factors, which, in most cases, results in overestimation of rainfall.

1.2 Objectives

There are two objectives in this study. One is concerned with the sampling error associated with space-borne measurement of rainfall. The other is concerned

with the measuring error, specifically, it is concerned with the effects of wind and non-precipitating clouds on passive microwave rainfall retrieval. We call these effects environmental noises. On the sampling error issue, we will use the radar rainfall data set collected over Darwin, Australia, which exhibits different characteristics from the well-studied GATE data set. We want to answer a few key questions:

- What are the mean and variance of Darwin rainfall?
- How strong is the diurnal cycle?
- What is its autocorrelation?
- What is the spatial variability of these quantities?
- How do these quantities vary with areal averaging?
- How does the diurnal cycle affect the sampling error?
- How does Darwin rainfall differ from the GATE rainfall in terms of these quantities?

On the issue of environmental noises, our goal is to develop an algorithm which removes the bias caused by the noises. Key questions are:

- What is the observational evidence of the noise effects?
- What are the magnitude and variability of the noise effects?
- How to differentiate the noise from the rain effects?
- How to parameterize the noise effects?
- How to calibrate the noise parameter?

- How does a model that considers the noise effects differ from those that ignore such effects?

1.3 Structure of the Thesis

This thesis consists of 6 major chapters.

Chapter 1 provides the background and specifies the objectives of the study.

Chapter 2 deals with the issue of sampling error. We first formulate the sampling error for both stationary and non-stationary processes. This is followed by a literature review on the study of sampling error. We then analyze Darwin rainfall data in terms of mean, variance, correlation, and diurnal cycle. Finally, the sampling error is quantified by using both stationary and non-stationary models, and by performing empirical sampling experiments using observed data.

Chapter 3 reviews major papers on passive microwave remote sensing of rainfall that deal with the development of models, rather than the application of existing models. Through the literature review, we highlight a common weakness in these previous studies: they have largely ignored the variability of sea surface emissivity.

Chapter 4 presents observational evidence of the effects of wind and non-precipitating clouds on the upwelling brightness temperature. The magnitude of such effects are quantified by our own calculations and by using the results of early studies on sea surface emissivity.

In Chapter 5, we develop a model to take into account the noise effects. The model relates the brightness temperature to the fractional rainfall coverage within a field of view (FOV). The FOV average rain rate is then related to

the fractional rainfall coverage through an empirical relation. Simultaneous radar/satellite data are used to calibrate the model. An algorithm is then proposed which considers the noise effects and which relies on satellite data only. Finally, the proposed algorithm is compared with two existing models and is shown to be better in terms of removing the noise-induced bias.

Chapter 6 provides major conclusions and identifies areas of future research.

Chapter 2

Sampling Error

The sampling error arises from the fact that an orbiting satellite generally views a certain area at discrete times only. In the proposed Tropical Rainfall Measuring Mission (TRMM), for example, the low-altitude, low-inclination satellite would fly over a given area about twice daily (Simpson et al. 1988). The space-time rainfall estimated using the discrete measurements is different from the true rainfall. The sampling error is a function of the satellite geometry (altitude, inclination, swath width, etc) and the statistical properties of rainfall. Satellite geometry will determine how frequently a given area is visited and what portion of the area is intersected by the swath during each visit. Statistical properties of rainfall that affect the sampling error include the mean, variance and autocorrelation and their variation with time. While the satellite geometry can be controlled through proper design, the rainfall statistics are location-dependent and need to be quantified by observation.

2.1 Sampling Error Formulation

To define the sampling error, consider a surface rain rate process $r(\mathbf{x}, t)$, where $\mathbf{x}$ represents a two-dimensional space (ground surface) and t is time. The rain rate averaged over an area of interest A, which we call areal rain, is

$$r_A(t) = \frac{1}{A}\int_A r(\mathbf{x}, t)d\mathbf{x} \tag{2.1}$$

Further averaging over a period of time T gives the space-time average

$$r_{AT} = \frac{1}{AT}\int_T\int_A r(\mathbf{x}, t)d\mathbf{x}dt \tag{2.2}$$

Suppose that during period T (say 30 days) the satellite makes N (say 60 in the case of twice-daily sampling frequency) complete snapshots of area A with perfect rainfall measurements. The space-time rain r_{AT} may be estimated as the sample average

$$\hat{r}_{AT} = \frac{1}{N}\sum_{i=1}^{N} r_A(t_i) \tag{2.3}$$

where $t_1, t_2, \ldots, t_N$ are times of visits.

The estimation error is

$$\epsilon = \hat{r}_{AT} - r_{AT} \tag{2.4}$$

Our interest is in the "sampling error", which is defined here as the square root of the second moment of ϵ, or the standard deviation of ϵ if ϵ has zero mean

$$\sigma_\epsilon = \sqrt{< (\hat{r}_{AT} - r_{AT})^2 >} \tag{2.5}$$

The operator $< \cdot >$ indicates expected value. To further expand the above equation, the rainfall statistics have to be known. Let the process $r_A(t)$, with time-dependent mean $m(t)$, variance $\sigma^2(t)$, and autocorrelation $\rho(t_1, t_2)$, be sampled N times during period T at times $t_1, t_2, \ldots, t_N$. Then (2.5) can be expanded as

$$\sigma_\epsilon = \sqrt{X + Y + Z} \tag{2.6}$$

where

$$X =< [\frac{1}{N}\sum_{1}^{N} r_A(t_i)]^2 >= \frac{1}{N^2}\sum_{i=1}^{N}\sum_{j=1}^{N}[m(t_i)m(t_j) + \sigma(t_i)\sigma(t_j)\rho(t_i, t_j)]$$

$$Y =< \frac{1}{T^2}(\int_0^T r_A(t)dt)^2 >= \frac{1}{T^2}\int_0^T \int_0^T [m(t_1)m(t_2) + \sigma(t_1)\sigma(t_2)\rho(t_1, t_2)]dt_1 dt_2$$

$$Z =< -\frac{2}{NT}\sum_{1}^{N} r_A(t_i)\int_0^T r_A(t)dt >= -\frac{2}{NT}\sum_{i=1}^{N}\int_0^T [m(t_i)m(t) + \sigma(t_i)\sigma(t)\rho(t_i, t)]dt$$

When the rainfall statistics are time-dependent, (2.6) is the pr ,per expression to evaluate the sampling error. In the case when the rainfall process is stationary and visits are at constant interval $\Delta t = T/N$, (2.6) reduces to

$$\sigma_\epsilon = \sigma[\frac{1}{N} + \frac{2}{N^2}\sum_{k=1}^{N-1}(N-k)\rho(k\Delta t) + \frac{2}{T^2}\int_0^T \int_0^{t_1} \rho(t_1 - t_2)dt_2 dt_1 - \frac{2}{NT}\sum_{i=1}^{N}\int_0^T \rho(|t - t_i|)dt]^{1/2}$$

or

$$\sigma_\epsilon = \sigma\phi(\rho(\tau), N, T) \tag{2.7}$$

where σ is constant, $\rho(\tau)$ depends only on lagtime τ, and $\phi(\rho, N, T)$ quantifies the dependence of sampling error on the autocorrelation and the sampling frequency.

In the stationary case, the sampling error expressed as a fraction of the

process mean, is simply

$$\frac{\sigma_\epsilon}{m} = \frac{\sigma}{m}\phi(\rho, N, T) = CV \cdot \phi(\rho, N, T) \tag{2.8}$$

where CV is the coefficient of variation of the area-averaged rainfall process $r_A(t)$.

The sampling error can be evaluated explicitly if the time-dependent or -independent mean, variance, and the autocorrelation of the rainfall process are known, and the sampling period T and sampling interval $\triangle t$ are given. In the above formulation, complete coverage of the area A by the sensor during each visit is assumed, which results in a lower bound on the sampling error for the case with partial coverage.

2.2 Sampling Error Literature Review

There have been a number of studies in which sampling errors associated with the TRMM-type rainfall measurements are quantified. Many of these studies have used rainfall data from GATE (Global Atmospheric Research Program (GARP) Atlantic Tropical Experiment) in which rainfall was measured from radars aboard ships in the Intertropical Convergence Zone area of the Atlantic (centered at 8.5° N, 23.5° W) during the summer of 1974. The GATE consisted of a 18-day Phase 1 experiment and a 15-day Phase 2 experiment. The rain data are spatially binned into a 100 by 100 array of 4-km square boxes.

Laughlin (1981) used a first-order Markov model to generate time series of areal rain rate. The sampling error associated with the rainfall estimate based on discrete measurements was studied. It was found that for a 280 km by 280 km area and a 12-hour sampling interval, the sampling error for monthly

rainfall was less than 10%.

In McConnell and North (1987), GATE rainfall rates were divided into roughly equal volume contributing categories: 0–5, 5–10, 10–20, and above 20 mm h^{-1}, and each category was studied separately. An imaginary satellite was flown over the 400×400 km^2 GATE area every 650 minutes. An ensemble of nine estimates of rain rate was developed for each rainfall category and for each GATE phase. The first member of the ensemble was obtained by starting the first visit at 0800 LST on the first morning of a GATE phase, returning 650 minutes later, and continuing through the entire period of that phase; similarly the second member of the ensemble was started at 0900 LST. The nine estimates for each category and each phase were compared with the true rain rate. The study found that for each category the bulk of the estimates are within $\pm 10\%$ of the true averages, with the spread being larger for the more intense categories. They concluded that the result is consistent with earlier studies and that their findings can be expected to be stronger, in the sense that some cancellation of random sampling errors may occur when the four intensity categories are put together to obtain the total rain amount. They acknowledged, however, that two factors could invalidate the conclusion that percentage errors of 5–10% in estimating monthly rainfall over 500-km grid boxes are achievable by twice-daily snapshots: (1) GATE data cover only two relatively short periods, and (2) GATE data might not be representative of other tropical areas.

Kedem et al. (1990) fitted a mixed distribution to GATE rain rate, which contained an atom at zero and a continuous part for the non-zero rain rate. It was shown that a lognormal distribution provides a very close fit to the non-zero area-averaged rain rates. With such a distribution, they were able to estimate the sampling error for the two GATE phases. With a 350 km by 350

km area and 12-hour sampling interval, they found that for GATE 1 (18 days) the sampling error was 0.05 mm h^{-1} on a mean of 0.44 mm h^{-1}; for GATE 2 (15 days) it was 0.04 mm h^{-1} on a mean of 0.37 mm h^{-1}.

Bell et al. (1990) studied the sampling error problem using a stochastic model of space-time rainfall. The model generates a field of rain rate on a grid, the value at each grid point representing the rain rate averaged over the surrounding grid square. The field evolves in time. The distribution of non-zero rain rate generated at any one grid point is lognormal. The fraction of time that it rains, and the mean and standard deviation of the logarithm of non-zero rain rates, must be supplied to establish the distribution. The model first generates a temporally and spatially correlated Gausian field $g(x,t)$, and the rain rate field is obtained from the Gausian field with the transformation $r(x,t) = R(g)$, where R is 0 for values of g below some threshold g_0 (chosen such that the probability of generating zero rain rate agrees with observation) and increases smoothly from 0 for values of $g > g_0$ in such a way that the rain rates generated are lognormally distributed when g is normally distributed. The spatial and temporal correlation of the g field is adjusted until the correlation structure of the r field agrees with observation. For the sampling error study the model parameters were determined using the space-time statistics of GATE rainfall. Rainfall was generated over a 512×512 km^2 area and a satellite visit over the area was simulated about once every 12 hours. The satellite could see the area completely or partially. The Monte Carlo study showed that, for area latitudes of 10–25°, orbital altitudes of 300–450 km, and an inclination of 30°, the sampling error for monthly rainfall is 6–10% of the mean. In their conclusions, they pointed out that the model is wholly based on GATE statistics from one 400-km-diameter spot, and that even GATE data themselves are

subject to considerable uncertainty. Furthermore, the estimates of sampling error do not include the effect of diurnal and spatial variation of the statistics within an averaging box.

North et al. (1993) used a simple rainfall model in which the stochastic rainfall process $\psi(\mathbf{r}, t)$ is governed by the differential equation

$$\tau_0 \frac{\partial \psi(\mathbf{r}, t)}{\partial t} - \lambda_0^2 \nabla^2 \psi(\mathbf{r}, t) + \psi(\mathbf{r}, t) = F(\mathbf{r}, t) \tag{2.9}$$

where τ_0 and λ_0 are inherent time and length scales of the rainfall process and $F(\mathbf{r}, t)$is a zero-mean noise. This model represents a first-order continuous auto-regressive process in time and an isotropic second-order auto-regressive process in space. The reason that this model was chosen is that it is easy to analyze spectrally and it is reasonably accurate in describing the GATE data, according to the authors. Using this model, with a 350-km orbit altitude, a 35° inclination and a 600-km swath, the sampling error associated with the estimation of monthly rainfall over a 500×500 km^2 area near the equator was estimated to be 11.2% of the mean. When complete coverage is assumed for each visit, the error reduces to 5.3%. In their study, the coefficient of variation of the area-averaged rain rate, defined as the standard deviation divided by the mean, was estimated as 1 by extrapolating the available data to 500×500 km^2 area .

Oki and Sumi (1994) used radar-AMeDAS composite data over Japan to quantify sampling errors. The data consisted of 43 months of hourly rainfall within a 5 km by 5 km grid, and was derived from a radar network calibrated by a raingage network called Automatic Meteorological Data Acquisition System (AMeDAS). They performed empirical sampling experiments in which an

imaginary TRMM-type satellite was flown during the data period. It was found that for a 5°× 5° area the sampling error for monthly rain over Japan region would be 16%–20% depending on the swath width of the sensor. For a 2.5°× 2.5° area and with the swath width of the TRMM precipitation radar, the error was found to be 24%. These estimates are larger than previous results using GATE data, which the author attributed to the fact that their data included both midlatitude cyclonic rain and tropical convective rain and that the study area involves both ocean and land. They further found a strong seasonal variation in the sampling error. For example, for the 5°×5° area and with the TRMM microwave imager swath width, the sampling error was 13% in the summer rainy season (June–September) and 19% in the dry season (November–March).

The estimate of sampling error apparently depends on the rainfall statistics or rainfall model used. The rainfall models used in earlier studies are stationary, without diurnal cycles. Indeed, there is little evidence of diurnal cycle in the GATE data; for example, Figure 5 of Bell et. al (1990) shows no enhanced correlation at a lag time of 24 hours. In this study, we analyze radar rainfall data collected in the vicinity of Darwin, Australia, in terms of the mean, variance, temporal correlation, and their diurnal variation, and study the sampling error associated with such rainfall statistics. At Darwin, the diurnal cycle of rainfall is very pronounced. When appropriate, comparisons are made between Darwin and GATE.

2.3 Darwin Rainfall Data Analysis

2.3.1 The Data

The rainfall data used in the sampling error study was collected during the Down Under Doppler and Electricity Experiment (DUNDEE), which was carried out in the northern coast of Australia during two wet seasons (Nov. 1988–Feb. 1989 and Nov.1989–Feb. 1990) (see Rutledge et al. 1992). The MIT C-band (5.4 cm) doppler radar was installed at Darwin, Australia, to collect detailed rainfall data (Figure 2-1). Darwin's latitude is 12° S in the southern portion of the maritime continent. Two types of rainfall regimes can be observed over the course of the wet season, i.e., the classical "hot towers" embedded in the monsconal convection on the axis of the equatorial trough and the more vigorous and more sparsely distributed thunderstorms displaced from the equatorial trough. The radar covered three types of surfaces: continental land, sea, and an island. During rainfall events, PPI (Plan Position Indicator) scans were made at time intervals ranging from 5 to 20 minutes. Ranges of 56-km, 113-km, and 226-km were used depending on the storm location (the range is the radius of the circular area covered by the radar scan). The intermediate range, 113-km, was used most often. During periods of no significant rain (mostly during the early morning periods), measurements could be terminated based on the operator's judgment. In this study, zero rain is assumed for any period of no measurement, except for periods of known instrument failure. There are several short periods (a few hours) of no measurement between periods of heavy rain. Such no-measurement periods have been filled in with rainfall estimated through linear interpolation from the rainfall measurements on both sides.

Our analysis has been limited to the second season because its record is

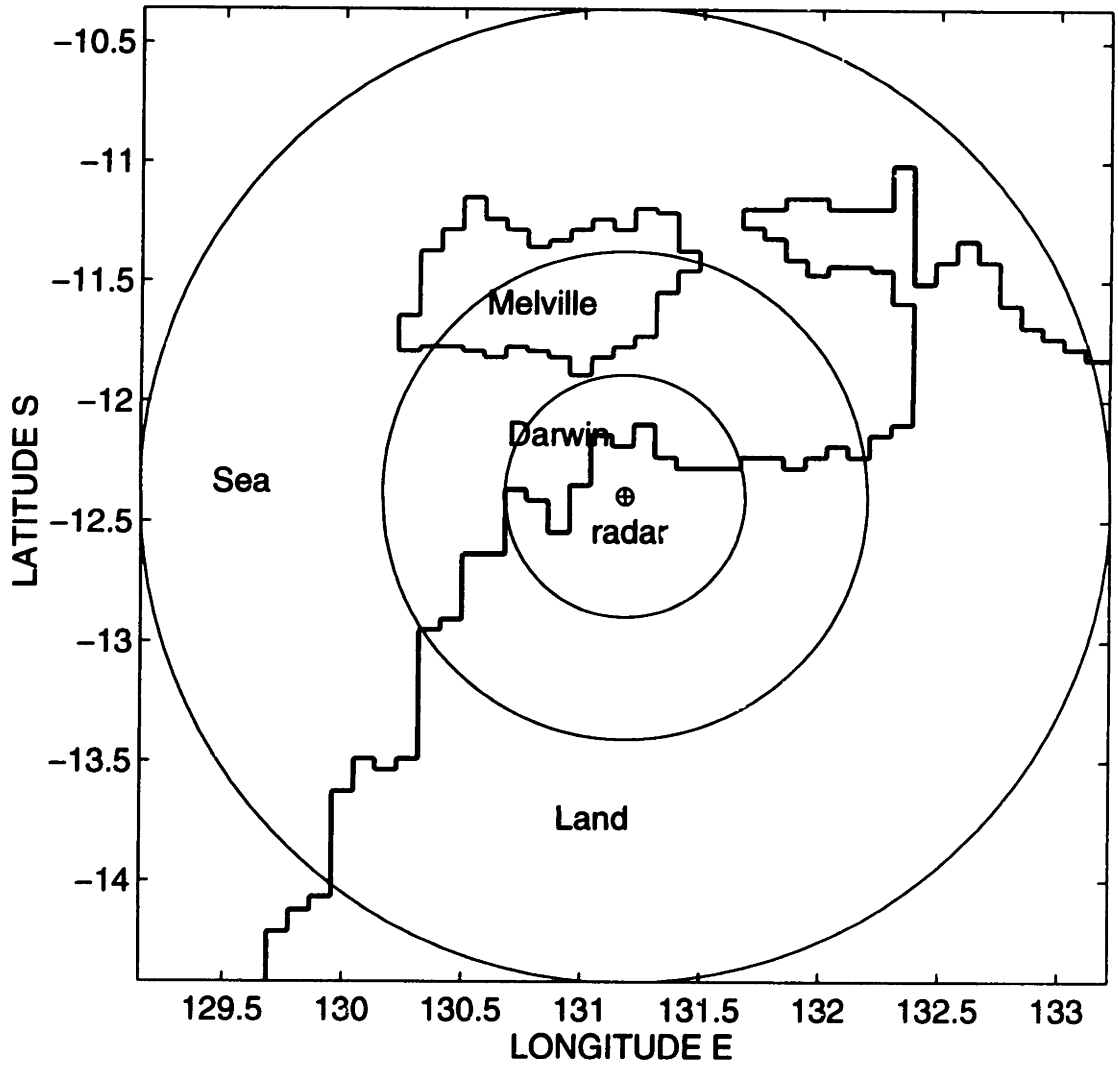

Figure 2-1: Vicinity of Darwin and location of the MIT radar. The three circles indicate the 56-, 113-, and 226-km ranges, respectively. Within the radar coverage are land, sea, and part of the Melville island.

much more continuous and has finer temporal resolution than that of the first season. Except for two relatively long breaks, the data used cover the period from Nov. 10, 1989 to Feb. 18, 1990 nearly completely. In the original polar coordinates, the beam width is 1.4° and the bin lengths are 1/4, 1/2, and 1 km for ranges of 56-km, 113-km, and 226-km, respectively. The polar coordinates have been converted into cartesian coordinates with spatial resolution of 1 km $\times$ 1 km. For individual pixels the reflectivity has been converted to rain rate using the relationship $Z = 400R^{1.3}$ where Z is in mm^6 m^{-3} and R is in mm h^{-1}. For widespread monsoon-type rainfall events, however, Williams et al. (1992) have found that using this relationship results in total rainfall estimates that are smaller than raingage based measurements by a factor of 5. Thus, in the present application the rain rate derived from the above relationship has been multiplied by 5 to obtain areal rain.

C-band radars are known for their attenuation by heavy rain. Attenuation results from the fact that the signal backscattered from the raindrops in a given pixel and received by the radar is weakened by raindrops located on the path of the radar beam between the radar and that given pixel. To investigate this issue for the Darwin data we looked at the relationship between the measured rain rate at a pixel and the thickness of the rain cells that the radar beam has to penetrate between the radar and the pixel. This was done using all the available instantaneous surface rain maps during DUNDEE. For a given rain map, each pixel was examined. If it was raining in the pixel, we then counted the number of raining pixels located on the straight line linking the radar and the pixel under question. This enabled us to calculate the distance or thickness of the raining cells through which the radar beam penetrated. A scatter plot could be made if we plot the observed rain rate of the pixel and the penetrating

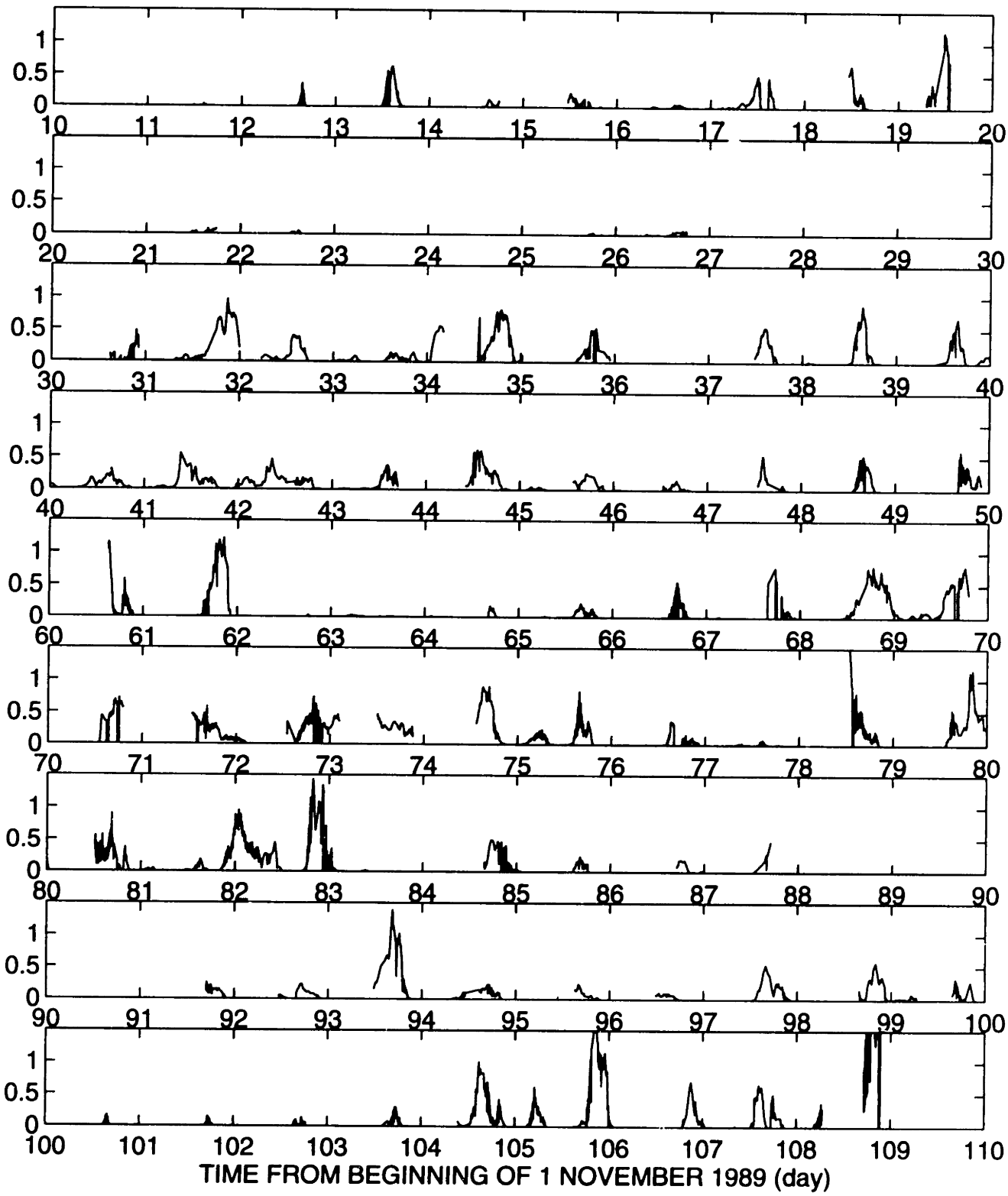

Figure 2-2: Rain rate (mm h^{-1}) averaged over the 113-km range. 10 November 1989–18 February 1990.

distance. To remove the scatter and better see the attenuation effect, we have averaged the rain rate at a given distance, and plotted the averaged rain rate against the distance in Figure 2-3 for both the land and the sea surfaces. The rationale for making such a plot is that the average or climatological rain rate can be assumed to be constant over the same type of surface, so that if the radar measurement is not affected by attenuation, the observed rain rate should be independent of the penetrating distance, and the rain–distance plot should be a horizontal line. Figure 2-3 shows that the radar-observed rain rate at a pixel is affected by the amount of rain cells that block the radar beam, as the rain rate decreases with the penetrating distance. For small distance, where attenuation is expected to be small, the average radar-observed rain rate is about 7 mm h^{-1} over the land surface and about 5 mm h^{-1} over the sea. This is the case when the rainfall is of convective nature and the rain cells are small in size and are sparsely distributed in space. For large penetrating distance, which is the case with wide-spread monsoon-type rainfall, the average radar-observed rain rate is greatly reduced. For example, at 100-km distance the rain rate is 2 mm h^{-1} and 1 mm h^{-1} over the land and the sea, respectively. This means that if the distance of rain penetrated by the radar beam is 100 km, the average radar-observed rain rate is smaller by a factor of 3.5 and 5 for pixels over the land and the sea, respectively, than the unattenuated values. This is consistent with Williams et al. (1992) where the radar-based measurements were found to be smaller than the raingage-based values by a factor of 5. As mentioned previously, the radar-based measurements have been multiplied by a factor of 5 to obtain our final rainfall.

Figure 2-2 is an example of the rainfall data, which shows the instantaneous rain rate averaged over the 113-km radius circular area (113-km range) scanned

by the radar. The horizontal axis represents time from 0000 LST 1 November 1989. Records of rain rate averaged over areas of various sizes have also been obtained from the raw data. Notice that no measurements were made from day 50 to day 60 and from day 88 to day 91; these two periods have been excluded from our analysis. Also notice that relatively small amounts of rain occur during the initial 20 days, particularly the second 10 days. These 20 days might represent a transition from the dry season to the wet season and hence correspond to a different rainfall regime from the rest of the data set. In our analysis these 20 days have also been excluded.

2.3.2 Statistics of Rain

a)Mean, Variance, Diurnal Cycle, and Intermittence

Rain statistics have been computed over the land and sea portions for various averaging areas. The spatial characteristics can be demonstrated by using relatively small areas such as 10 km by 10 km boxes. The local mean rainfall within 10 km by 10 km boxes is shown in Figure 2-4. It can be observed that, on average, mean rainfall intensity over the land is larger that that over the sea by a factor of about 2, and variability exists within each type of surface. The standard deviation, which is shown in Figure 2-5, shows larger values over the land than over the sea. However, owing to difference in the mean, the coefficient of variation (CV), which is the the standard deviation divided by the mean, is larger and more variable over the sea (see Figure 2-6). Specifically, the CV varies between 9 and 13 over the sea, but only between 8 and 9 over the land. It is appropriate to point out that, because of the large uncertainties associated with the radar-derived rain rates, absolute values of rainfall cannot be determined with high confidence. But if we assume that the radar-derived

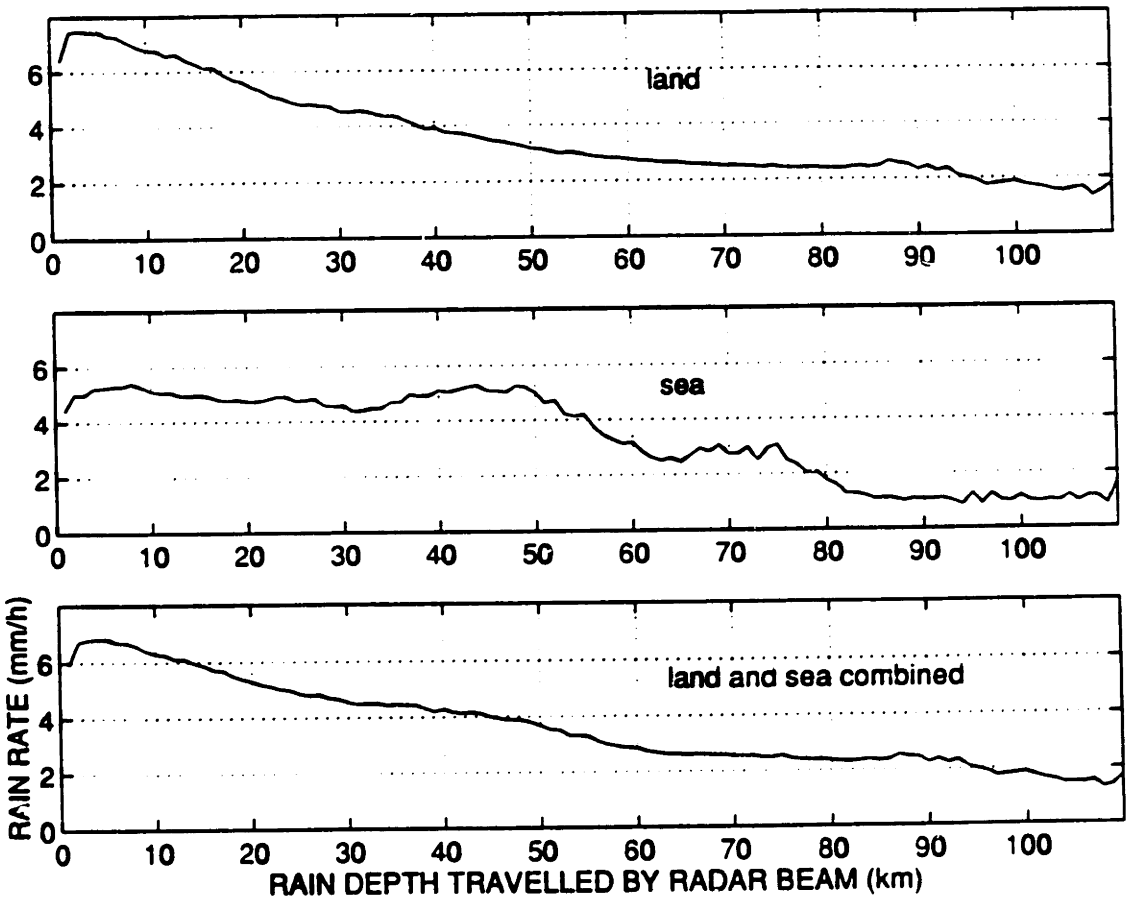

Figure 2-3: Average rainfall intensity versus rain distance penetrated by the radar beam.

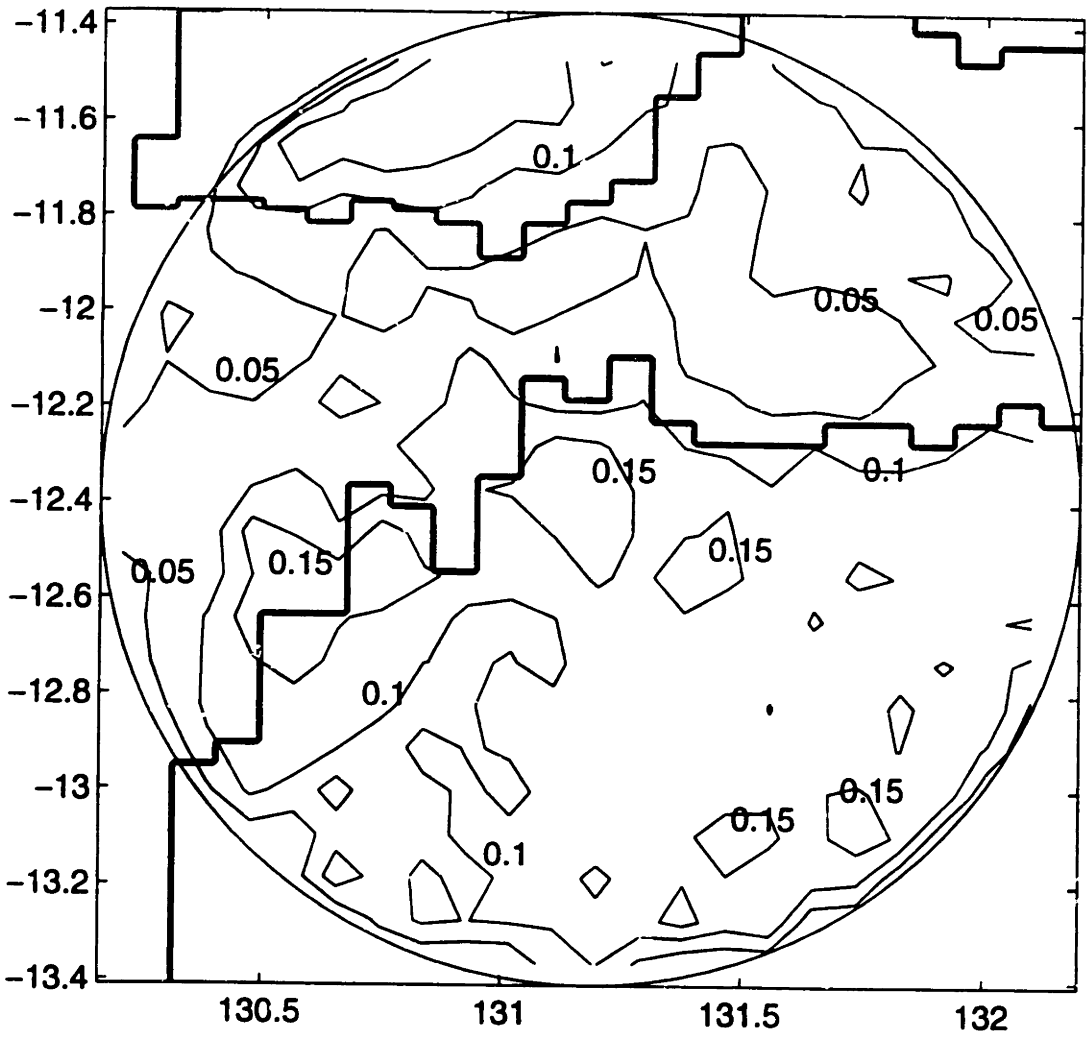

Figure 2-4: Spatial distribution of mean rain (mm h^{-1}) for 10 km by 10 km areas.

rain rate differs from the true rain by a fixed factor, then CV can be determined correctly. Notice that the above three figures are for 10 km by 10 km boxes. As the size of the box increases, the mean remains stable while the standard deviation decreases, leading to smaller CVs. The dependence of CV on the area size is presented in Figure 2-7 where the average CV for area size A is plotted against $\log A$, for the land and the sea separately and combined. Results for GATE, adopted from North et. al (1993), are also plotted for comparison. Figure 2-7 shows that, for Darwin, the sea portion generally has larger CV than the land, but the difference becomes smaller as the area increases. And Darwin as a whole shows larger CV than GATE. However, the CV for Darwin decreases with increasing area at a faster rate, which may be due to the fact that Darwin rainfall is mainly contributed by isolated local convective storms which have weak spatial correlation. When rainfall is averaged spatially, the variance at Darwin is reduced more effectively than for the GATE rainfall which is spatially more widespread. The $\oplus$ signs in Figure 2-7 are for areas in which both land and sea are included. These areas have been taken as circles centered at the radar site. Below 30 km radius (about 3000 km^2) the circles remain entirely on the land, so the $\oplus$ signs are consistent with the star signs (which represent land). Above 30 km radius, however, the circles begin to include sea surface, which has larger CV, resulting in the deviation of the $\oplus$ signs away from the stars. It should be pointed out here that the sea portion within the radar coverage is a coastal water surface which is strongly influenced by the nearby continent, and its rain statistics should not be interpreted as representative of open oceans.

The Darwin rainfall exhibits a strong diurnal cycle, especially for the island and the continental land portions. Figure 2-8 shows the diurnal cycle of mean

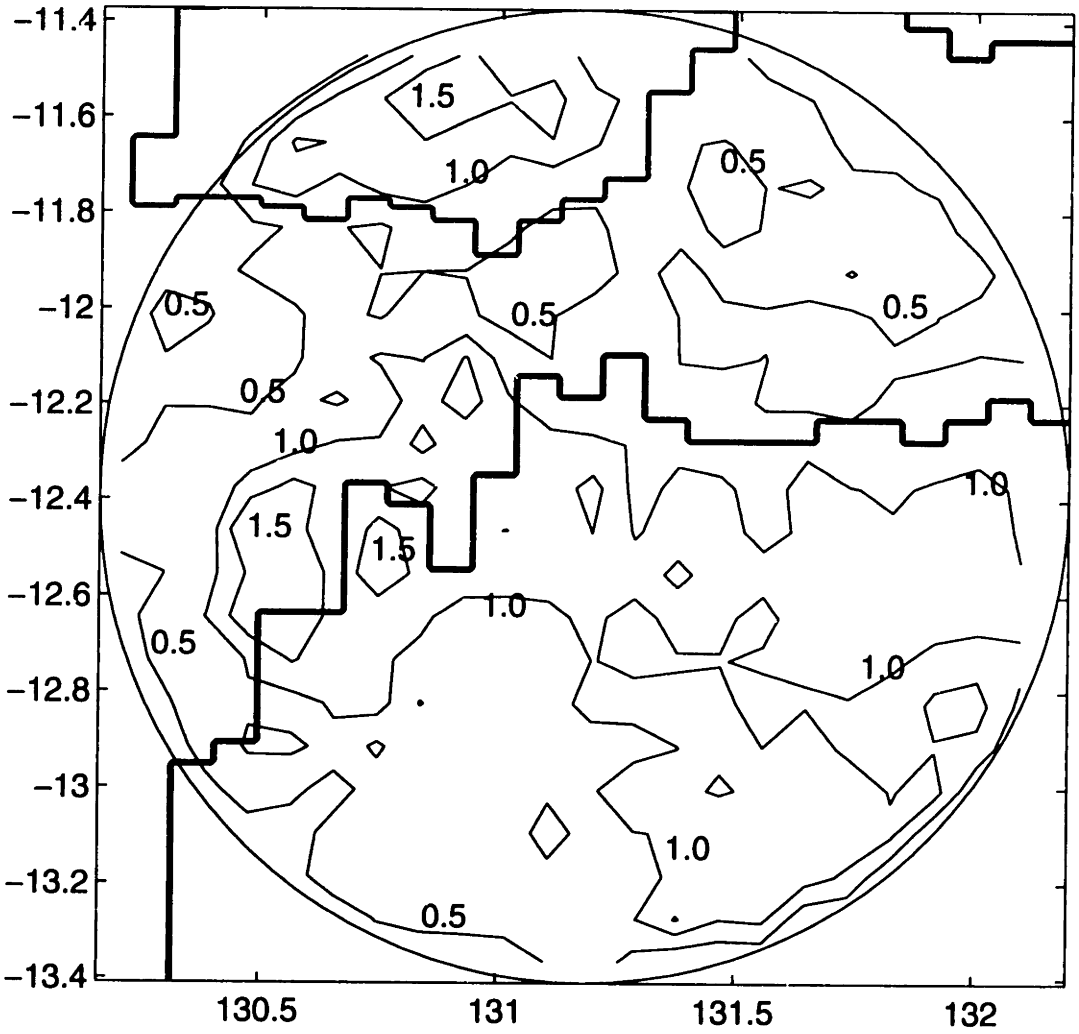

Figure 2-5: Spatial distribution of the standard deviation of rain rate (mm h^{-1}) averaged over 10 km by 10 km areas.

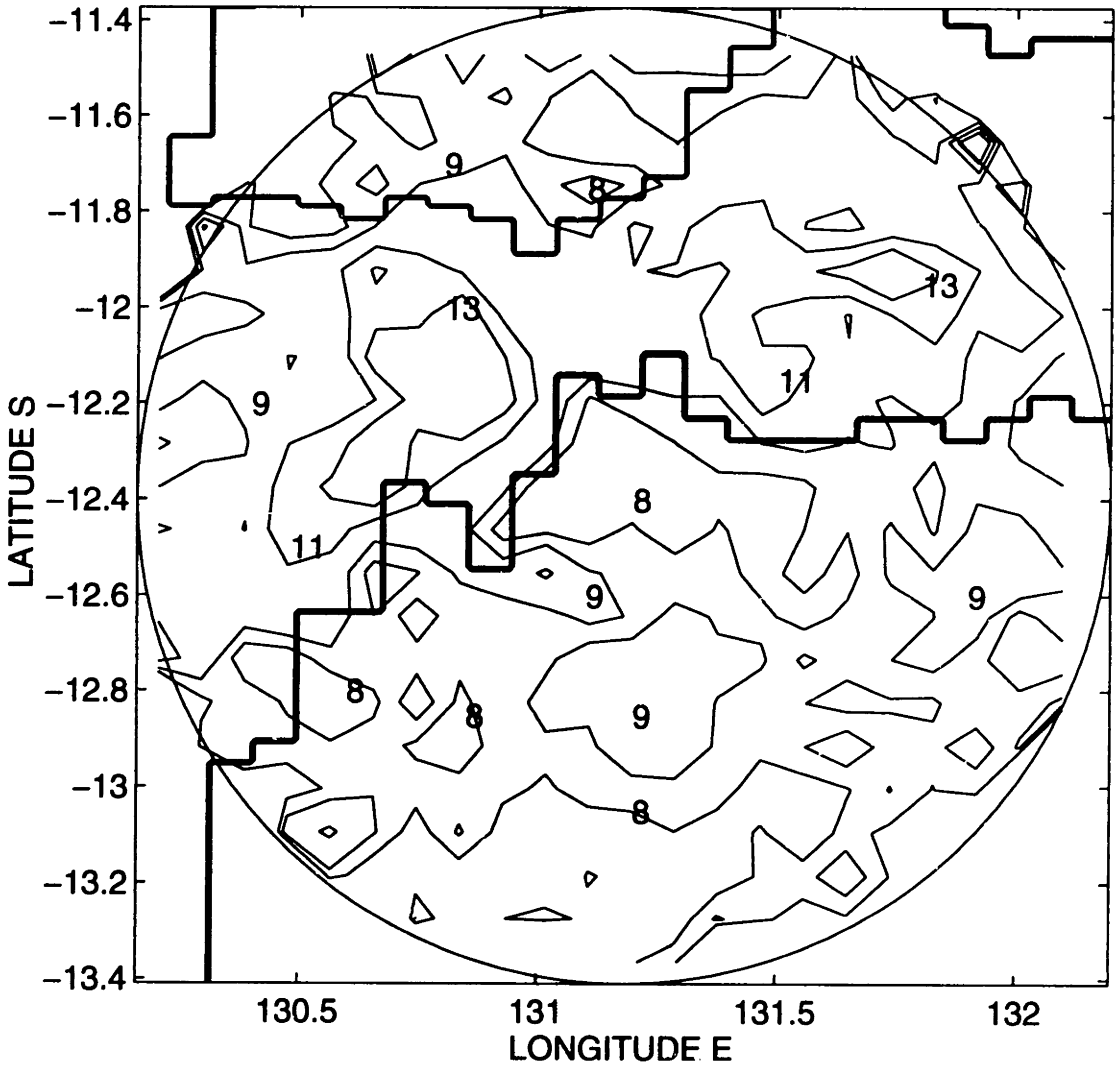

Figure 2-6: Spatial distribution of CV for rain averaged over 10 km by 10 km areas.

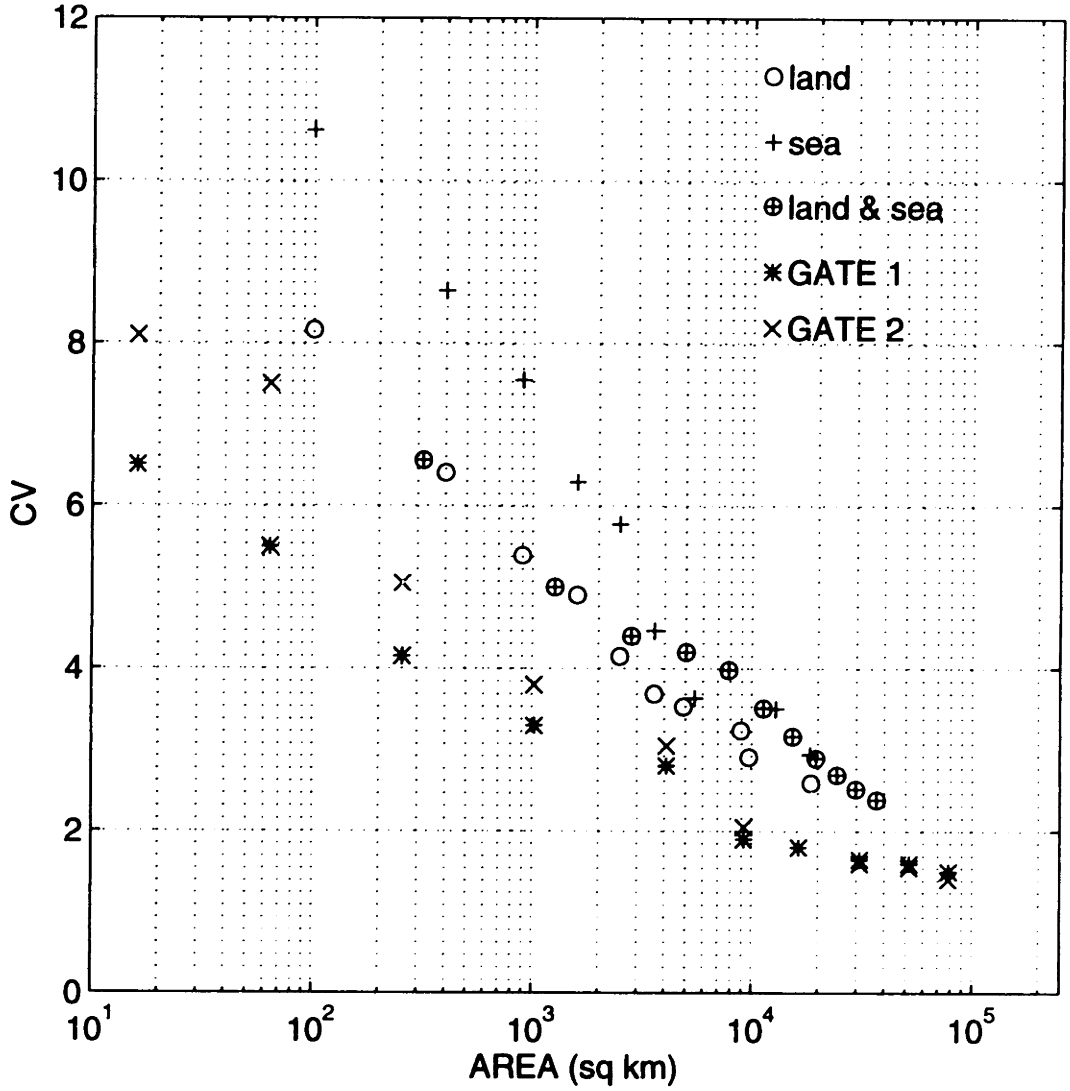

Figure 2-7: Relationship between CV and area size. The $\oplus$ signs are for circles centered at the radar site.

rain over the land, sea, and the island within the 113-km radius radar coverage. Figure 2-9 presents the diurnal cycles of the mean, standard deviation, and CV at 1-h bins for the areal rain within the 113-km radius coverage (i.e., in this case, the land, sea, and the island are combined). As Figure 2-8 shows, rainfall over the sea also shows a diurnal pattern, although less pronounced. It is interesting to note that there is generally more rain over the sea than over the land during the night, although both are small in magnitude; during the day rainfall over the land is much larger than over the sea. The diurnal cycle over the island is extraordinarily strong, with a well-defined peak in the afternoon. This is likely due to the abundant vapor supply from the surrounding water surface coupled with the heated ground surface over the island in the afternoon.

Intermittence is another distinctive feature of Darwin rainfall. Most rainfall occurs in the afternoon hours and the duration of each storm is short. There is not much rainfall during the early morning hours. Analysis shows that, at a random point of time, the probability of rain anywhere within a 25 km by 25 km box is about 0.1, with smaller values over sea than over land (see Figure 2-10). Associated with the intermittence, Darwin rainfall is very localized. In most rainfall events there are only a few isolated rain cells within the radar coverage. This is demonstrated in Figure 2-11 where the average raining area within a 25 km by 25 km box is shown. When it is raining, only about 10% of a 25 km by 25 km box is covered by the rain.

b) Autocorrelation

Since rainfall has been measured at irregular intervals, a new data set with a constant time interval of 10 minutes has been created by linearly interpolating the original data. The autocorrelation is computed using the new data set. Notice that what we are dealing with here is the area-averaged rain rate.

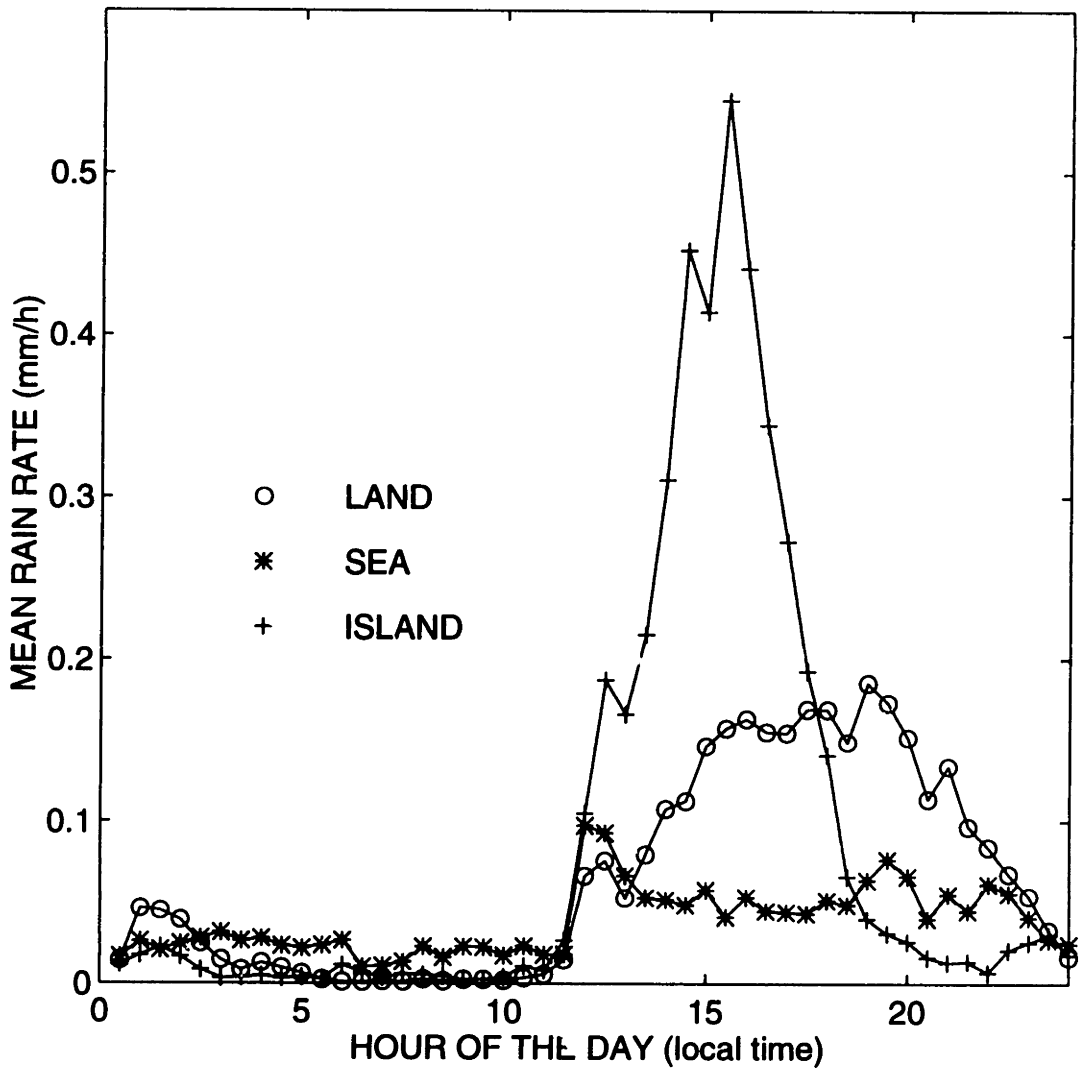

Figure 2-8: Diurnal cycle of mean rain over the land, sea, and island portions.

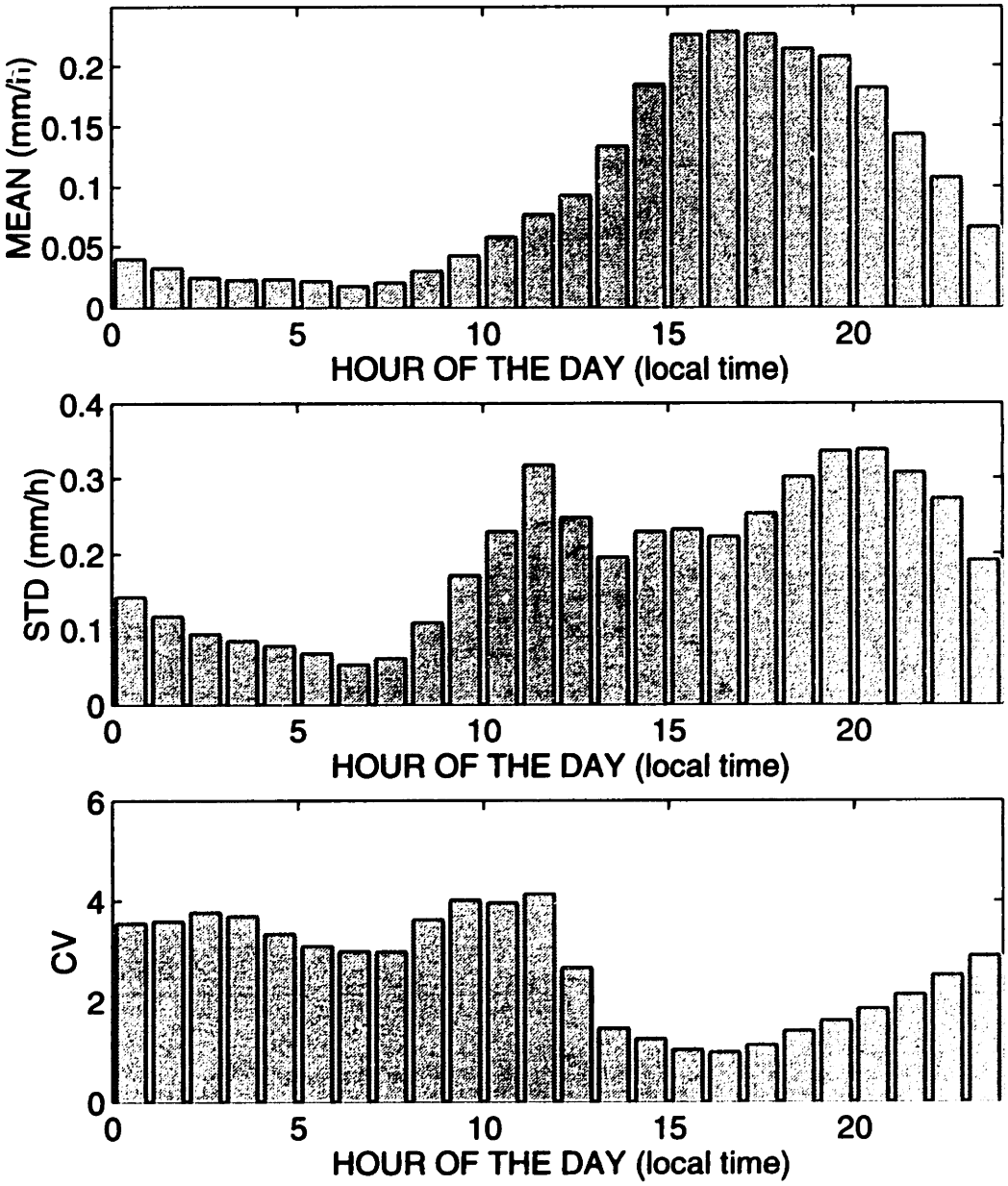

Figure 2-9: Diurnal variation of mean, standard deviation, and CV for the areal rainfall averaged over the 113-km range.

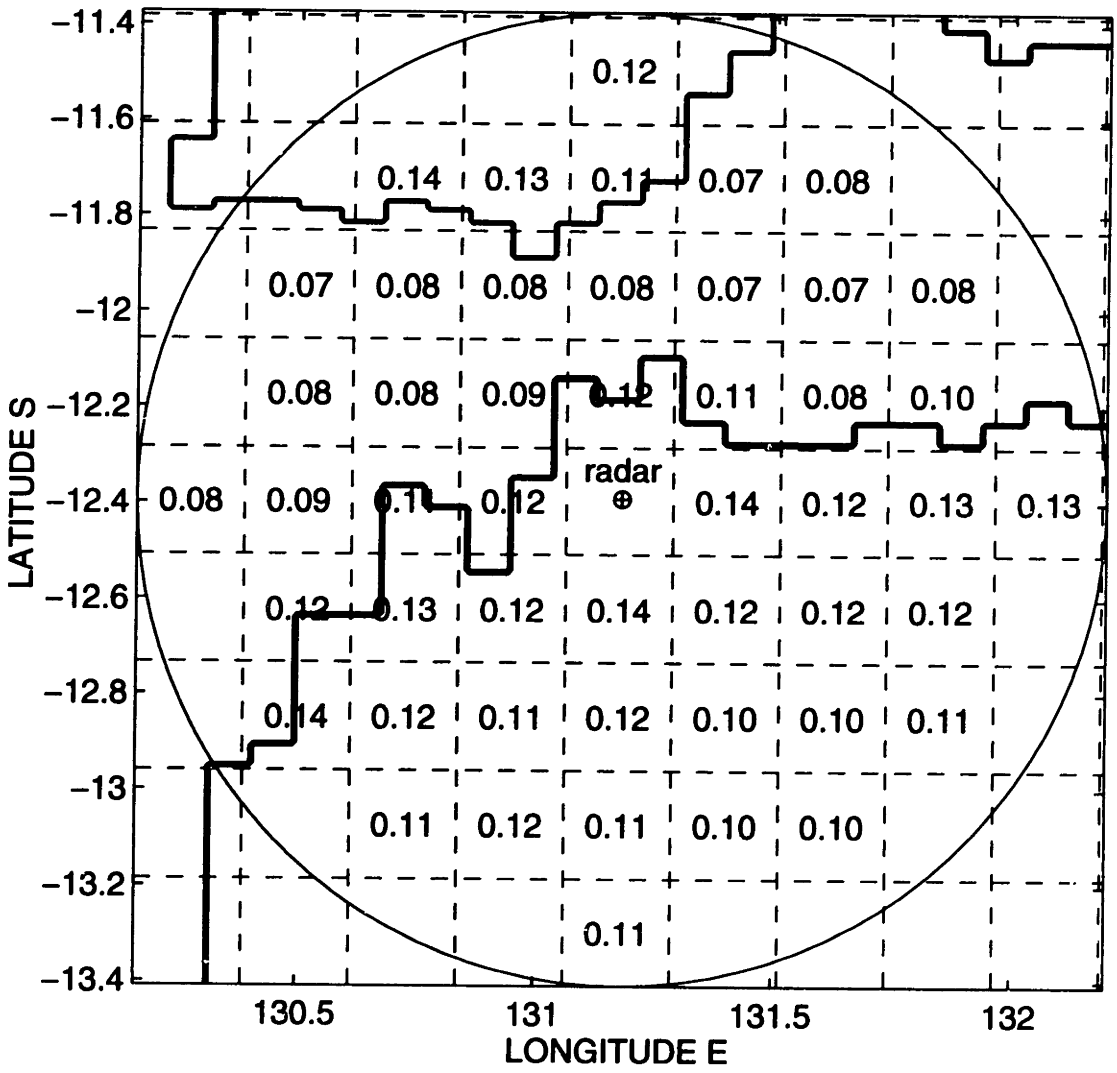

Figure 2-10: Probability of rain (in time) within a 25 km by 25 km box.

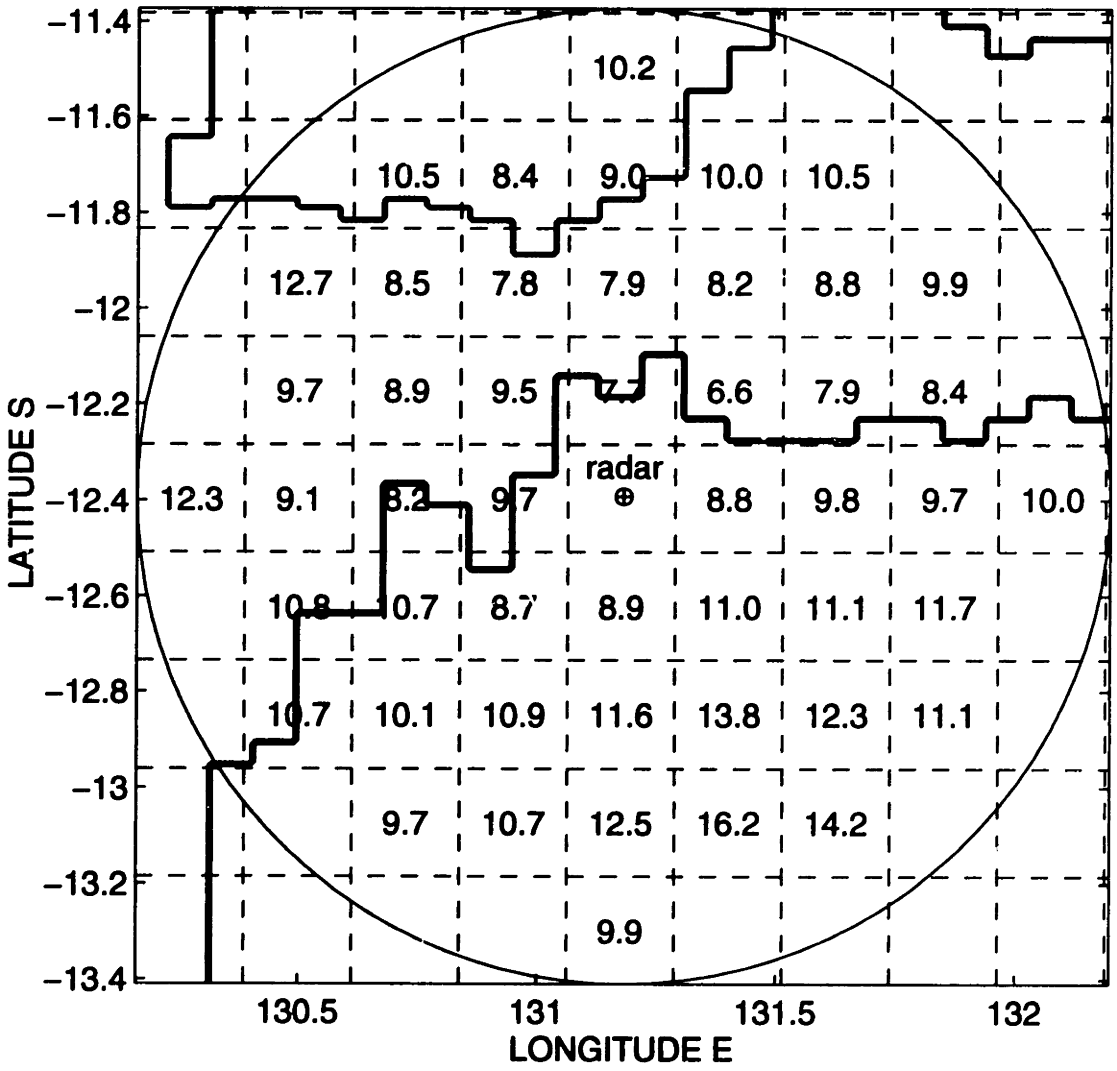

Figure 2-11: Percentage area covered by rain within a 25 km by 25 km box when the box as a whole is experiencing non-zero rain.

The correlation can be computed in two different ways. One is to treat the whole rainfall process as stationary with constant mean and variance and with correlation that depends only on lagtime. The other is to account for the diurnal cycle and treat the process as non-stationary, with a diurnally varying mean and variance and with correlation which depends not only lagtime, but also on absolute time.

Examples of autocorrelation resulting from the stationary treatment are shown in Figure 2-12. The correlation has peaks around multiples of 24 hours, which is an indication of diurnal cycle. However, the peaks are not always located at exact multiples of 24 hours, due to the fact that, throughout the whole period, heavy rain does not always occur at a fixed time of day. For example, in the early part of the DUNDEE project, most rainfall occurs from noon to 1600 LST, while in the later part of the period heavy rainfall occurs mainly from 1600 LST to 2000 LST. At small lag time τ, $\rho(\tau)$ decays rapidly, indicating weak temporal correlation within each storm (Figure 2-13, which shows the first 12 h of Figure 2-12). If a correlation time scale τ_0 is defined as the lagtime at which the correlation drops to e^{-1}, then a τ_0 can be computed for each area size. Figure 2-14 shows the relationship between the correlation time scale and the area size. Results for GATE 1, adopted from Bell et al. (1990), are also plotted. For a given area size, Darwin rainfall has a much shorter correlation time scale.

Autocorrelations for the rain rate averaged separately over the land and sea portions are shown in Figure 2-15. As the two regions have roughly the same area, Figure 2-15 indicates that the land has a slightly stronger correlation than the sea.

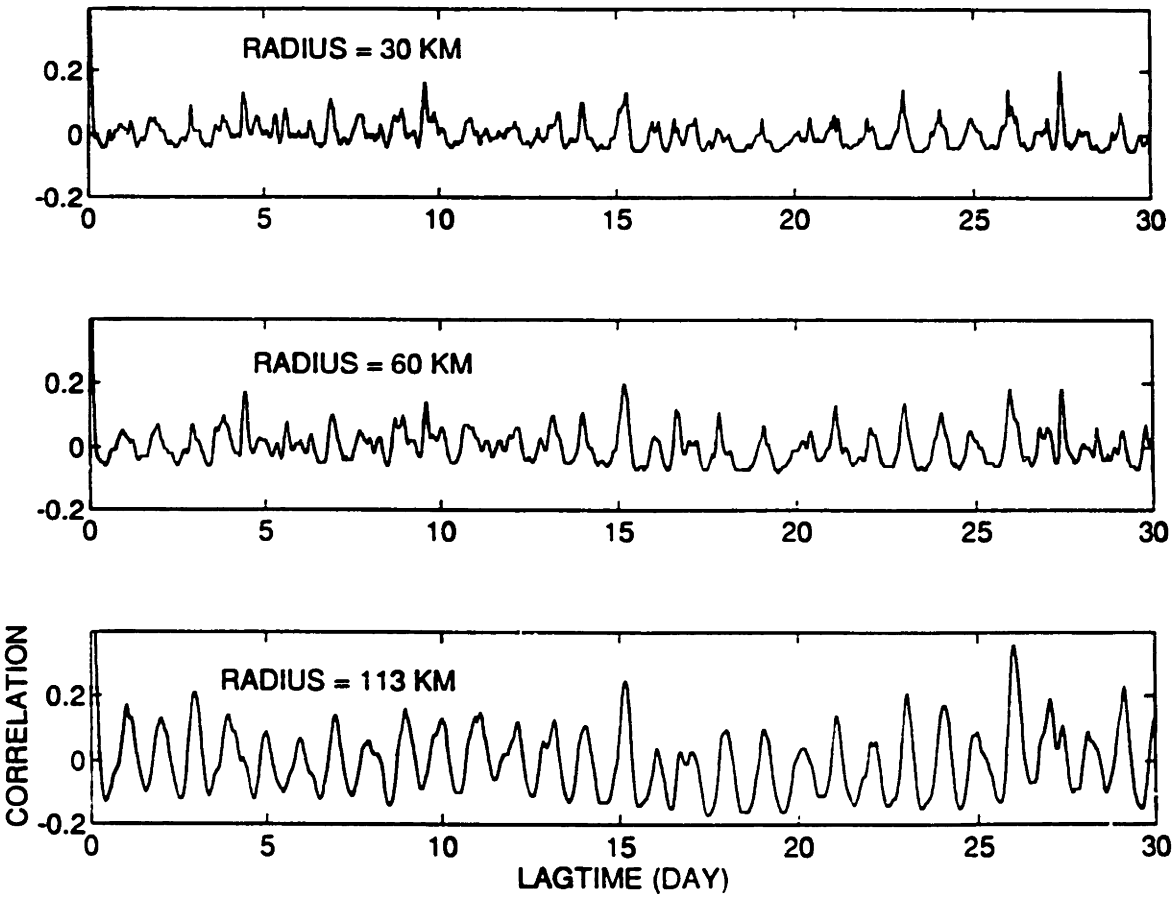

Figure 2-12: Autocorrelation of areal rain rate over 30-km, 60-km, and 113-km radii; for lagtimes up to 30 days;stationary model.

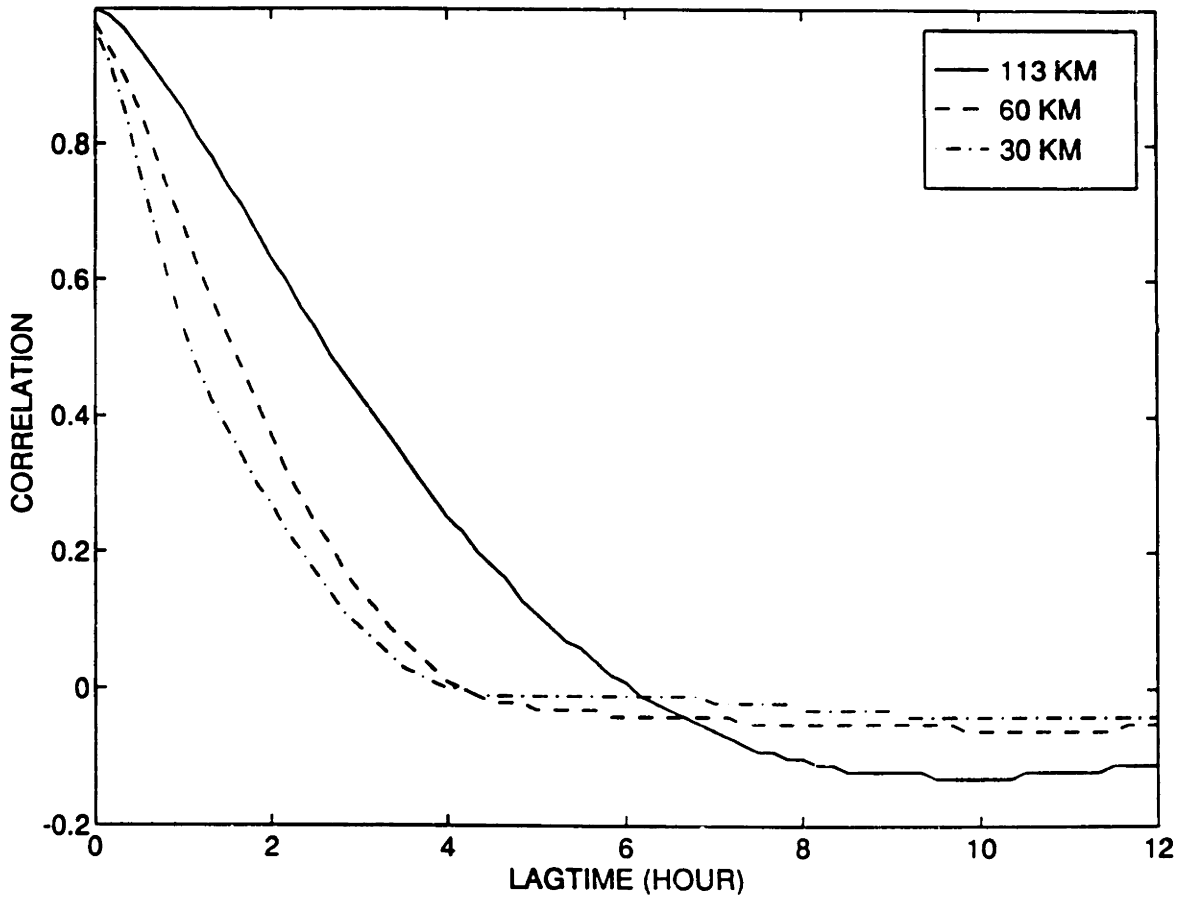

Figure 2-13: Autocorrelation of areal rain rate over 30-km, 60-km, and 113-km radii; for short lagtimes.

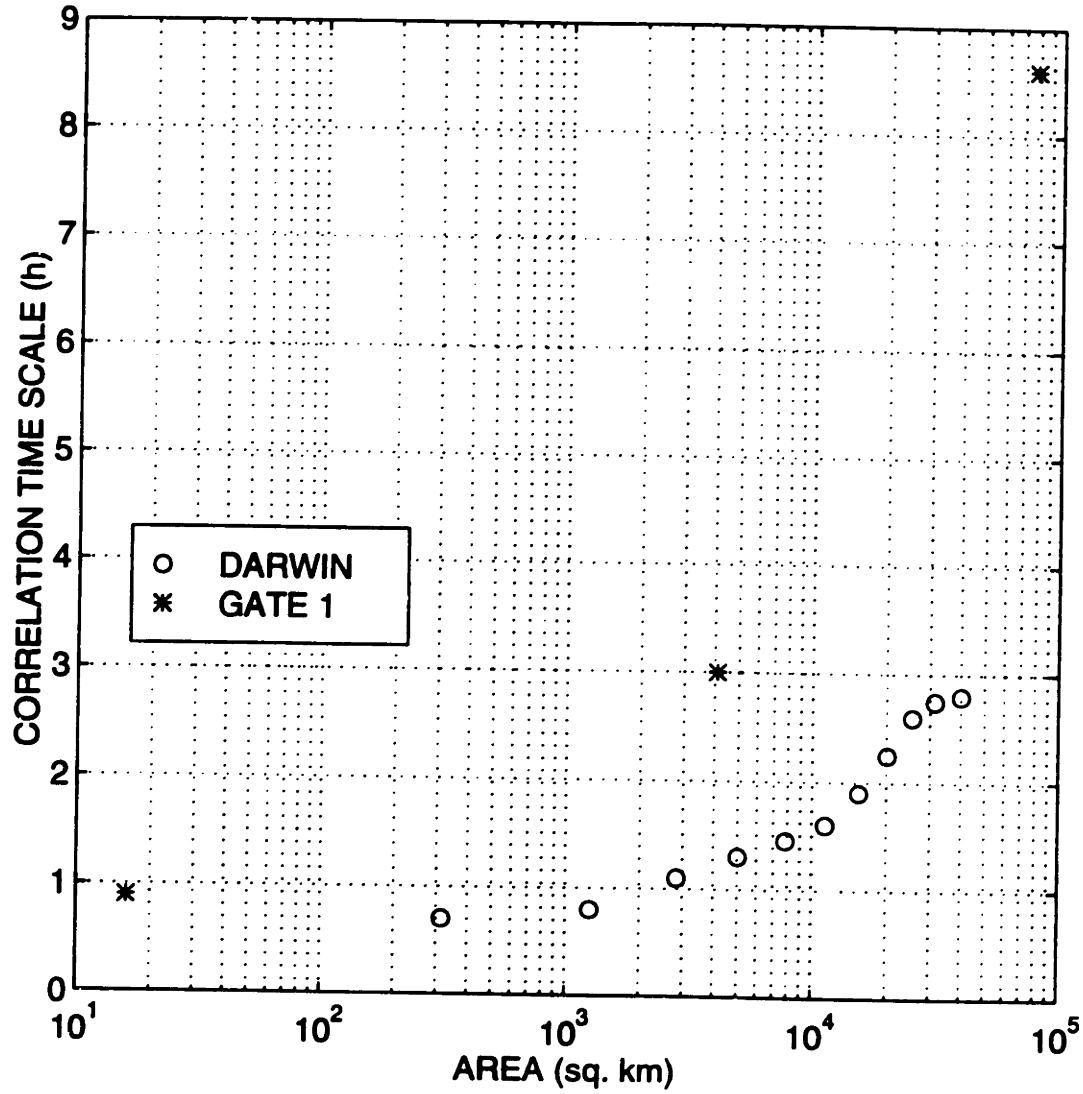

Figure 2-14: Relationship between correlation time scale and area size.

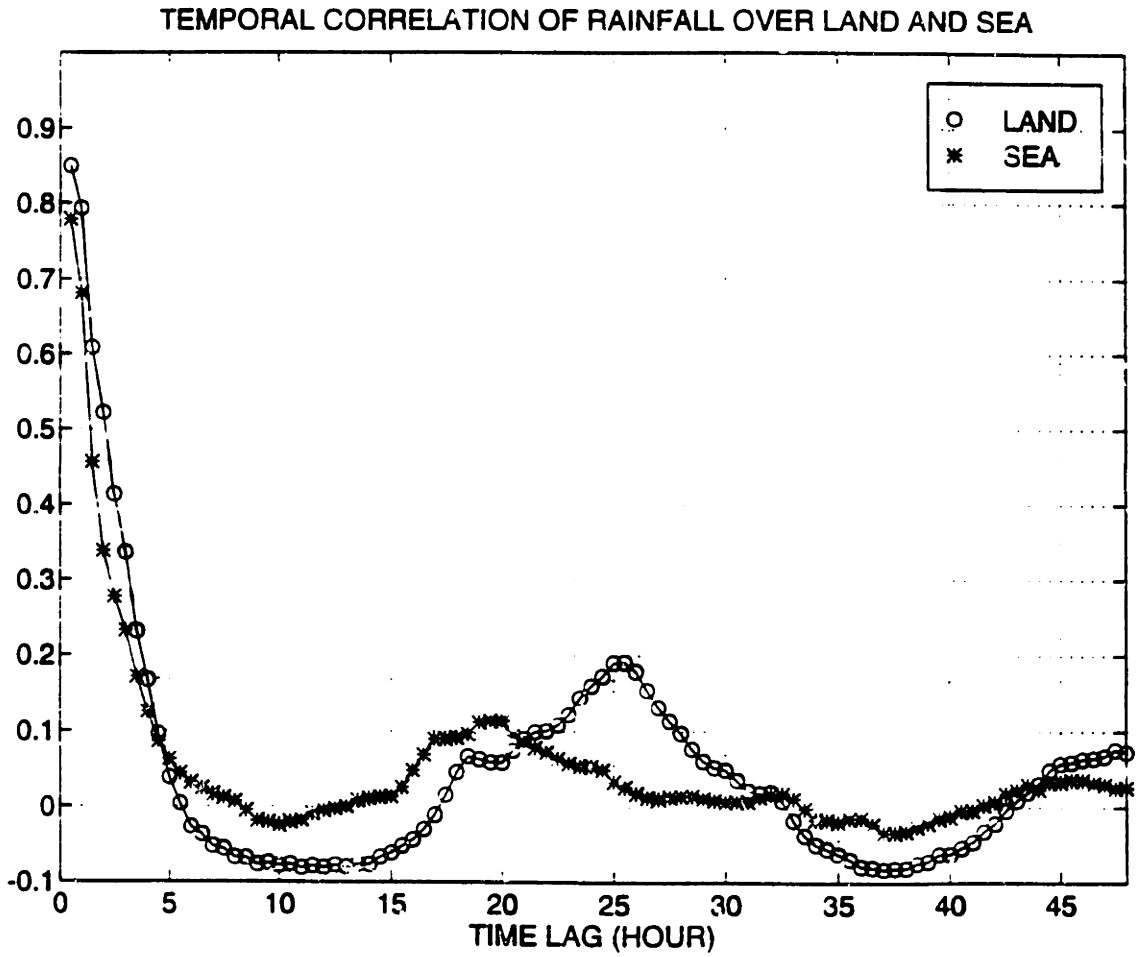

Figure 2-15: Autocorrelation of areal rain rate over land and sea.

In the non-stationary treatment, the autocorrelation is computed as

$$\rho(t_1, t_2) = \frac{Cov(t_1, t_2)}{\sigma(t_1)\sigma(t_2)} \tag{2.10}$$

where $Cov(t_1, t_2)$ =E$[(r(t_1) - m(t_1))(r(t_2) - m(t_2))]$, and $m(t)$ and $\sigma(t)$ are the time-dependent mean and standard deviation. Here we consider only diurnal variation, i.e., $m(t + 24n) = m(t)$ and $\sigma(t + 24n]) = \sigma(t)$, where time is in hours and n is an integer. To reflect the diurnal cycle of rain, a whole day is divided into 24 1-h bins, with bin 1 covering from midnight to 0100 LST, and bin 2 from 0100 LST to 0200 LST, etc. Each bin has a mean and a variance. The correlation $\rho(t_1, t_2)$ is computed and made into a look-up table as a function of the bins and the number of days apart that correspond to t_1 and t_2. A portion of the table is shown in Tables 2.1 and 2.2 for the the region with 113-km radius centered at the radar site. For example, suppose t_1 and t_2 are within the same day, t_1 is 0130 LST and t_2 is 0220 LST (meaning that t_1 belongs to bin 2 and t_2 belongs to bin 3). Then from Table 2.1 one finds that the correlation is $\rho(t_1, t_2) = \rho(t_2, t_1) = 0.88$. The computation of correlation involves averaging within a bin; therefore even if both t_1 and t_2 belong to the same bin (but they are usually not exactly the same time), the correlation is less than 1. Suppose now that t_1 and t_2 are not located within the same day, but t_1 is one day ahead of t_2, say t_1 is 2230 LST 1 December 1989 and t_2 is 0120 LST 2 December 1989. Then we look at Table 2.2 with $t_1 = 23$ and $t_2 = 2$, and find that the correlation is $\rho(t_1, t_2) = 0.35$. The various columns in Table 2.1 correspond to the correlation between a particular bin (t_2) and all the other bins (t_1). It can be observed that the correlation decays with increasing lagtime. It is interesting, however, to note that the correlation between morning and night hours of the

same day is quite high (e.g., for $t_1 = 23$ and $t_2 = 7$ the correlation is 0.77). This is because rain is usually small during these two periods of the day, and occasional rainfall that occurs both during the morning and the night on the same day will contribute to such high correlation. However, because the mean rain rate and standard deviation during the morning and the night hours are low, this high correlation has only a small impact on the actual sampling error of monthly rainfall. Another feature to note about the correlation structure is that there are no peaks around multiples of 24 hours. The diagonal elements in Table 2.2 correspond to correlation at 24-hour lagtime, and they are very small. This means that the diurnal cycle has been accounted for in the diurnally varying mean and standard deviation.

2.4 Quantification of Sampling Error

2.4.1 Stationary Process

Assuming a stationary rainfall process and using information about the mean, CV, and correlation obtained in the previous section, the sampling error associated with the estimate of space-time rainfall for various sampling frequencies can be evaluated using (2.8). Equation (2.8) contains two factors, CV and ϕ, where CV is the coefficient of variation of the rainfall process and ϕ is a function of the rainfall autocorrelation and the sampling frequency. When the measuring period T is fixed at 30 days, ϕ can be computed for various sampling frequencies, as shown in Figure 2-16. One can see from Figure 2-16 that, although large areas tend to have smaller values of ϕ, the differences are generally small except at some particular hours. At Δt=12 h, for example, the four areas shown in the figure all have ϕ values around 0.1. Generally, ϕ increases

t1 and t2 are located within the same calendar day										
t1	t2=1	2	3	4	5	6	7	8	9	10
1	0.97	0.86	0.57	0.44	0.35	0.35	0.25	0.34	0.20	0.14
2	0.86	0.97	0.88	0.77	0.56	0.45	0.29	0.41	0.28	0.19
3	0.57	0.88	0.99	0.95	0.69	0.46	0.26	0.37	0.26	0.17
4	0.44	0.77	0.95	0.99	0.79	0.51	0.27	0.33	0.20	0.13
5	0.35	0.56	0.69	0.79	0.93	0.81	0.49	0.35	0.14	0.08
6	0.35	0.45	0.46	0.51	0.81	0.95	0.78	0.52	0.16	0.08
7	0.25	0.29	0.26	0.27	0.49	0.78	0.97	0.69	0.25	0.07
8	0.34	0.41	0.37	0.33	0.35	0.52	0.69	0.90	0.78	0.57
9	0.20	0.28	0.26	0.20	0.14	0.16	0.25	0.78	0.96	0.92
10	0.14	0.19	0.17	0.13	0.08	0.08	0.07	0.57	0.92	0.98
11	0.08	0.13	0.11	0.08	0.03	0.01	0.01	0.43	0.88	0.96
12	0.00	0.02	0.03	0.00	-0.04	-0.06	-0.05	0.42	0.84	0.92
13	-0.03	0.00	0.01	-0.02	-0.07	-0.10	-0.08	0.27	0.69	0.79
14	-0.10	-0.07	-0.06	-0.08	-0.13	-0.17	-0.12	0.10	0.35	0.42
15	-0.14	-0.11	-0.08	-0.09	-0.14	-0.18	-0.15	-0.01	0.15	0.19
16	-0.17	-0.13	-0.08	-0.06	-0.11	-0.16	-0.16	-0.06	0.07	0.11
17	-0.17	-0.10	-0.03	-0.01	-0.05	-0.11	-0.13	-0.09	-0.02	0.01
18	-0.15	-0.05	0.05	0.09	0.09	0.11	0.30	0.14	0.00	-0.05
19	-0.01	0.08	0.15	0.18	0.21	0.27	0.50	0.29	0.04	-0.04
20	0.17	0.25	0.29	0.33	0.50	0.56	0.61	0.37	0.09	0.02
21	0.12	0.19	0.23	0.27	0.51	0.63	0.62	0.32	0.02	-0.04
22	0.22	0.24	0.21	0.23	0.45	0.63	0.72	0.41	0.07	-0.02
23	0.32	0.30	0.21	0.20	0.46	0.65	0.77	0.45	0.10	0.01
24	0.14	0.14	0.10	0.09	0.32	0.56	0.75	0.40	0.07	-0.01

Table 2.1: A portion of the correlation look-up table. t1 and t2 are located within the same calendar day.

t1 is one calendar day ahead of t2										
1	0.08	-0.02	-0.03	-0.05	-0.07	-0.07	-0.06	-0.07	-0.05	-0.04
2	0.13	-0.01	-0.02	-0.03	-0.06	-0.07	-0.08	-0.07	-0.05	-0.04
3	0.12	-0.02	-0.03	-0.03	-0.05	-0.07	0.07	-0.07	-0.05	-0.05
4	0.10	-0.02	-0.03	-0.04	-0.06	-0.07	-0.07	-0.06	-0.04	-0.05
5	0.14	-0.01	-0.02	-0.02	-0.06	-0.08	-0.08	-0.06	-0.05	-0.06
6	0.28	0.08	0.03	0.04	-0.01	-0.06	-0.09	-0.08	-0.06	-0.06
7	0.51	0.22	-0.02	-0.04	-0.06	-0.06	-0.08	-0.08	-0.06	-0.06
8	0.29	0.09	-0.05	-0.07	-0.08	-0.08	-0.07	0.06	-0.04	-0.05
9	0.07	0.01	-0.03	-0.03	-0.06	-0.06	-0.01	0.05	0.04	0.00
10	0.00	0.00	0.01	0.00	-0.02	-0.02	0.04	0.15	0.11	0.03
11	-0.02	-0.03	-0.02	-0.02	-0.05	-0.05	-0.01	0.06	0.04	0.01
12	-0.04	-0.03	-0.02	-0.03	-0.04	-0.05	-0.02	0.02	0.01	-0.02
13	-0.07	-0.05	-0.04	-0.04	-0.03	-0.02	0.00	0.00	-0.03	-0.05
14	-0.11	-0.07	-0.04	-0.02	0.09	0.14	0.19	0.05	-0.04	-0.07
15	-0.14	-0.11	-0.08	-0.02	0.20	0.29	0.31	0.08	-0.06	-0.07
16	-0.15	-0.13	-0.10	-0.04	0.18	0.26	0.24	0.02	-0.11	-0.12
17	-0.15	-0.15	-0.12	-0.08	0.06	0.08	0.04	-0.08	-0.15	-0.16
18	0.27	0.08	-0.09	-0.10	-0.05	0.01	0.06	-0.04	-0.11	-0.13
19	0.43	0.19	-0.05	-0.10	-0.11	-0.09	0.00	-0.06	-0.10	-0.11
20	0.44	0.19	-0.02	-0.07	-0.07	-0.08	-0.04	-0.08	-0.09	-0.09
21	0.42	0.18	0.01	-0.02	-0.05	-0.04	-0.02	-0.06	-0.08	-0.07
22	0.59	0.28	0.03	-0.01	-0.04	-0.03	-0.01	-0.02	-0.04	-0.05
23	0.65	0.35	0.09	0.03	0.00	0.01	0.04	0.03	-0.01	-0.02
24	0.83	0.56	0.26	0.19	0.13	0.15	0.13	0.17	0.08	0.05

Table 2.2: A portion of the correlation look-up table. t1 is one calendar day ahead of t2.

with increasing Δt, but sometimes a larger Δt produces a smaller ϕ. This is due to the particular shape of the empirical autocorrelation function. At Δt=24 h, ϕ has a jump and larger areas tend to have larger ϕ values, which is the result of the diurnal cycle (rainfall averaged over larger areas has stronger diurnal signal, see Figure 2-12 where rainfall averaged over the 113-km radius has the largest amplitude of correlation at multiples of 24 hours).

To get the estimate of the percentage sampling error, one only needs to multiply the ϕ function by the coefficient of variation CV. The CV can be obtained from Figure 2-7. For example, for radar coverage radii of 30, 60, 90, and 113 km (i.e., circles covering both land and sea), for instance, the CV is found to be 4.4, 3.5, 2.6, and 2.3, respectively. Multiplication of ϕ by CV produces the plots in Figure 2-17, which give the sampling error as a fraction of the mean for various areas and sampling frequencies. For example, at Δt=12 h, sampling errors are about 42%, 38%, and 26% for radii of 30, 60, and 113 km, respectively. For an estimate of the sampling error for larger areas, say 500 km $\times$ 500 km, visual extrapolation of Figure 8 yields a CV value around 1.0, if such extrapolation can be validly made. Assuming that the ϕ function for the 500 km $\times$ 500 km area does not change from that for the 113-km radius, the sampling errors at Δt=12 h and Δt=24 h are found to be about 11% and 37% for complete coverage of the area at each visit.

The sampling error is proportional to the value of CV. Since the CV for the Darwin rainfall decreases with increasing area at a much faster rate than the GATE CV, its sampling error also decreases at a faster rate. For smaller areas, the sampling error for Darwin is expected to be larger than that of GATE because of the larger CV. For larger areas the difference in the sampling errors for the two sites may be reduced, with Darwin having a somewhat larger error

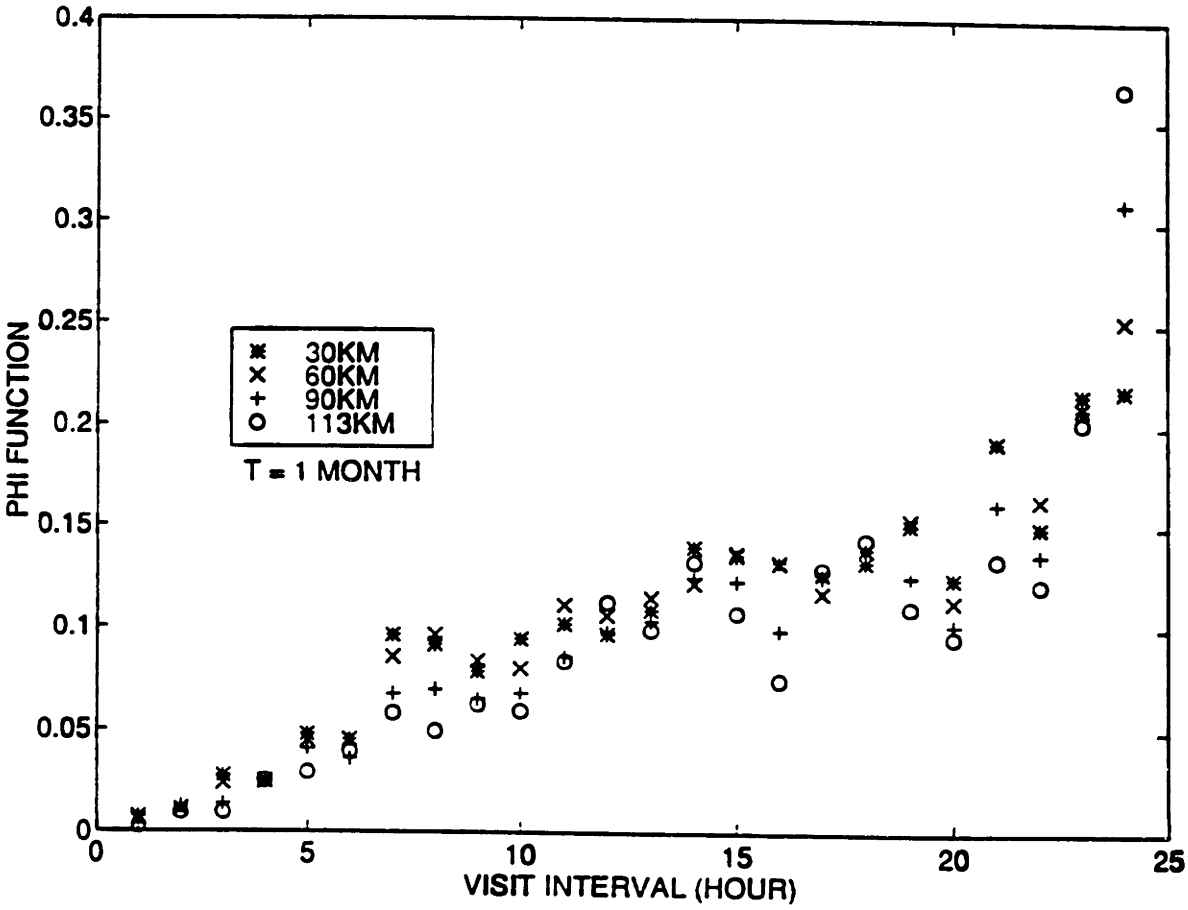

Figure 2-16: ϕ as a function of sampling interval for 30-km, 60-km, 90-km, and 113-km radii.

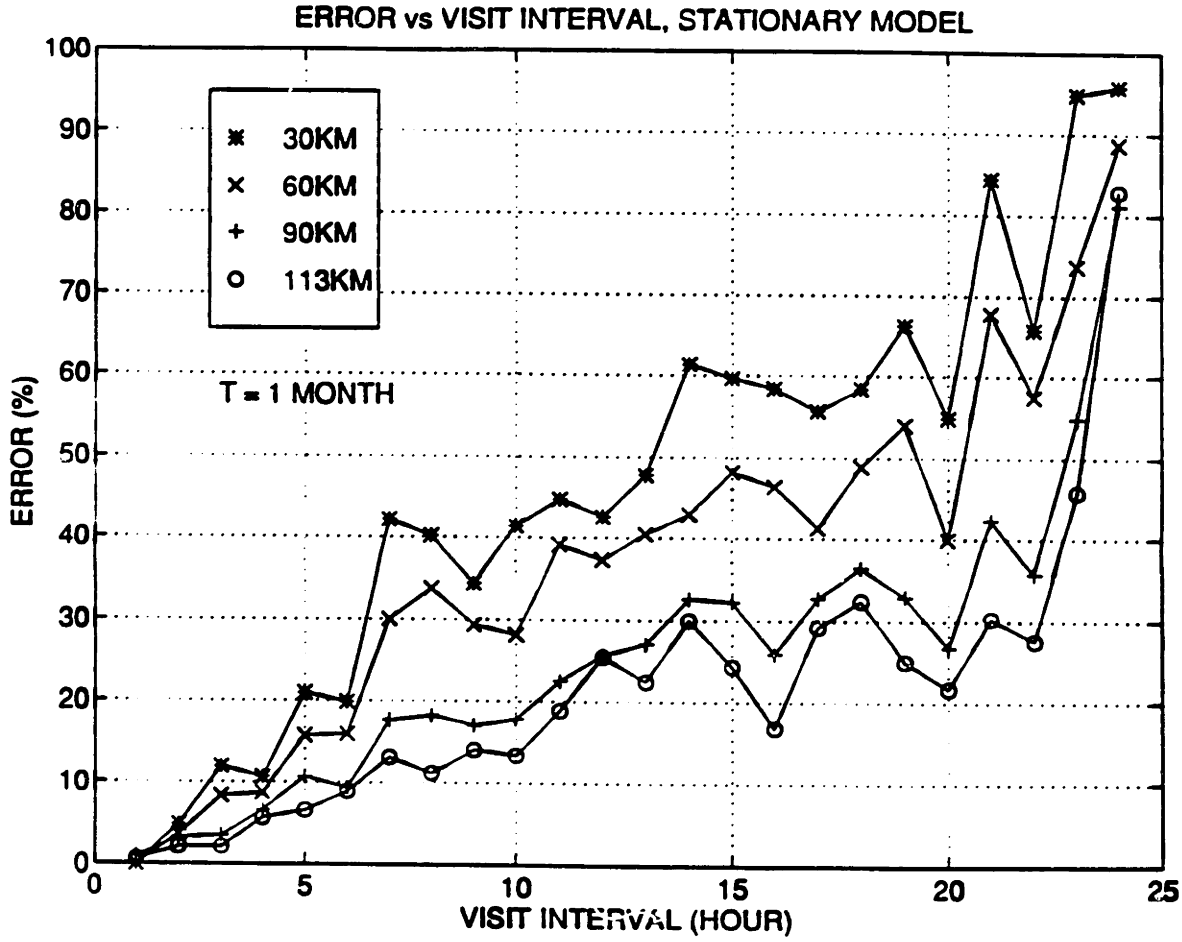

Figure 2-17: Sampling error as a function of sampling interval for 30-km, 60-km, 90-km, and 113-km radii; stationary model.

than those reported by Bell et al. (1990) and North et al. (1993).

2.4.2 Non-stationary process

The stationary treatment described in 2.4.1 ignores the fact that rainfall has a diurnal cycle in the mean and variance. It treats this diurnal cycle only implicitly in the autocorrelation function. The error estimates obtained from such stationary treatment do not depend on the specific times at which the samples are taken. To allow the error estimates to vary with the absolute sampling time, the non-stationary model of (2.6) must be used. This model requires the quantification of the time-dependent mean, variance, and autocorrelation of the rainfall process. These quantities have been computed and discussed in Section 2.3. Using the model, sampling errors for monthly rainfall over areas of various sizes can be evaluated as a function of sampling frequency and starting sampling time. Figure 2-18 shows the sampling errors of monthly rainfall for the 113 km radius. Each small plot corresponds to a sampling frequency and the bars in the plot correspond to various starting sampling times. For example, the first plot (upper-left) has a visit interval of dt=1 h and the only bar represents the sampling error of monthly rainfall when the sampling starts from 0100 LST of the first day. Since the visit interval is 1 hour, starting from 0100 or any other hour will result in the same hours being visited and hence in the same sampling error. Thus only one bar is shown in this first plot. Generally the sampling errors increase with increasing visit interval. For some visit intervals, such as 12-h, the errors change with the starting time and the maximum error can be twice as large as the minimum. For some other visit intervals, such as 5-h, however, the errors stay nearly the same for all starting times. This is because for certain visit intervals, not all hours of the day are

sampled during the month, and different starting times result in different sets of hours being visited. For example, for a 12-hour interval, if the sampling starts at 0100 of the first morning, the only two times that are sampled during the month are 0100 and 1300; similarly, if the sampling starts at 0200 of the first morning, only 0200 and 1400 are sampled. Such different sampling times result in different sampling errors due to the diurnal cycle of rain. For other visit intervals, almost every hour of the day is sampled during the month regardless of the starting time, resulting in a nearly constant error estimate. At an interval of 5 hours, for example, each hour of the day is sampled 6 times during the month no matter when the sampling starts (although the starting time must be located within the first day).

Cyclicity can be observed in some of the plots in Figure 2-18. For example, with visits at 18-h interval there are three cycles in the bar chart. The reason is that starting at 0100, 0700, and 1300 results in the same set of hours of the day being visited; likewise, starting at 0200, 0800, and 1400 results in another identical set of hours being visited, thus producing the cyclicity. The same phenomenon happens for the 20-h interval (middle column, second plot from bottom), where there are 5 cycles of period 4 in the bar chart.

Figure 2-18 is intended to show the effect of starting time on the sampling error when the diurnal cycle is explicitly considered in the non-stationary model. Compared with the stationary model, the non-stationary model provides more detailed information. When the results of the non-stationary model are averaged over starting times, they reduce to the stationary model results. This is shown in Figure 2-19 where the circles represent stationary model results and the cross signs are averages of the non-stationary model errors over all starting times, for various visit intervals. The match is quite good.

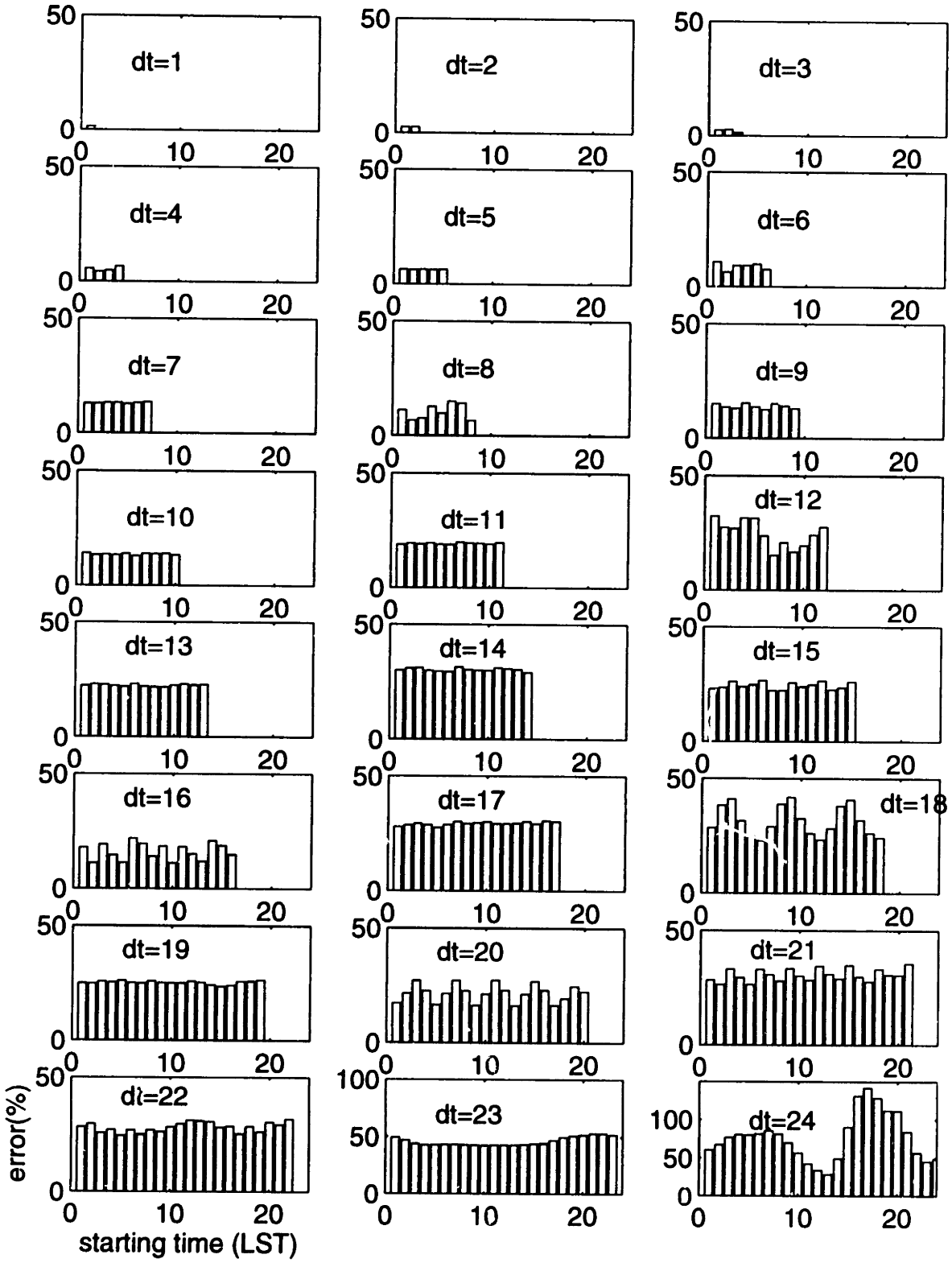

Figure 2-18: Sampling error (as a percentage of mean) versus sampling interval (dt in hours) and starting time (local time); non-stationary model.

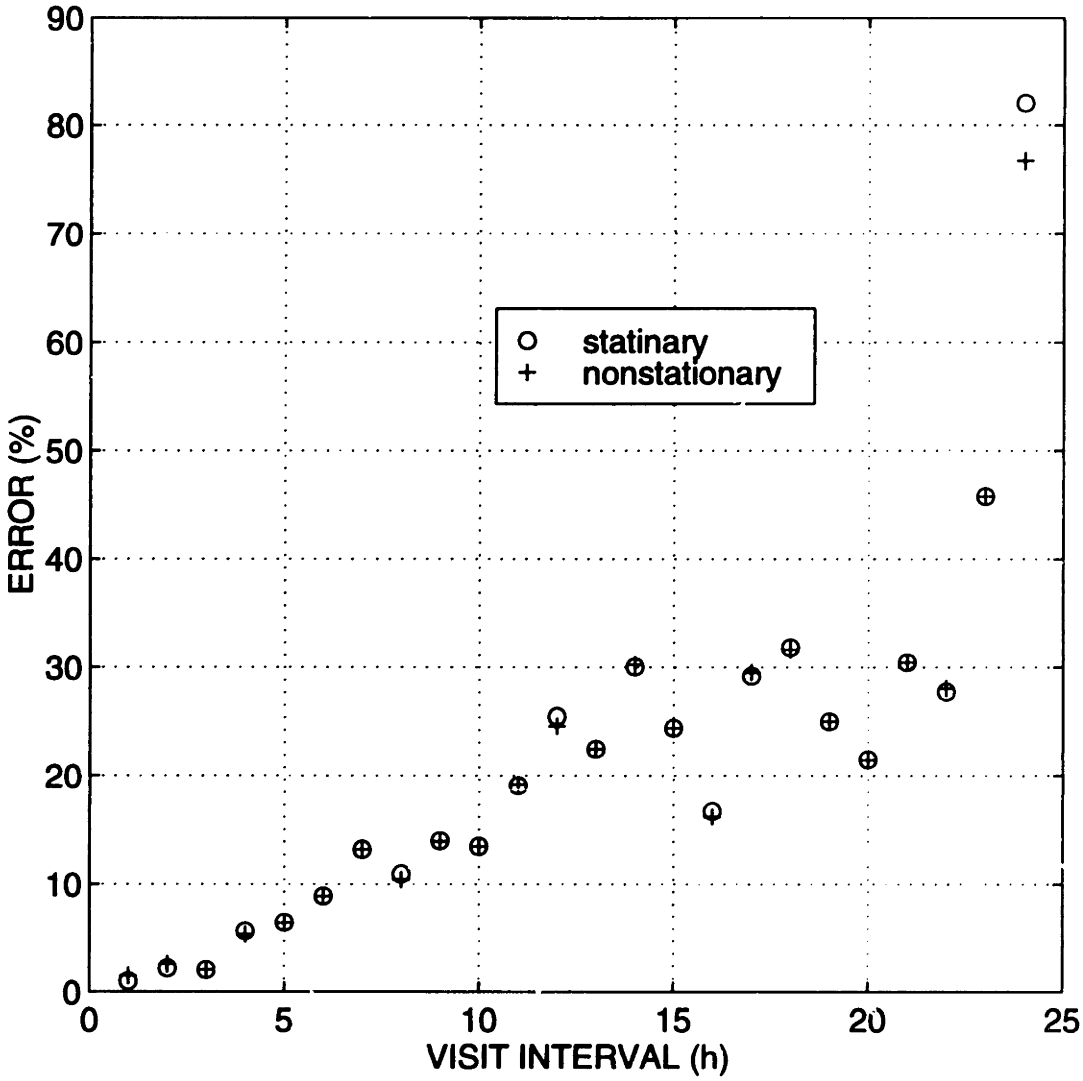

Figure 2-19: Comparison between stationary and non-stationary models.

2.4.3 Sampling Experiments Using Observed Data

Another way of estimating the sampling error is to use the original rainfall data to perform sampling experiments. The sampling errors obtained this way are realizations of a sampling process and may deviate considerably from the pattern of standard deviations produced by the models. McConnell and North (1987) have used this method to study GATE rainfall and found that the errors are within 10% of the true rain for a 400 km × 400 km box and periods of 15–18 days. Their results do not depend on the exact sampling time, apparently due to the lack of diurnal cycle in the GATE rainfall.

We considered a period of 30 days, consisting of day 61 to day 88 and day 92 to day 93 (there were no measurements from day 89 to day 91; see Figure 2-2).

The rainfall process is sampled at intervals ranging from 1 to 24 hours and with various starting times. These experiments have been done with the 113 km radius data. The sampling errors are presented in Figure 2-20 as percentages of true rain. It can be observed that the sampling error varies with starting times. For example, for a 12-h sampling interval, starting at 0100, 0200, 0900, 1000, 1100, and 1200 results in underestimation of the monthly rainfall, while starting at 0400, 0500, 0600, 0700, and 0800 results in overestimation of rainfall.

As this is only a single experiment, the errors for each starting time and each visit interval cannot be easily compared with the statistical results of the non-stationary model. However, when averages are taken over various starting times, comparison with the stationary model should be possible. This is shown in Figure 2-21 where the cross signs represent the averaged results (standard deviation) of the experiments and the circles are the stationary model

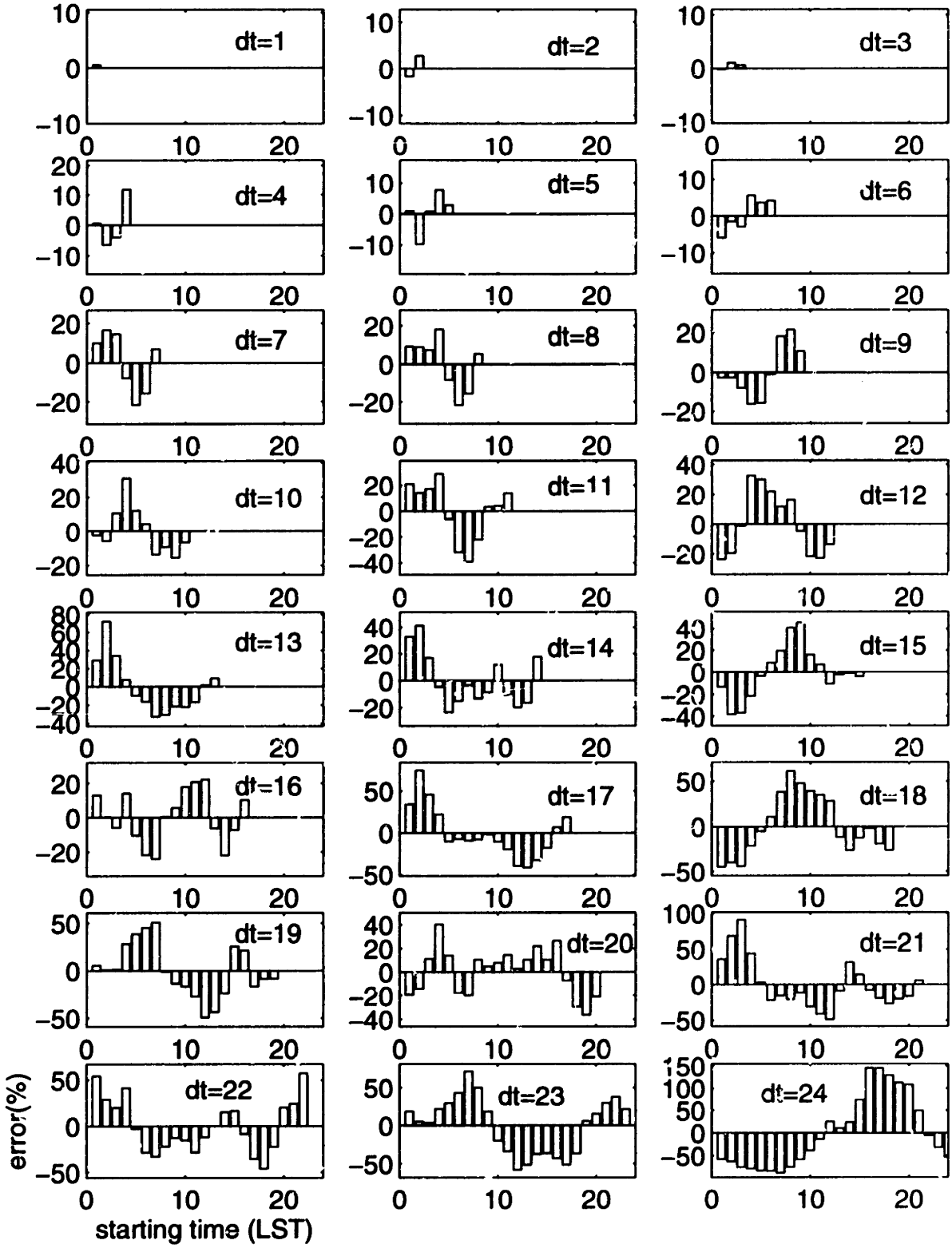

Figure 2-20: Sampling error (as a percentage of mean) versus sampling interval (dt in hours) and starting time (local time); empirical sampling experiment using radar-observed data.

results. Considering that the experiments consist of only one month of data, the correspondence is quite good.

2.5 Sampling Error Summary

Rainfall data from Darwin have been analyzed for the variability in mean, variance, temporal correlation, and the errors associated with discrete sampling schemes. Within the radar coverage, the rainfall over the central portion of the sea surface generally has a smaller mean than on land, while near the coast the sea rainfall is strongly influenced by local land. The standard deviation of area-averaged rain shows a similar pattern, being larger over the land and smaller over the sea. The coefficient of variation (CV) is smaller and is spatially more stable over the land, varying from 8 to 9 for a 10 km by 10 km area; while over the sea the CV varies from 9 to over 13 for the same area size. Up to the maximum area available within the radar coverage ($\sim 2 \times 10^4$ km^2), the CV remains larger over the sea than over the land. However, the CV decreases with area faster over the sea than over the land, and at large areas (beyond radar coverage) they may converge. Compared with GATE, the Darwin rainfall has larger CV at the small areas for which data are available, which means that the sampling error is expected to be larger for Darwin.

The temporal correlation of area-averaged rain over Darwin is weak at short lag times compared with the GATE data, a manifestation of short-lived storms. On the other hand, a strong diurnal cycle exists which peaks in the afternoon. The diurnal cycle is strongest for the island, followed by the continental land and the sea. One feature is that although rainfall over both land and sea is rare and has moderate intensity during the early morning hours, the sea receives

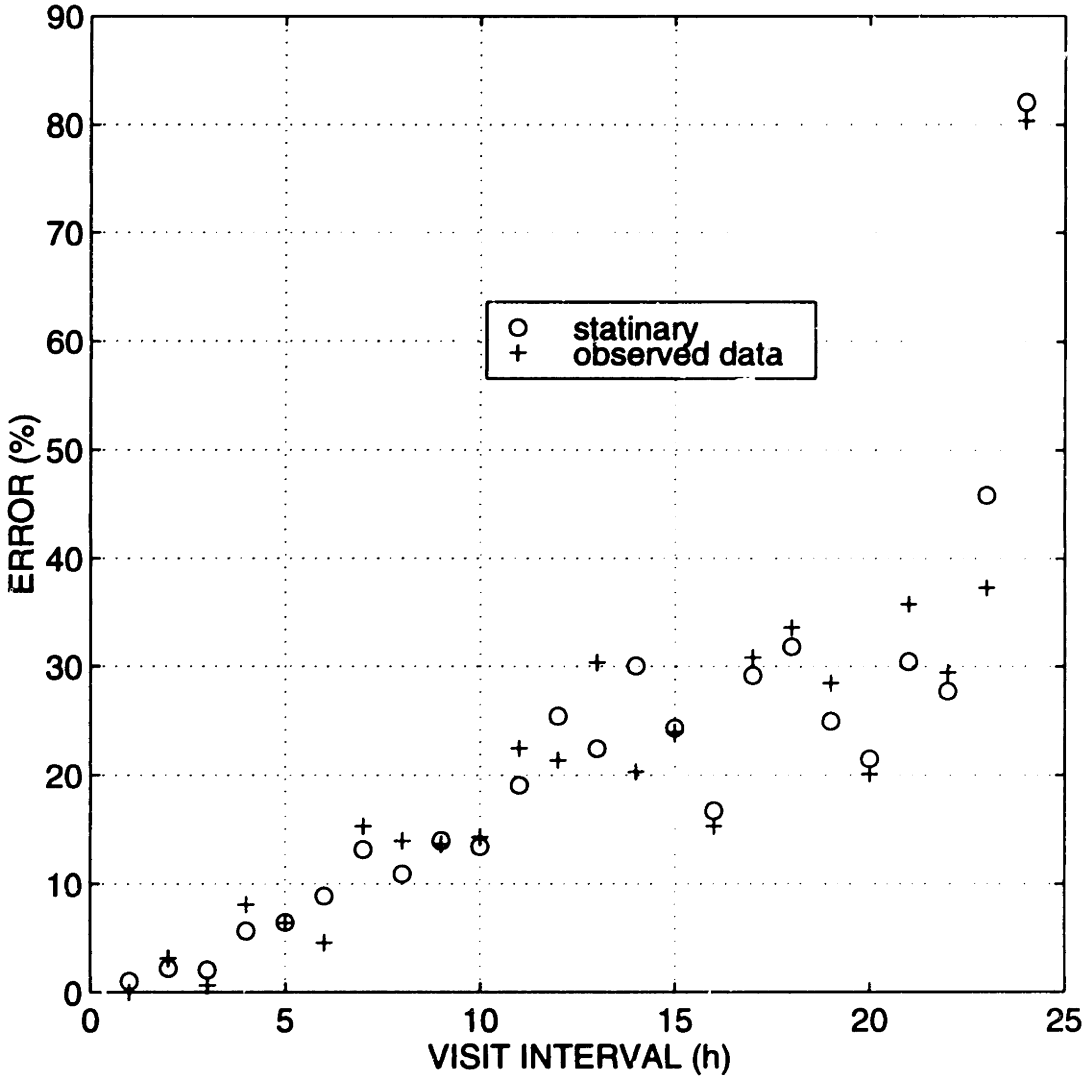

Figure 2-21: Comparison between model and empirical results.

more rain than the land during that period. During the day, this trend is reversed and the land receives much more rain than the sea.

The intermittent and localized nature of the Darwin rainfall has also been studied. For a 25 km by 25 km box, the probability of rain at a generic point in time is about 0.1, with lower values over the sea (0.07–0.11) than over the land (0.10–0.14). On average, only about 10% of the area within such a box receives rain when the box as a whole experiences non-zero rain. This percentage value is smaller over the sea (6.6–12.7) than over the land (8.8–16.2). Such features have implications on space-based rainfall measurement in that low probability of rain creates difficulty for the satellite to catch rainy scenes and increases sampling error. Also, highly localized rain cells are smaller than the sensor's field of view and thus decreases the sensitivity of the sensor to the rain.

Both stationary and non-stationary models have been used to quantify the sampling error associated with space-based measurements of space-time rainfall. The non-stationary model provides important information about the effect of the diurnal cycle on the sampling error. This effect is absent in stationary rainfall representations. When a diurnal cycle is present, the sampling error is generally sensitive to the starting sampling time.

Empirical sampling experiments, in which the sampling errors are calculated directly from the rainfall data, also show sensitivity of the sampling error to the starting time. This is different from the GATE results (McConnell and North 1987). When the results of the experiments are averaged over various starting time, they match the stationary model results quite well.

Chapter 3

Overview of Passive Microwave Remote Sensing of Rainfall

3.1 Basic Principles

Remote sensing of rainfall from space started in the 70's when satellite imagery became available. Early studies focused on the use of visible and infrared imagery, which tried to statistically relate the brightness of the observed cloud (visible frequency) or the upwelling long wave radiation (infrared frequency) to the surface rainfall. These techniques are called indirect since the rain drops are not directly observed at these wavelengths. Because rain drops are not observed directly the indirect method is not able to determine the instantaneous rain rate with good accuracy. In contrast to the visible and infrared frequencies, radiation at microwave frequencies is strongly modulated by precipitation-sized particles. Upon making some reasonable assumptions about the raining cloud and the underlying surface, the surface rain rate can be quantitatively related to the upwelling microwave radiation through radiative transfer calculations. This property makes the microwave remote sensing of rainfall more physical,

and hence it is called a "direct method". It is this direct method that we are dealing with in this study.

To give a brief account of the basic principles of passive microwave remote sensing of rainfall, let's start by mentioning that any object with temperature above 0 °K emits electromagnetic radiation at all frequencies. The amount of the radiated energy within any frequency band depends on the physical temperature and the emissivity ϵ of the material. Virtually all materials have emissivity less than 1. An ideal object with an emissivity of 1 at all frequencies is called a black body, whose radiation is described by Planck's law of radiation which expresses the radiation as a function of the physical temperature of the black body and the electromagnetic frequency. At a given temperature the amount of radiation is different at different frequency regions. The frequency at which the radiation is maximum is determined by Wein's law. At a temperature of about 6000 °K, for example, the sun emits most of its radiation in the visible region, while the Earth, at a global mean temperature around 250 °K, emits most of its radiation in the infrared region. This is why many Earth-observing sensors operate in the infrared region. For a real material, the radiation amount or intensity at a given frequency is determined as the black body radiation at the same physical temperature multiplied by the emissivity of the material at that frequency. One can see that the radiation emitted from a real material is always smaller than that emitted from a black body of the same temperature. Or, in other word, if a material and a black body emit the same amount of radiation, then one can be sure that the black body must have a lower physical temperature than the real material. The relationship between the two temperatures is $T_{blackbody} = \epsilon T_{material}$. The quantity $\epsilon T_{material}$ is called the brightness temperature, and it is the quantity that can be directly

obtained from the sensor's measurement of radiation without knowing the actual emissivity of the observed object. Thus, the brightness temperature is a measure of the radiation amount or intensity. A material with low emissivity then has brightness temperature much lower than its physical temperature, and is regarded as electromagnetically cold. The calm ocean surface, for example, has an emissivity of about 0.4–0.5 at the microwave region (at about 1 cm wavelength), while the land surface generally has much higher emissivity. The ocean surface thus has much lower brightness temperature than the land as measured by a microwave sensor. For example, at the 37 GHz frequency (0.81 cm wavelength) the brightness temperature of the equatorial ocean under clear-sky conditions measured by a space-born sensor is about 175 °K, while the brightness temperature of land surface can be as high as 280 °K.

The upwelling radiation from the surface is modulated by the various constituents in the atmosphere. The radiation observed by the satellite sensor at the top of the atmosphere is the result of such modulation. Thus the radiation or brightness temperature observed by the sensor may be higher or lower than that of the surface, depending on the type of constituent in the atmosphere and the frequency region at which the sensor operates. In the microwave region two effects of rain particles are important, i.e., emission and scattering. Emission refers to the fact that rain particles (cloud droplets, rain drops, ice crystals, etc.) emit some radiation which is received by the sensor; the effect is to increase the observed brightness temperature. Scattering refers to the fact that the radiation which would otherwise be received by the sensor is scattered away from the sensor's viewing direction by large rain drops and ice crystals; the effect is to decrease the observed brightness temperature. At the lower frequency end of the microwave region or for small particles, the emission ef-

fect dominates, while the scattering effect dominates at the higher frequency end or for larger particles. In the intermediate frequency region, both effects exist. At frequencies such as 19 and 37 GHz and for small rain drops, emission dominates; while for large rain drops both emission and scattering play a role in modulating the upwelling brightness temperature. There observational evidence that at extremely high rain rate the presence of large rain drops and ice crystals actually causes the 37-GHz brightness temperature to decrease with increasing rain rate, due to scattering effects.

3.2 Literature Review

Singer and Williams (1968) reported one of the earliest observations of oceanic rainfall by passive microwave radiometers. The observations were made from an aircraft over the Florida Strait in October 1966 and February 1967 in four channels, including 15.8 GHz (1.9 cm). They were able to observe a few showers over relatively calm sea surfaces. The location of showers were monitored simultaneously by the U.S. Weather Bureau radar. The increase in T_B from the observed showers ranged from 10 °K to 75 °K over an ocean background with waves of 0.5 to 1.5 meters. The authors believed that these observations were of great implication on satellite oceanography and tropical meteorology, i.e., it is possible to locate from a satellite areas of rain comparable to the size of the antenna beam within large cloud systems, day or night. They pointed out that the ability to correlate the temperature increment with the rainfall intensity to the required degree of accuracy to permit inference of rainfall intensities from satellite would depend on a more detailed understanding of the scattering and attenuation effects of various types of rain and on understanding

and separating ocean temperature and emissivity from sea surface roughness variations. In a laboratory simulation, the authors showed that the roughening of the ocean surface by falling rain will produce a small additional T_B increase and that wind above 15 knots will produce an increase through the mechanism of foam generation, which will be some function of wind speed and which for extremely high winds may give T_B increments approaching those from moderate rain.

Wilheit et al. (1977) was perhaps the first to quantify the relationship between the upwelling microwave radiation and rainfall using a reasonably realistic cloud model. This work has influenced and served as a starting point for many subsequent efforts. The cloud model consists of a rain layer extending from the ocean surface to the freezing level. A modified Marshall-Palmer drop size distribution is assumed throughout the rain layer. The relative humidity is assumed to vary linearly from 80% at the surface to 100% at the freezing level. To compensate for the lack of cloud water content in the Marshall-Palmer distribution, a cloud with a density of 25 mg cm^{-2} is distributed through the 0.5 km beneath the freezing level. The ocean surface is assumed to have the reflectivity given by the Fresnel relations for a specular (smooth) surface. A lapse rate of 6.5 °C km^{-1} is assumed and the surface temperature (or, equivalently, the freezing level) is adjusted as a free parameter. Above the freezing level, the relative humidity given by the 1962 U.S. Standard Atmosphere for that altitude is assumed. Water droplets are described by the Lane and Saxton (1952) dielectric data. The angular distribution of reflection from the ocean surface is assumed to be Lambertian. The upwelling radiation from the ocean surface is modified by the clouds as it propagates upwards. Its variation with

height is governed by the equation of radiative transfer

$$\frac{dT_B(\theta)}{dz} + \gamma_{ext} T_B(\theta) = \gamma_{sca} \int_0^{\pi} T_B(\theta_s) F(\theta, \theta_s) sin\theta_s d\theta_s + \gamma_{abs} T(z) \qquad (3.1)$$

for an axially symmetric distribution of the γ's and T, and an axially symmetric scattering process. Here $T_B(\theta)$ is the radiance in the direction specified by the polar angle (θ), expressed as an equivalent black body temperature or brightness temperature. The coordinate z is distance along a ray path; θ_s is the scattering angle; γ_{ext} is the total attenuation due to scattering and absorption; γ_{sca} is the scattering coefficient; and γ_{abs} is the absorptivity. $F(\theta, \theta_s)$ is the angular distribution of the scattering integrated azimuthally and normalized such that $\int_0^{\pi} F(\theta, \theta_s) sin\theta_s d\theta_s = 1$; $T(z)$ is the thermodynamic temperature of the absorbing medium (hydrometeors). Physically, the first term on the left-hand side of the equation expresses the change in the radiance in a particular direction. The second term gives the contribution to this change due to both absorption and scattering away from the specified angle. The integral term on the right-hand side expresses the increase in radiance in the θ direction due to scattering from other angles, and the second term represents the thermal emission of the medium.

The extinction (= absorption + scattering) and absorption cross section of a liquid water droplet are given as

$$\sigma_{ext} = \frac{\lambda^2}{2\pi} R_e \sum_{n=1}^{\infty} (2n+1)(a_n + b_n) \qquad (3.2)$$

$$\sigma_{abs} = \frac{\lambda^2}{2\pi} R_e \sum_{n=1}^{\infty} (2n+1)(|a_n|^2 + |b_n|^2) \qquad (3.3)$$

where a_n and b_n are the magnetic and electric 2^n-pole coefficients. The absorp-

tivity of a volume of droplets can be related to the absorption cross section of a single droplet by

$$\gamma_{abs} = \int N(D)\sigma_{abs}(D)dD \tag{3.4}$$

where $N(D)dD$ equals the number density of the droplets within the radius interval $[D, D + dD]$.

Wilheit et al. used the Marshall-Palmer drop-size distribution $N(D) = N_0 e^{-\lambda D}$, where $\lambda = 81.56R^{-0.21}$, $N_0 = 0.16$ cm^{-4}, D is in cm, and R is the nominal rain rate in mm h^{-1}. The rain rate resulting from a given drop-size distribution can be calculated, ignoring updraft velocity, as

$$R' = \frac{4\pi}{3} \int V(D)D^3 N(D)dD \tag{3.5}$$

where Wilheit et al. used an expression for $V(D)$ given by Waldteufel (1973) as $V(D) = 965 - 1030e^{-12D}$ (cm s^{-1}). With the Marshall-Palmer distribution and assuming a wavelength of 1.55 cm (which is equivalent to a frequency of 19.4 GHz) and two cases of sea surface temperature of 273 °K and 293 °K, Wilheit et al. performed numerical integration to obtain coefficients of extinction and scattering as functions of rain rate R'. The results for the two different temperature cases were found to be within 10% of each other at all rain rates.

Using this model, the upwelling and downwelling brightness temperature was computed for a set of atmospheres and a range of rain rates for a wavelength of 1.55 cm. The surface temperatures were 279.6, 286.1, 292.6, 299.1 and 305.6 °K, giving freezing levels of 1, 2, 3, 4, and 5 km, respectively. Results showed that, above rain rate 1 mm h^{-1}, the brightness temperature increased sharply with increasing rain rate to a maximum at 20–50 mm h^{-1}. At higher rain

rates, the strong scattering by larger droplets actually decreased the brightness temperature. Generally, there was about a 50% change in rain rate for every kilometer increase in freezing level at a given brightness temperature.

Wilheit et al. also compared the model calculations with microwave brightness temperatures at a wavelength of 1.55 cm measured by the Electronically Scanning Microwave Radiometer (ESMR) on the Nimbus-5 satellite and rain rate derived from WSR-57 meteorological radar measurements. A specially designed ground-based verification experiment was also performed wherein upward viewing microwave brightness temperature measurements at wavelengths of 1.55 and 0.81 cm were compared with directly measured rain rates. It was shown that over the ocean areas, brightness temperature measurements from ESMR might be interpreted in terms of rain rate with about an accuracy of a factor of two over the range 1–25 mm h^{-1} and for a spatial scale equal to the field of view of the ESMR (25 km at nadir and degraded significantly with scan angle).

Kidder and Vonder Haar (1977) used Nimbus 5 ESMR data to study how frequently tropical oceanic precipitation occurred during the season December 1972 through February 1972. Their methodology involved determination of a zonal threshold T_B for the detection of precipitation during the season December–February. This was accomplished by combining the zonal mean freezing levels with the T_B–Rain results from an early version of the Wilheit et al. (1977) model. Brightness temperatures corresponding to the 0.25 mm h^{-1} rainfall rate were selected as the threshold to differentiate raining from nonraining observations on the basis that the T_B–Rain curves of the Wilheit model become flat at 0.25 mm h^{-1}. The authors acknowledged that the use of a threshold temperature to detect precipitation has several problems; among them are

that: (1) precipitating areas which do not fill the beam (500 km^2 at nadir) may not be detected and (2) local atmospheric and surface conditions may deviate from those used to calculate the T_B–Rain curves. ESMR data were stratified by position (5° latitude-longitude square) and local time, and the fraction of the observations above each of the zonal T_B thresholds was calculated, which may be interpreted as the frequency of precipitation regardless of intensity. The resulting frequency of precipitation reproduced the expected general patterns: (1) narrow convergence bands, (2) dry eastern oceans, and (3) the splitting of the ITCZ in the mid-Pacific. The authors warned that precipitation frequencies in the northwest oceans might have been biased upwards by the more frequent occurrence of strong winds in those areas.

Allison et al. (1974) used a model similar to that of Wilheit et al. (1977) to relate T_B at 19.35 GHz to surface rain rate. Since their objective was the application of the model to hurricane rainfall estimation using the Electronically Scanning Microwave Radiometer (ESMR) data, the details of the model were only briefly described. In essence, the model contains 30 1-km layers, from the surface to 30 km height. The mean temperature, pressure, density, water vapor, and molecular oxygen for each layer are used. Saturation, a constant liquid water content, and a uniform Marshall-Palmer drop size distribution are assumed for a given rain rate up to the freezing level (about 4 km). A "calm" ocean surface at a physical temperature of 300 °K is used in the model. A smooth surface is also assumed for which reflectivity can be calculated using the Fresnel equation for either horizontally or vertically polarized radiation. The model shows that T_B increases rapidly for low rain rates and becomes asymptotic to 280 °K at higher rates. Thus, unfortunately, only low rain rate (<10 mm h^{-1}) can be distinguished by the ESMR T_E values. For the higher rain rates, the ex-

tinction within the precipitating cloud is so large that only the freezing level at the top of the rain column is observed. The authors pointed out that in tropical cyclones, where surface winds are much above 7 m s^{-1}, sea surface roughness and foam may enhance the T_B considerably. Nonetheless they justified their use of a calm ocean by arguing that the emission from the sea surface is largely attenuated or eliminated by moderate (2–7 mm h^{-1}) to heavy rain rates (> 7 mm h^{-1}) which occur within 100–200 km of the storm center. Obviously, their justification requires that the rough sea surface is always fully covered by rain. In view of the uncertainty associated with sea states, the authors stated that the rain rate would only be semi-quantitatively characterized in their study.

This model was applied to a number of tropical cyclones. The estimated rain rate was grouped in three categories: < 2 mm h^{-1}, 2–7 mm h^{-1}, >7 mm h^{-1}. Spatial rainfall maps were shown to resemble the shape of the cyclone, including the spiral. However, it can be noticed that the spatial coverage of the estimated rain is very large. For example, the area covered by low rain rate could continuously span several hundred km, sometimes over 1000 km.

Since a raining cloud much smaller than the resolution of the sensor can be quite transparent, the early plane-parallel models of precipitating clouds was questioned by subsequent researchers. To quantify this effect, Weinman and Davis (1978) developed a model to compute the microwave radiances emerging from horizontally finite clouds. The model can compute the radiances emerging from the sides as well as from the top of the clouds. Their computation showed that T_B from horizontally finite clouds is lower than that emitted by plane-parallel clouds of the same thickness. They pointed out that, since the FOV subtended by 37-GHz radiometers covers an area of the earth which is frequently much larger than individual rain cells, the ambiguity in mean rain due

to such finite-cloud effect can be as large as a factor of 2 for a given brightness temperature.

Olson (1989) developed a model-based multi-channel algorithm for cyclone rainfall retrieval using the Scanning Multi-spectral Microwave Radiometer (SMMR) data. His model computes the brightness temperature from a 22.5 km by 22.5 km grid element covered with a finite-size raining cloud. The model has many parameters, including the total liquid water content (LWCT) and the fractional raining area (f). When applying the model to retrieve rainfall, all other parameters are prescribed and only the above two are allowed to vary until the model-calculated brightness temperature matches observation. The algorithm uses a variational method to determine the values of LWCT and f in all grid elements simultaneously. The optimal values of LWCT and f are sought which minimize the difference between the model-calculated and the observed brightness temperatures in all channels and in all grid elements. In the model, the vertical distribution of the hydrometeors includes liquid drops up to 4.8 km and ice hydrometeors from 4.8 to 9.8 km. A columnar water content for precipitation-sized ice hydrometeors is prescribed to be 0.35 of that for the liquid hydrometeors. The semi-empirical formulae of Wentz (1983) is used to express the ocean emissivity as a function of sea surface temperature and friction velocity u^* at the SMMR frequencies and viewing angle. The friction velocity in a cyclone situation is a function of the distance from the hurricane eye and the maximum wind speed at the 10-m elevation in the storm. The maximum 10-m wind speed can be estimated from data collected by ocean buoys, and the hurricane eye can be located by a local minimum in the 37-GHz T_B field. This algorithm was initially applied to SMMR imageries of three hurricanes utilizing the 37, 21, 18, and 10.7 GHz data (both polarizations), with a

maximum 10-m wind speed of 40 m s^{-1}, a maximum liquid water content of non-precipitating cloud of 0.2 g m^{-3}, and a height of the liquid layer of 4.8 km. The resulting rain retrievals were higher than the radar-derived rain rates by an average of 2.08 mm h^{-1}. Assuming that this bias was due to an error in the prescribed model parameters, somewhat altered parameters were specified to help reduce the bias. For each of the three hurricanes the maximum 10-m wind speed was increased by 10 m s^{-1}, the maximum liquid water content of non-precipitating cloud was increased from 0.2 to 0.4 g m^{-3}, and the height of the liquid layer was increased from 4.8 to 5.8 km. With these altered parameter values the total retrieval bias for the three hurricanes was reduced to 0.19 mm h^{-1}.

Kummerow et al. (1989) developed a multi-channel statistical approach and applied it to retrieve rainfall rates from brightness temperatures observed by passive microwave radiometers flown on a high-altitude NASA aircraft. The Microwave Precipitation Radiometer (MPR) on board the ER-2 aircraft measured at 18 and 37 GHz and the Advanced Microwave Moisture Sounder (AMMS) measured at 92 and 183 GHz. At a nominal altitude of 20 km, the ground resolution was ~3 km for the MPR channels and ~0.7 km for the 92-GHz channel. Their approach involved generating statistical relationships between the model parameters (rain, cloud water, surface properties, etc.) and the upwelling multi-channel T_Bs. For a given set of observed multi-channel T_Bs, the model parameters can be changed in all possible combinations until the model-calculated T_Bs agree with the observed values. Their cloud model consists of five independent layers. The first layer, which is below the freezing level, contains cloud water and precipitating water, and the higher layers contain varying amount of precipitating and non-precipitating water and ice. In applying the

model to a case study of light stratiform precipitation observed on 1 July 1986 off the coast of the Delmarva Peninsula near Wallops Island, Virginia, only the lowest two layers were assumed to contain hydrometeors. The layer which extends from the surface to the freezing level (4 km) was assumed to contain a uniform rain rate, R_L, and cloud liquid water, Q_L. The layer above the freezing level was initially assumed to be 2 km thick, to consist of ice particles, and to have an ice water content (IWC) of $0.5R_L$. The remaining three layers were assigned absorption properties of the U.S. Standard Atmosphere. To generate statistics of T_Bs at the MPR channels, the rain rate R_L, cloud liquid water Q_L, surface temperature T_S, and the surface wind speed U_0 were randomly varied. Since the rain rate was known to be light in this case, the rain rate, R_L, was allowed to vary between 0 and 20 mm h^{-1}. The cloud liquid water, Q_L, was allowed to vary between 0 and 0.7 g m^{-3}. The ocean surface temperature, T_S, was allowed to vary between 290 and 295 °K, while the surface wind speed, U_0, was allowed to vary between 3 and 9 m s^{-1}. The ranges of the last two variables were commensurate with local observations. The final root-mean-square difference in the brightness temperature using this single cloud model for the entire flight line was 4.6 °K, which, the authors concluded, was small in comparison to the size of the signal produced by rain or clouds (~50 °K). It was shown that the retrieved rainfall rate compared well with the radar-derived values. In studying the potential applications of this model to satellite rainfall retrieval, the authors considered an imaginary satellite measuring dual-polarized T_Bs at 18, 37, and 85 GHz with uniform ground resolution of 20 km. Satellite-observed T_Bs were simulated by randomly selecting values for the rainfall rate, the fractional raining area, and the non-precipitating cloud liquid content. Homogeneous non-precipitating clouds were assumed to fill the

entire footprint. With the simulated parameters serving as ground truth, the statistical approach was applied to the simulated data. The results showed that if the same model structure, which had been used to generate the data, was also used in the retrieval, the agreement was excellent (rms was 2.3 °K). In a second case where the five-layer simplification of the Wu and Weinman (1984) model was used in the retrieval, the rms increased to 2.5 °K (still considered small). In a final case where a very simple, 2-layer model was used to retrieve the rain, the errors were found to be quite large (rms was 13.1 °K).

Kummerow and Giglio (1994) extended the five-layer cloud model of Kummerow et al.(1989). A lognormal distribution was used for the rain rate in the raining portion of the footprint. In actual rain retrieval applications, the first step is to identify potential cloud structures. A cloud structure consists of a five-layer description of all hydrometeors in terms of the lowest-layer rain rate. Different sets of cloud structures were constructed based on the height of the freezing level to account for different climatic regimes. Their algorithm allowed freezing levels from 2.0 km to 4.5 km, at 0.5 km intervals. For each freezing level, statistics were derived for 27 cloud vertical structures. The surface rain rate, the fractional raining area, and the surface wind speed were treated as unknown variables. Rain rate was divided into four categories. The fractional raining area was allowed to vary between 0.5 and 1, and the surface wind speed was allowed to vary between 0 and 30 m s^{-1}. This algorithm was applied to Darwin, Australia and Japan. While the agreement between the algorithm and radar was good over Japan, there were cases of overestimation over Darwin. The authors attributed this overestimation to the difficulty the cloud-only algorithm was having, which resulted in the misinterpretation of cloud-only pixels as potentially raining. The authors also referred to the attenuation of the radar

signals.

Alongside the modeling approach which has been based on detailed calculations of radiative transfer through raining clouds, a number of researchers have taken an empirical or semi-empirical approach. Spencer et al. (1983a) compared the data taken by the higher-resolution channel (37 GHz) of SMMR with radar rain rates over the Gulf of Mexico, and found a correlation of 0.85. They pointed out that the primary modulator of the brightness temperatures was not rain opacity or rate, but instead the degree of filling of the 37 GHz footprint by the showers.

Petty and Katsaros (1990) related the polarization difference of T_B to raining area over the oceans and applied that relationship to map regions of precipitation using the SMMR data. Their approach was based on the fact that the microwave radiation from the water surface is highly polarized. At the oblique viewing angle (50.3°) of the SMMR on Nimbus 7, the microwave sea surface emissivity is larger for vertical than for horizontal polarization, so that over the unobscured ocean there is typically a 40–70 °K difference between the measured 37-GHz T_B in the two polarizations. The atmosphere, including rain, both attenuates and emits nearly independently of polarization, so that the polarization difference ($T_{B,V} - T_{B,H}$, where the subscripts V and H refer to vertical and horizontal polarization) associated with rain over the oceans is much smaller. The authors defined a normalized polarization difference P as

$$P = \frac{T_{B,V} - T_{B,H}}{(T_{B,V} - T_{B,H})_{CLR}} \tag{3.6}$$

where the subscript CLR indicates clear-sky conditions. By definition P equals unity when no clouds are present. When sufficiently heavy rain is present

throughout the sensor's field of view, P approaches zero. P can be thought of as a measure of the visibility of the sea surface through or between clouds and rain as seen by a microwave sensor from space, relative to a cloudless atmosphere under otherwise similar conditions. For the ideal situation in which rain and clouds in the FOV are uniformly distributed in the horizontal layer, the authors stated that P is approximately equal to the square of the slant-path transmittance, τ, through the raining clouds. In the case of extreme inhomogeneity, i.e., when most of the area of the FOV consists of regions of no rain together with regions of optically thick rain, the authors related P to the fractional coverage, f, of the FOV by rain as

$$P = 1 - f \tag{3.7}$$

Two advantages were cited for using P as an independent variable: (1) It allows simple (yet distinct) quantitative physical interpretations in both the horizontally homogeneous case and the extremely inhomogeneous case and (2) variations in P are expected to be more directly related to rain effects alone, because changes in microwave signature due to large-scale variability of sea surface emissivity, temperature, and atmospheric opacity due to gaseous components are, to a great degree, factored out when normalizing by the clear-sky polarization difference. In studying several tropical cloud clusters over the South China Sea, P was shown to be linearly related to $T_{B,H}$. When P was plotted against the rain rate averaged over the entire FOV, it was found that non-zero rain primarily occurred where $P < 0.8$. Beyond this, P appeared to contain little information about the actual average rain rate. The correlation coefficient between P and the FOV rain rate (for $P < 0.9$ only) was unimpressive

(r = -0.48). A scatter plot of P versus fractional coverage by radar echo (f_E), however, clearly showed a systematic increase in f_E with decreasing P. The correlation coefficient between P and f_E was much higher in this case (r = -0.81). The observed relationship was tentatively expressed as

$$f_E = 1 - \frac{P}{0.9} \tag{3.8}$$

for $P < 0.9$ and $f_E = 0$ for $P > 0.9$. This relationship was applied to the SMMR observations of cloud clusters to obtain estimates of the total area coverage by precipitation within the SMMR swath, as well as average fractional coverage by precipitation within the active regions of the clusters. The authors concluded that, despite the apparent lack of skill of the SMMR 37-GHz polarization measurements at retrieving rain intensities on a pixel-by-pixel basis, it is expected that the fractional coverage of rain obtained with these channels will prove to be usefully related to area-averaged rain rate for large enough samples.

Petty and Katsaros (1992) expanded on the results of Petty and Katsaros (1990, here after referred to as PK) by examining the relationship between the SMMR 37-GHz normalized polarization difference and the radar observations of oceanic precipitation during the Taiwan Area Mesoscale Experiment (TAMEX). Here, P was related to both the FOV average rain rate and the fractional coverage, f_Z, by radar echoes exceeding various reflectivity thresholds. In contrast to the results found by PK for two tropical cloud clusters over the South China Sea, there was recognizable correlation between P and the FOV rain rate, although the scatter was still large. The large scatter was attributed to the inhomogeneous rain within a FOV. Also in contrast to PK, no simple, straight-line relationship was found between P and the fractional coverage by

the radar echo at any reflectivity threshold. Nonetheless, the authors were able to derive theoretically a relationship between P and the radar reflectivity factor (Z) and used that relationship to obtain the upper and lower bounds of P for a given fractional echo coverage at a given reflectivity threshold. They equated P to the square of the slant-path transmittance τ,i.e.,

$$P = \tau^2 = exp(\frac{-2\sigma}{cos\theta}) \tag{3.9}$$

Where σ is the total liquid water optical depth

$$\sigma = K_{e,R}H + K_{e,L}L \tag{3.10}$$

In the above, $K_{e,R}$ is the mean volume extinction coefficient corresponding to rain rate R, H is the rain-layer depth, $K_{e,L}$ is the average mass extinction coefficient of non-precipitating cloud liquid water, and L is the column-integrated non-precipitating cloud water content. They used Savage's (1976) relation between $K_{e,R}$ at 37 GHz and R,

$$K_{e,R}(km^{-1}) = 0.077R^{0.97} \tag{3.11}$$

and the Marshall-Palmer $Z - R$ relationship $Z = 200R^{1.6}$ to arrive at a direct relationship between 37-GHz extinction and radar reflectivity factor of the form $K_{e,R}(\mathrm{km}^{-1}) = 3.1 \times 10^{-3}Z^{0.606}$. They further used $K_{e,L} = 0.267\ \mathrm{m}^2\ \mathrm{kg}^{-1}$ and a subjectively chosen linear relationship between L and $\log Z$ of the form $L(\mathrm{kg\ m}^{-2}) = 0.2 + 0.02\mathrm{db}Z$. With $\theta = 50°$ and $H = 4.5$ km, the following closed form for P and Z was obtained

$$P = 0.847Z^{-0.0722}exp(-0.0434Z^{0.606}) \tag{3.12}$$

This relationship was applied to radar reflectivity data (Z) to simulate the FOV average P and rain rate data. The relationship between P and the climatological mean rain rate was then obtained.

Prabhakara et al. (1992) developed an empirical relationship between the 37-GHz T_B and the FOV rain rate. Their algorithm was based on the empirical finding that the effective rain area, A, can be related to the logarithm of rain rate R as

$$log(1 + R) = aA \tag{3.13}$$

where a is a positive constant. Further, the brightness temperature above a certain threshold T^* was related to the rain area, i.e.,

$$T_B - T^* = bA \tag{3.14}$$

Combining the two equations yields

$$log(R + 1) = (a/b)(T_B - T^*) \tag{3.15}$$

A more general form was proposed as

$$log(R + 1) = (a/b)(T_B - T^*)^\chi \tag{3.16}$$

which allows for a possible nonlinear relationship. The FOV rain rate was given by

$$R = exp[\beta(T_B - T^*)]^\chi - 1 \tag{3.17}$$

where β^χ replaces a/b. This equation indicates that precipitation starts when T_B is higher than the threshold T^*. The authors suggested that T^* should be taken as the brightness temperature at the maximum in the probability density

function (pdf) or histogram of T_B. Determining T^* this way implicitly assumes that the portion of the histogram with $T_B > T^*$ corresponds to rain. Thus the parameters in the R–T_B model, β and χ, can be determined by matching the observed frequency distribution of R and T_B (with $T_B > T^*$). Data analysis showed that T^* can be further expressed as

$$T^* = T_{min} + 15 \tag{3.18}$$

where T_{min} is the minimum observed T_B for a region and during a season. And T_{min} in turn determines the water vapor content in the atmosphere as

$$w(gcm^{-2}) = (T_{min} - 126)/6.8 \tag{3.19}$$

Since the water vapor content varies with time and space and it influences the magnitude of the observed T_B, it was incorporated into the model which results in a modified R–T_B relationship

$$R = exp[\beta(w)(T_B - T^*)]^{\chi} - 1\gamma(w) \tag{3.20}$$

The dependence of β and γ on w and the magnitude of the constant χ were determined by tuning the R–T_B relationship to (1) July rainfall statistics obtained during GATE and (2) the summer rainfall climatology over the North Atlantic developed by Dorman and Bourke (1981), with the results $\chi = 1.7$, $\beta(w) = 0.012 + 0.003w$, and $\gamma(w) = 1.5 - 0.1w$. This model was used to obtain seasonal mean rain rate maps over the oceans between 50° N and 50° S. The retrieved rainfall patterns agreed well with the summer and winter maps of Dorman and Bourke (1979, 1981). The model was also used to retrieve the in-

stantaneous rain maps of three storms off the east coast of Florida using SSM/I data. The thresholds for the three storms were determined to be 170, 168, and 156 °K, respectively. The SSM/I-derived rain patterns were in general similar to those observed by radar. But in detail the SSM/I retrieval showed a rain area larger than that given by radar. The authors attributed this discrepancy to the alleged systematic underestimation by radar.

Instead of instantaneous rain rate, a number of algorithms have been designed to retrieve rain amount over one month or longer periods. Prabhakara et al. (1986) developed an algorithm for monthly rainfall over a large area (about 150 km on a side) using Nimbus 7 SMMR data. Their procedure involved (1) an estimate of liquid water content and (2) the estimate of rainfall based on an empirical relationship between surface rainfall and the liquid water content in the atmosphere. The liquid water content was estimated using the 6.6- and 10.7-GHz channels. The first step in their algorithm is to compute the quantity

$$\delta T_\nu = T_\nu - T_\nu{}^0 \tag{3.21}$$

where $T_\nu{}^0$ is the minimum observed brightness temperature at frequency ν in a given month and location, which is supposed to correspond to the undisturbed sea surface under clear-sky conditions; T_ν is the brightness temperature at a particular time during that month at the same location. Thus the deviation δT_ν indicates the effects of either sea surface roughness produced by wind or an appreciable amount of liquid water in the atmosphere associated with rain and clouds. A parameter, $r = \delta T_{10.7}/\delta T_{6.6}$, is used to distinguish between divergent and convergent wind. The authors argued that when $r > 1.2$, the presence of liquid is indicated (hence the wind is convergent). And under such condition the

difference between the deviations at 10.7 and 6.6 GHz may be used to deduce the liquid water content in the atmosphere as

$$l = a(T)(\delta T_{10.7} - \delta T_{6.6}) \tag{3.22}$$

where $a(T)$ is a coefficient that depends on the temperature of the liquid drops. The absorption by the droplets decreases by a factor of about 3 as temperature increases from -20 °C to 20 °C. The magnitude of $a(T)$ was determined through model simulations. In these simulations, $T_{10.7}$ and $T_{6.6}$ were first calculated for a number of model atmospheres (with different temperature and water vapor profiles) without liquid water. Then the two brightness temperatures were calculated again, adding to each model atmosphere a 1 km thick liquid droplet cloud with its base 1 km above the sea surface. The deviations $\delta T_{10.7}$ and $\delta T_{6.6}$ due to the liquid in the clouds was deduced for each case. A functional fit to the model results was given as

$$l = 20 \times \frac{\delta T_{10.7} - \delta T_{6.6}}{exp(\frac{31 - T_s}{T_s})} \tag{3.23}$$

where T_s is sea surface temperature in °C and l is expressed in mg cm^{-2}. To obtain surface rainfall from liquid water content, the authors produced mean seasonal maps of liquid water using 3 years of data and compared these maps with the rainfall climatology developed by Dorman and Bourke (1979, 1981). An empirical relationship between precipitation R (mm/season) and liquid water content l (10^{-3} g cm^{-2}) measured by SMMR was obtained as

$$R = 75(l - 2.3) \tag{3.24}$$

The linear relationship holds good at low rain amounts, but as the rainfall amounts get large ($\sim$ 1000 mm/season), as in the tropics, there is considerable amount of scatter. The authors commented that the scatter could be due to the poor climatology in the tropics where Dorman and Bourke's analysis was based on sparse amount of ship data.

Wilheit et al. (1991) developed an algorithm for the estimation of monthly rain totals for 5° cells over the oceans from histograms of SSM/I brightness temperature. The instantaneous FOV rain rate is assumed to follow lognormal distribution with mean r_0, variance ${\sigma_r}^2$, and probability of rain p. For a set of (r_0, σ^2, p), a rainfall distribution can be generated. With the freezing levels determined by the histograms of the vertically polarized brightness temperatures at 19 GHz and 22 GHz, each rain rate in this distribution is converted into a brightness temperature using an analytic approximation to the results of a radiative transfer model similar to that of Wilheit et al. (1977). After suitable renormalization, this set of brightness temperatures becomes the rain portion of the predicted histogram. An assumed normal distribution of non-rain T_B with mean T_0 and variance ${\sigma_0}^2$ is added to complete the predicted histogram. The comparison between the observed and the predicted histograms then is used to adjust r_0, p, ${\sigma_r}^2$, T_0, and ${\sigma_0}^2$. The final values of the lognormal parameters determine the monthly rainfall total. The most severe shortcoming of the algorithm, according to the authors, is the lack of correction for beam filling. This is expected to cause an underestimation of rainfall by as much as a factor of 2 with significant geographical variability. Because of this, the authors warned that the retrieved product must be considered an index rather than a measurement.

While the majority of algorithms are of the emission-type, a number of

studies have focused on the higher frequencies where the scattering by ice crystals is dominant. Wilheit et al. (1982) reported on a set of aircraft-borne microwave observations of Tropical Storm Cora. The results showed a strong inverse relationship between rainfall rate derived from 19 GHz observations and the microwave brightness temperatures at 92 and 183 GHz. Wilheit et al. demonstrated that only the presence of scattering by frozen hydrometeors over a 4-km thick cloud could explain the observations. Their results suggested that higher frequency observations might be useful in discriminating between liquid and frozen particles. Hakkarinen and Adler (1988) confirmed this with observations in a variety of situations over both land and water. Spencer et al. (1983b) also revealed the presence of very low brightness temperatures in SMMR 37 GHz observations over land. In all cases, the very low temperatures were observed to coincide with heavy convective rainfall and were attributed to the presence of a thick layer of precipitation-sized frozen hydrometeors. While this finding may make the scattering-based algorithms feasible, they are less direct than those based on the relationships between liquid droplets and rain rate in the case of absorption.

SSM/I instruments, whose highest frequency is 85.5 GHz, may provide a more robust capability for rain estimation. Some studies have show that SSM/I has strong scattering signals in the 85.5 GHz measurements in the presence of convection in the tropics. Spencer et al. (1989) have suggested that a technique using polarization corrected 86 GHz brightness temperature could provide quantitative estimates of areally averaged rainfall for both land and ocean areas in the mid-latitudes, as well as the tropics.

In most of these studies, four satellite-borne passive microwave imaging instruments have been used extensively. These are the Electronically Scanning

Microwave Radiometer (ESMR)-5 and ESMR-6 on Nimbus-5 and Nimbus-6, respectively, and the Scanning Multichannel Microwave Radiometer (SMMR) on Seasat and Nimbus-7, and the Special Sensor Microwave/Imager (SSM/I) on the DMSP (Defense Meteorological Satellite Program)-5D spacecraft. ESMR-5 and ESMR-6 make measurements only at single frequency of 19.35 GHz and 37 GHz, respectively. SMMR measured at 6.6, 10.7, 18, 21 and 37 GHz. SSM/I measured at 19, 22, 37, and 85.5 GHz.

Researchers have identified several common problems with microwave rainfall algorithms. In a discussion about the sources of error in the microwave measurement, Wilheit (1986) quoted (1) sampling, (2) inhomogeneity, (3) details of radiative transfer models, and (4) the scattering regime as major issues. The diurnal cycle and infrequent satellite visits are the sources of sampling error. Inhomogeneity of rain rate within a single field of view can lead to underestimation of average rain rate, because the relationship between rain rate and brightness temperature is highly nonlinear. This may result in a significant bias when many observations are averaged. Another source of error in microwave estimation of rain concerns the details of the radiative transfer model, where the freezing level, or the rain layer thickness, is the foremost important free parameter that controls the accuracy of the model. The model assumption of a liquid rain layer extending from the surface to the freezing level is clearly inadequate in warm-rain situations. Also the water vapor dependence of the brightness temperature is another degree of freedom that can introduce errors in the determination of rain intensity at low rain rates (less than about 5 mm h^{-1}), although this may be dealt with by multi-frequency observations. The issue of the scattering regime is not so well understood. The ice is usually modeled as an ensemble of spheres, but the shapes of the particles actually

found in a rainstorm are much more varied. Moreover, the distribution of ice particles for a given rain rate is completely unknown, and it is unlikely to be even approximately unique.

It is appropriate to point out here that the studies concerning microwave remote sensing of rainfall have been focusing on the cloud structure and the radiative transfer through it. Most of them have ignored the wind effects on the sea surface emissivity, and assumed a constant emissivity for all situations. Some of them have assumed random wind that is uncorrelated with local rain. As will be shown in the next chapter, such models will predict rainfall for a high brightness temperature where instead the high brightness temperature is caused by wind-enhanced emissivity of the sea surface and by factors other than rain.

Chapter 4

High Brightness Temperature Caused by Factors Other Than Rain

According to existing microwave rainfall retrieval algorithms (e.g., Wilheit et al. 1977), the increase in the brightness temperature at the lower microwave frequencies (<37 GHz) against the cold ocean background is mainly attributed to the absorption and emission of rain drops. In this chapter we will present observations which show that, contrary to these algorithms, a high brightness temperature is not always associated with surface rainfall. We will offer an explanation which attributes such high brightness temperature to wind and non-precipitating clouds. We will also discuss some earlier studies where wind effects might have been misinterpreted as rain.

4.1 Observations

4.1.1 Darwin, Australia Area

Simultaneous radar and satellite microwave observations of storms are available over Darwin, Australia during the Down-Under Doppler and Electricity Experiment (DUNDEE) which was carried out during two wet seasons (November 1988 – February 1989 and November 1989 – February 1990) (see Rutledge et al. 1992). The MIT C-band radar was installed near Darwin to collect rainfall data. The radar range was 56, 113, or 226 km, depending on the location of the storm. When the storm was close to the radar site, the short range was used to provide finer spatial resolution. Darwin is located on the north coast of Australia, so that the radar covered both land and sea surfaces (see Figure 2-1). Both PPI (Plan Position Indicator) scans with various tilts and RHI (Range Height Indicator) scans were made during storm events. For surface rain rate calculation the reflectivity measurements from the lowest tilt (about 1°) PPI scans have been used. The reflectivity data are converted from the original polar coordinates into Cartesian coordinates with 1 km by 1 km resolution, and rain rate is initially computed for the 1 km by 1 km grid using the $Z - R$ relation $Z = 400R^{1.3}$, where Z is the reflectivity factor in mm^6 m^{-3} and R is rain rate in mm h^{-1}. To account for the attenuation discussed in Chapter 2, however, the final rain rate has been obtained by multiplying the rain rate based on the above relationship by a factor of 5.

The microwave data we have used is from the SSM/I (Special Sensor Microwave/Imager). SSM/I is a microwave sensor flown on the Defense Meteorological Satellite Program (DMSP) satellites (Wentz 1991). There are now three SSM/I's in operation. The first was launched on 19 June 1987 aboard the DMSP

F-08 satellite. The second was launched on 1 December 1990 on the F-10 satellite. And the third was launched on 28 November 1991 on the F-11 satellite. The orbits are near-circular, sun-synchronous, and near-polar, with an inclination of 98.8°. The SSM/I consists of 7 separate total-power radiometers, each simultaneously measuring the microwave emission coming from the Earth and intervening atmosphere. Dual-polarization measurements are taken at 19.35, 37.0, and 85.5 GHz, while at the 22.235-GHz water vapor channel only vertical polarization is observed. The sensor uses an offset parabolic reflector of dimensions 61 by 66 cm to collect the microwave radiation. The reflector focuses the radiation into a corrugated, broad-band, 7-port feedhorn. The reflector and feedhorn spin as a unit about an axis parallel to nadir. The rotation period is 1.9 s. Earth observations are taken during a 102.4° segment of the rotation. The 102.4° arc is centered on the spacecraft subtrack and corresponds, for F-08 and F-10, to a 1400 km wide swath on the Earth's surface. Relative to the spacecraft velocity vector, the F-08 SSM/I is looking aft, and the F-10 and F-11 SSM/I are looking forward. The 1400-km swath and the orbit inclination of 98.8° provide complete coverage of the Earth in two to three days, except for two small circular sectors of 2.4° centered on the North and South poles. During each scan, the 85-GHz channels are sampled 128 times over the 102.4° arc. The integration period for a single sample is 3.89 ms. This sampling scheme results in 128 vertical polarization footprints and 128 horizontal polarization footprints, each having an effective 3-dB spatial resolution of 15 km. Observations at the lower three frequencies are taken only every other scan. Thus 64 samples of each of the lower channels are taken over the 102.4° arc, with the integration time being 7.95 ms.

Our SSM/I data were purchased from Remote Sensing Systems, Inc., and are

stored in 8-mm tapes (one tape contains one month of global data). To match the SSM/I data with the radar observations made during the DUNDEE experiment, we used data from the F-08 satellite. We first searched for all the available SSM/I swaths that run over the Darwin area during the two months December 1989 and January 1990. Next, each of these SSM/I measurements was matched with the temporally closest radar observation. If the time gap between the satellite and the radar observations is small (say, less than 20–30 min), we use the two as simultaneous observations. In situations where intense rainfall is occurring over the study area, radar measurements are usually available at high temporal resolution ($\sim$5 min). Thus for intense rainfall events the time gap between the satellite and the radar observations is usually small. These simultaneous observations were divided into two groups: rainy and non-rainy. The non-rainy group consists of observations that contain no radar-detected rainfall; the rainy group consists of observations in which there is radar-detected rainfall.

The non-rainy group can be used to quantify the clear-sky conditions, i.e., conditions of the atmosphere and the sea surface that prevail when no rain is detected by the radar. Figure 4-1 and 4-2 are examples of the observed 37-GHz brightness temperature under clear-sky conditions. Each dot in the figure indicates the center of a field of view (FOV) which is about 25 km by 25 km in size, and the number indicates the observed 37-GHz T_B (horizontal polarization). The lower portion of the figure corresponds to land which exhibits high brightness temperature due to the soil's high emissivity at this frequency. The upper portion of the figure is sea with an island in it. The brightness temperature for the sea portion is much lower than the land portion, because water surface has very low emissivity at this frequency. From the figure it can

be seen that under clear-sky conditions the 37-GHz brightness temperature of the sea surface in Darwin area is about 165 °K. FOVs close to land tend to have higher T_B. This is potentially due to the error in matching the location of the satellite FOVs with the radar pixels. The magnitude of the error in determining the FOV location is about 10 km. Thus near the coast, FOVs that appear to cover only sea surface may actually contain some land surface, making the T_B higher. Even if a FOV is entirely over water, its T_B can still be influenced by land radiation if it is close to land. This is why in the application of many algorithms to map oceanic rainfall the FOVs that are less than a few hundred km from the coast are ignored in order to eliminate possible contamination from land radiation. In our case we notice that the FOVs located between the island and the coast have relatively higher T_B. These FOVs are most likely to be contaminated by land.

The histograms (probability density function) of the horizontally polarized T_B at 19 and 37 GHz under clear-sky conditions are shown in Figure 4-3 and 4-4, respectively. Except for a few FOVs which might have been contaminated by land, most of the FOVs have T_B less than 180°K (at 37 GHz) or 170°K (at 19 GHz). In contrast to the low brightness temperature under clear-sky conditions, T_Bs from the sea surface can reach very high values during storm events. Figure 4-5 and 4-6 show two relatively large storm events for which simultaneous observations by radar and SSM/I are available. In these two figures the areas with rain rate above 0.5 mm h^{-1} are shaded, which can be used to roughly delineate the area of moderate rain. One immediately notices that, consistent with existing models such as that of Wilheit et al. (1977), the FOVs covered by rain cells exhibit high brightness temperature. On the 14 January 1990 map (Figure 4-6), for example, FOVs inside the large rainy

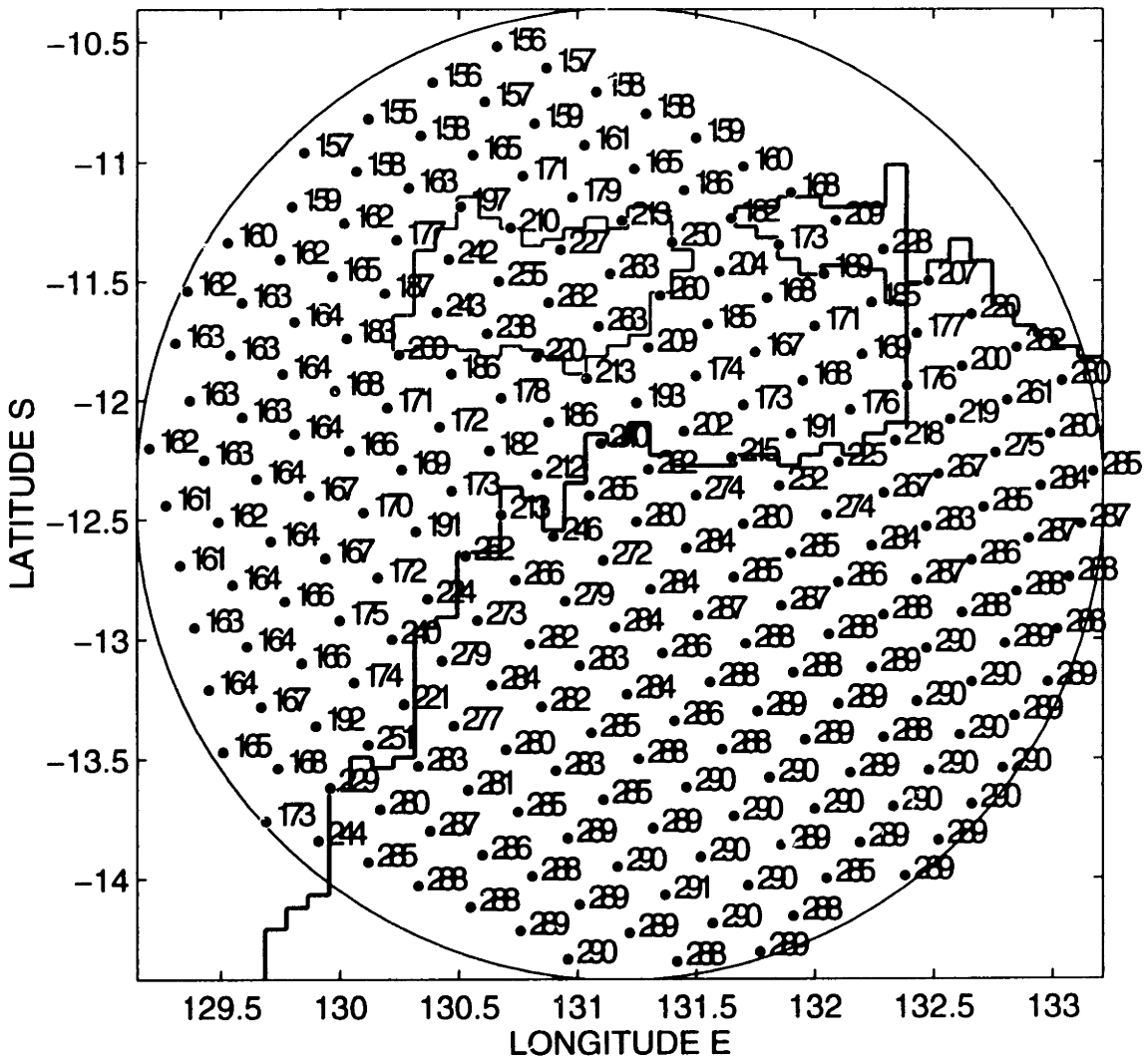

Figure 4-1: Observed horizontally polarized brightness temperature at 37 GHz under clear-sky conditions, Darwin area; 09:33 6 December 1992; lower portion of the figure is land.

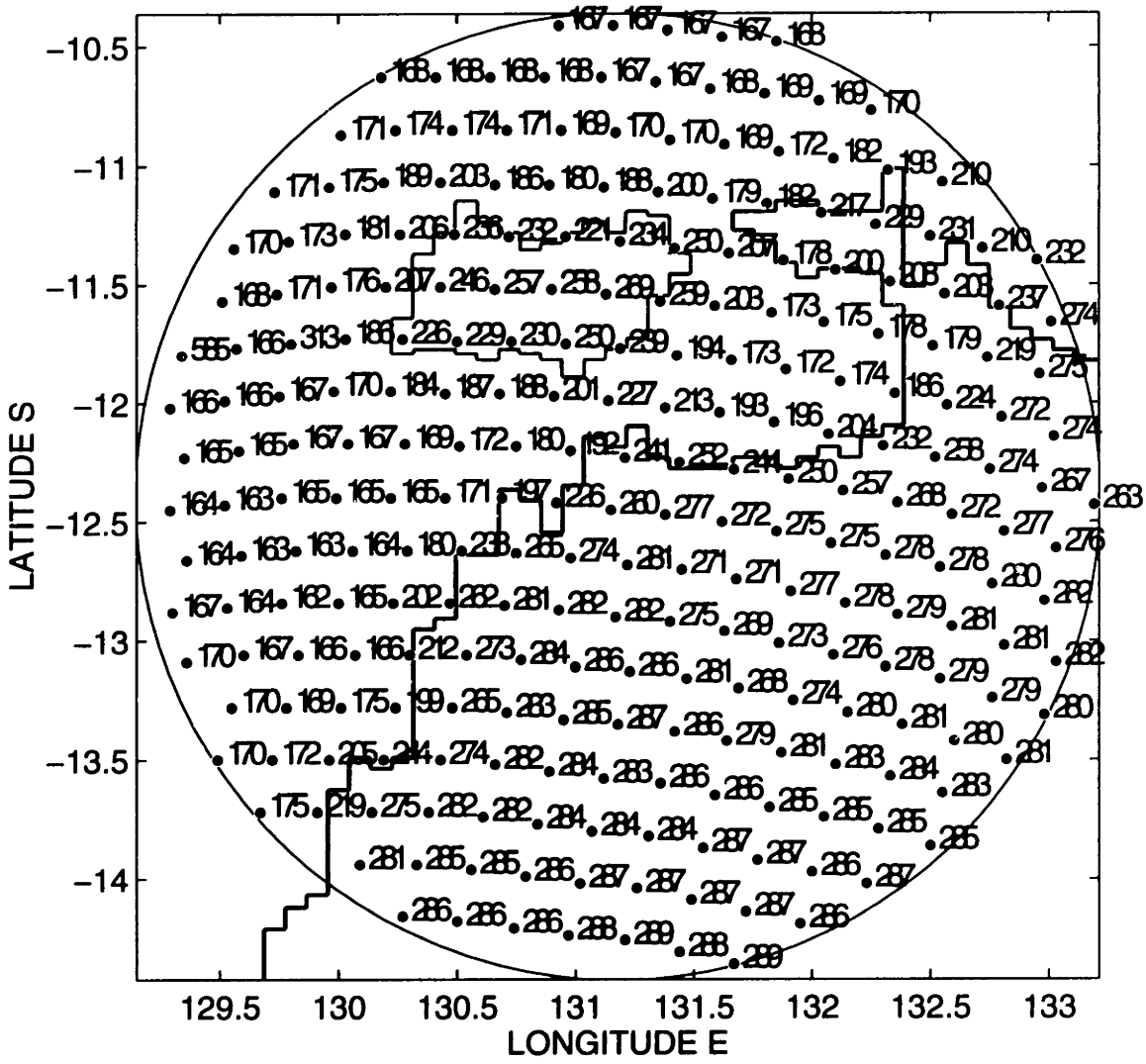

Figure 4-2: Observed horizontally polarized brightness temperature at 37 GHz under clear-sky conditions, Darwin area; 19:47 7 December 1992; lower portion of the figure is land.

area to the west of the island have T_Bs above 250°K. However, it can also be noticed that many FOVs in the rain-free areas also exhibit quite high brightness temperature. Although not as high as those located within rain cells, the rain-free FOVs have T_Bs that are much higher than those found under clear-sky conditions (see Figure 4-1 and 4-2).

To further illustrate this phenomenon, the 37-GHz T_B is plotted against the 19-GHz T_B for clear-sky and stormy conditions, as shown in Figure 4-7. It is clearly shown that under clear-sky conditions (normal sea surface), the 37-GHz T_B seldom exceeds 180 °K. Under storm conditions (January 13 and 14 events), it exceeds 180 °K for all the FOVs within the radar coverage (452 km diameter), even though a majority of the FOVs do not contain any radar-detected rain. To quantitatively relate the brightness temperature to the rainfall information within the FOV, the 37-GHz T_B is plotted against the FOV average rain rate and the fractional rainfall coverage in Figures 4-8 and 4-9. The fractional rainfall coverage is the ratio of raining area within a FOV to the total area of the FOV. In Figure 4-9, the reflectivity level of 20 dBZ has been used to distinguish raining area from rain-free area. Both figures show a cluster of data points along the lower portion of the T_B axis, indicating that essentially there is no rain for 37-GHz T_B up to about 210 °K. Another interesting feature is that the brightness temperature saturates quickly, approaching and fluctuating around 255 °K.

4.1.2 TOGA-COARE Area

The tropical western Pacific is characterized by an expansive pool of warm sea surface temperatures (SSTs) that cover nearly 7.5 million km^2. This warm pool has been shown to be a critical source of energy in the global circulation

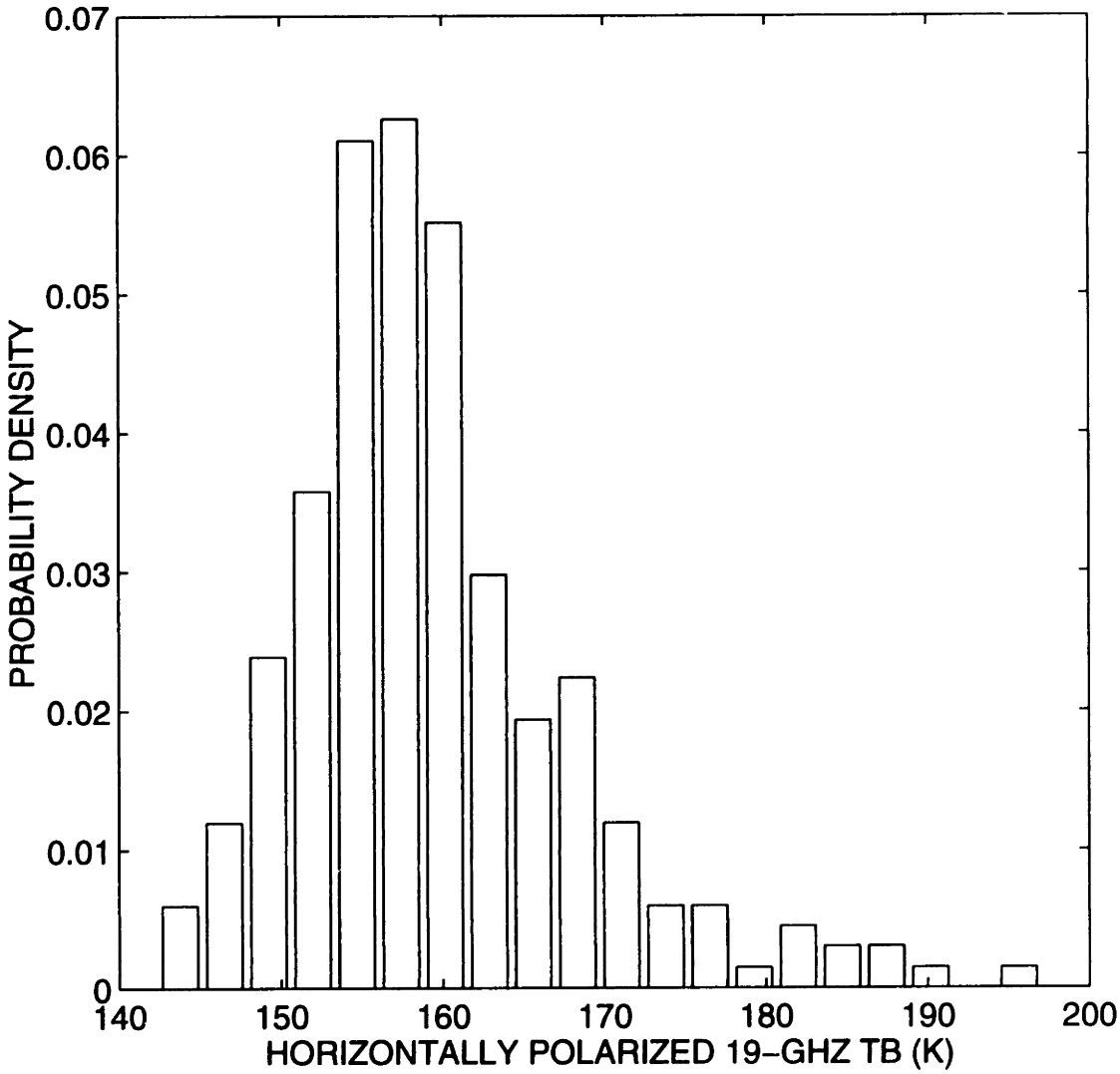

Figure 4-3: Histogram (or probability density function) of the observed horizontally polarized brightness temperature at 19 GHz for Darwin area under clear-sky conditions.

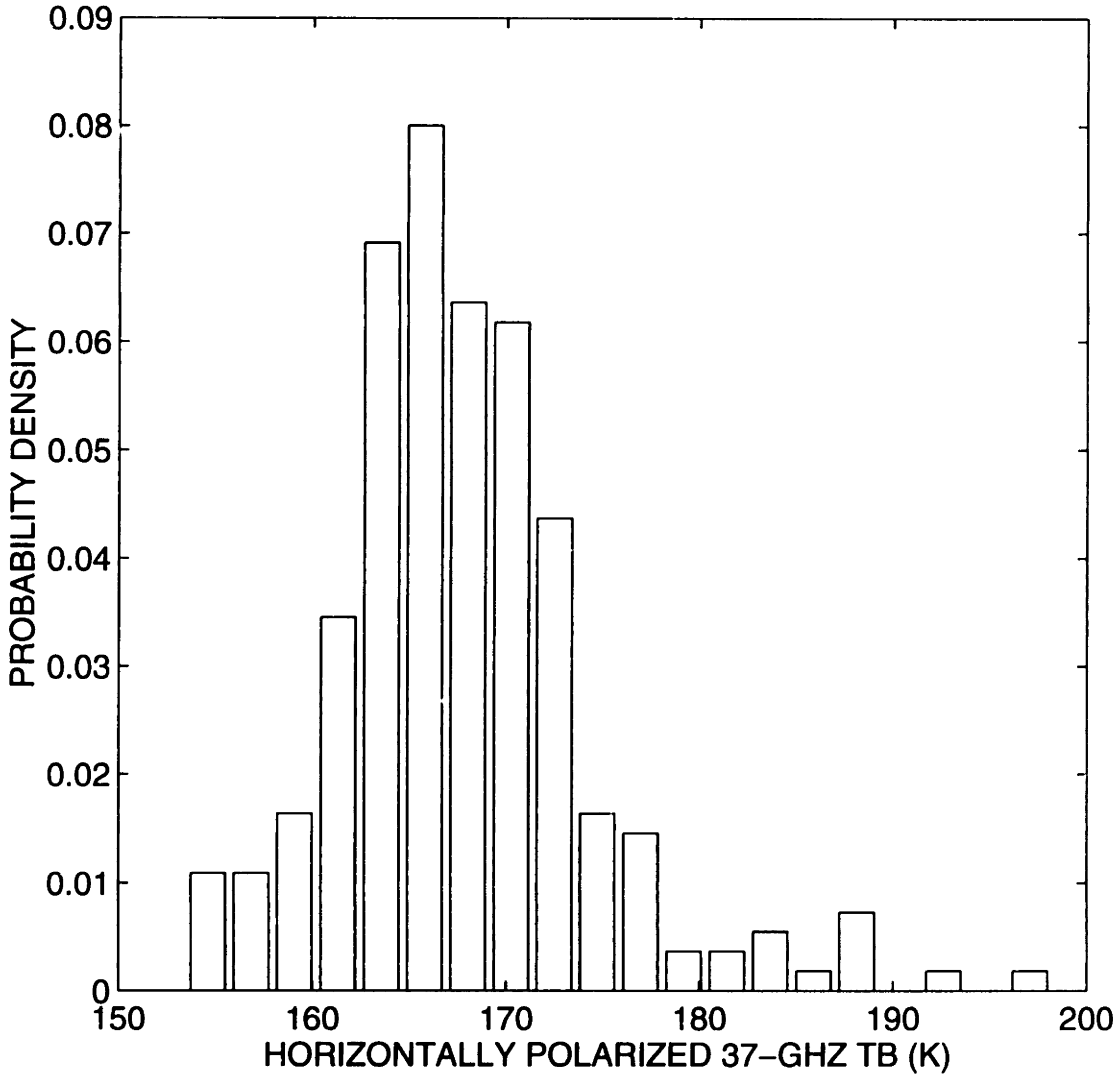

Figure 4-4: Histogram (or probability density function) of the observed horizontally polarized brightness temperature at 37 GHz for Darwin area under clear-sky conditions.

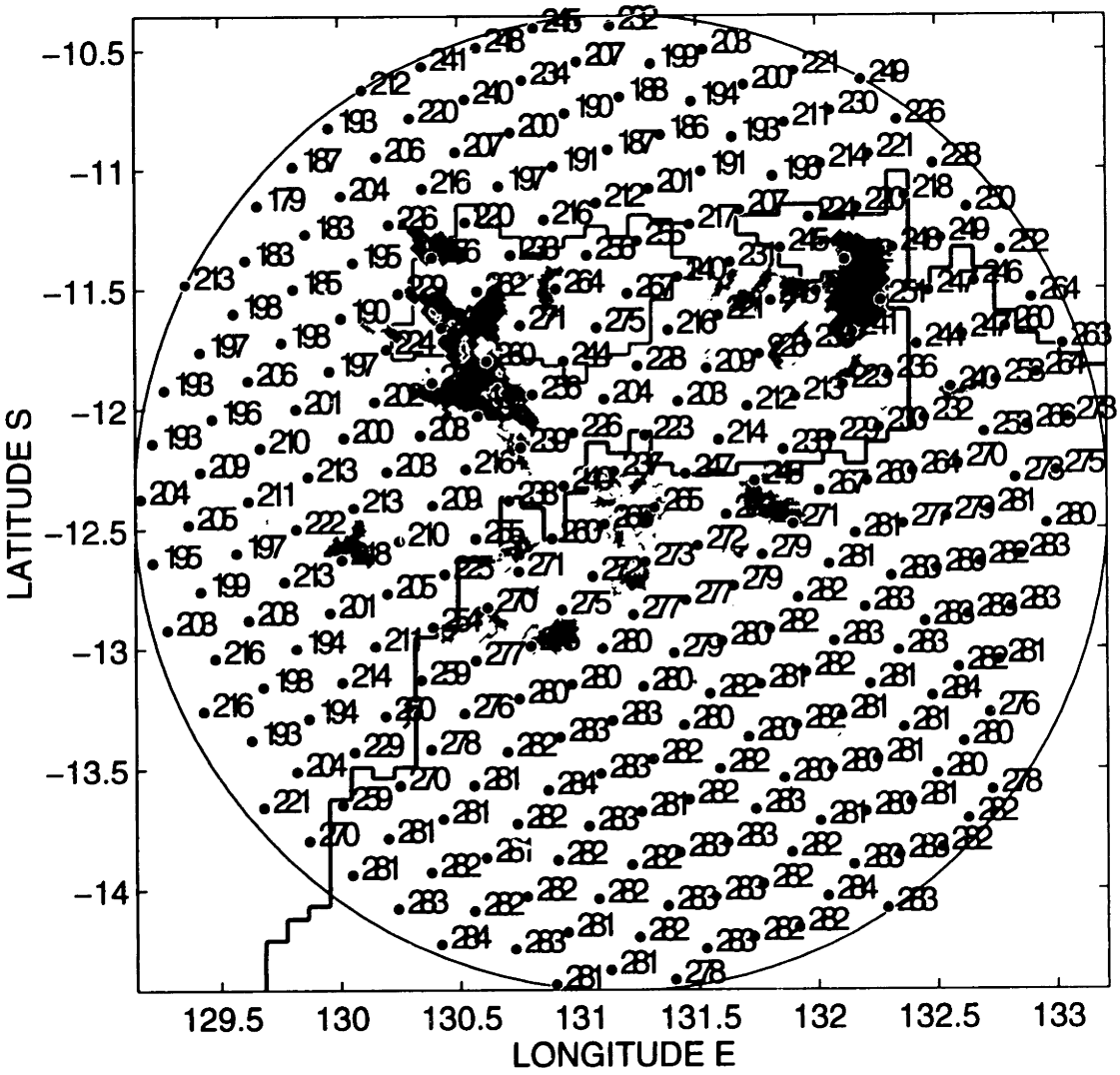

Figure 4-5: Simultaneous observations by radar and SSM/I over Darwin area. 13 January 1990, radar time: 09:46, SSM/I time: 09:41 . Areas with rain rate over 0.5 mm h^{-1} are shaded. Each dot in the figure represents the center of a field of view and the number to the right of the dot indicates the horizontally polarized 37-GHz brightness temperature.

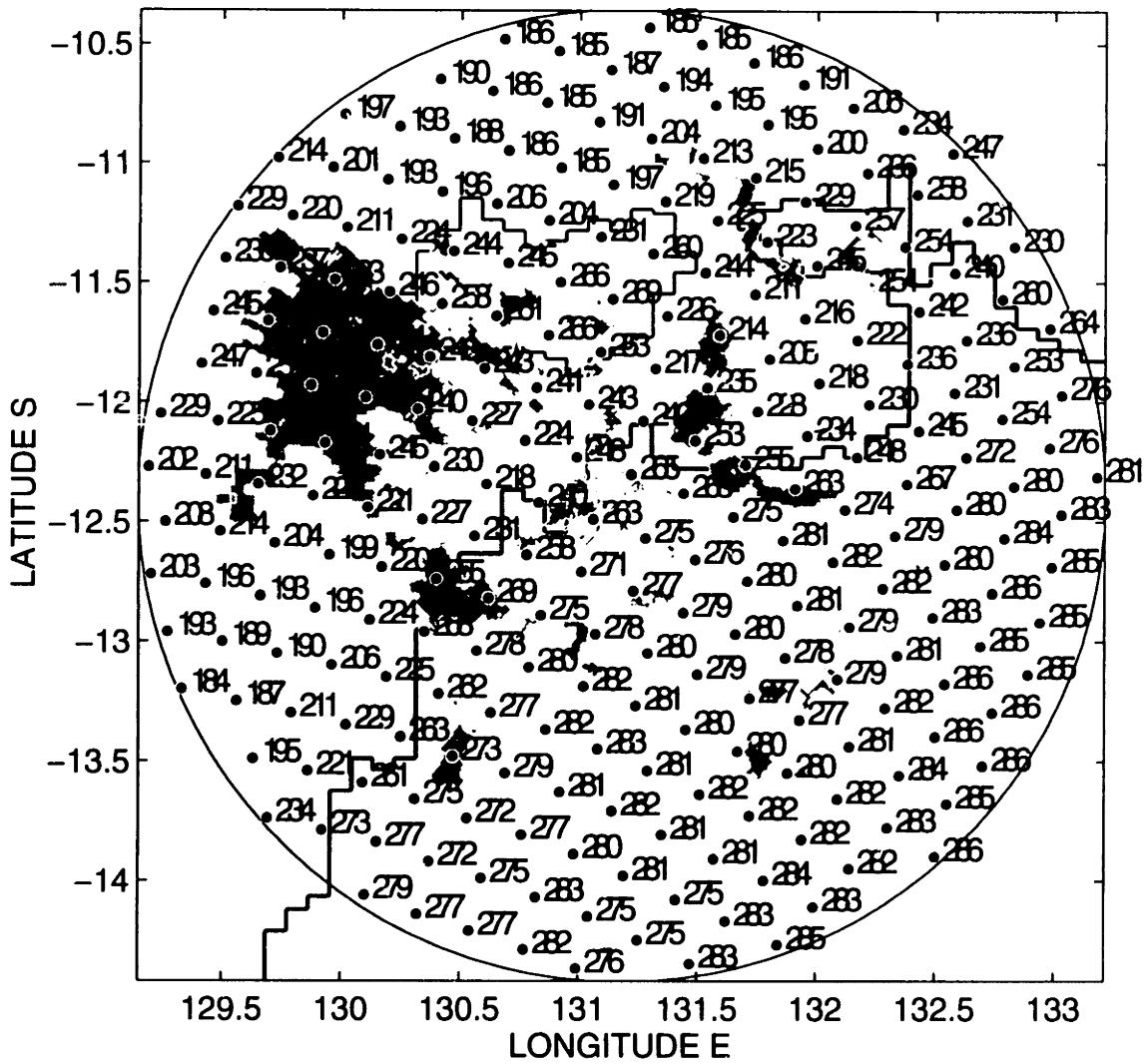

Figure 4-6: Simultaneous observations by radar and SSM/I over Darwin area. 14 January 1990, radar time: 09:23, SSM/I time: 09:28 . Areas with rain rate over 0.5 mm h^{-1} are shaded. Each dot in the figure represents the center of a field of view and the number to the right of the dot indicates the horizontally polarized 37-GHz brightness temperature.

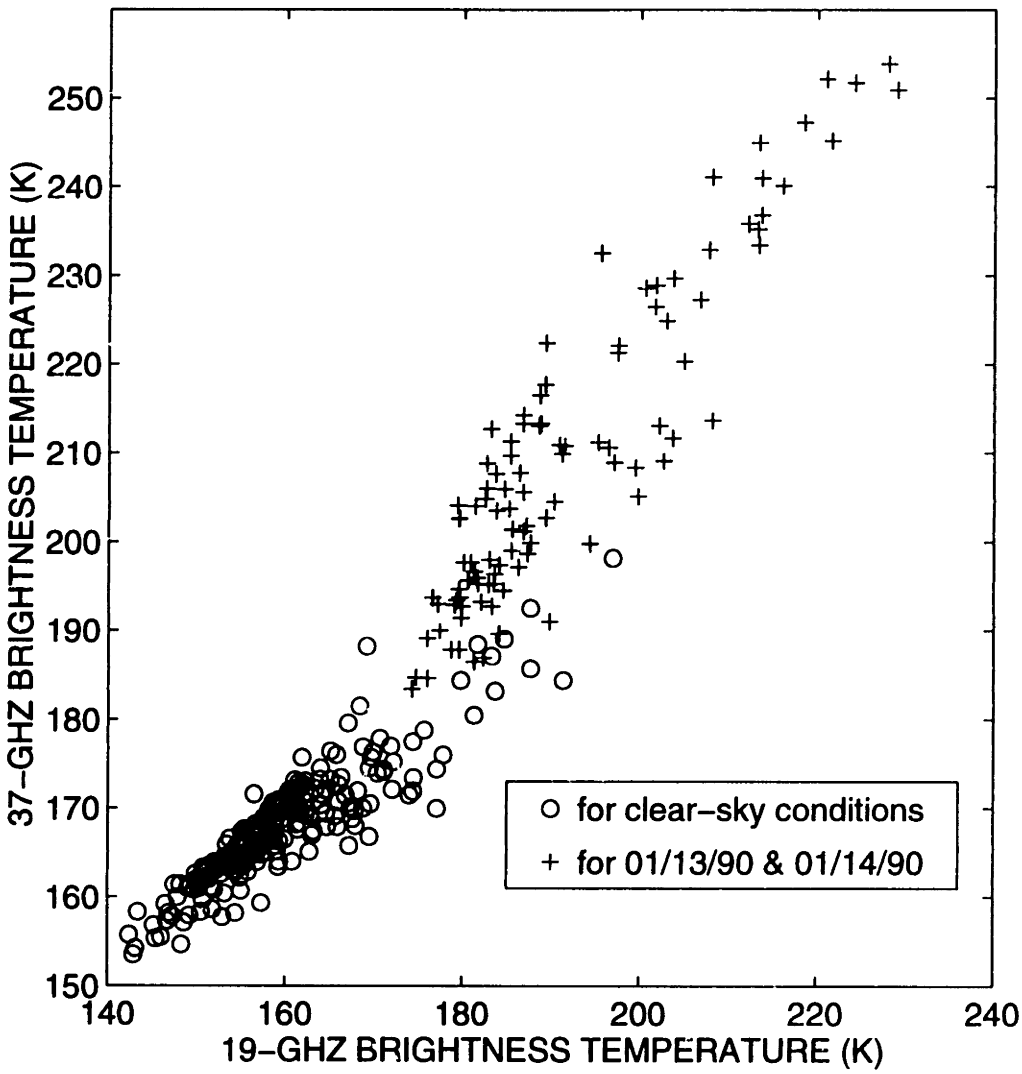

Figure 4-7: 37-GHz T_B versus 19-GHz T_B under clear-sky and storm (January 13 and January 14, 1990) conditions; horizontal polarization.

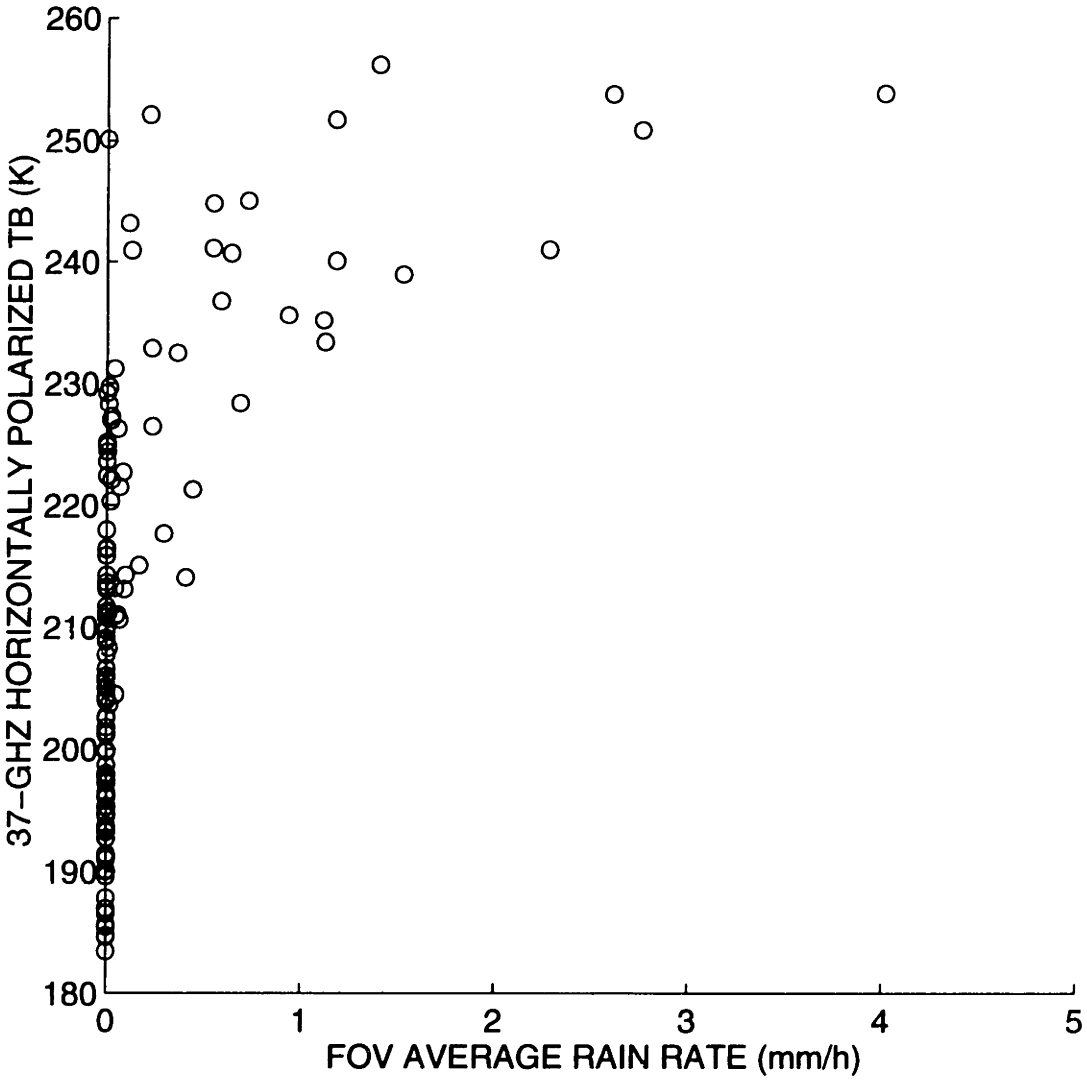

Figure 4-8: 37-GHz T_B versus FOV average rain rate; data from January 13 and 14 events; Darwin area.

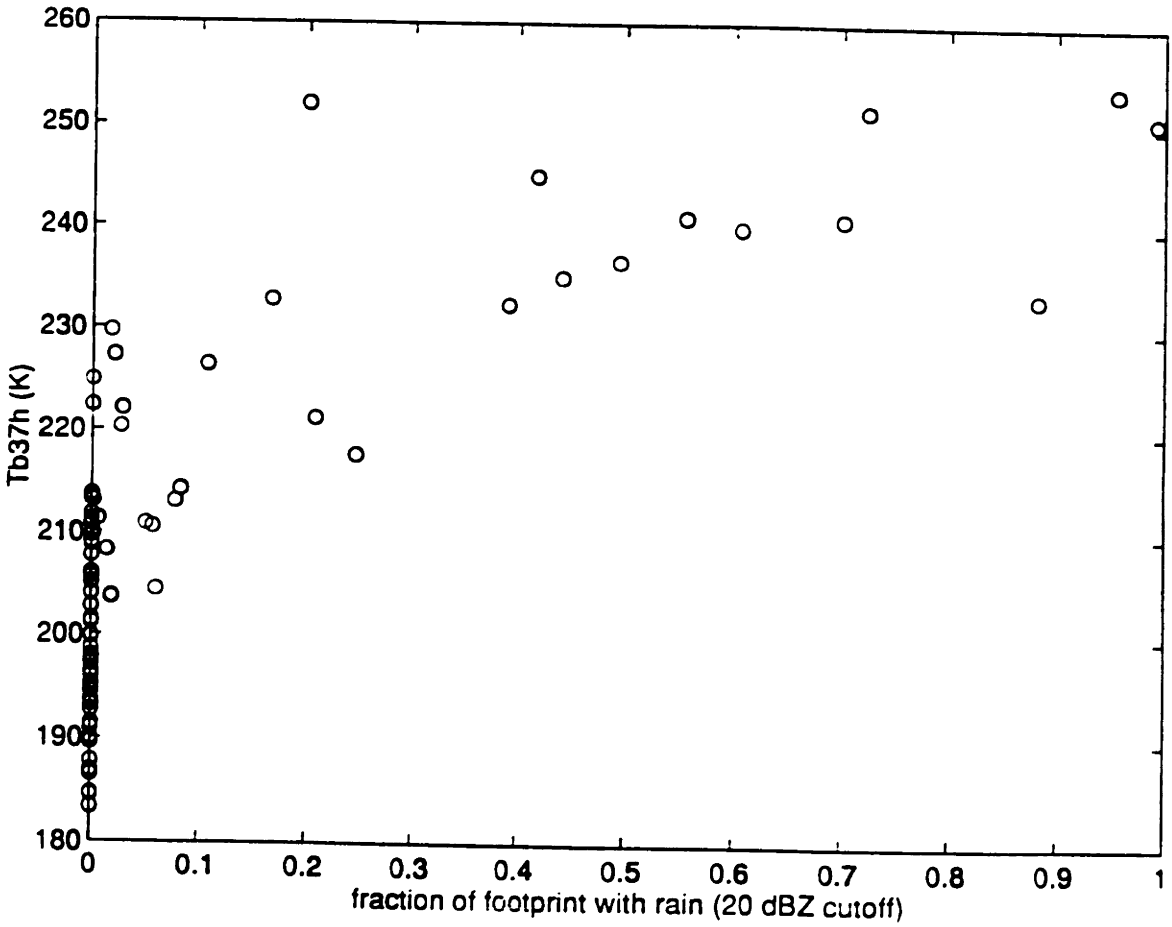

Figure 4-9: 37-GHz T_B versus fractional coverage of rain within the FOV; data from January 13 and 14 events.

system. Significant variations in the warm pool occur in conjunction with short-term climate changes. For example, during El Niño, the warm SSTs extend eastward toward the west coast of South America. These variations in SST and the accompanying disruption in atmospheric circulations are believed to play a role in droughts in Australia, India, and Africa, floods in South America, and severe winter storms in the United States.

The Coupled Ocean-Atmosphere Response Experiment (COARE) of the Tropical Ocean and Global Atmosphere (TOGA) program was designed to gain understanding of the role this warm pool plays in the tropical ocean and global atmosphere system. It includes a one-year extended monitoring phase and an embedded four-month intensive observation period (IOP, November 1992–February 1993). The experiment covers a broad region between 20° N and 20° S, bounded by Indonesia on the west and dateline on the east. Within this broad region are the three principal COARE domains: The COARE large-scale domain (LSD), the COARE outer sounding array (OSA), and the intensive flux array (IFA) (see Figure 4-10). The IFA is centered at 2° S, 156° E and bounded by the polygon defined by the meteorological stations of Kapingamarangi and Kavieng and two ships (Figure 4-11). The principal aim of the IOP is to determine the interfacial fluxes within a relatively small area of the warm pool and to understand the atmospheric and oceanic effects of these fluxes. Several meteorological radars have been used for this purpose. Figure 4-11 shows the radar coverage during IOP within the IFA. The two Doppler radars (one is MIT and the other is TOGA radar) are located on an east-west line, separated by 200 km. Whereas the highest priority of the radar network is to provide estimates of precipitation over the IFA, on occasion the two ships could be moved to within 50 km of each other to perform dual-Doppler experiments. Measurements by

these radars can be used to make quantitative estimates of rain rate. Surface rain rate has been calculated from the lowest tilt PPI scans, and corrections have been made to account for the evaporation of rain drops. The temporal resolution of the radar measurements is 10 min and the data are continuous except for a few days break. The surface rainfall dataset that is made available to the public by the NASA TRMM office has a spatial resolution of 2 km.

Both the DMSP F-10 and F-11 satellites were operational during the TOGA-COARE IOP and the passive microwave data can be obtained from the SSM/I sensors on board these satellites. We have secured two months of data from F-11 SSM/I (December 1992 and January 1993). Since the satellite data were limited compared with the radar data, in selecting simultaneous satellite/radar observations the satellite data were screened first for all available swaths over the COARE area regardless of whether or not each of these swaths contains any rainfall. Next, the closest radar scan was identified for each of these SSM/I swaths. The time gap between the closest radar/satellite scenes is generally satisfactory small thanks to the excellent temporal resolution and continuity of the radar observations. For the two-month period, 46 simultaneous radar/satellite scenes have been identified and selected for analysis. 11 out of these 46 scenes contain varying amount of radar-detected surface rain. The radar/satellite comparisons of these 11 scenes are shown in Figure 4-12 through Figure 4-22, where the 37-GHz horizontally polarized T_Bs are superimposed on the radar-observed rainfall fields. Areas with rain rate larger than 0.5 mm h^{-1} in these figures are shaded.

Among these 11 rainy events, the 20 December 1992, 21 December 1992, 25 December 1992, and 31 January 1993 events show relatively larger spatial spread of rain. Similar to the cases shown for the Darwin area, one can also

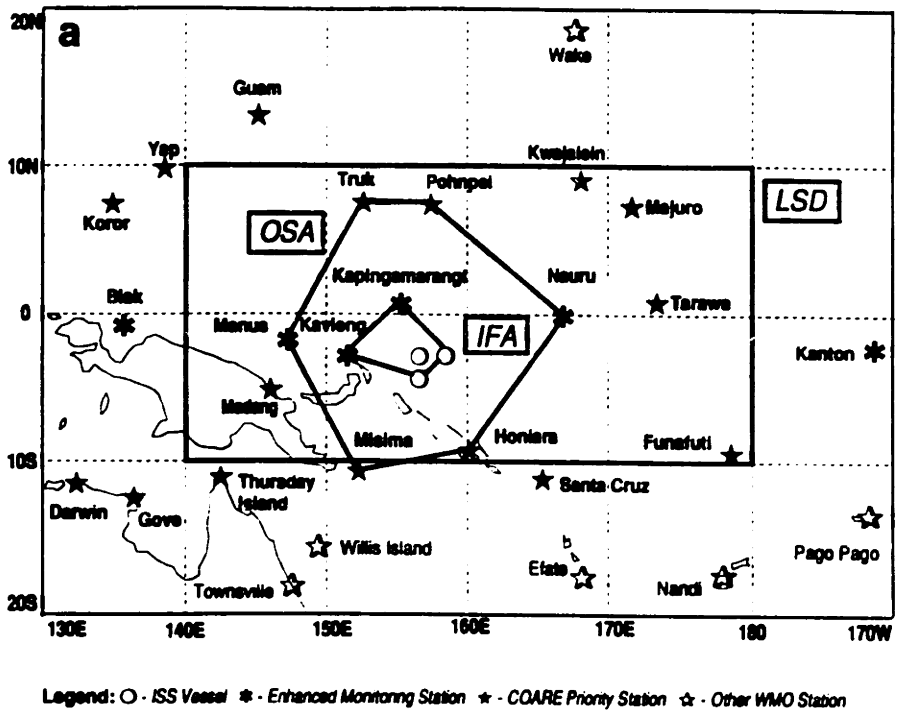

Figure 4-10: Schematic of the TOGA-COARE region (from Webster and Lukas 1992)

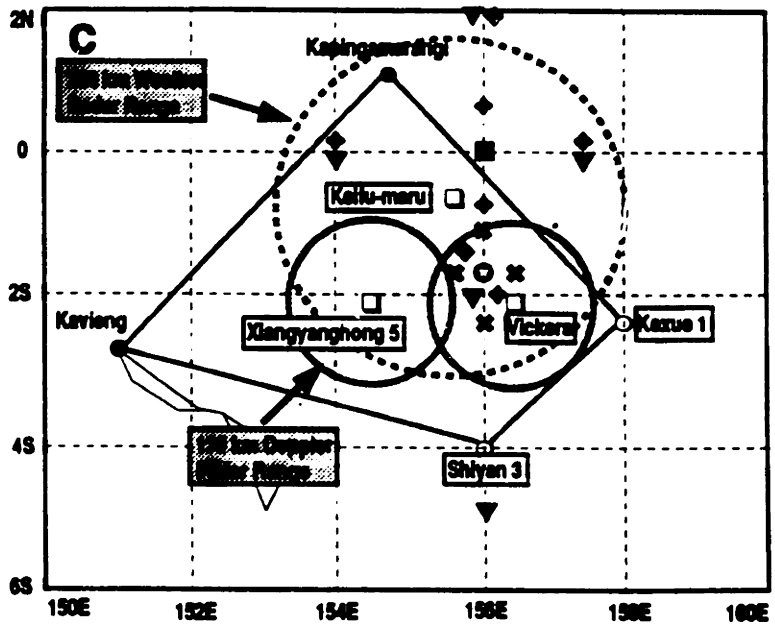

Figure 4-11: Radar coverage of the Intensive Flux Array during the Intensive Observation Period of TOGA-COARE (from Webster and Lukas 1992)

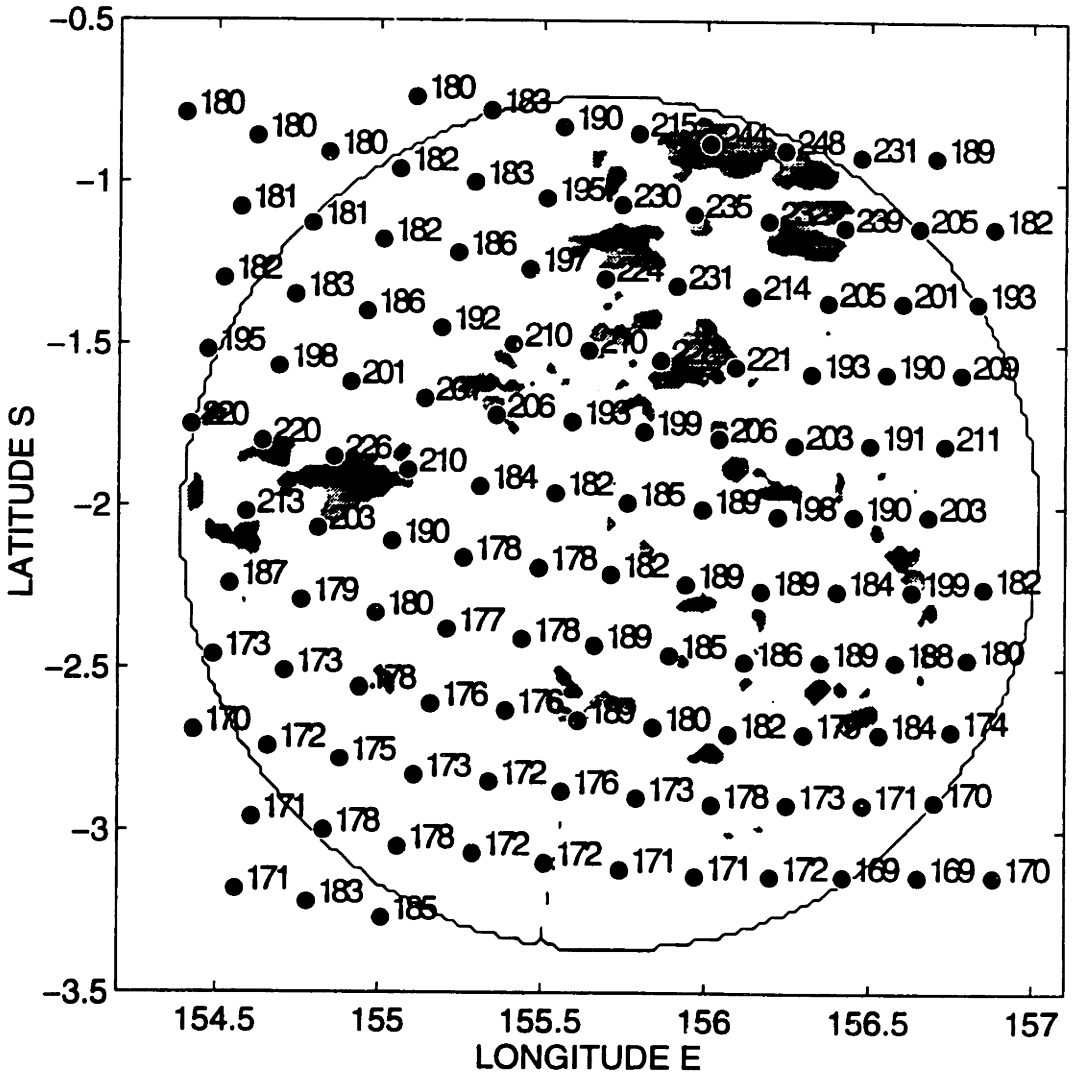

Figure 4-12: Simultaneous observations by radar and SSM/I over TOGA-COARE area. 19 December 1992, radar time: 19:01, SSM/I time: 18:59. Areas with rain rate over 0.5 mm h^{-1} are shaded. Each dot in the figure represents the center of a field of view and the number to the right of the dot indicates the horizontally polarized 37-GHz brightness temperature.

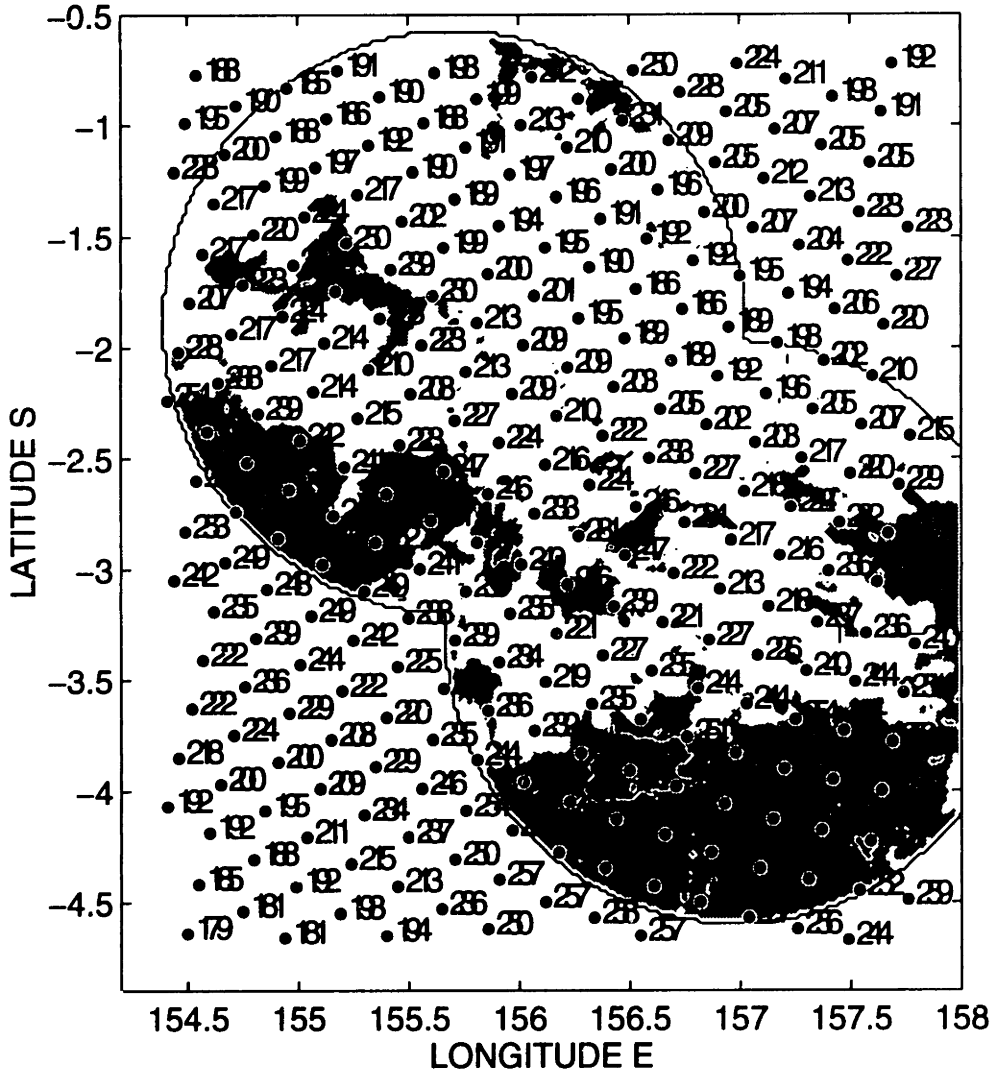

Figure 4-13: Simultaneous observations by radar and SSM/I over TOGA-COARE area. 20 December 1992, radar time: 18:41, SSM/I time: 18:44. Areas with rain rate over 0.5 mm h^{-1} are shaded. Each dot in the figure represents the center of a field of view and the number to the right of the dot indicates the horizontally polarized 37-GHz brightness temperature.

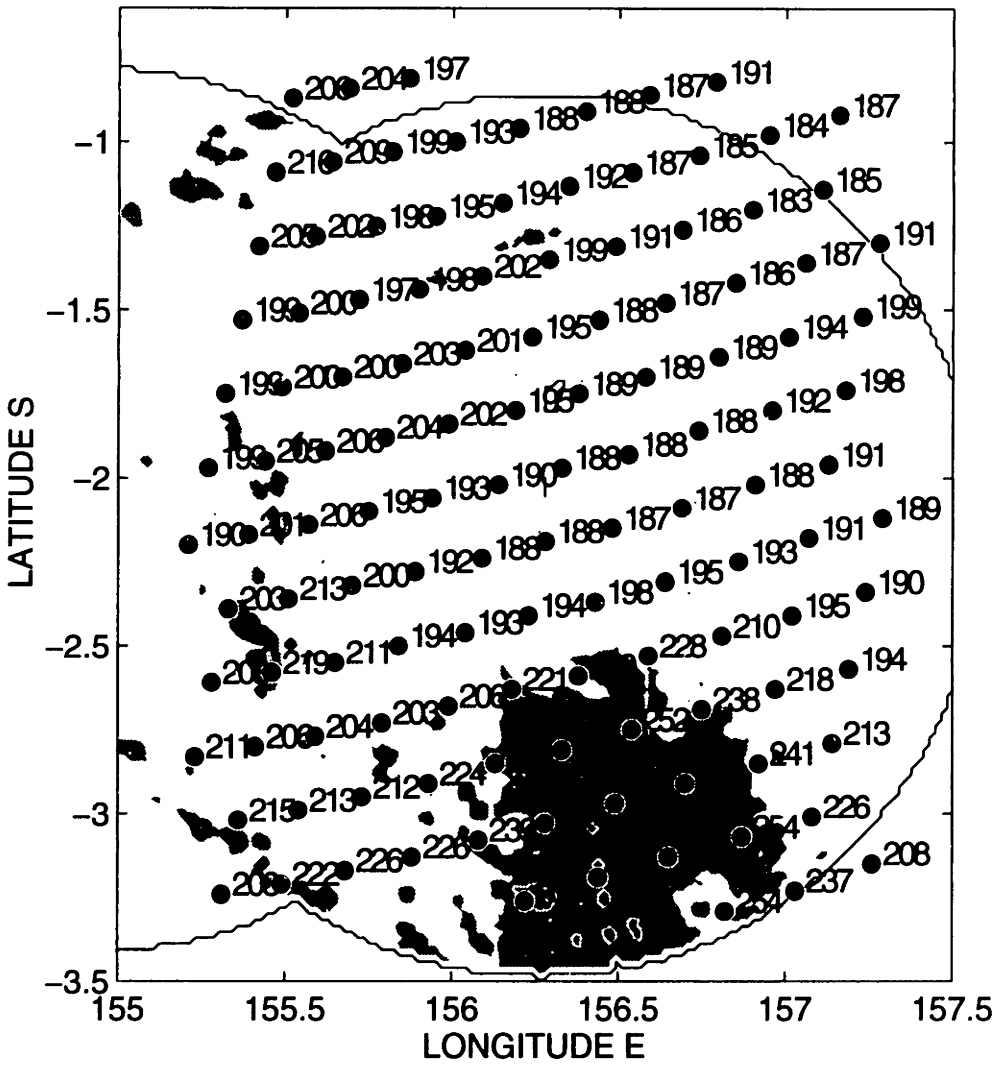

Figure 4-14: Simultaneous observations by radar and SSM/I over TOGA-COARE area. 21 December 1992, radar time: 18:31, SSM/I time: 18:32. Areas with rain rate over 0.5 mm h^{-1} are shaded. Each dot in the figure represents the center of a field of view and the number to the right of the dot indicates the horizontally polarized 37-GHz brightness temperature.

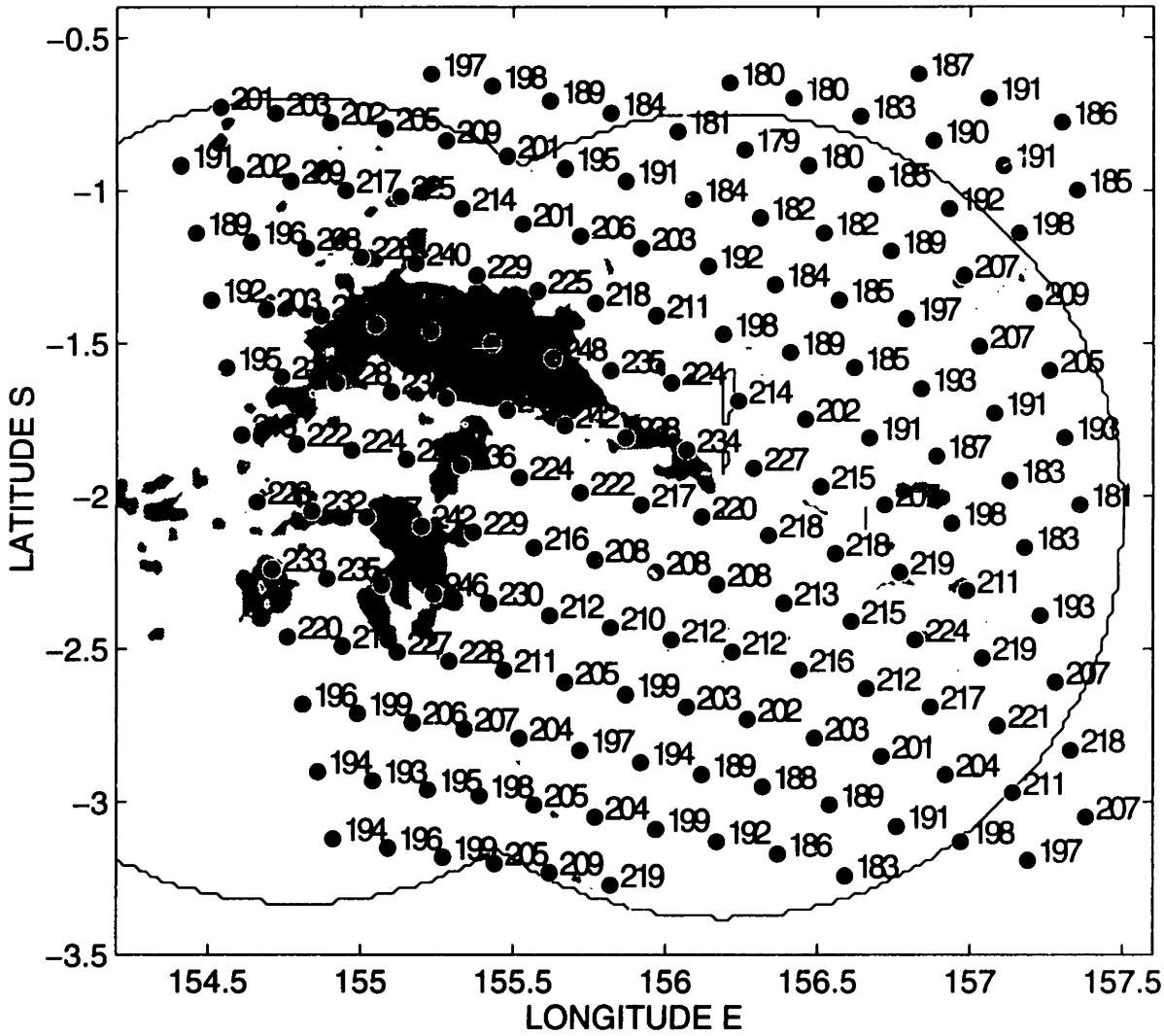

Figure 4-15: Simultaneous observations by radar and SSM/I over TOGA-COARE area. 25 December 1992, radar time: 06:31, SSM/I time: 06:36. Areas with rain rate over 0.5 mm h^{-1} are shaded. Each dot in the figure represents the center of a field of view and the number to the right of the dot indicates the horizontally polarized 37-GHz brightness temperature.

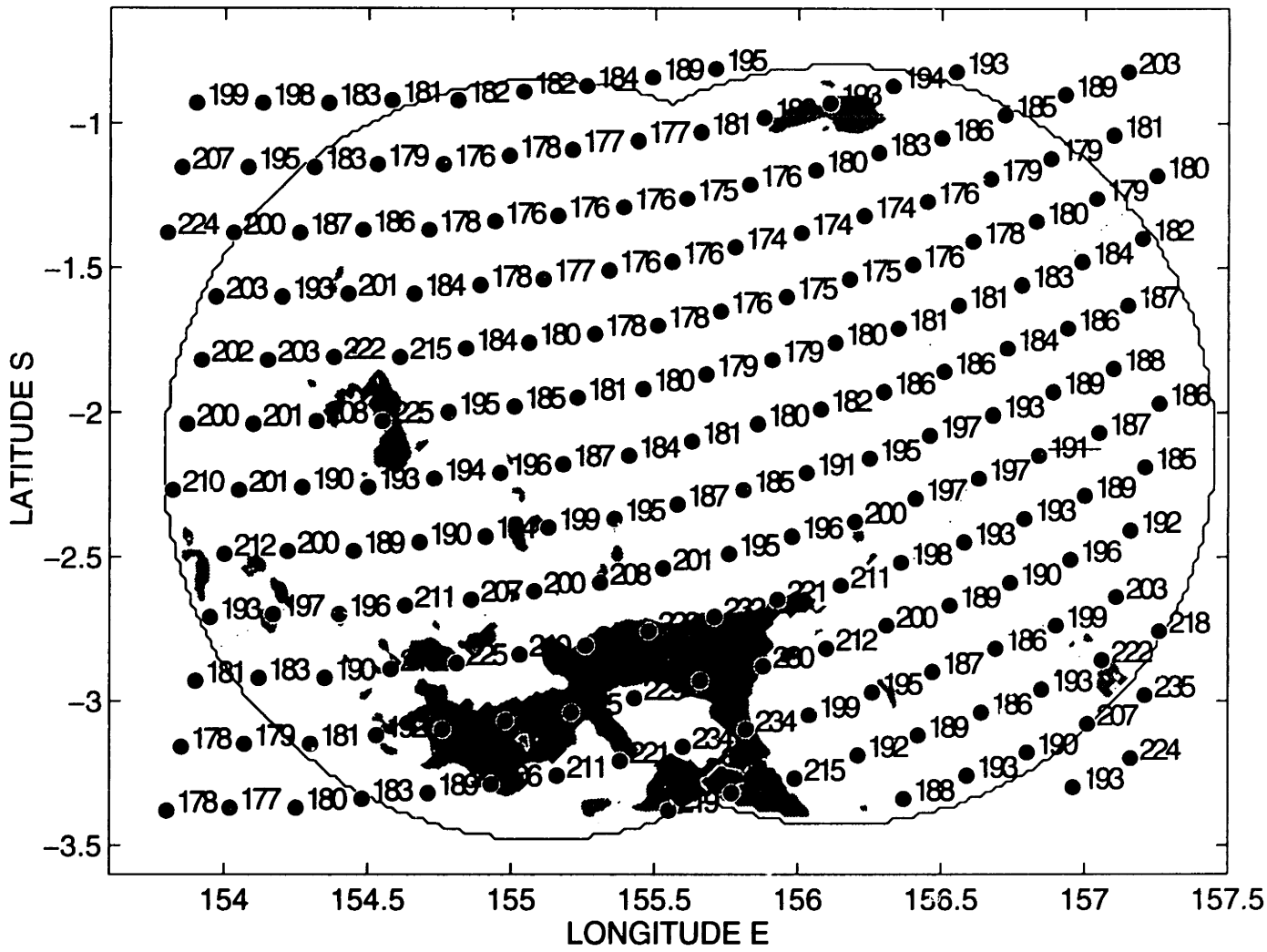

Figure 4-16: Simultaneous observations by radar and SSM/I over TOGA-COARE area. 26 December 1992, radar time: 19:11, SSM/I time: 19:08. Areas with rain rate over 0.5 mm h^{-1} are shaded. Each dot in the figure represents the center of a field of view and the number to the right of the dot indicates the horizontally polarized 37-GHz brightness temperature.

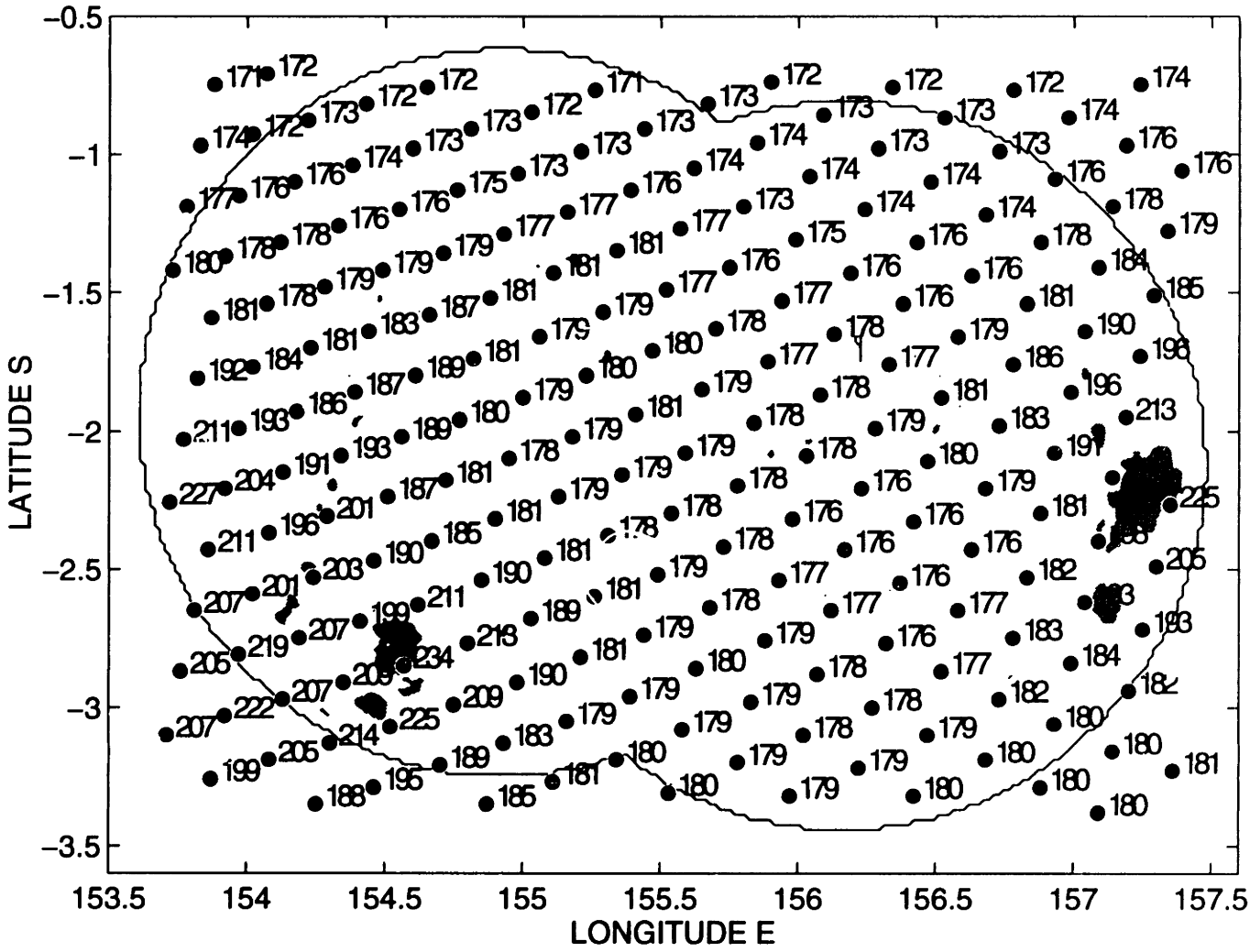

Figure 4-17: Simultaneous observations by radar and SSM/I over TOGA-COARE area. 28 December 1992, radar time: 18:41, SSM/I time: 18:42. Areas with rain rate over 0.5 mm h^{-1} are shaded. Each dot in the figure represents the center of a field of view and the number to the right of the dot indicates the horizontally polarized 37-GHz brightness temperature.

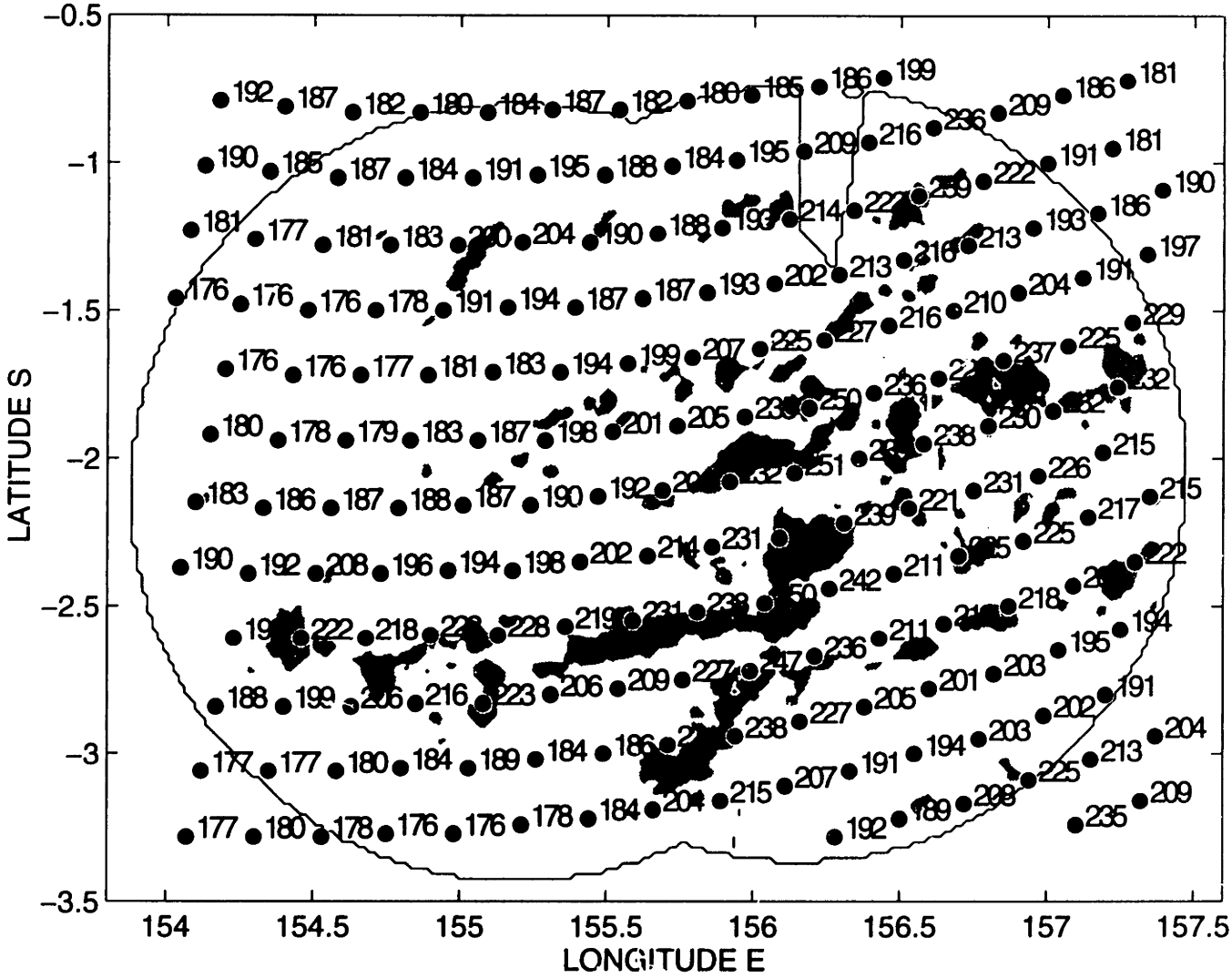

Figure 4-18: Simultaneous observations by radar and SSM/I over TOGA-COARE area. 3 January 1993, radar time: 19:01, SSM/I time: 19:05. Areas with rain rate over 0.5 mm h^{-1} are shaded. Each dot in the figure represents the center of a field of view and the number to the right of the dot indicates the horizontally polarized 37-GHz brightness temperature.

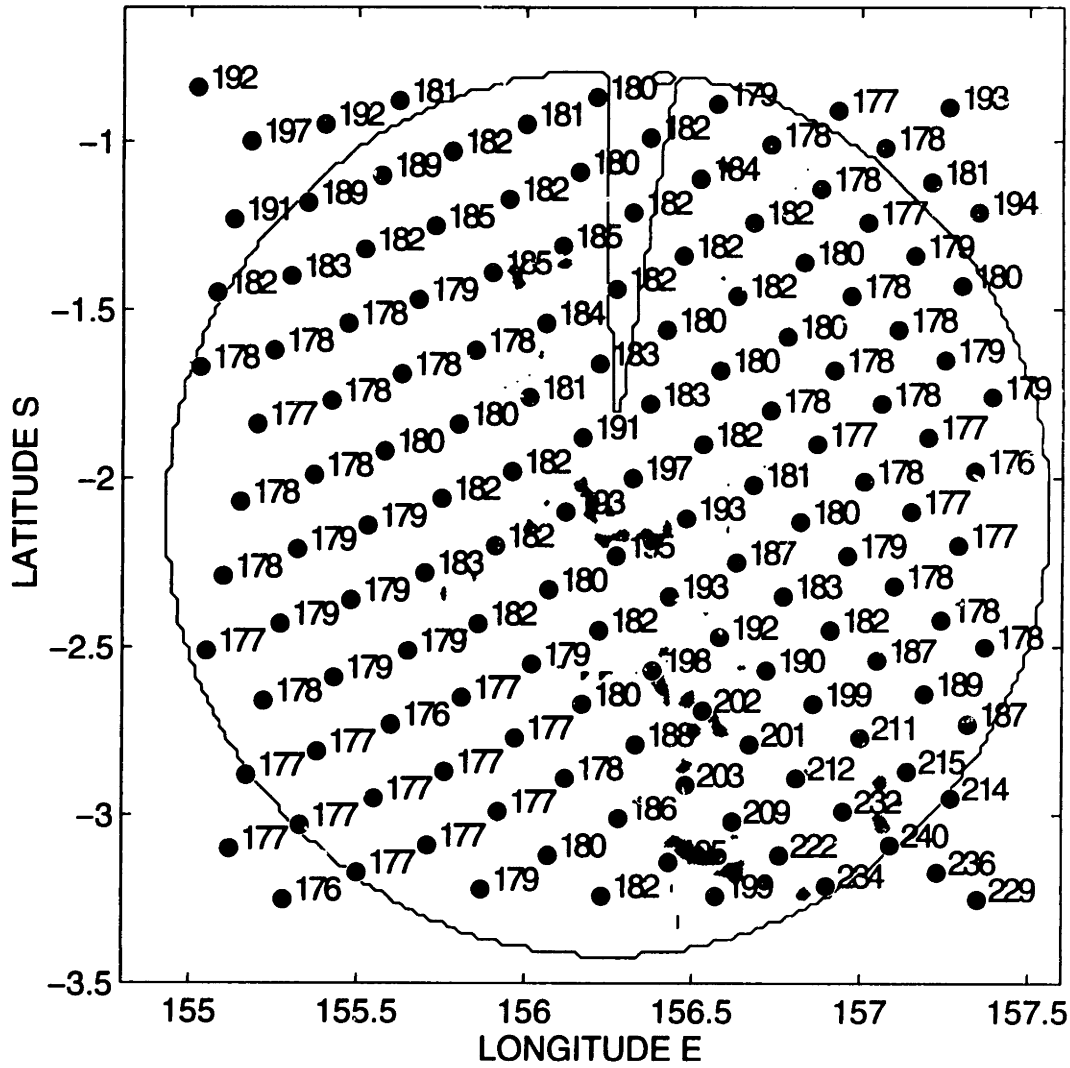

Figure 4-19: Simultaneous observations by radar and SSM/I over TOGA-COARE area. 18 January 1993, radar time: 19:11, SSM/I time: 19:13. Areas with rain rate over 0.5 mm h^{-1} are shaded. Each dot in the figure represents the center of a field of view and the number to the right of the dot indicates the horizontally polarized 37-GHz brightness temperature.

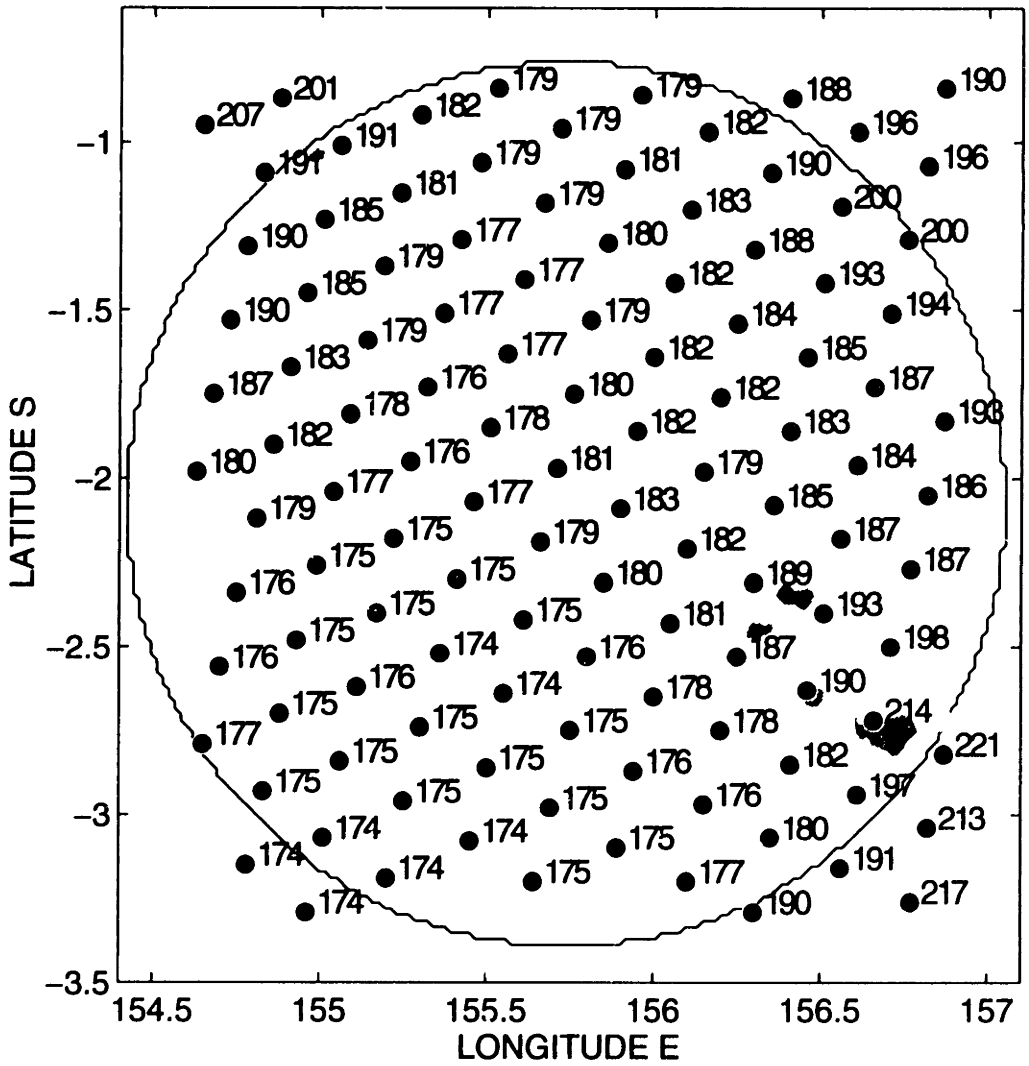

Figure 4-20: Simultaneous observations by radar and SSM/I over TOGA-COARE area. 28 January 1993, radar time: 18:41, SSM/I time: 18:45. Areas with rain rate over 0.5 mm h^{-1} are shaded. Each dot in the figure represents the center of a field of view and the number to the right of the dot indicates the horizontally polarized 37-GHz brightness temperature.

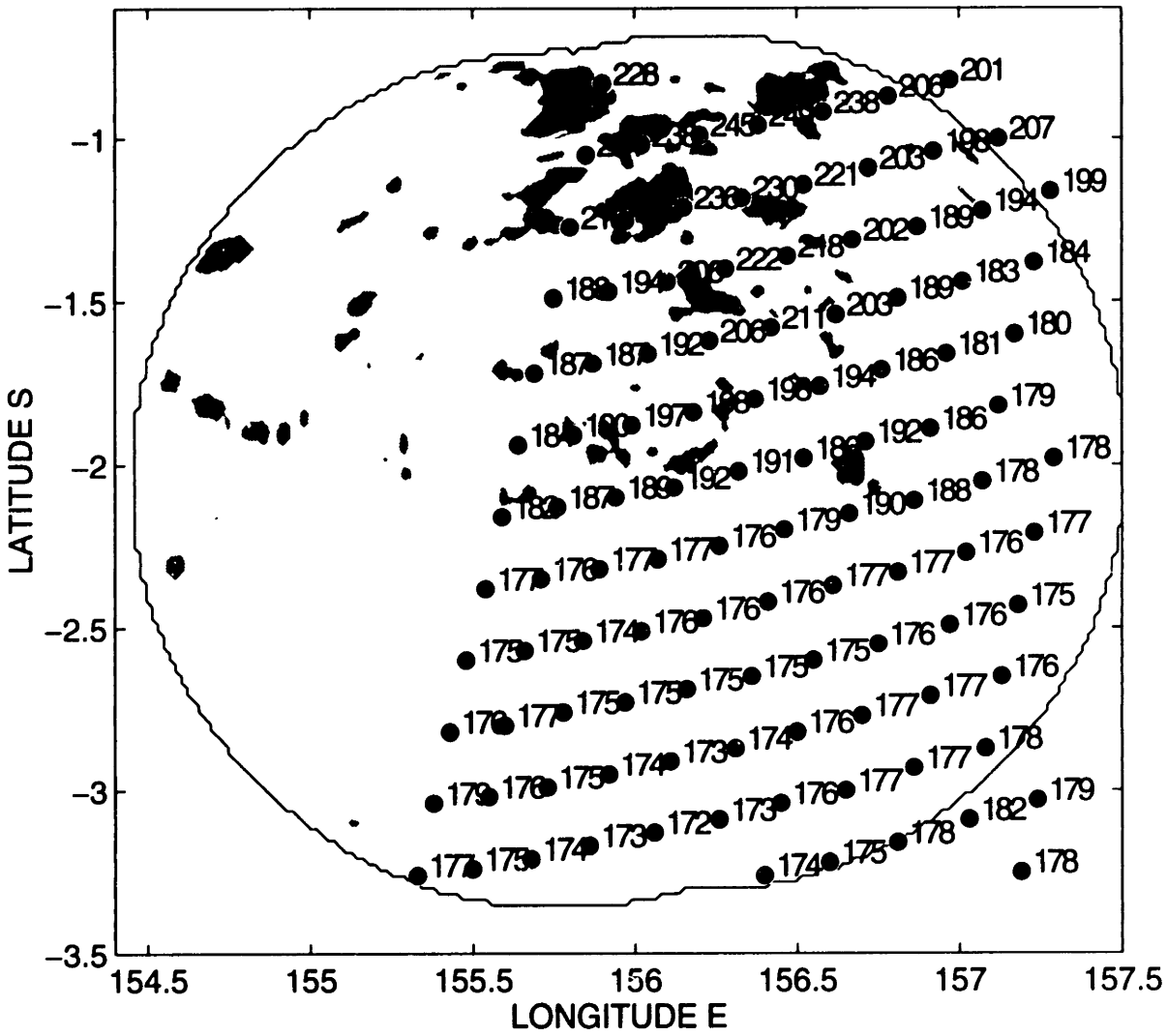

Figure 4-21: Simultaneous observations by radar and SSM/I over TOGA-COARE area. 29 January 1993, radar time: 18:31, SSM/I time: 18:32. Areas with rain rate over 0.5 mm h^{-1} are shaded. Each dot in the figure represents the center of a field of view and the number to the right of the dot indicates the horizontally polarized 37-GHz brightness temperature.

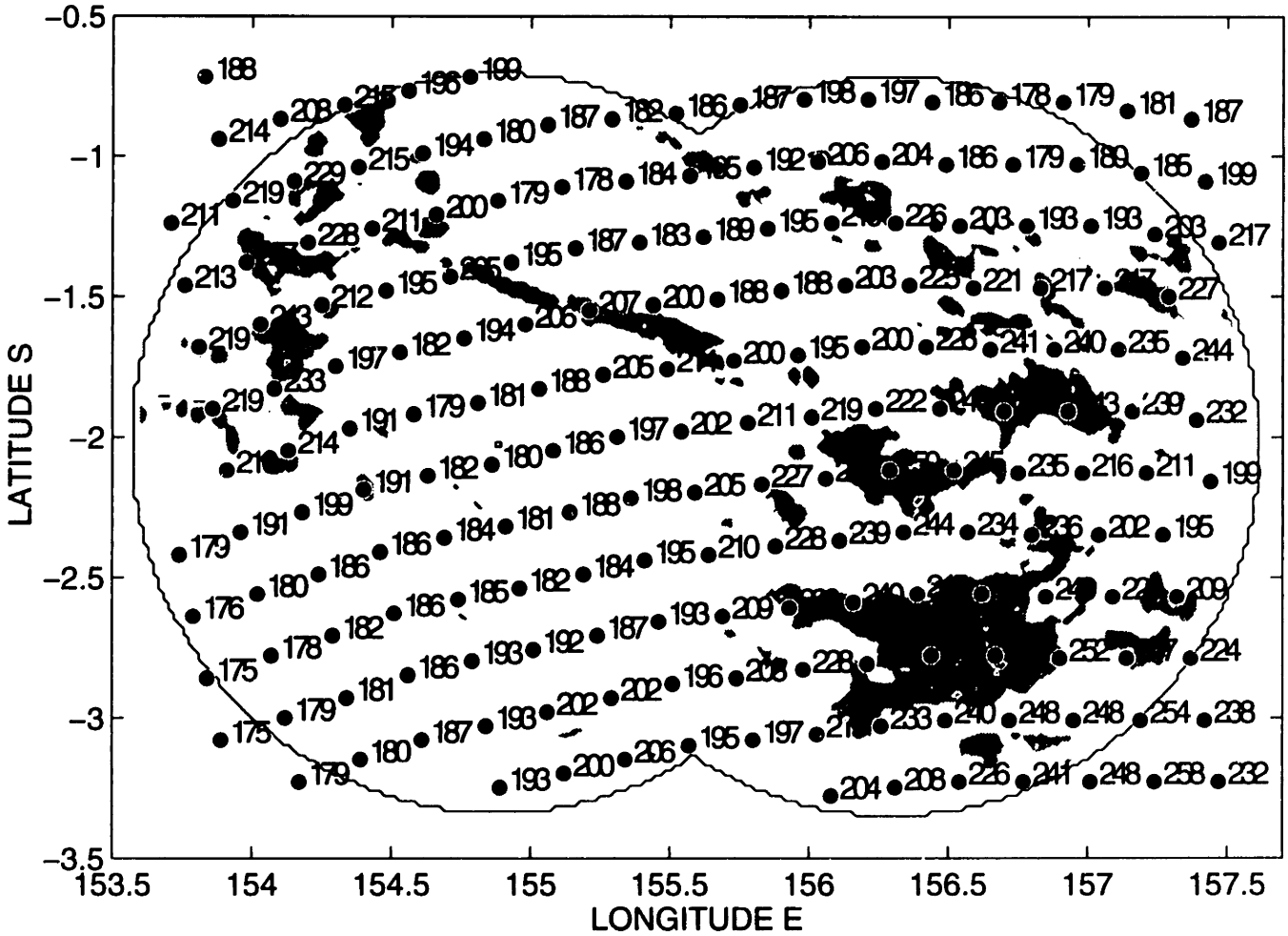

Figure 4-22: Simultaneous observations by radar and SSM/I over TOGA-COARE area. 31 January 1993, radar time: 07:01, SSM/I time: 07:03. Areas with rain rate over 0.5 mm h^{-1} are shaded. Each dot in the figure represents the center of a field of view and the number to the right of the dot indicates the horizontally polarized 37-GHz brightness temperature.

observe many high-T_B FOVs that contain very little rain or no rain at all. To give an idea of how the T_Bs of these rain-free FOVs are higher than the normal sea surface T_B, the histogram of the 37-GHz T_B is shown in Figure 4-23, which is based on all available data during December over the COARE region. The histogram peaks at about 175 °K, which can be interpreted as the brightness temperature of a normal sea surface observed by SSM/I. Compared with this normal background T_B of 175°K, however, many FOVs within the rain-free areas in Figure 4-12 through Figure 4-22 have T_Bs that are considerably higher. For example, the upper-right portion of the 20 December 1992 scene (Figure 4-13) contains very little rainfall, nonetheless the brightness temperatures for those FOVs are quite high (up to 220 °K). Similar phenomena can be observed in all other figures. It can also be noticed that the closer a rain-free FOV is to a major rain cell, the higher its T_B can get.

As in the cases shown for the Darwin area, the brightness temperature is plotted against the fractional coverage of rain within the FOV. Here the fractional coverage of rain, designated as f, is the fractional area within the FOV that is covered with rain rate higher than 0.5 mm h^{-1}. Figure 4-24 shows the $T_B \sim f$ plots for the 11 scenes. All the plots show a cluster of points along the lower portion of the T_B axis, indicating that there are a bunch of FOVs whose rainfall is zero but whose brightness temperature span a range up to as high as 220 °K. One can observe that the maximum T_B for the rain-free FOVs is different for different scenes (e.g., 210 °K for 19 December 1992, and 230 °K for 20 December 1992). One can also notice that, similar to the Darwin area, the T_B increases rapidly with increasing f, and seems to saturate towards a maximum T_B.

This phenomenon of high T_B without rain has also been observed by other

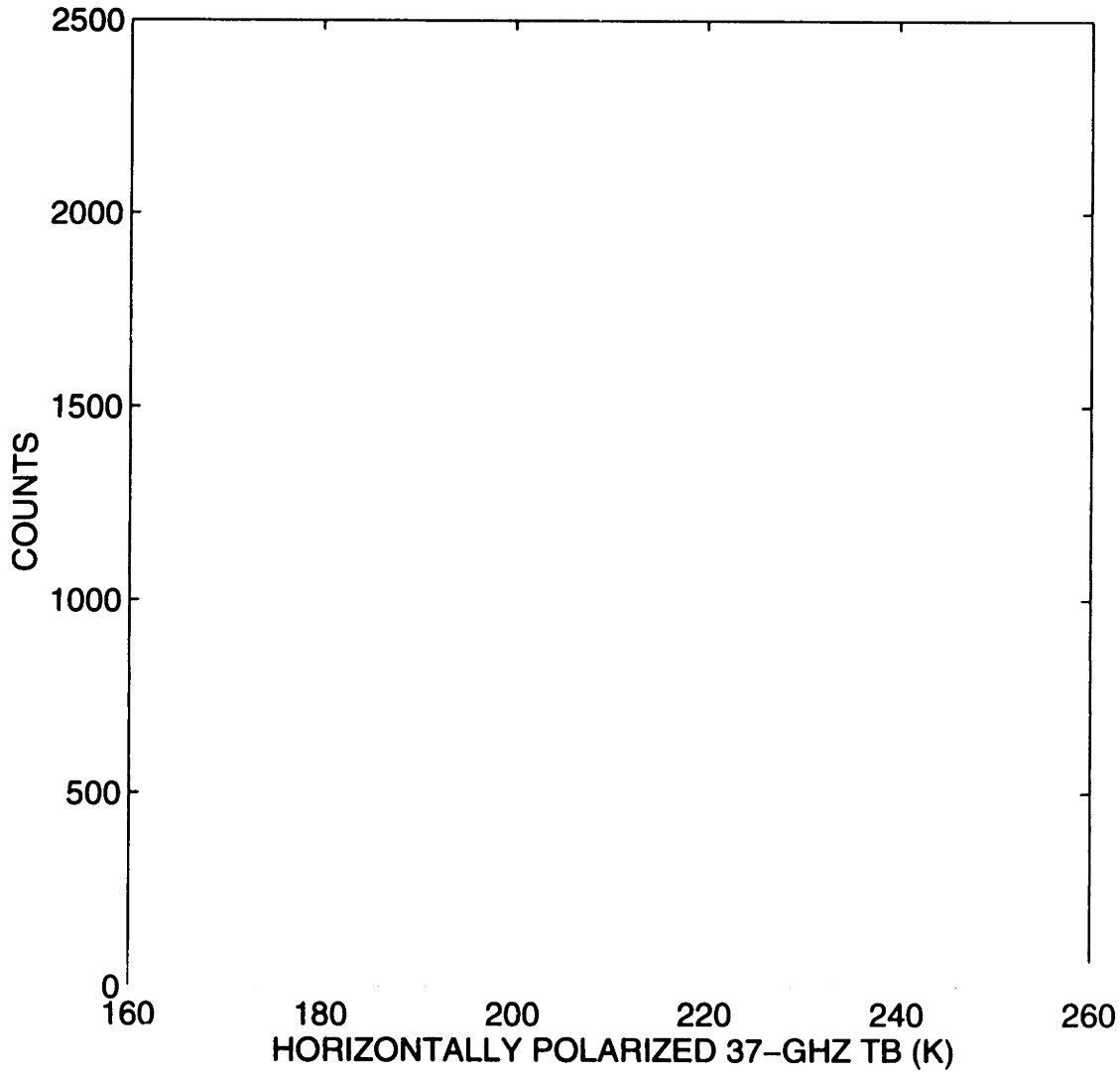

Figure 4-23: Histogram of the 37-GHz horizontally polarized brightness temperature over TOGA-COARE region; data from December 1992.

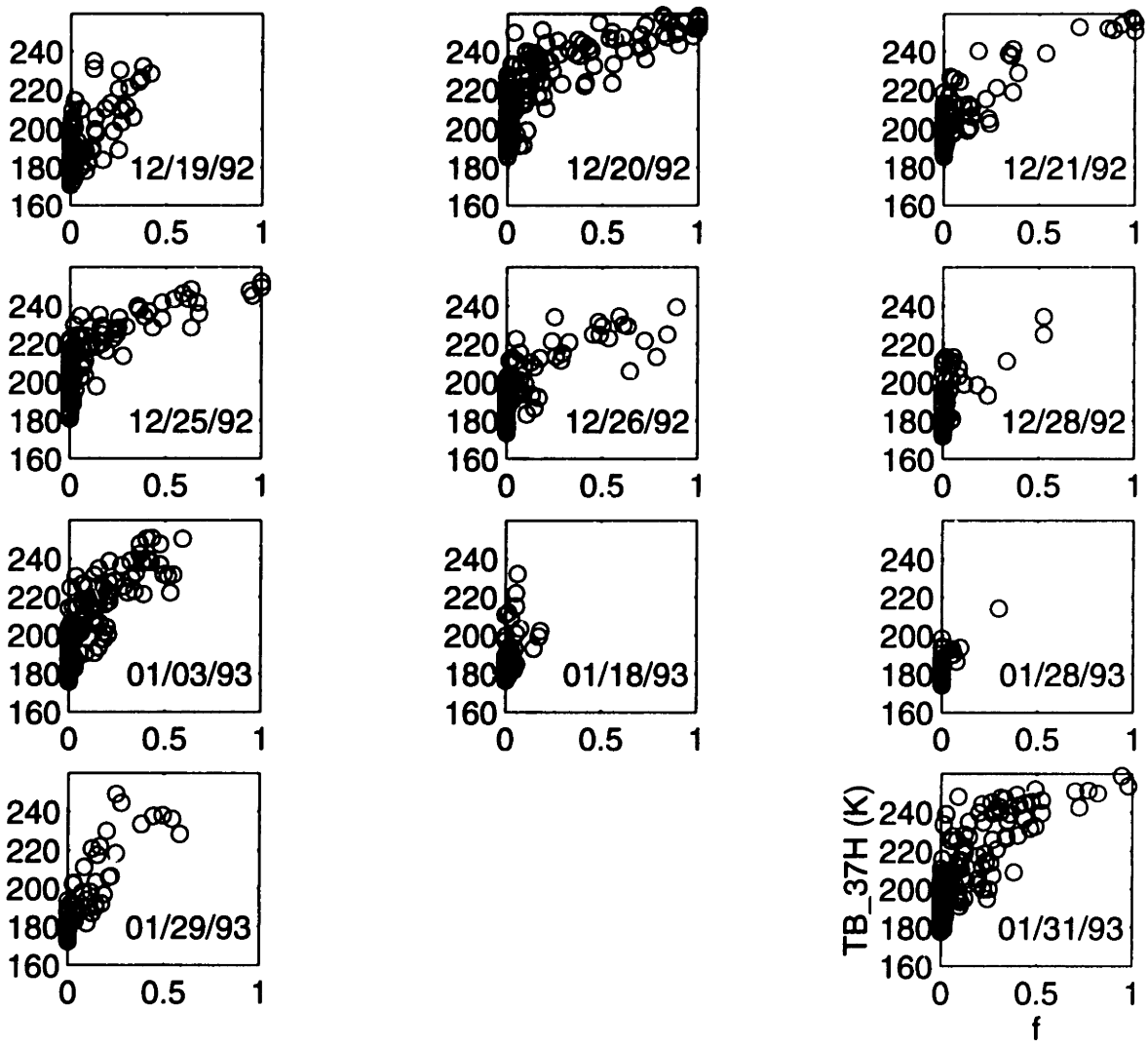

Figure 4-24: 37-GHz horizontally polarized T_B versus fractional coverage of rain within the FOV.

researchers. Adler and Hakkarinen (1991), when comparing aircraft passive microwave and ground-based radar observations, found that rain was not detected until the 37GHz horizontally polarized T_B reached about 190 °K, while the clear-sky T_B was as low as 155 °K. Petty and Katsaros (1990) presented a plot of rain rate versus polarization difference P, which showed that rainfall did not occur until P dropped below 0.7. Values of P below 0.7 correspond roughly to T_B above 190 °K.

4.2 Effects of Non-Precipitating Clouds and Wind

In this section, we will explore the causes of the high brightness temperatures in the rain-free areas of a cloud cluster. We postulate that such high T_Bs are caused mainly by wind and non-precipitating clouds. In a mesoscale cloud cluster, cloud and wind tend to affect areas larger than the raining cells embedded in the cluster. Although not as effective as rain a non-precipitating cloud can increase T_B through absorption and emission. Wind can also cause significant T_B increases by raising the emissivity of the sea surface. These effects are quantitatively evaluated in this section.

4.2.1 Non-Precipitating Clouds

Cloud droplets usually have sizes smaller than 100 μm, much smaller than the microwave wavelength (8.1 mm at 37 GHz and 15.5 mm at 19 GHz). When a droplet is much smaller than the wavelength, its scattering effect is much smaller than the absorption effect and can be ignored in the radiative transfer calculation. Thus the following equation can be used to describe the microwave

transfer in a non-precipitating cloud

$$\frac{dT_B(\theta, z)}{dz} = -\gamma_{abs} T_B(\theta, z) + \gamma_{abs} T(z) \tag{4.1}$$

where T_B is brightness temperature, T is air temperature; γ_{abs} is the absorption coefficient of cloud, θ is view angle which is the angle formed by the vertical line and the view line, and z is the distance along θ.

Assuming a constant γ_{abs}, the solution of this equation is

$$T_B(\theta, z) = \{T_B(\theta, 0) + \int_0^z T(\xi)\gamma_{abs} e^{\gamma_{abs}\xi} d\xi)\} e^{-\gamma_{abs} z} \tag{4.2}$$

where $T_B(\theta, 0)$ is the brightness temperature of the underlying ocean surface. Thus the brightness temperature observed at z is contributed in part by the ocean surface and in part by the cloud. If the absorption is very weak (i.e., γ_{abs} is very small), the ocean surface term dominates and the sensor mainly sees the surface $T_B(\theta, 0)$; on the other hand, if the absorption is strong, the surface term vanishes and the observed T_B is affected mainly by the temperature of the upper layer of the cloud.

The absorption coefficient represents the collective effect of all cloud droplets and is obtained by integrating the absorption cross section, $\sigma_a(\rho)$, of a single droplet of radius ρ over the number density function $N(\rho)$

$$\gamma_{abs} = \int \sigma_a(\rho) N(\rho) d\rho \tag{4.3}$$

The absorption cross section $\sigma_a(\rho)$ has the dimension of area, and $\sigma_a(\rho)/(\pi\rho^2)$ represents the fraction of the energy incident on the droplet that is absorbed. $N(\rho)d\rho$ is the number of droplets with radius between ρ and $\rho + d\rho$ per unit

volume. Hence, γ_{abs} has dimension (length)$^{-1}$.

For single cloud droplet of radius ρ

$$\sigma_a(\rho) = \frac{\lambda^2}{2\pi} 2(\frac{2\pi\rho}{\lambda})^3 Im(-K) = \frac{6\pi}{\lambda} V(\rho) Im(-K) \tag{4.4}$$

where λ is wavelength, $K = (m^2 - 1)/(m^2 + 2)$, m is the complex refractive index (which is the square root of the complex dielectric constant) and can be obtained from Lane and Saxton (1952) or Gunn and East (1955), and $V(\rho)$ is the volume of a droplet with radius ρ. Thus, σ_a is proportional to the volume of the droplet. Integration over $N(\rho)$ gives

$$\gamma_{abs} = \frac{6\pi}{\lambda} \cdot M \cdot Im(-K) \tag{4.5}$$

where M is cloud water content in g m^{-3}, λ is wavelength in mm, and γ_{abs} is in km^{-1}. In (4.2), the controlling factor is $\gamma_{abs}z$ which is equal to

$$\gamma_{abs}z = \frac{6\pi}{\lambda} \cdot Q \cdot Im(-K) \tag{4.6}$$

where $Q = Mz$ is the cloud water content per unit area (kg m^{-2}) in the θ direction.

Assuming $T_B(\theta, 0)$=175 °K (clear-sky, calm-sea T_B observed from top of atmosphere), two cases of mean air temperature within the cloud of 283 °K and 293 °K, and dT/dz=-6 °C km^{-1}, one can use (4.2) to calculate the upwelling T_B as a function of Q. This is shown in Figure 4-25. For the range of Q shown (up to 1 kg m^{-2}), T_B increases almost linearly with Q, the slope is about 22 °K/(kg m^{-2}). According to observation (Akvilonova et al., 1971), a cloud water content of 0.5 kg m^{-2} is the dividing line between non-precipitating and precipitating clouds.

Thus , according to the calculation, a non-precipitating cloud can produce a T_B increase up to about 10 °K at 37 GHz and less at 19 GHz. This is consistent with earlier studies (e.g., Lovejoy and Austin, 1982; Gunn and East, 1955).

In addition to absorption, clouds can enhance the upwelling T_B through reflection when the view angle of the sensor is large. The T_B of the cloud, which is much higher than the sky background, is reflected by the nearby water surface, causing the water to have a T_B higher than it would otherwise do. Given that the usual height of a cloud is only a few km, however, the reflection effect should be limited to a small area around the cloud.

4.2.2 Wind

Wind can increase sea surface emissivity in two ways. First, it creates waves whose emission characteristics are different from those of a smooth sea; second, if wind speed is above about 7 m s^{-1}, it produces whitecaps and foams which have emissivity much higher than that of sea water (e.g., Nordberg et al., 1971). We will discuss these two kinds of wind effect separately.

1) Waves

For a specular (perfectly smooth) sea surface, the emissivity ϵ at a view angle θ can be derived from the Fresnel formula as

$$\epsilon_h(\theta) = 1 - ((\kappa - 1 + cos^2\theta)^{\frac{1}{2}} - cos\theta)((\kappa - 1 + cos^2\theta)^{\frac{1}{2}} + cos\theta)^{-1} \qquad (4.7)$$

and

$$\epsilon_v(\theta) = 1 - ((\kappa - 1 + cos^2\theta)^{\frac{1}{2}} - \kappa cos\theta)((\kappa - 1 + cos^2\theta)^{\frac{1}{2}} + \kappa cos\theta)^{-1} \qquad (4.8)$$

where the subscripts h and v indicate horizontal and vertical polarization,

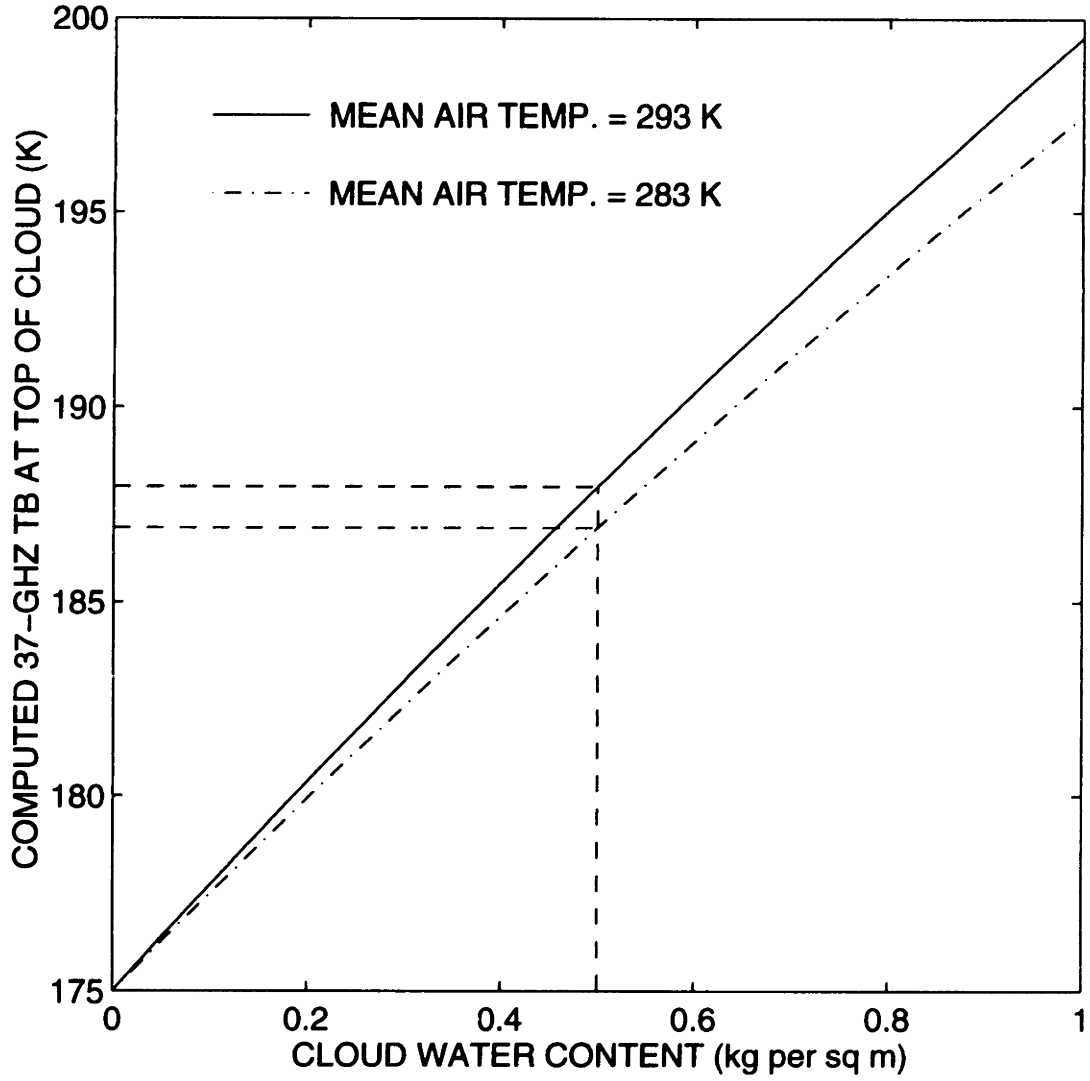

Figure 4-25: Upwelling brightness temperature at 37 GHz as a function of non-precipitating cloud water content

respectively; κ is the complex dielectric constant of sea water which is a function of temperature and frequency, and θ is the view angle. For a fixed κ, ϵ_h decreases with θ while ϵ_v increases with θ.

A curved sea surface can be approximated by many facets with different slopes, and each facet can be treated as a smooth surface. A footprint of the radiometer will contain many such facets. To a sensor looking at a view angle θ with respect to the horizontal surface ($x - y$ plane), these facets will have view angles different from θ. Since the emissivity depends on the view angle, these facets will have different emissivity in the view direction of the sensor, resulting in an observed emissivity that is different from that of a smooth surface.

The distribution of sea surface slopes has been investigated by a number of researchers. Cox and Munk (1955) proposed a two-dimensional normal distribution of the form

$$f(s_x, s_y) = \frac{1}{\pi\sigma^2} exp(\frac{s_x^2 + s_y^2}{\sigma^2}) \tag{4.9}$$

where $s_x = d\xi/dx$ and $s_y = d\xi/dy$ are slopes in the x and y directions, respectively, and ξ is surface elevation. The variance σ^2 is related to the 12.5-m wind speed w as

$$\sigma^2 = 0.003 + 0.00512w \tag{4.10}$$

where w is in m s^{-1}. Using a slope distribution similar to this, Stogryn (1967) showed that the horizontally polarized T_B increases substantially with wind speed , especially for large θ. Figure 4-26 is based on Stogryn (1967) and shows the T_B increase as a function of wind speed and view angle. For a wind speed of 7 m s^{-1}, for example, the T_B increase at 35 GHz and 53° view angle is about 7–8 °K; a wind speed of 14 m s^{-1} and at 19 GHz results in about a 20 °K increase in T_B. It was also shown by Stogryn, on the other hand, that the vertically

polarized T_B is not as sensitive to wind. Particularly at θ=53° (view angle for SSM/I), no change occurs.

Most recently, Atlas (1994) presented cases where the enhanced backscattering observed by synthetic aperture radar (SAR) over oceans has been attributed to the storm-induced waves. It was argued that the combination of rain and wind effects changes the surface radar cross section as compared with a calm sea surface, and such changes would impact spaceborne measurements of surface wind by scatterometer and rainfall measurements by radar.

A series of experiments were carried out to measure the microwave emission from the wind-driven foam-covered water surface in late 60s and early 70s (e.g., Singer and Williams 1968; Williams 1969; Hollinger 1970; Nordberg et al. 1971; Webster et al. 1976). In these experiments, the increase in T_B was observed in both polarizations, with relatively more for the horizontal and less for the vertical polarization. Nordberg et al. (1971) observed a linear increase of T_B with wind when the wind is above 7 m s^{-1}. As they were viewed at nadir (θ=0°), the observed T_B increase cannot be explained by the wind-induced waves based on the theory. Observation and calculation have shown that the high-emissivity foam induced by high-speed wind can also contribute to the T_B increase, independent of the view angle and polarization.

2) Foam

Above a certain critical wind speed, waves begin to break. Foam resulting from wave-breaking has emissivity much higher than the water surface. Droppleman (1970) has calculated the emissivity of a smooth water surface covered with a uniform layer of foam. The foam was assumed to consist of a mixture of air and water with the size of the bubbles restricted to being less than a wavelength. The addition of a layer of foam alters the emissivity of the smooth

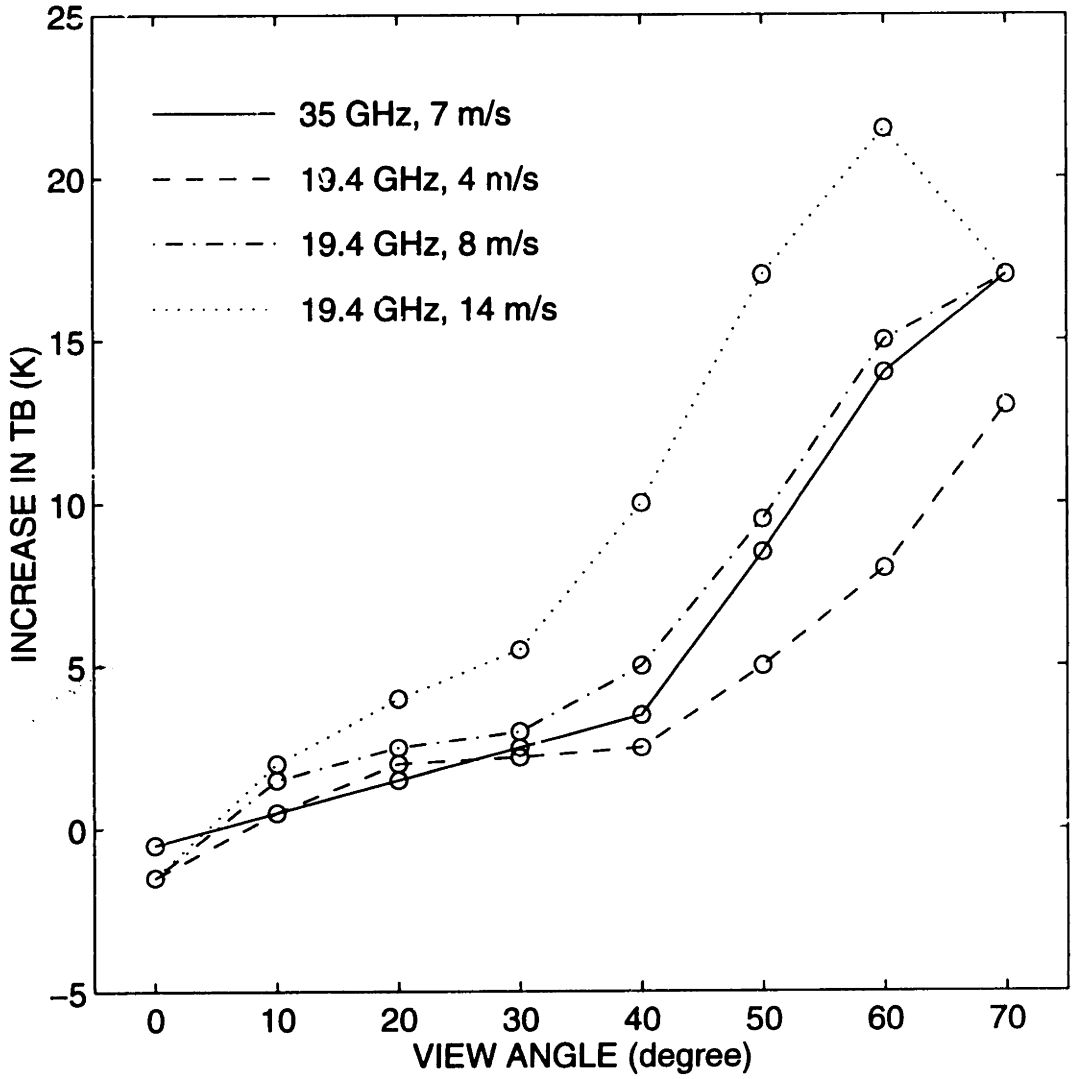

Figure 4-26: Increase in horizontally polarized brightness temperature due to wind as a function of view angle (based on Stogryn 1967).

water surface due to absorption and reflection from the upper air-foam and the lower foam-water interfaces. The foam was treated as a porous material, the relative dielectric constant of which was given by

$$\kappa_f = \kappa_w[1 - \frac{3R}{(2\kappa_w + 1)/(\kappa_w - 1) + R}] \tag{4.11}$$

where κ_w is the dielectric constant of sea water; the dielectric constant of the air was assumed to be 1; and R is the ratio of the volume of air to the total volume. At R=0 and 1, $\kappa_f = \kappa_w$ and there is no foam present. Droppleman calculated emissivity of the foam as a function of R at a number of frequencies for a foam depth of one wavelength. The result showed that the emissivity increases with R and approaches maximum (close to 1) for R=0.94~0.99, and decreases afterwards, approaching that of water. It was predicted that the T_B of the sea surface will approach the thermodynamic temperature if the sea foam exists over a significant portion of the sensor's FOV.

A number of experiments were carried out to measure the T_B of foam-covered sea surface. Singer and Williams (1968) discussed briefly the effect of background emission. Their laboratory simulation showed that roughening of the ocean surface by falling rain will produce a small additional increase and that winds above 15 knots will produce an increase through the mechanism of foam generation, which will be some function of wind velocity and which for high wind velocity may raise T_B to those corresponding to moderate rain.

Williams (1969) reported an experiment where the brightness temperatures from smooth water surface, water surface with spray, and water surface with foam were compared. It was shown that spray on water could cause a 50 °K increase at 22.2 and 34 GHz, and the presence of a blanket of foam produced a

large increase of about 100 °K for all frequencies.

Hollinger (1970) performed an experiment to study the dependence of microwave emission on sea state, wind, and foam. The observation was made at 8.36 and 19.34 GHz from an island tower. Results showed that the horizontally polarized T_B increases with wind speed. The role of foam in raising emissivity was also confirmed.

Aircraft observations reported by Webster et al. (1976) showed that the combination of surface roughness and white water causes the brightness temperature to depend significantly on wind speed over a wide range of microwave frequencies. They used a linear regression to determine the best fit to the T_B versus wind speed data. The slopes were 1.39±0.1 (19 GHz horizontal), 0.6 (19 GHz vertical), 1.33±0.38 (37 GHz horizontal), and 0.48±0.14 °K/(m s^{-1}) (37 GHz vertical).

The above observations are generally consistent with each other and point to the fact that the vertically polarized T_B is mainly affected by the foam while the horizontally polarized T_B is affected by both the wave structure and the foam, and that the amount of foam is controlled by surface wind speed. Based on these observations, Wilheit (1979) proposed an approximate expression for the emissivity increase due to foam

$$\triangle\epsilon = a(1 - e^{f/f_0})(w - 7) \tag{4.12}$$

where f is frequency in GHz, f_0=7.5 GHz, a=0.006 s m^{-1}, and w is wind speed (m s^{-1}) at 20 m height. For wind speed less than 7 m s^{-1}, there is no foam effect. And for a wind speed of 17 m s^{-1} and at 37 GHz, for example, the emissivity increase due to foam is 0.06, which translates into a T_B increase of about 18 °K

for a normal sea water temperature in the tropical regions.

4.3 Gust Front Associated With Storm Outflows

The gust front originating from a thunderstorm can propagate along the surface at very high speed. Although most of the gust fronts studied in the literature have been observed over land, gust fronts can occur over the oceans. The main source of cold air behind the gust front is the thunderstorm downdraft which is driven by the precipitation drag and the evaporative cooling of rain drops. Upon reaching the underlying surface, the downdraft spreads out and affects an area much larger than the thunderstorm itself. The low-level structure of the gust front has been studied extensively (e.g., Goff, 1976; Mahoney, 1988; Wakimoto, 1982; Intrieri et al., 1990; Mueller and Carbone, 1987). Wakimoto (1982) identified four stages in the development of a gust front, i.e., formative, early mature, late mature, and dissipating stages. Except for the last stage, the speed of the gust front can easily exceed 10 m s^{-1} and approach 30 m s^{-1}. In several cases he studied, he found that the distance traveled by a single gust front exceeded 100 km. Mahoney (1988) summarized the characteristics of 30 gust fronts observed in eastern Colorado. It was found that the mean propagation speed was 8.6 m s^{-1} with a standard deviation of 3.0 m s^{-1}, and the mean maximum speed was 14.5 m s^{-1} with a standard deviation of 2.3 m s^{-1}.

It is intuitive that the gust front and, correspondingly, its effect on the sea surface, will weaken as it travels away from the originating rain cells. Thus, the increase of T_B in the no-rain FOVs should decrease with increasing distance from the surrounding rain cells. Such pattern can be recognized in Figure 4-5,

4-6, and 4-12 through 4-22.

4.4 Discussion of Some Previous Studies

Petty and Katsaros (1990, 1992) defined a normalized polarization difference $P = \triangle T_B / \triangle T_{B,Clr}$, where $\triangle T_B = T_{B,V} - T_{B,H}$ is the observed polarization difference and $\triangle T_{B,Clr}$ is the polarization difference expected in the absence of cloud and rain; and$T_{B,V}$ and $T_{B,H}$ are, respectively, the vertically and horizontally polarized brightness temperature. Because radiation from the water surface is highly polarized while radiation from a raining cloud is essentially unpolarized, small P should be diagnostic of rain. Petty and Katsaros showed that $T_{B,H}$ and P are linearly correlated. Such correlation was also found in our data (Figure 4-27). Petty and Katsaros attributed the reduction in P to the partial coverage of the FOV by rain cells, and developed a linear relationship between P and the fractional coverage of rain. However, since our radar showed no rain for the 37-GHz $T_{B,H}$ below about 210 °K, the reduction of P in situations where $T_{B,H}$ is less than 210 °K can not be explained by the mechanism of partial rainfall coverage. We suspect that wind could play a role, since, as shown before, wind can produce a linear $P \sim T_B$ relationship through the differential growth rate of $T_{B,H}$ and $T_{B,V}$ with wind speed. For the intermediate T_B range, the reduction in P (and correspondingly the increase in T_B) could be due to wind effects alone.

In studying SMMR and SSM/I data, Prabhakara et al. (1992) found that the values of T_B at 19 GHz and 37 GHz are nearly linearly related and that $T_{B,V} - T_{B,H}$ is also linearly related to $T_{B,H}$, over almost the entire range of the observed T_B values. However, their cloud model produced a highly nonlinear $T_{B,H,37} \sim T_{B,H,19}$ relationship. They commented that the observed linear relationship

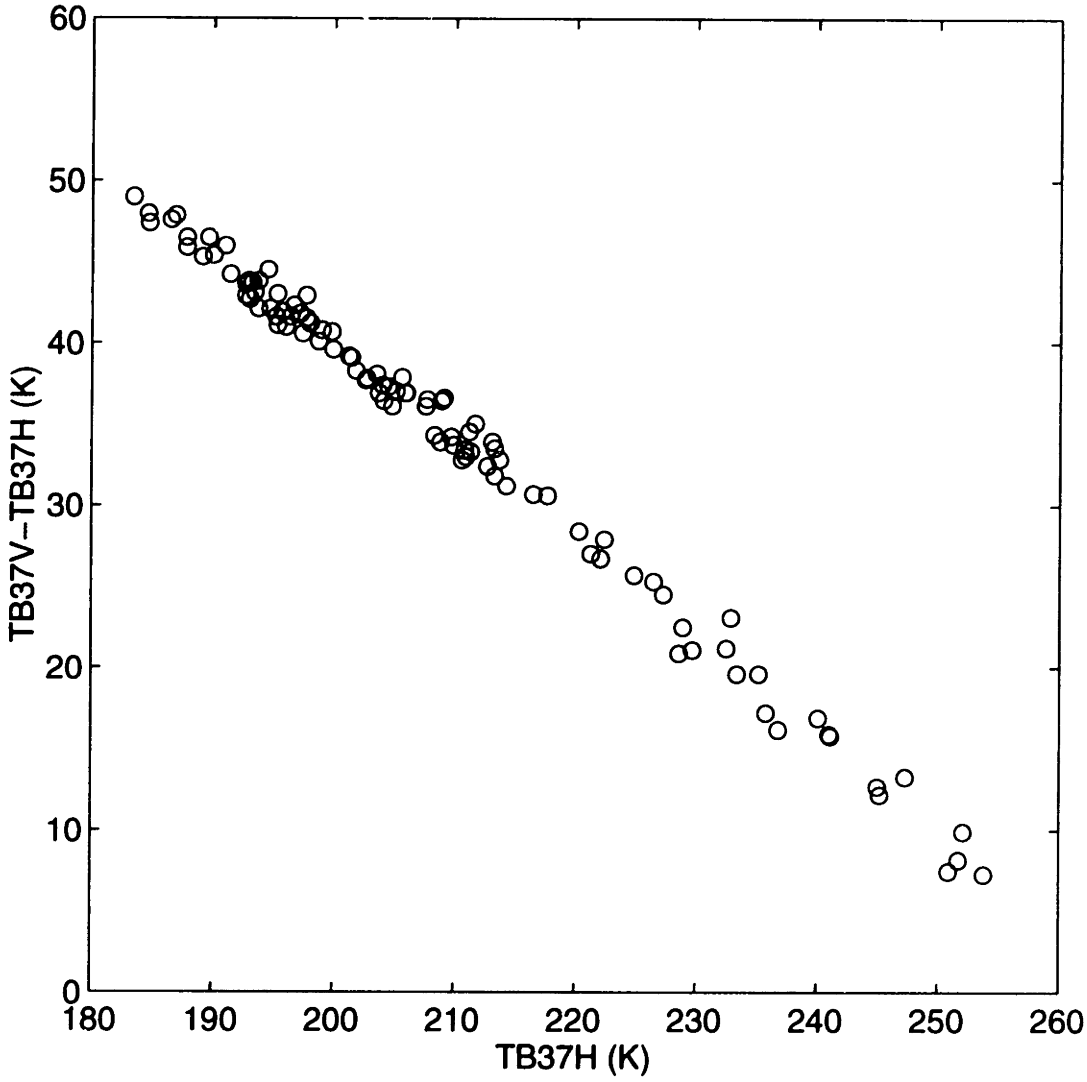

Figure 4-27: Polarization difference (TB37V-TB37H) versus TB37H, where TB37V and TB37H refer to the 37-GHz brightness temperature in the vertical and horizontal polarization, respectively. Data are taken from the 13 and 14 January 1990 events over Darwin area.

between $T_{B,V} - T_{B,H}$ and $T_{B,H}$ can be accounted for in terms of the effective rain area in the FOV, and that the nonlinear $T_{B,H,37} \sim T_{B,H,19}$ relationship produced by the model was due to the difficulties in defining realistic spatial distributions of rain and clouds in the model (fractional rain coverage is almost 1 in the model). Thus the results of the model represent only intense rainfall events.

Another explanation of the phenomenon described in Prabhakara et al. (1992) can be given in terms of the wind effects on sea surface emissivity. Notice that when $T_{B,H,19}$ is plotted against $T_{B,H,37}$, all satellite observations are used. Only a small portion of the data can possibly correspond to raining FOVs, which most likely correspond to points in the high-T_B range. The linear relation over the low-T_B range should be due to the wind. Based on what we have found using our data, FOVs that actually contain rainfall are those with very high T_Bs. Thus one might expect to observe some nonlinearity at the high T_B end of the $T_{B,H,19} \sim T_{B,H,37}$ scatter plot, as suggested by the results of model simulations in Prabhakara et al (1992) (the nonlinearity results from the fact that the T_B at 37 GHz saturates at lower rain rate than the T_B at 19 GHz does). This is indeed evident in Figure 4-28 which is based on data from the TOGA-COARE region. Figure 4-28 shows that the relationship between T_B at 37 GHz and 19 GHz is nearly linear for almost the entire range of the observed T_B values. Based on the observation that rain does not occur until the 37-GHz T_B reaches about 210 °K (see Figure 4-24), we can conclude that the linear relationship in the range with T_B less than 210 °K can not be attributed to rain, rather it should be the effect of wind. At the high-T_B end, where the FOVs are expected to contain (potentially intense) rainfall, we do observe some nonlinearity: The plot begins to level off as the 37-GHz T_B starts to saturate at high rain rate,

while the 19-GHz T_B still increases with increasing rain rate. The fact that the nonlinearity observed in the data is not as severe as that simulated by the model implies that the intense rain rate and large rainfall coverage used in the model seldom occur in nature.

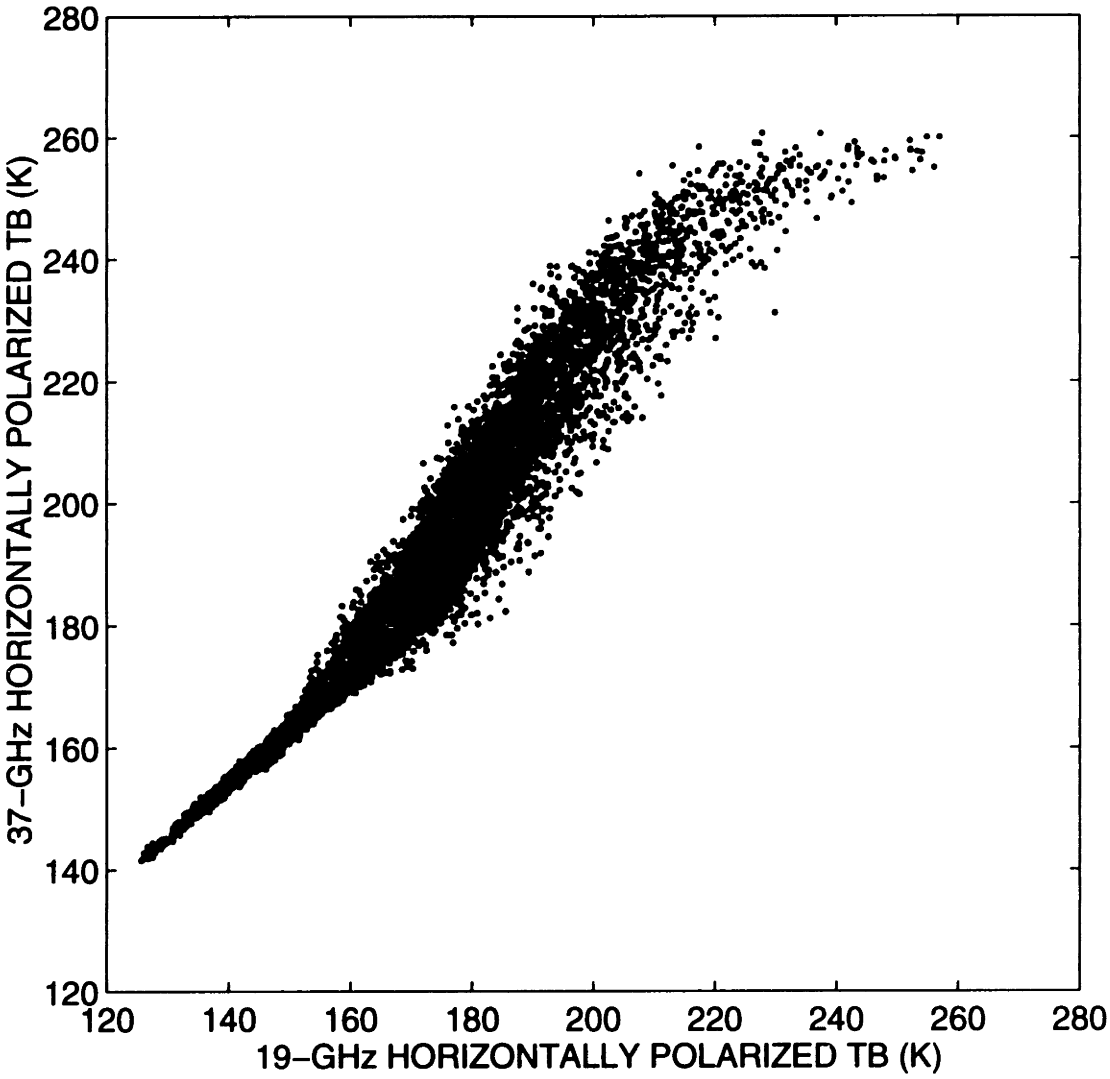

Figure 4-28: Scatter plot between the horizontally polarized brightness temperature at 19 and 37 GHz; data cover December 1992–January 1993 over the TOGA-COARE Intensive Flux Array region.

Chapter 5

A New Algorithm for Passive Microwave Rainfall Retrieval Considering the Effects of Wind and Clouds

There are several ways to quantify the effects of cloud and wind, and to partition the total T_B into contributions by rain, cloud, and wind. One way is to couple a numerical cloud model with a radiative transfer model, where the surface rainfall, together with non-precipitating cloud water and surface wind, is simulated by the cloud model and the upwelling T_B is computed by the radiative transfer model. By analyzing the model results, one might be able to suggest an algorithm by which the non-rain effects can be eliminated under various conditions. Adler et al. (1991), for example, used a detailed cloud model to simulate upwelling T_B from convective storms and generated a relationship between T_B and rain rate at various frequencies. However, Adler et al. did not explicitly separate rain from non-rain effects.

As an alternative to numerical modeling, we have used a statistical approach to extract information from a considerable number of simultaneous radar and satellite observations. In this chapter we derive a relationship between the T_B of a FOV and the fractional rainfall coverage (f) within that FOV, and examine how this $T_B \sim f$ relation can lead to a $T_B \sim R$ relation, where R is the average rain rate within the FOV.

Our model is based on the fact that rainfall occurs in spatially isolated rain cells, and each rain cell is quite small in size. It is typical for a FOV to be only partially covered by rain. To validate this, we have analyzed the radar rainfall data of TOGA-COARE to see the spatial characteristics of surface rainfall field. We divided the area covered by the two radars into grid boxes with size comparable to that of a FOV at 37 GHz. Since the resolution of the available radar data is 2 km, the size of the grid box we used was set to 24 km by 24 km (144 original radar pixels). We looked at every radar scan and counted the number of raining pixels (N) within each 24 km by 24 km box. A pixel is classified as raining if its rain rate is above 0.5 mm h^{-1}. The fractional rainfall coverage (f) has been calculated as

$$f = \frac{N}{144} \tag{5.1}$$

By looking at all the available radar scans, we obtained the probability density function of f. Since we are concerned mainly with the fractional rainfall coverage when it is raining in the FOV, we have obtained the cumulative probability function of f conditioned on rain within the FOV, which is shown in Figure 5-1. We can see that about 70% of all raining FOVs have fractional rain coverage less than the mean (0.18). Thus when we evaluate the observed T_B from a rain-

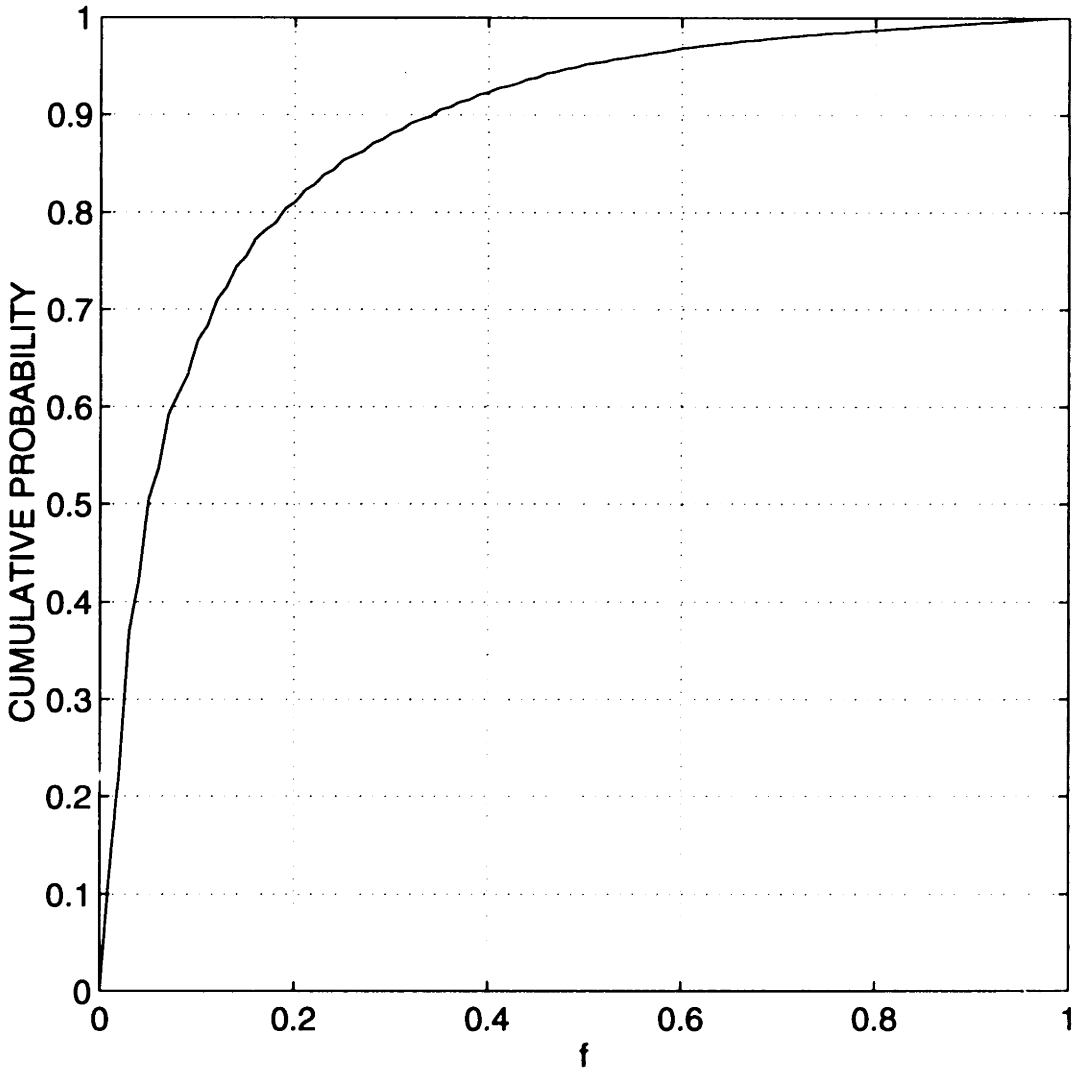

Figure 5-1: Cumulative probability of fractional rainfall coverage within a FOV of 24 km by 24 km; based on TOGA-COARE radar data.

ing FOV, we know that generally the T_B is due only partially to the rain cells, and the rest comes from sea surface. Our model deals with the partition of the FOV T_B into contributions from the rain cells and the rain-free sea surface.

5.1 Emission From Rain

The microwave emission from a raining cloud depends mainly on the rain rate. When rain rate is high enough, the brightness temperature from rain can saturate. In both the Darwin area (e.g., Figure 4-6) and the TOGA-COARE area (e.g., Figure 4-13 and 4-14), it can be observed that, whenever a FOV is entirely located inside a rain cell, its brightness temperature tends to saturate at a very high value (around 255 °K). Although there is some fluctuation around this saturation level, for simplicity we assume in our model that the brightness temperature from any raining area saturates at the same value $T_{B,max}$.

5.2 Emission From Sea Surface

As discussed in previous sections, the brightness temperature from the sea surface is enhanced by wind and rain effects. In the vicinity of rain cells, the brightness temperature from the sea surface can be high even though the entire FOV is rain-free. When the FOV contains rain cells, the increase in the surface brightness temperature is even larger. Thus, in a simple model, brightness temperature from the sea surface can be expressed as

$$T_{B,min} + \Delta T \cdot f^{\alpha} \tag{5.2}$$

where $T_{B,min}$ is the minimum value of sea surface brightness temperature when a rain system is present in the general area, f is the fractional rainfall coverage within the FOV, $\triangle T$ is the maximum increase in brightness temperature due to the presence of rain in the FOV. Notice that $T_{B,min}$ is not the normal sea surface brightness temperature as described in Chapter 4, rather, it is, in an average sense, the brightness temperature of the rain-free areas within a cloud cluster. It is obviously higher than the sea surface brightness temperature under clear-sky conditions. As will be shown later, $T_{B,min}$ is an important parameter in our model, and needs to be determined using data.

5.3 $T_B \sim f$ Relationship

By combining sea surface and rain effects, the observed brightness temperature of a FOV is expressed as

$$T_B = (1 - f)(T_{B,min} + \triangle T \cdot f^{\alpha}) + f \cdot T_{B,max} \tag{5.3}$$

where the first term on the right-hand side is the contribution from the sea surface in the non-rainy portion of the FOV and the second term is the contribution from the rainy portion. $T_{B,min}$, $T_{B,max}$, $\triangle T$, and α are parameters to be determined. Examples of the $T_B \sim f$ curves are shown in Figure 5-2, where the lower curve has [$T_{B,min}$=175 °K, $\triangle T$=0 °K] and represents the case of constant surface emission and no-wind effect; the middle curve has [$T_{B,min}$=200 °K, $\triangle T$=0 °K] and is an example of constant wind effect, i.e., the increase of surface brightness temperature is independent of the raining condition in the FOV; the top curve has [$T_{B,min}$=200 °K, $\triangle T$=55 °K, α=0.5] and is a case where the increase in surface brightness temperature depends on f. All the curves

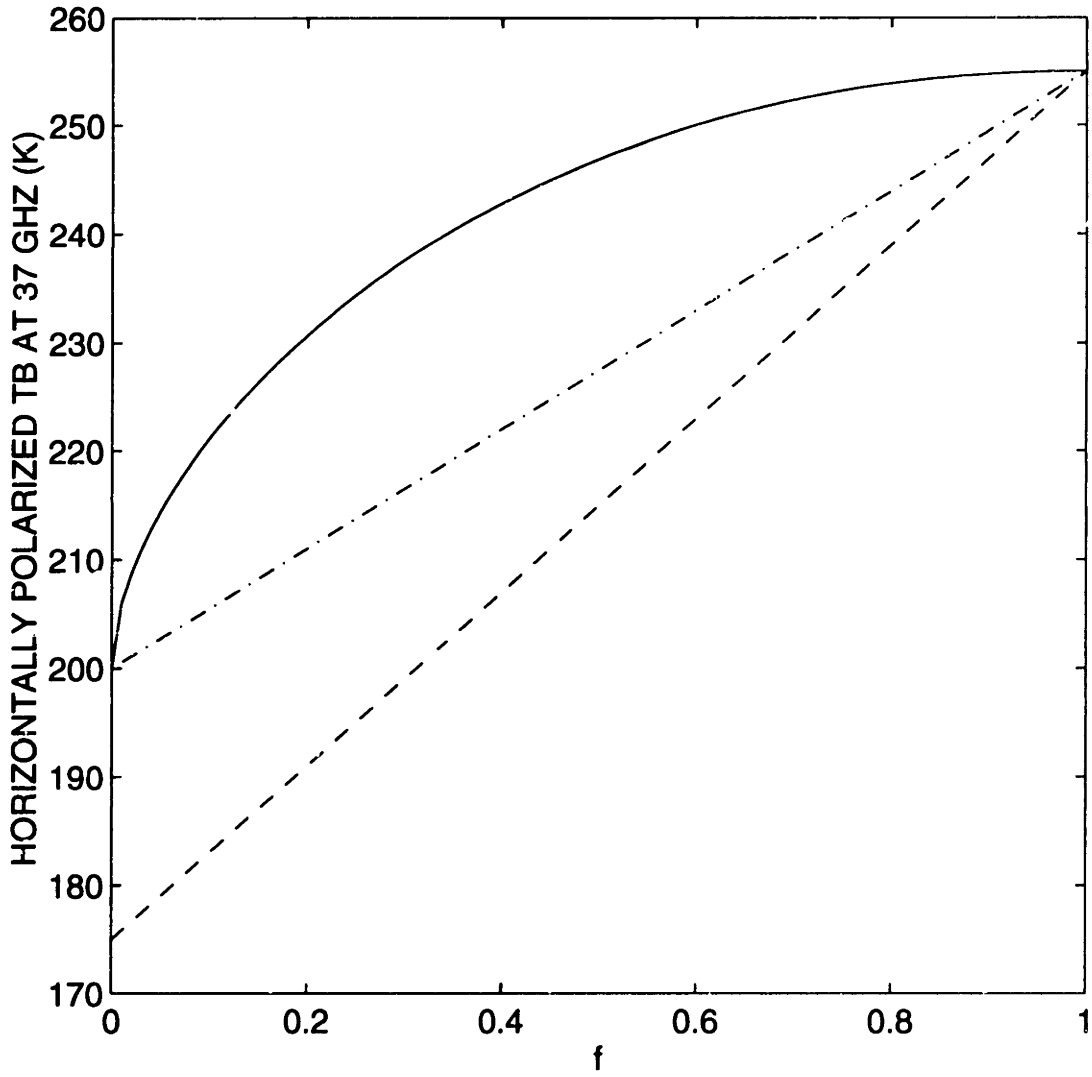

Figure 5-2: Examples of the model $T_B \sim f$ relationship. Lower curve: $T_{B,min}$ = 175 °K, ΔT = 0 °K; middle curve: $T_{B,min}$ = 200 °K, ΔT = 0 °K; top curve: $T_{B,min}$ = 200 °K, ΔT = 55 °K, α = 0.5; all curves have $T_{B,max}$ = 255 °K.

have $\alpha = 0.5$ and $T_{B,max} = 255$ °K. The four parameters can be determined by fitting the model to data, as will be described later.

5.4 $f \sim R$ Relationship

The ultimate goal of an algorithm is to relate T_B to surface rain rate R. However, the above model relates T_B to f only. One needs to establish a relationship between R and f. The HART (Height-Area Rainfall Threshold) method (Atlas et al. 1990, Rosenfeld et al. 1990) is of particular relevance in this context. It has been shown both theoretically and empirically that accurate estimation of the area-wide instantaneous rain rate from convective storms over a large area (about 10^4 km^2) can be made by using the area within a threshold rain intensity isopleth. With data from South Africa, Texas, GATE phase 3 and Darwin, Rosenfeld et al. (1990) found very good correlation between the areal rain intensity and the fractional area covered with rain intensities greater than 6 mm h^{-1}. Their work has essentially confirmed the findings of Chiu (1988a, b) who studied GATE phase 1 and 2 data.

Although operating at a much smaller spatial scale (FOV scale), the concept of relating areal rain rate to the fractional rainfall coverage can be used here. Using TOGA-COARE radar-observed rainfall data, we obtained the FOV mean rain rate as a function of f. The threshold for computing f has been set to 0.5 mm h^{-1}. This threshold is much smaller than that used in the above-referenced studies because we are dealing with a much smaller spatial scale. A high threshold would result in too low a fractional coverage. Since the resolution of the radar data is 2 km, the FOV size in this case has been taken as 24 km by 24 km (144 original pixels). Figure 5-3 shows this relationship, which is nearly

linear except for high f. The flattening (for standard deviation in particular) in the high f range may be due to the fact that when f is large, some of the rain may be of stratiform type and thus has smaller intensity and variability. The standard deviation is about the same as the mean, which means that the instantaneous FOV rain rate can be estimated from f with an error factor of about 2. This error may seem large when compared with other applications which relate R to f over large areas, but it is reasonable considering the small size of the FOV.

5.5 Fitting the $T_B \sim f$ Relation to Data

5.5.1 Initial Fitting

The $T_B \sim f$ model has four parameters which have to be determined from data. We selected 11 TOGA-COARE storm events observed simultaneously by both radar and SSM/I. Information about each event is listed in Table 5.1. The time gap between radar and SSM/I observations is a few minutes at most. The radar rainfall patterns for each of these events, together with the 37-GHz horizontally polarized brightness temperature, have been shown in Figures 4-12 through 4-22. The shaded areas have rain rate above 0.5 mm h^{-1}. Of all the events, the 12/20/92, 12/21/92, 12/25/92, 01/03/93, and 01/31/93 events show relatively larger spatial spreads of rainfall compared with the rest. Initially, the model was fitted to the 11 events, with $T_{B,max}$ fixed at 255 °K and $\Delta T = T_{B,max} - T_{B,min}$. α and $T_{B,min}$ were adjusted to produce the best fit by visual inspection, resulting in the parameter values listed in Table 5.2. The best values of $T_{B,min}$ and α for an event appear to depend on the strength of the event, i.e., its spatial spread and the intensity of rainfall. The rationale is that a more intense event should

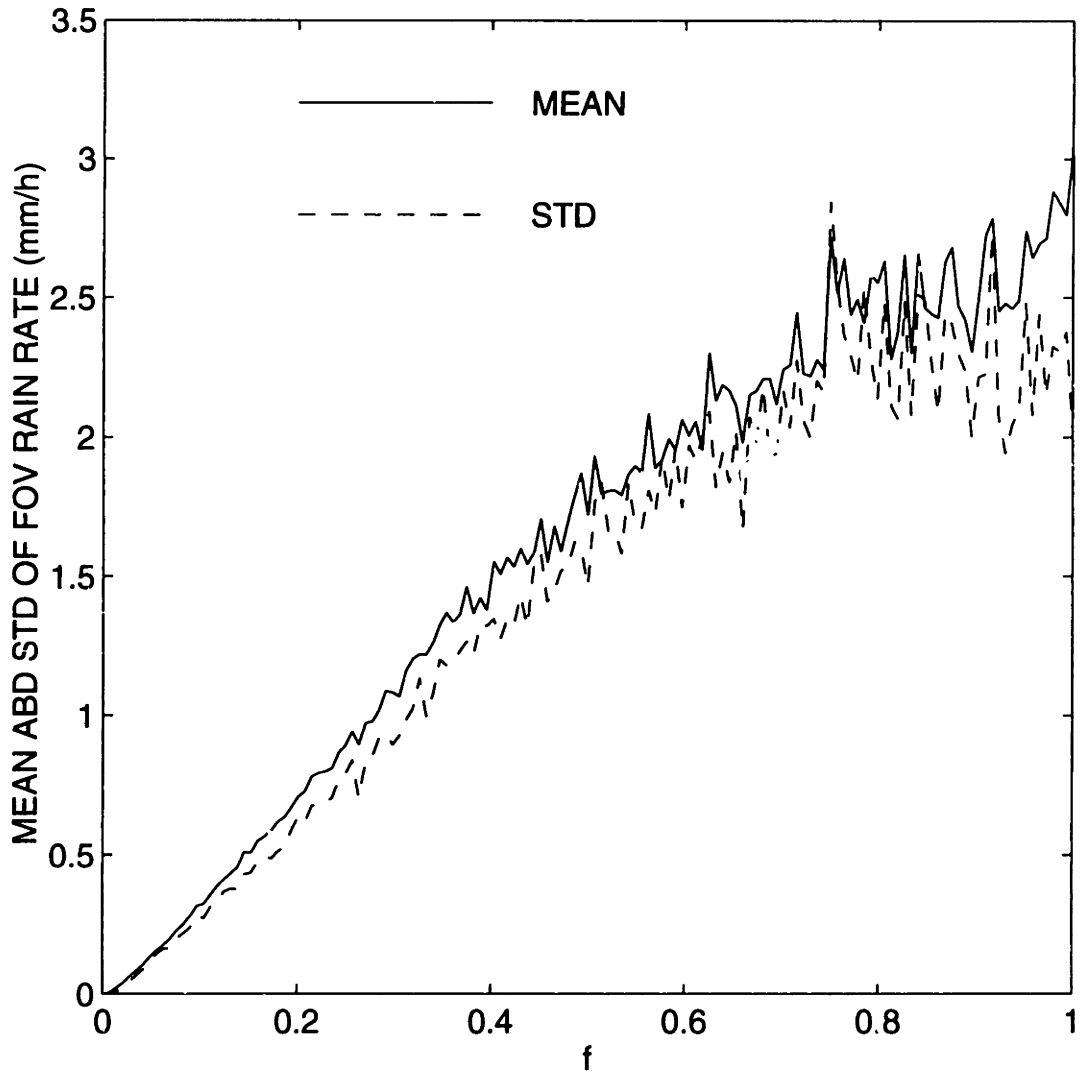

Figure 5-3: Relationship between the mean and standard deviation of FOV rain rate and the fractional coverage of rain within that FOV (size of FOV is 24 km by 24 km), data from TOGA-COARE December 1992–January 1993.

generate stronger wind and cloud effects, resulting in a higher $T_{B,min}$ and a smaller α.

5.5.2 Quantifying the Strength of the Storm

To further quantify the relationship between the optimal parameter values and the strength of an event, we must design a parameter which can be used to measure the strength of a storm. There are potentially several ways to do this. One straightforward method is to measure the wind directly at various locations and the model parameters are then related to the measured wind speed; another method is to use infrared channel to infer the cloud height which can be viewed as representative of the storm strength. However, in operational application it is ideal, if possible, to rely on a single source of data to make the algorithm simple and easy to use. Thus it is best to design a parameter which relies on the microwave data alone, since in actual applications of the algorithm satellite observations are the only available information. An inspection of the T_B field for various storm events (Figures 4-12 through 4-22) reveals that large storms tend to produce large areas of high brightness temperature. Based on this observation, the parameter which represents the strength of the storm has been defined as the fractional area within a cloud cluster that has T_Bs higher than 240 °K, i.e.,

$$frac[TB > 240] = \frac{A_{240}}{A_{total}} \tag{5.4}$$

where A_{240} is the area with T_B higher than 240 °K, and A_{total} is the total area of the cloud cluster. In actual application, the cloud cluster can not be sufficiently defined by the satellite data alone. Therefore, the determination of the total area of a cloud cluster has to be based on empiricism. In this study, we have

NO.	Date	Radar Time	SSM/I Time	Time Gap	Area (sq km)
1	12/19/92	19:01	18:58	3 min	51875
2	12/20/92	18:41	18:44	3	89375
3	12/21/92	18:31	18:32	1	63750
4	12/25/92	06:31	06:36	5	78750
5	12/26/92	19:11	19:08	3	81875
6	12/28/92	18:41	18:42	1	91250
7	01/03/93	19:01	19:05	4	80625
8	01/18/93	19:11	19:13	2	54375
9	01/28/93	18:41	18:45	4	55625
10	01/29/93	18:31	18:32	1	57625
11	01/31/93	07:01	07:03	2	88750

Table 5.1: Information about the 11 selected TOGA-COARE storms.

Event No.	TB,min (K)	ALPHA
1	180	1.0
2	210	0.25
3	200	0.5
4	210	0.5
5	190	1.0
6	200	1.0
7	200	0.5
8	190	0.5
9	190	0.5
10	190	0.75
11	200	0.5

Table 5.2: Values of $T_{B,min}$ and α for the 11 storms based on visual inspection.

taken the area covered by the radars as the total area of the cloud cluster (average area is about 7×10^4 km^2). In applications where radar data are not available, we suggest a linear size on the order of 250–300 km. This requires that the satellite swath be divided into boxes with 250–300 km to each side. The basis for using this size is that it is comparable to the size of a mesoscale cloud cluster and is appropriate for evaluating the effects of wind generated by the cloud cluster.

Although a temperature of 240 °K has been chosen, it should be understood that a slightly different temperature could also be used. If sufficient data are available, one could find an optimal temperature by doing sensitivity analysis. However, intuition and observation dictate that a value of 240 °K should be a reasonable first guess. In all the available simultaneous radar/satellite observations we see that, whenever there is rainfall there are FOVs with brightness temperature higher than 240 °K. The more extensive the storm, the more such FOVs.

This parameter has been computed for each of the 11 events, and related to the optimal values of α and $T_{B,min}$ (in Table 5.2), as shown in Figure 5-4. The correlation between $T_{B,min}$ and frac[$TB > 240$] is rather evident. While there appears to be also a negative correlation between α and frac[$TB > 240$], in this case the scatter of the points is large. In addition, the quality of the fit is not very sensitive to the α parameter. As a consequence, in formulating our final model the value of α is fixed at 0.5 for all the events, which leaves $T_{B,min}$ as the only parameter that depends on the strength of the event.

Based on Figure 5-4, a functional form has been suggested for the relation-

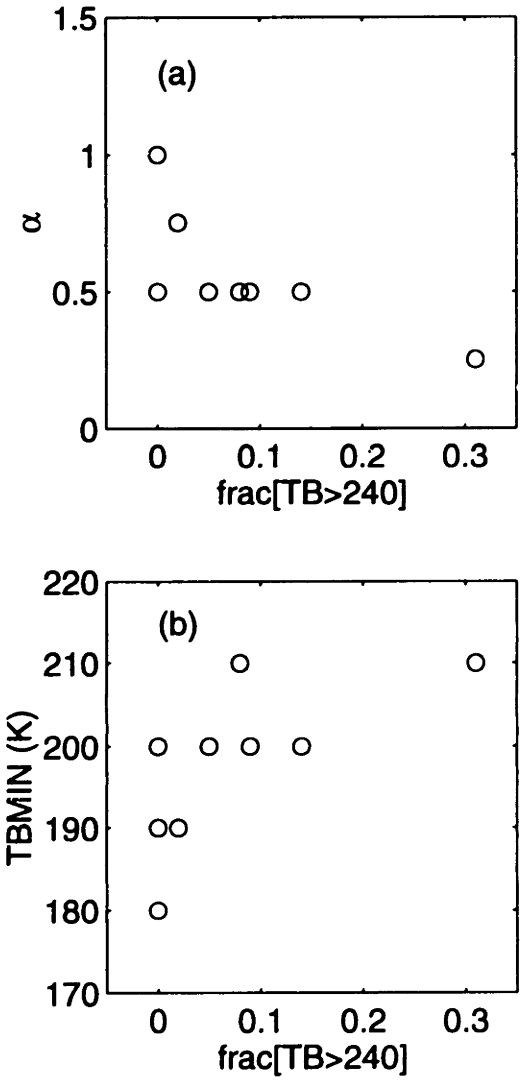

Figure 5-4: Relationship between (a) α and frac[$TB > 240$], (b) $T_{B,min}$ and frac[$TB > 240$].

ship between $T_{B,min}$ and frac[$TB > 240$],

$$T_{B,min} = a + c \cdot frac[TB > 240]^{1/2} \tag{5.5}$$

where a and c are chosen such that the rms error of the fit to the $T_B \sim f$ data is minimized. The minimization is done as follows.

5.5.3 Optimization of Model Parameters

For a set of (a, c) values, a $T_{B,min}$ can be computed for each of the 11 events based on their frac[$TB > 240$] using (5.5). This value of $T_{B,min}$ is used in the relationship $T_B = fT_{B,max} + (1 - f)(T_{B,min} + \triangle T f^{0.5})$ for each event. The error of this relation is quantified using the following two measures

$$E_1 = [\frac{1}{N}\sum_{i=1}^{N}[R(f(T_B(i))) - \hat{R}(i)]^2]^{1/2} \tag{5.6}$$

and

$$E_2 = \frac{1}{N}\sum_{i=1}^{N} R(f(T_B(i))) - \hat{R}(i) \tag{5.7}$$

where i indexes the FOV, $f(T_B)$ represents f as a function of T_B according to the T_B–f model, $R(f)$ is the FOV rain rate as a function of f (for which Figure 5-3 can be used), $T_B(i)$ is the satellite-observed FOV brightness temperature, $\hat{R}(i)$ is the radar-observed FOV rain rate, and N is the number of FOVs used. Thus E_1 is the root-mean-square error in FOV rain rate estimation and E_2 is the mean error of FOV rain. E_2 is also equivalent to the error of the areal rain rate estimate for the entire radar scan, because the areal rain rate is obtained by averaging all the FOV rain rate within the area. An E_2 equal to zero ensures that the large-area rain estimate is unbiased.

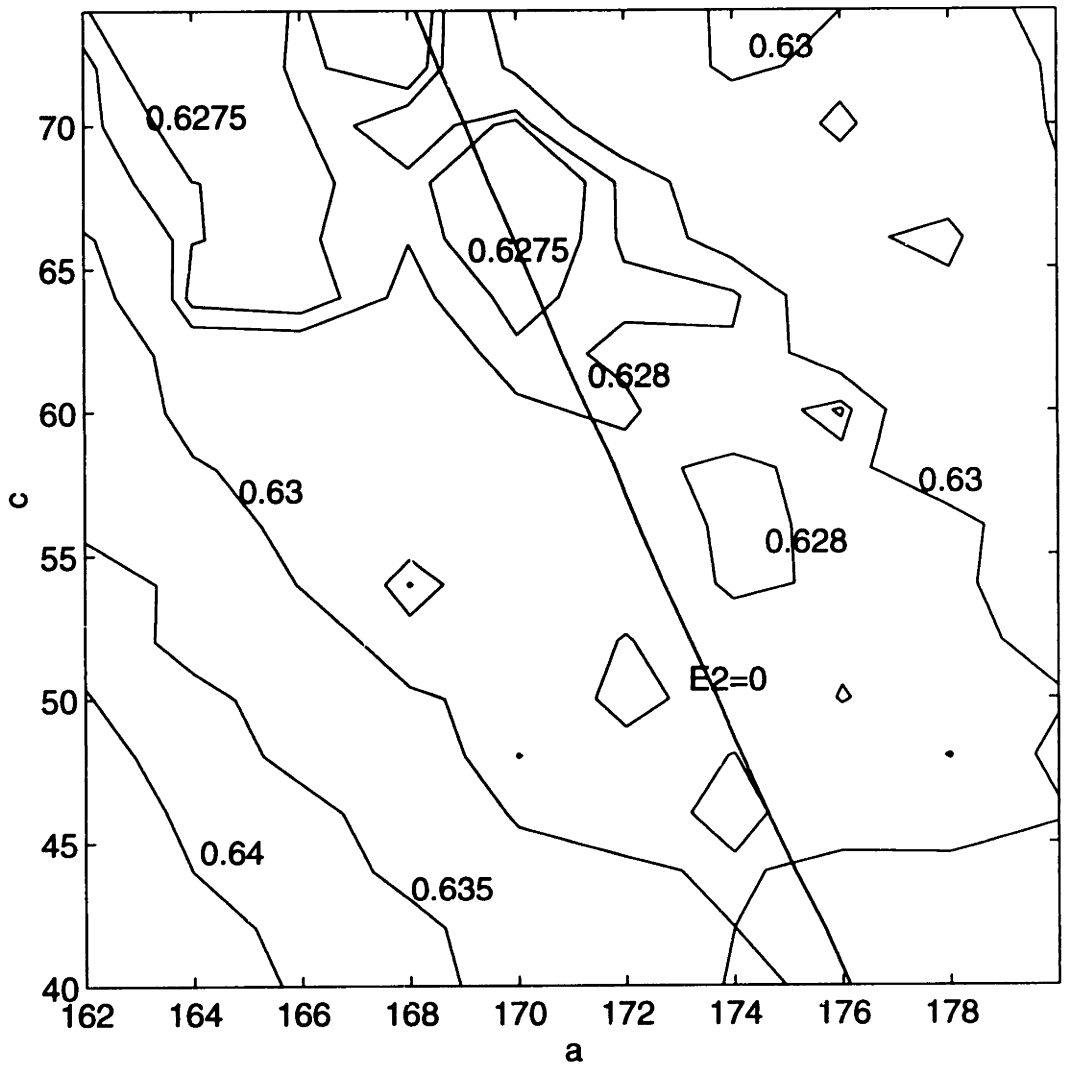

Figure 5-5: E_1 as a function of a and c. The nearly-straight line is for E_2=0. Data from all 11 storms are used

In evaluating E_1 and E_2, $\triangle T$ has been set to $T_{B,max} - T_{B,min}$ and a number of $T_{B,max}$ values have been tested, with $T_{B,max}$ = 255 °K being the best. With $T_{B,max}$ = 255 °K, E_1 as a function of a and c is plotted in Figure 5-5. The nearly straight line in figure 5-5 is the $E_2 = 0$ line. Since the criterion for selecting the best a and c is to make E_1 as small as possible while also maintaining a small E_2, the selection of [a=170, c=65] seems most appropriate, which results in the following expression for $T_{B,min}$

$$T_{B,min} = 170 + 65 frac[TB > 240]^{1/2} \tag{5.8}$$

Using this expression, the $T_{B,min}$ for each event has been computed based on frac[TB>240] and listed in Table 5.3.

With $T_{B,max}$ = 255 °K, $\triangle T = T_{B,max} - T_{B,min}$, α = 0.5, and $T_{B,min}$ from Table 5.3, the model fit to the 11 events are shown in Figure 5-6.

5.6 A Proposed Rainfall Retrieval Algorithm

Based on the $T_B \sim f$ model and the $f \sim R$ relationship, a rainfall retrieval algorithm is proposed for tropical regions with rainfall characteristics similar to the TOGA-COARE area, which consists of the following steps:

Step 1 Divide the swath into areas with linear scale of about 250–300 km.

Step 2 For each area, count the total number of FOVs and the number of FOVs with horizontally polarized T_B at 37 GHz higher than 240 °K. Compute frac[TB>240].

Step 3 Compute $T_{B,min}$ for each area according to (5.8).

Event No.	Frac[TB>240]	TB,min (K)
1	0	170
2	0.31	207
3	0.09	190
4	0.08	189
5	0	170
6	0	170
7	0.05	184
8	0	170
9	0	170
10	0.02	179
11	0.14	195

Table 5.3: frac[TB>240] and corresponding values of $T_{B,min}$.

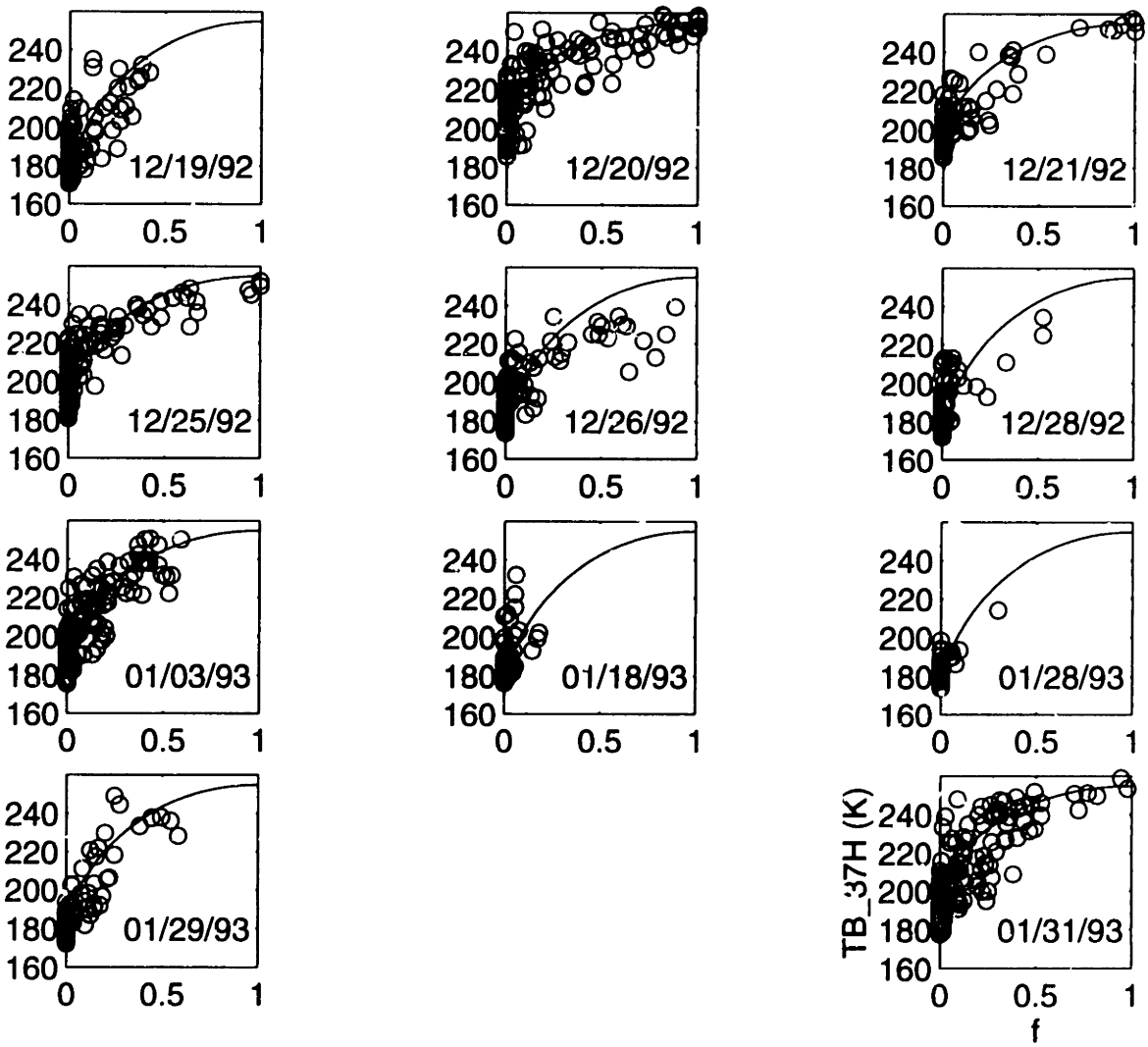

Figure 5-6: The $T_B \sim f$ model fitted to the 11 storms.

Step 4 Find the fractional rainy area f for each FOV according to (5.3). For TOGA-COARE area we recommend the following parameter values: $T_{B,max}$ = 255 °K, α = 0.5, and $\triangle T = T_{B,max} - T_{B,min}$.

Step 5 Use an independently derived $f \sim R$ relationship, such as the one shown in Figure 5-3, to obtain instantaneous FOV rain rate.

Step 6 Obtain the instantaneous areal rain rate by averaging the rain rate of all the FOVs in that area.

5.7 Application of the Algorithm and Comparison With Other Algorithms

As an example, we applied this algorithm to our 11 storms to obtain FOV rain rate and areal rain rate. The SSM/I estimate versus radar observations of FOV rain rate for each storm is shown in Figure 5-7. Some storms (e.g., 12/21/92 and 12/25/92) show better agreement than others (e.g., 01/03/93 and 01/31/93), which reflects the goodness of the corresponding $T_B \sim f$ fit. Overall, the agreement is judged satisfactory, considering the small area of a FOV. The areal rain rate estimate should improve since errors in FOV rain are largely canceled by averaging. The SSM/I estimate and radar-observed areal average rain rate for each event are listed in Table 5.4 and plotted in Figure 5-8, which shows that the algorithm is reasonably accurate and unbiased.

The improvement provided by this algorithm is the elimination of non-rain effects. As an illustration of such improvement, we make a brief comparison with two existing algorithms, i.e., that of Wilheit et al. (1977) and that of Prabhakara et al. (1992), both of which use single frequency data.

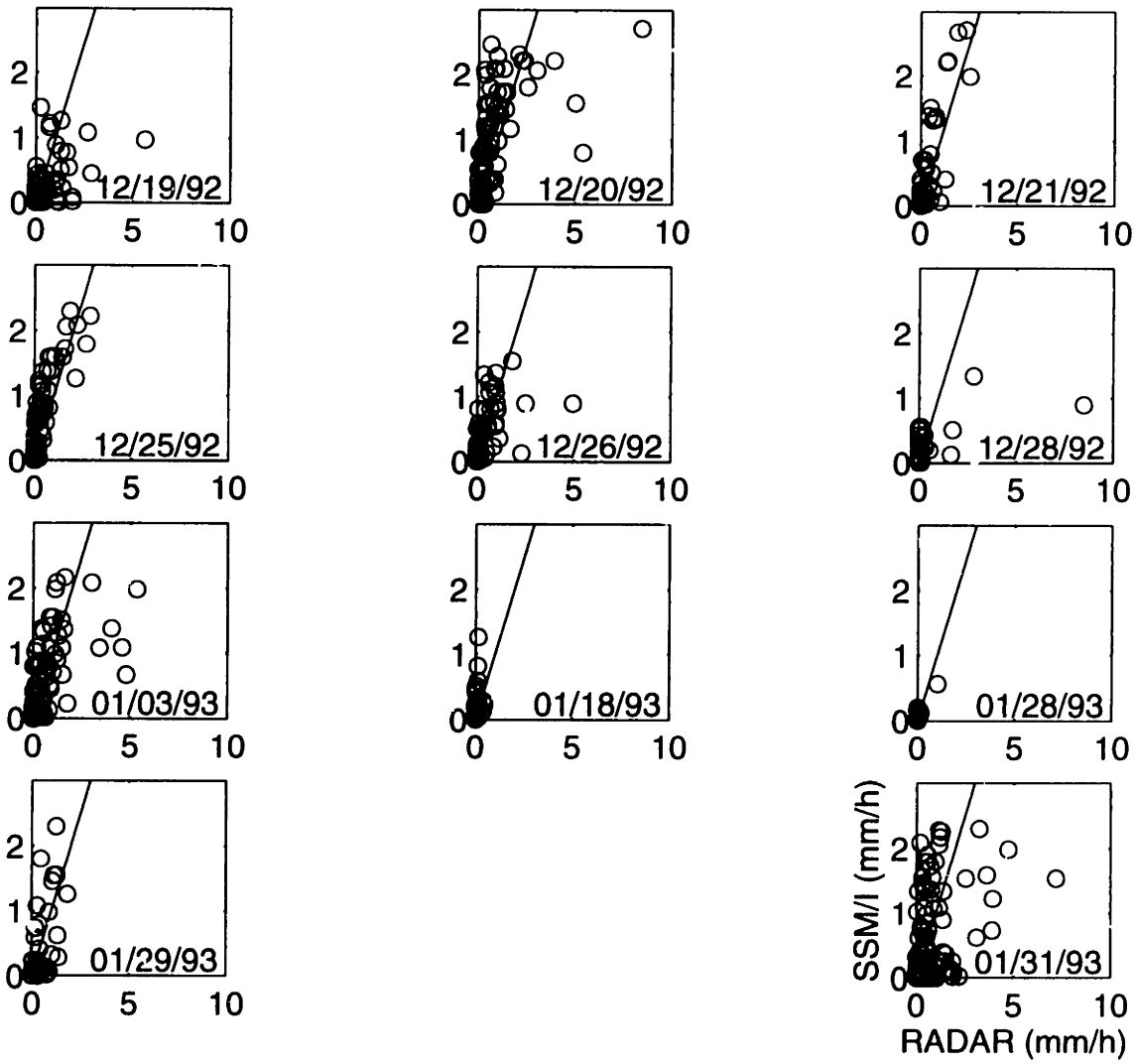

Figure 5-7: SSM/I estimate of instantaneous FOV rain rate versus radar observation.

Event no.	Radar Rain	SSM/I Rain
1	0.44	0.26
2	0.84	0.98
3	0.29	0.42
4	0.23	0.39
5	0.22	0.26
6	0.10	0.12
7	0.40	0.35
8	0.03	0.11
9	0.02	0.06
10	0.20	0.19
11	0.56	0.42

Table 5.4: SSM/I estimate of areal rain (mm h^{-1}) versus radar observation.

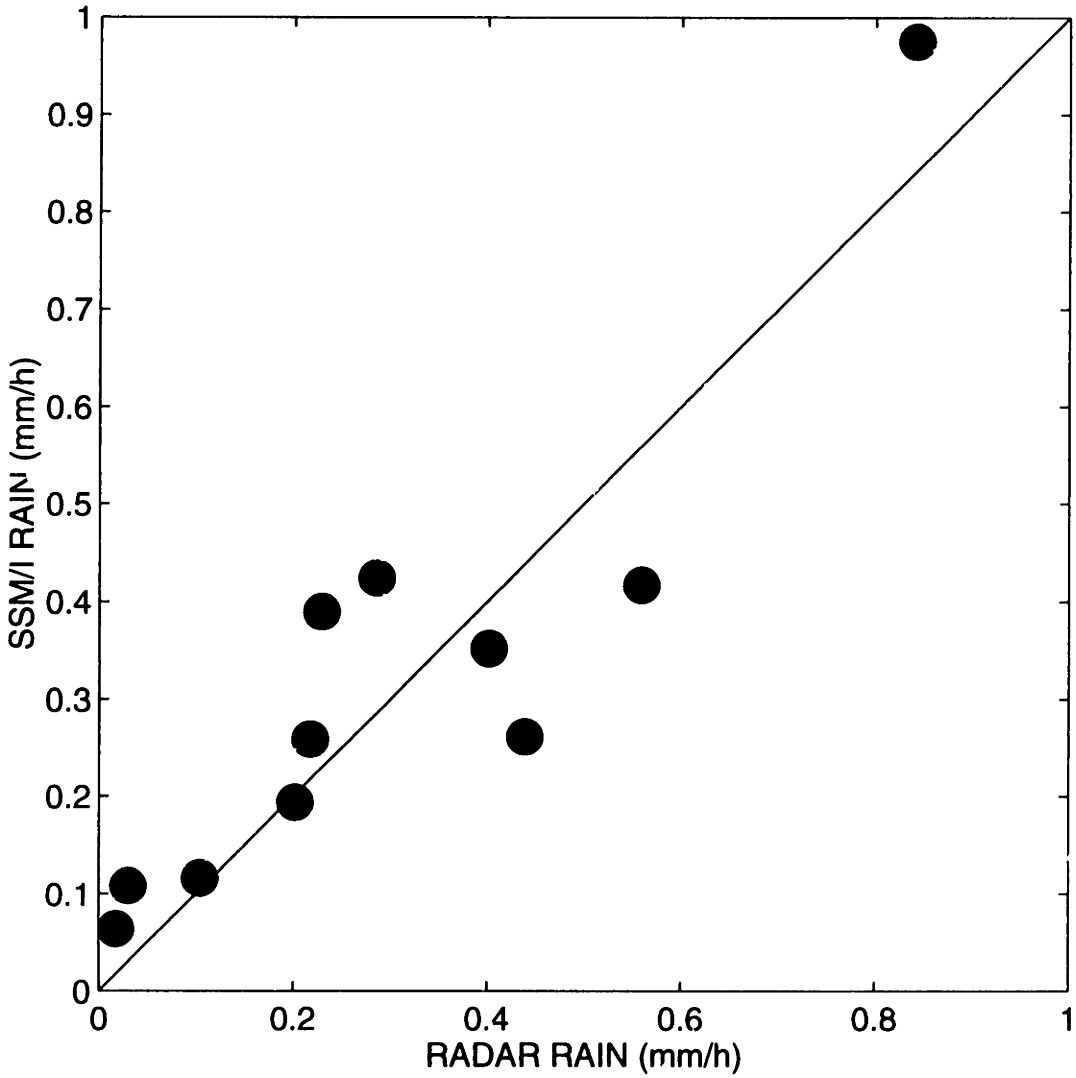

Figure 5-8: SSM/I estimate of areal rain rate versus radar observation.

The Wilheit model considers a uniform rain layer with the cloud height being a free parameter. The surface rain rate is related to T_B at 19 GHz through a radiative transfer calculation. Functional fits to the results of the model are available (Chiu et al. 1990; Short and North 1990). For a rain column of 4.5 km, Short and North (1990) obtain

$$T_B = A - Bexp(-CR) - DR \tag{5.9}$$

where T_B is the horizontally polarized brightness temperature at 19 GHz, A = 270 °K, B = 100 °K, C = 0.18 h mm^{-1}, D = 1.0 h mm^{-1}, and R is the instantaneous FOV rain rate in mm h^{-1}. The T_B–R curve is shown in Figure 5-9.

The Prabhakara model assumes that the increase in T_B is linearly related to the fractional rainy area within the FOV (see Chapter 3 for a review of this method). Rain rate is related to brightness temperature through

$$R = [exp[\beta(T_{37} - T^*)]^\chi - 1]\gamma(w) \tag{5.10}$$

where $T^* = T_{37min} + 15$, T_{37min} is the minimum observed T_B at 37 GHz horizontal polarization. Prabhakara et al. have calibrated the three parameters by tuning the $T_B - R$ relationship to GATE rainfall statistics and summer rainfall climatology over North Atlantic. This yields $\chi = 1.7$, $\beta(w) = 0.012 + 0.003w$, $\gamma(w) = 1.5 - 0.1w$, where w is the atmospheric vapor content and is related to T_{37min} as $T_{37min} = 126 + 6.8w$. In the present application, we set T_{37min} = 160 °K based on the histogram of T_B (Figure 4-23). The T_B–R relationship is shown in Figure 5-10.

The objective here is to apply our model and the above two models to the same rainfall events and compare the results with the radar-derived rain field.

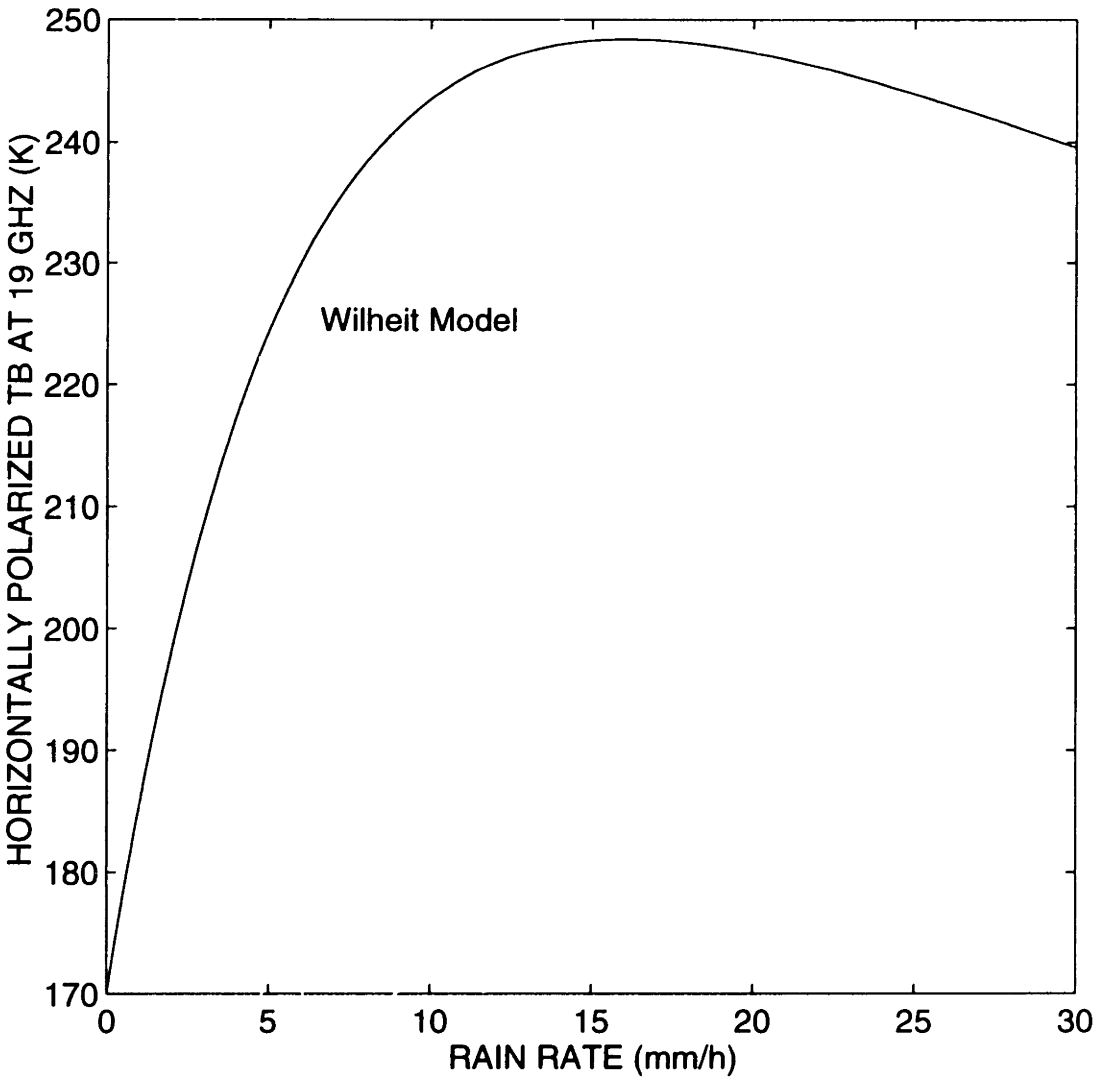

Figure 5-9: T_B–R relationship from the Wilheit model.

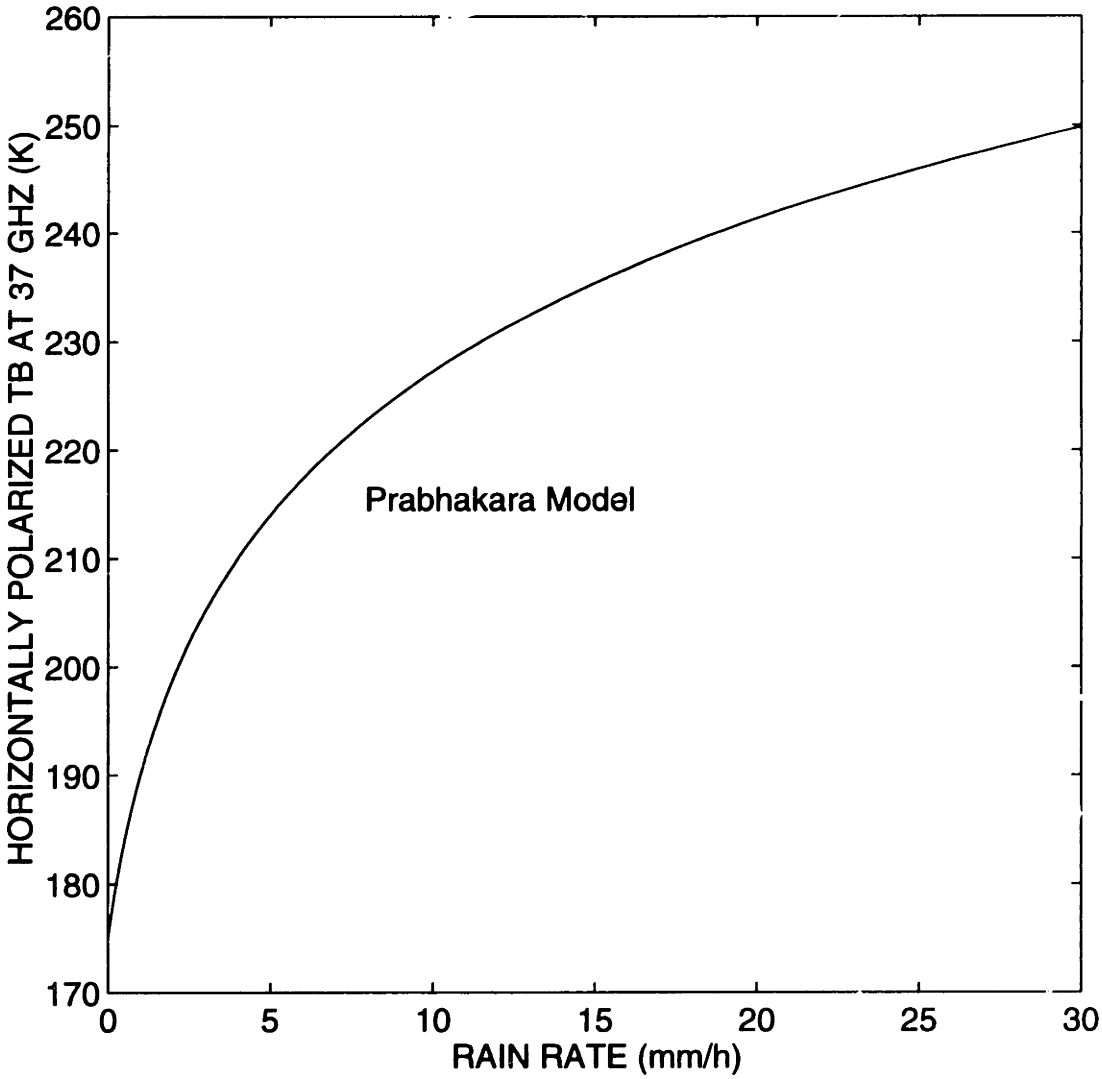

Figure 5-10: T_B–R relationship from the Prabhakara model.

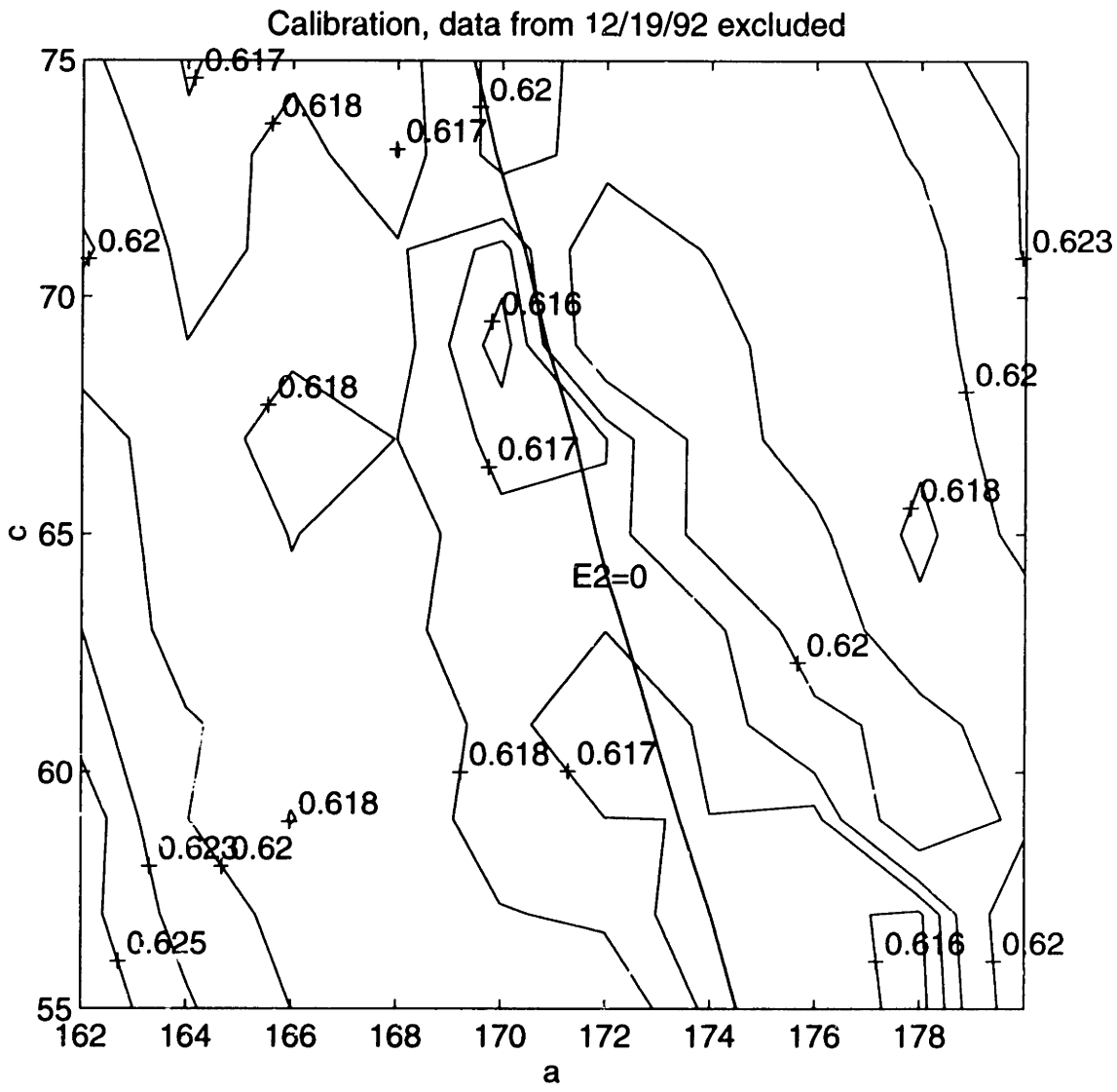

Figure 5-11: E_1 as a function of a and c. The nearly-straight line is for E_2=0. Data from 19 December 1992 are excluded.

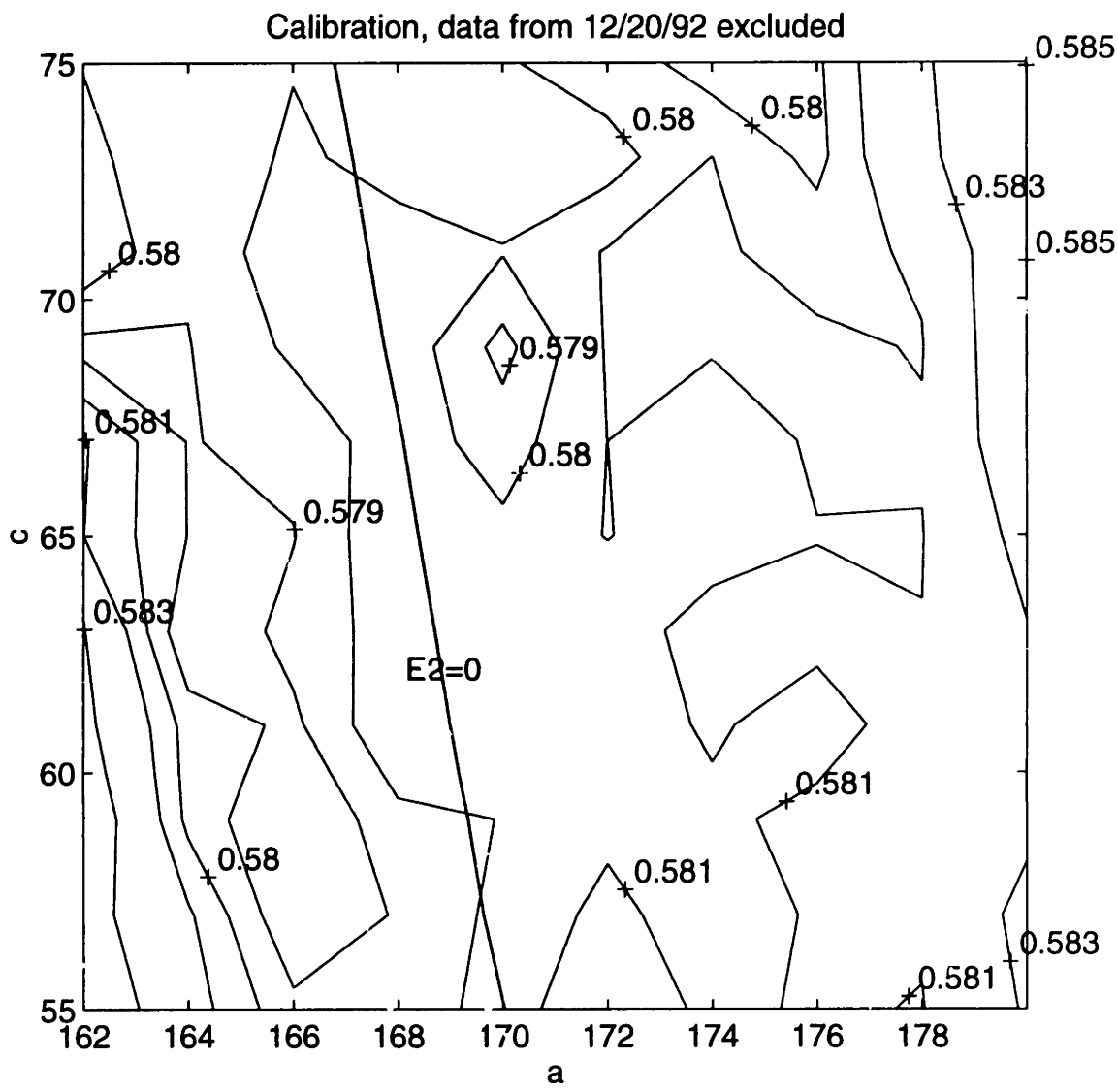

Figure 5-12: E_1 as a function of a and c. The nearly-straight line is for E_2=0. Data from 20 December 1992 are excluded.

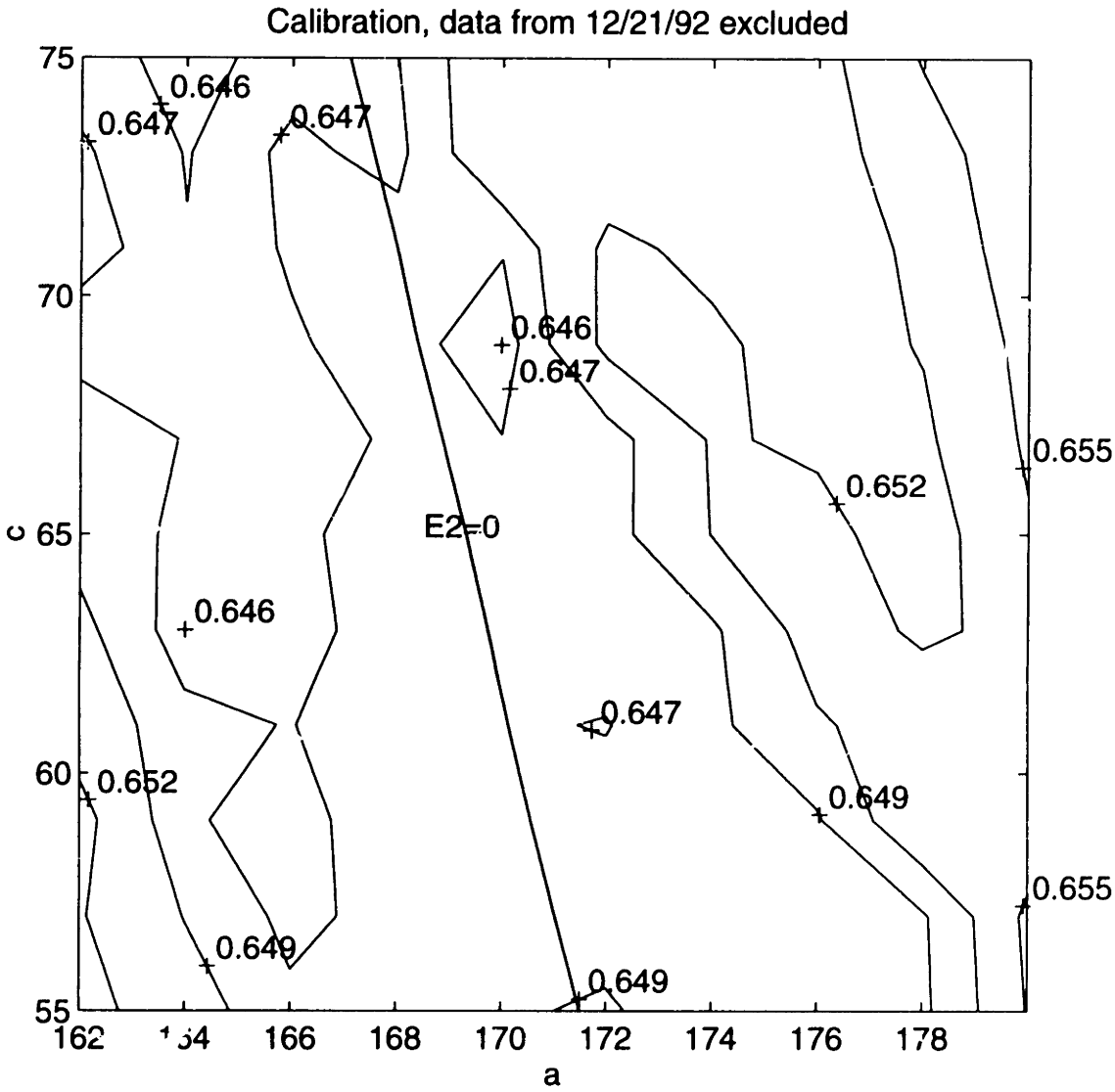

Figure 5-13: E_1 as a function of a and c. The nearly-straight line is for E_2=0. Data from 21 December 1992 are excluded.

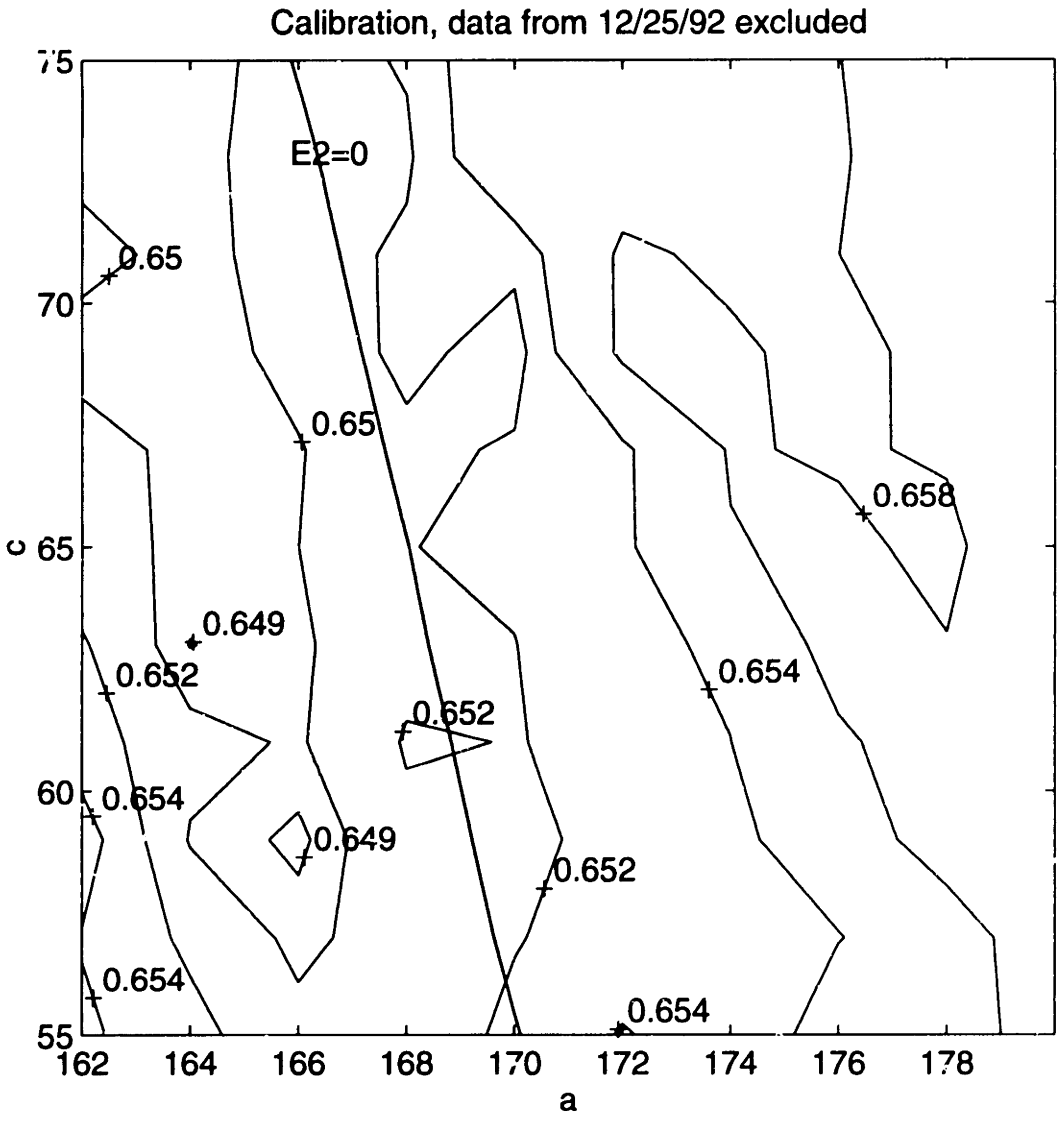

Figure 5-14: E_1 as a function of a and c. The nearly-straight line is for E_2=0. Data from 25 December 1992 are excluded.

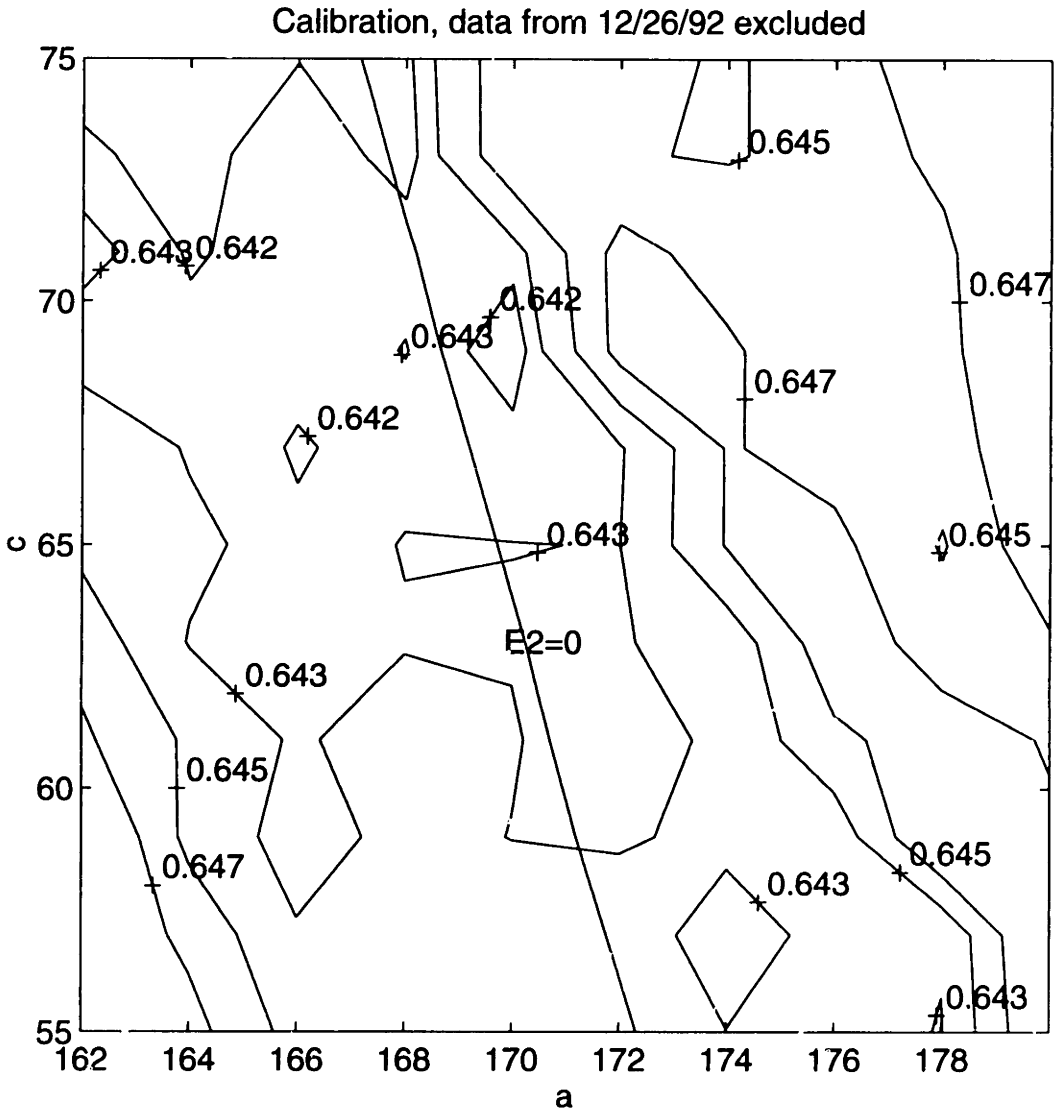

Figure 5-15: E_1 as a function of a and c. The nearly-straight line is for E_2=0. Data from 26 December 1992 are excluded.

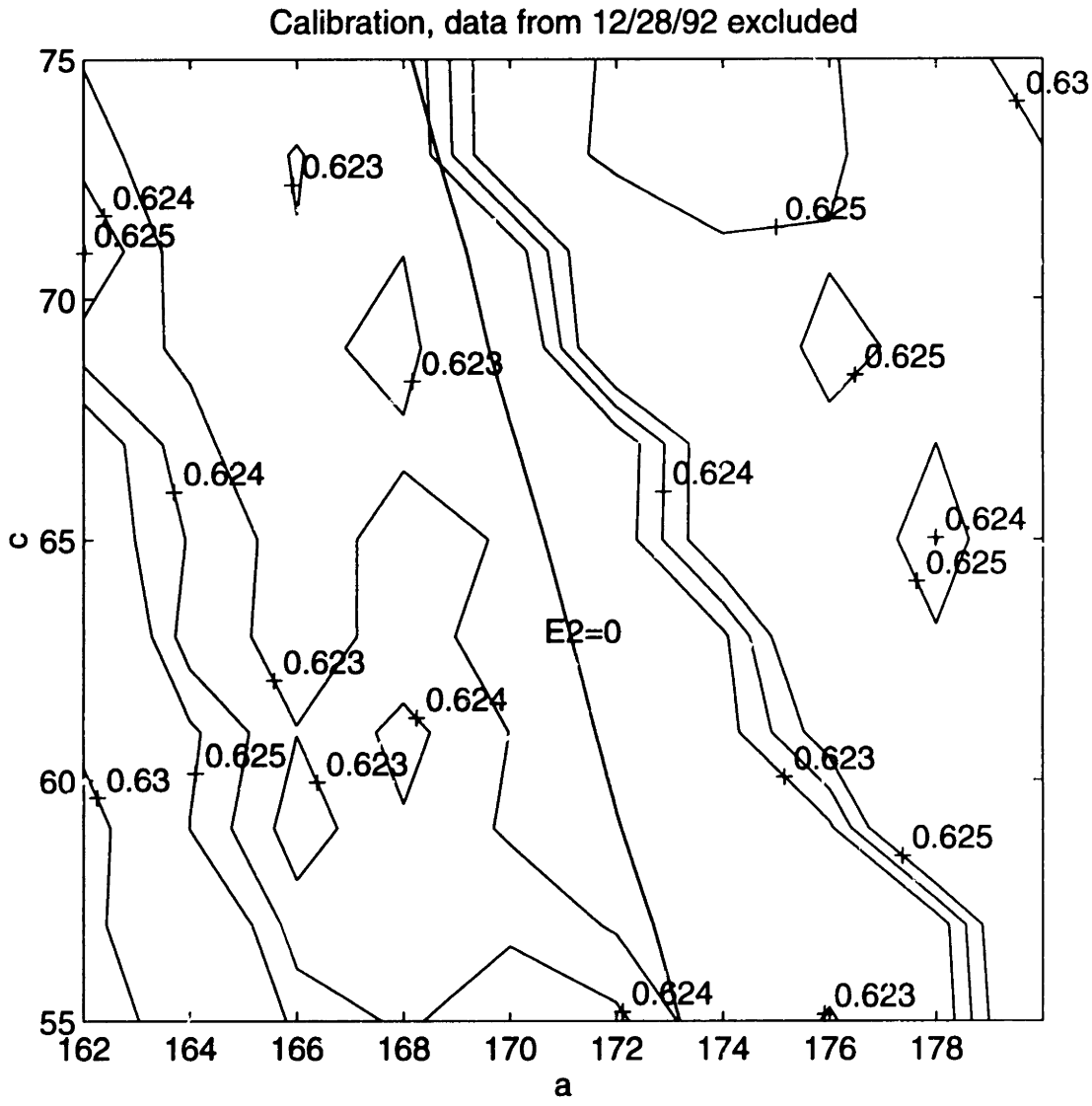

Figure 5-16: E_1 as a function of a and c. The nearly-straight line is for E_2=0. Data from 28 December 1992 are excluded.

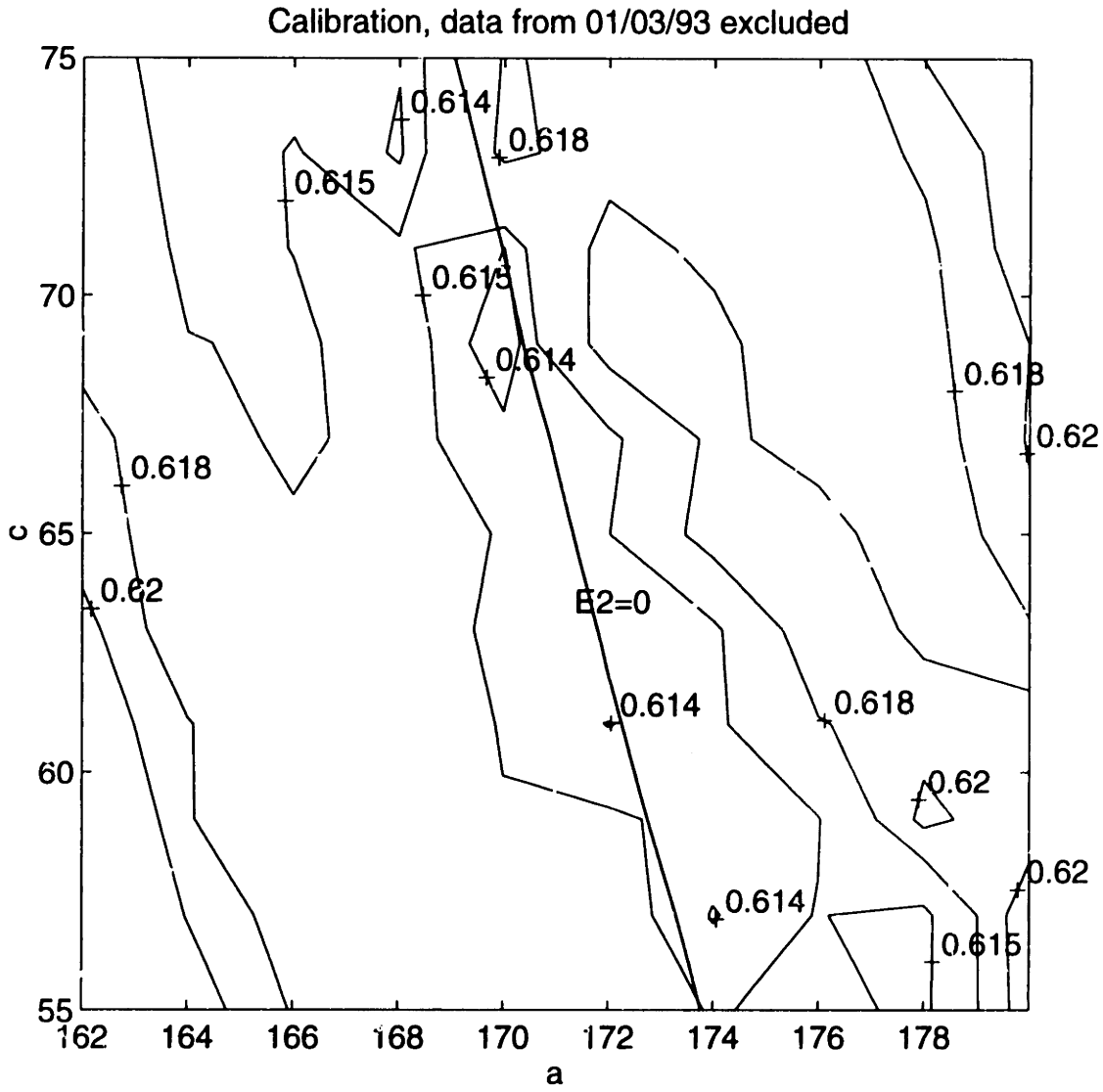

Figure 5-17: E_1 as a function of a and c. The nearly-straight line is for E_2=0. Data from 03 January 1993 are excluded.

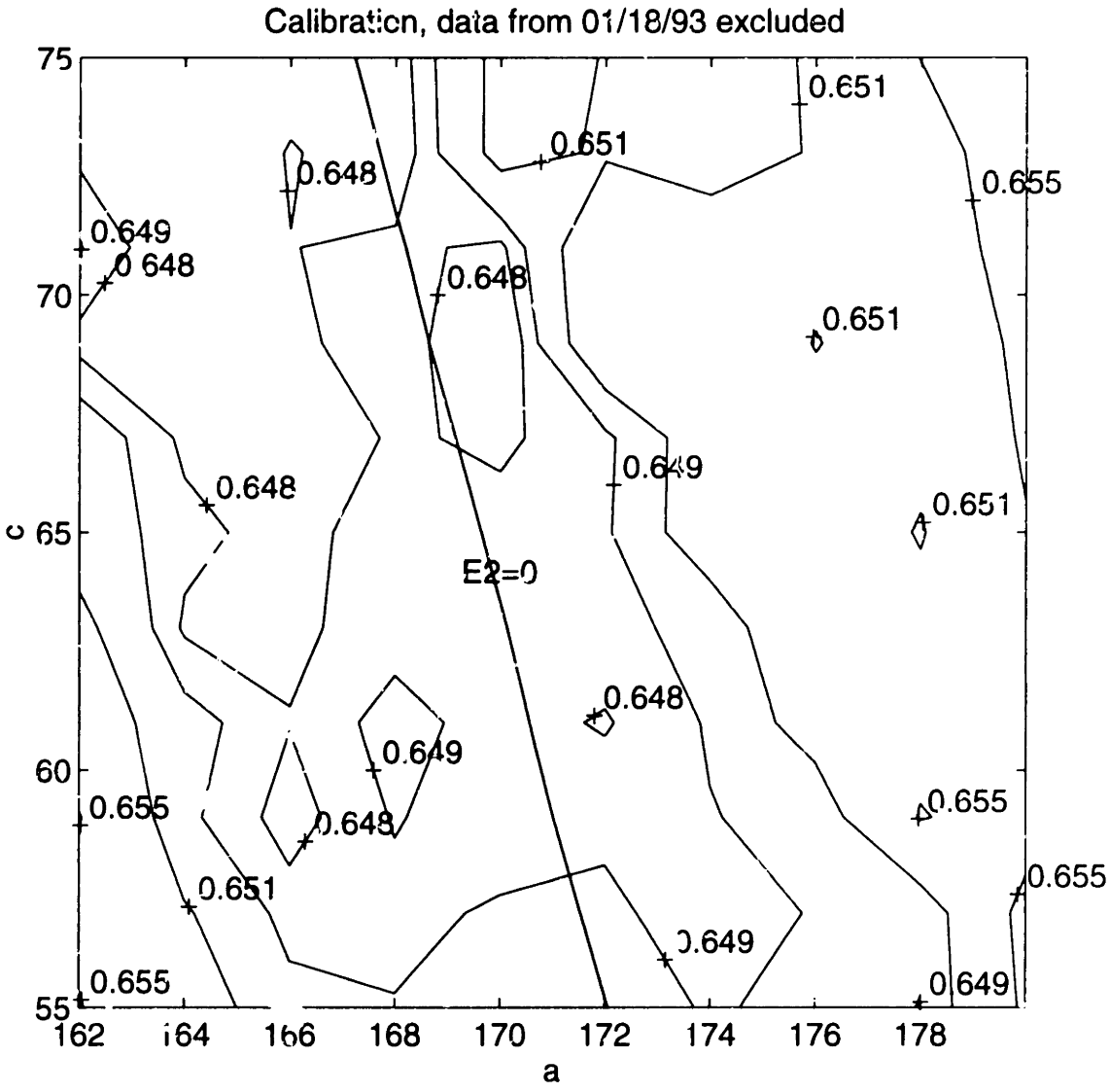

Figure 5-18: E_1 as a function of a and c. The nearly-straight line is for E_2=0. Data from 18 January 1993 are excluded.

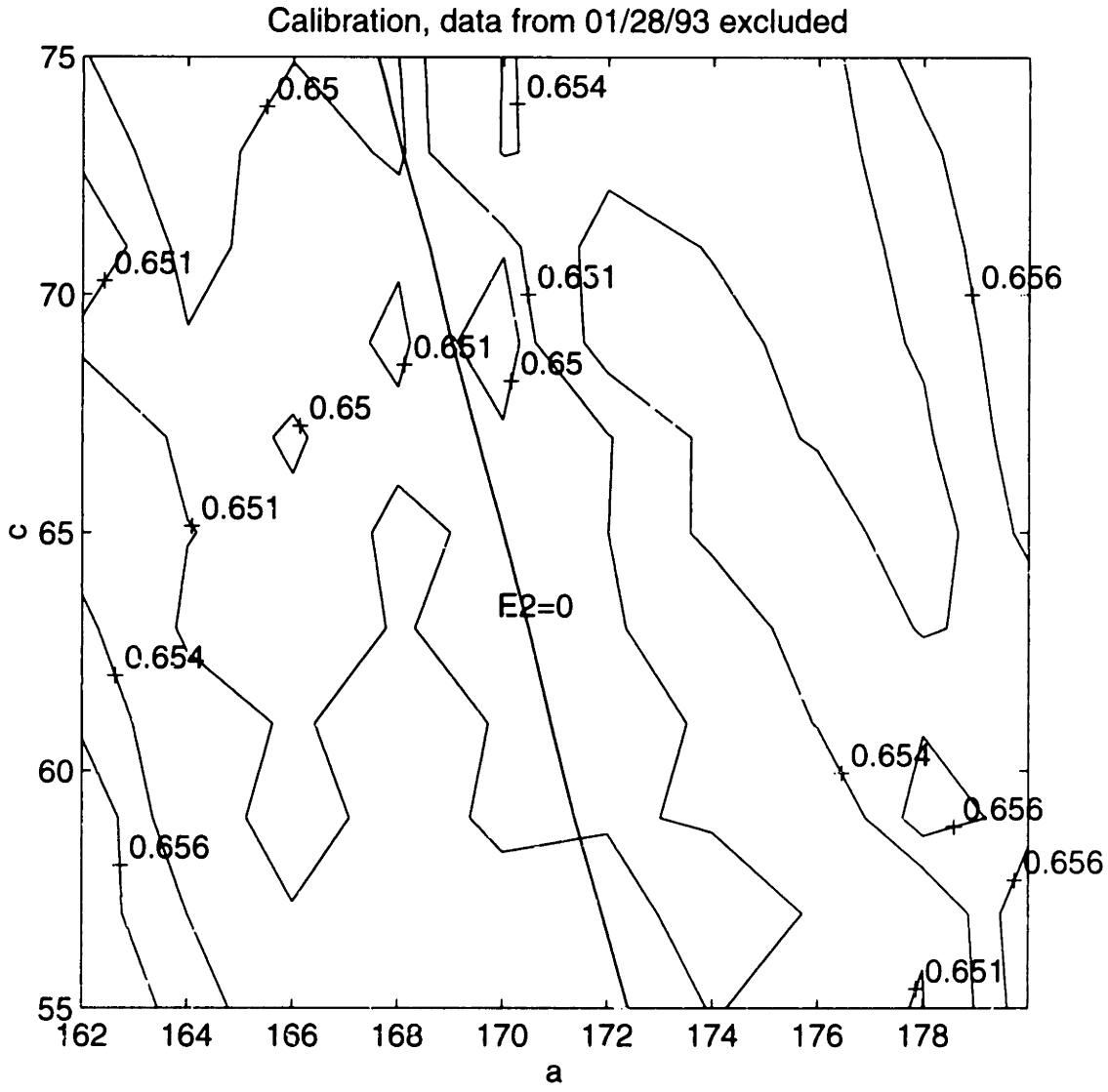

Figure 5-19: E_1 as a function of a and c. The nearly-straight line is for E_2=0. Data from 28 January 1993 are excluded.

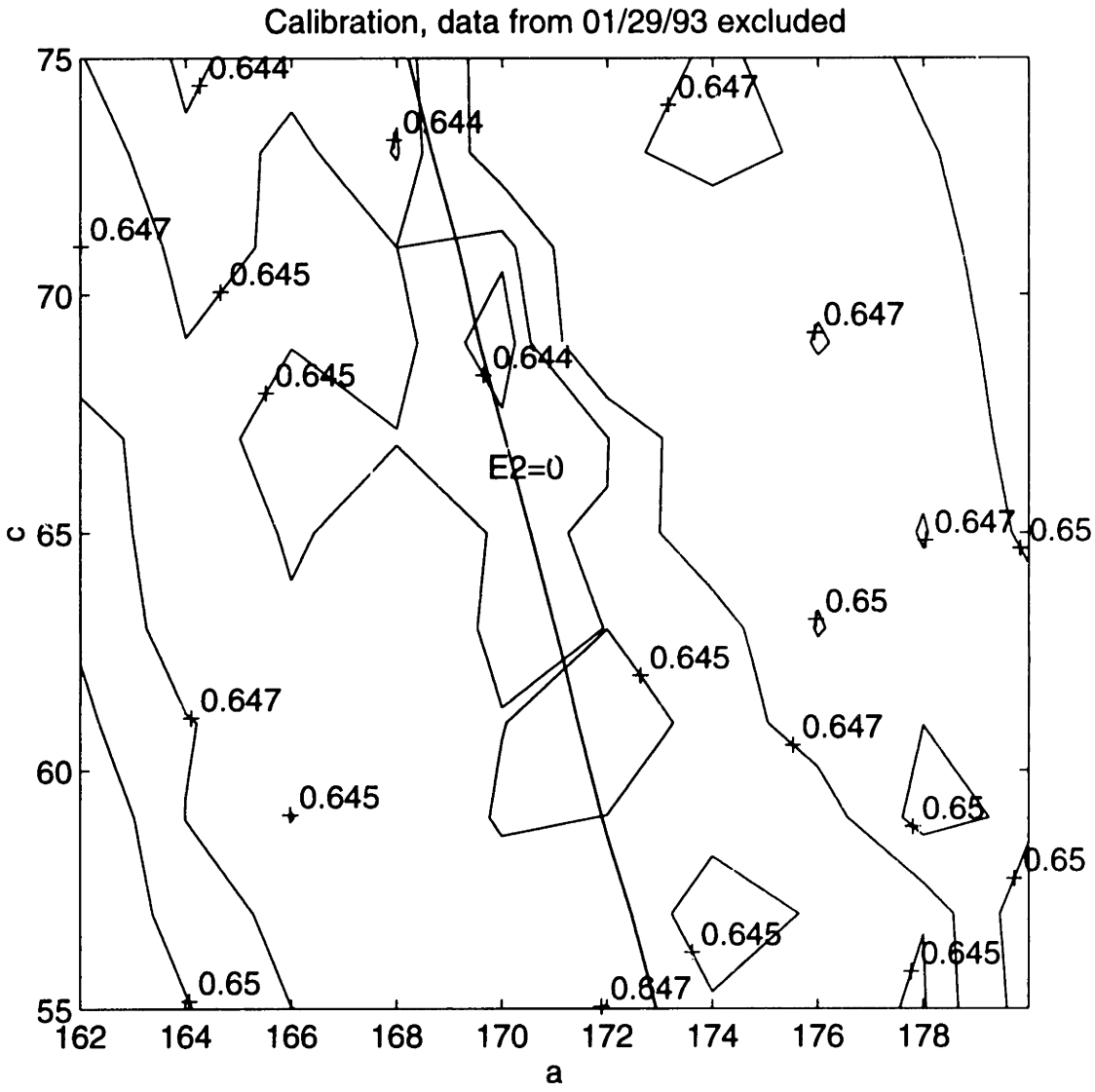

Figure 5-20: E_1 as a function of a and c. The nearly-straight line is for E_2=0. Data from 29 January 1993 are excluded.

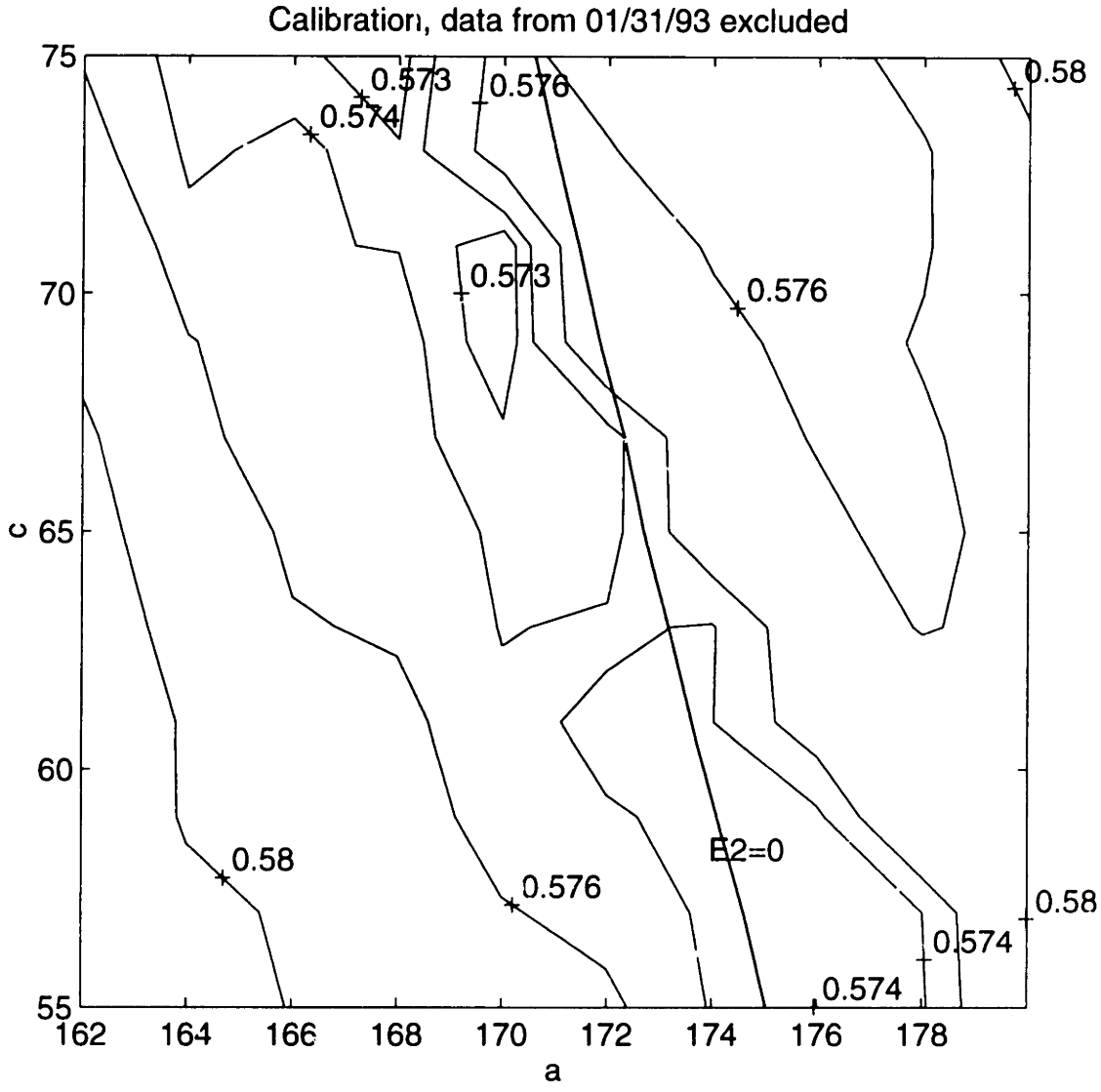

Figure 5-21: E_1 as a function of a and c. The nearly-straight line is for E_2=0. Data from 31 January 1993 are excluded.

No.	a	c	Frac[TB>240]	TB,min	TB,min*	TB0
1	171	69	0	171	170	171
2	168	66	0.31	205	207	185
3	168	69	0.09	189	190	183
4	168	66	0.08	187	189	179
5	168	70	0	168	170	174
6	169	70	0	169	170	171
7	172	65	0.05	187	184	176
8	169	70	0	169	170	176
9	169	69	0	169	170	174
10	170	68	0.02	180	179	174
11	170	68	0.14	195	195	175
TB,min* is based on all the 11 storms						
TB,min is based on storms excluding the current one						
TB0 is the lowest brightness temperature within radar scan						

Table 5.5: The values of (a, c) and $T_{B,min}$ for individual storms.

We use the radar as ground truth. The two models, judged from their structure and prior applications, do not require special calibration to be applied to the TOGA-COARE region. The Wilheit model does not depend on the sea states, and its free parameter is the height of the freezing level, which has been set to about 4.5 km in many applications (e.g., Short and North 1990). Although the Prabhakara model was tuned to the GATE data, it has been applied to retrieve rainfall off the east coast of Florida without any further calibration. Thus in this study, we will use these two models in their present form, without further calibration to the TOGA-COARE region.

Since our model has been calibrated to the COARE data, it may not be very appropriate to compare it to the other two models. To partially resolve this issue, we have made a change in our calibration procedure, i.e., the data of the compared storm are excluded from the calibration. The calibration results are shown in Figure 5-11 through Figure 5-21. Thus we have a different set of (a, c) values for each compared storm, from which we can compute the value of $T_{B,min}$ for each storm. These (a, c) and $T_{B,min}$ values are listed in Table 5.5. It is evident that the variation of the (a, c) and $T_{B,min}$ values from storm to storm is small. This is expected, since these storms are expected to have similar characteristics and a small change in the number of storms used in the calibration should not severely affect the resulting parameter values.

Figures 5-22 through 5-32 compare the spatial rainfall patterns obtained by radar with those from the three algorithms, for the 11 selected events. Compared with radar and with our model, the other two models show larger spatial extent of rain for the several events with larger spatial spread of rain, which are expected to have stronger wind effects. For weaker events, where the wind effects are expected to be relatively weak due to its small rain cells,

overestimation by those models, although still present, is smaller.

To show that our model can still perform well in an uncalibrated region, we have applied these three algorithms to the Darwin area. As described in Chapter 4, we have two relatively intense rainfall events in Darwin area with simultaneous radar and SSM/I observations: 13 January 1990 and 14 January 1990. Their rainfall and brightness temperature maps have been shown in Figure 4-5 and 4-6. Application of the algorithms to the Darwin area is made more difficult by the presence of the land area and the island. We need to select FOVs that are entirely over water, while keeping in mind the fact that FOVs close to the coast may contain some land area due to the colocation error of about 10 km.

The application of the Prabhakara model and the Wilheit model is straightforward. It only requires converting the observed brightness temperature, either at 37 GHz or at 19 GHz, into rain rate using the appropriate T_B–R relationships.

To apply our model, however, we need to compute the value of frac[TB>240]. As frac[TB>240] is defined as A_{240}/A_{total}, where A_{total} is the total area of the mesoscale cloud cluster and A_{240} is the area within the cluster with brightness temperature higher than 240 °K, we can take the total sea surface area within the radar coverage as A_{total}, which is about 6×10^4 km^2 and is comparable to the TOGA-COARE case. A_{240} can be obtained by counting the number of FOVs with brightness temperature higher than 240 °K. This led to frac[TB>240] values of 0.10 for the 13 January event and 0.16 for the 14 January event. Using the same frac[TB>240]$\sim T_{B,min}$ relationship as used for the TOGA-COARE area, i.e., (5.8), we obtained $T_{B,min} = 191$ °K for the 13 January event and $T_{B,min} = 196$ °K for the 14 January event. Using the same values for other parameters as

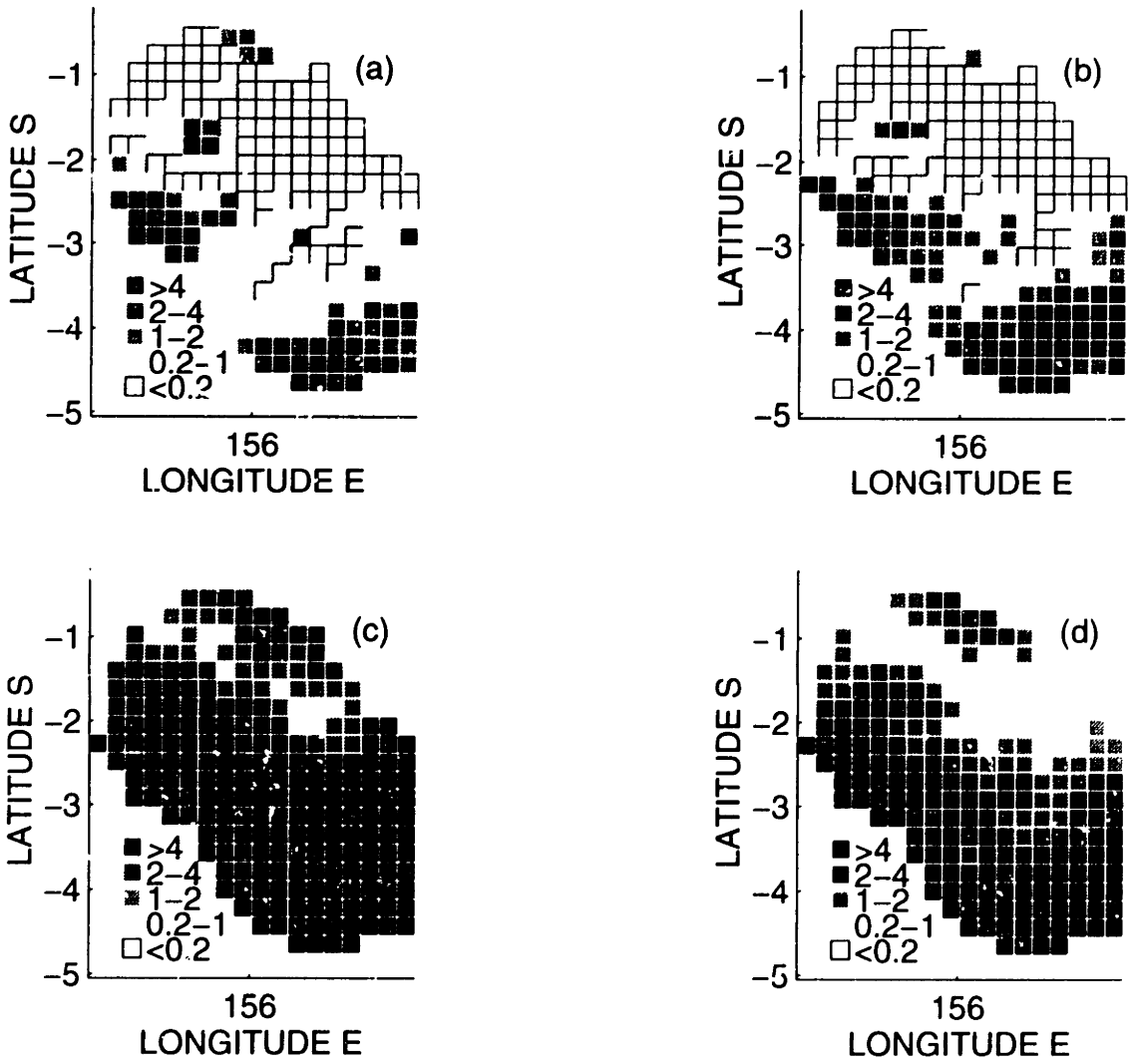

Figure 5-22: Comparison between spatial rainfall patterns obtained by radar and algorithms, 12/20/92, TOGA-COARE. Unit for rain rate is mm h^{-1}. (a) Radar; (b) this model; (c) Prabhakara model; (d) Wilheit Model.

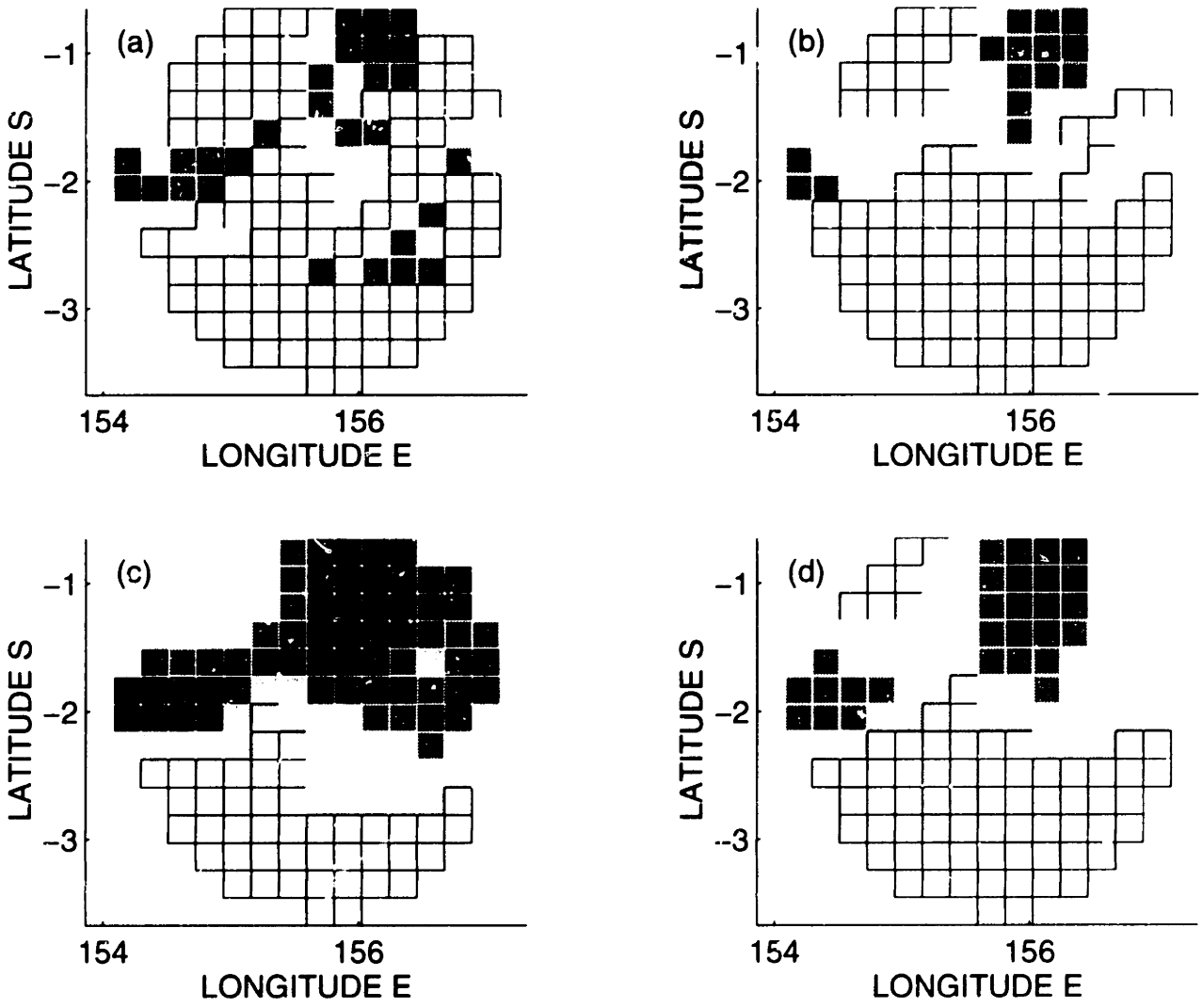

Figure 5-23: Comparison between spatial rainfall patterns obtained by radar and algorithms, 12/19/92, TOGA-COARE. (a) Radar; (b) this model; (c) Prabhakara model; (d) Wilheit Model. See Figure 5-22 for legend.

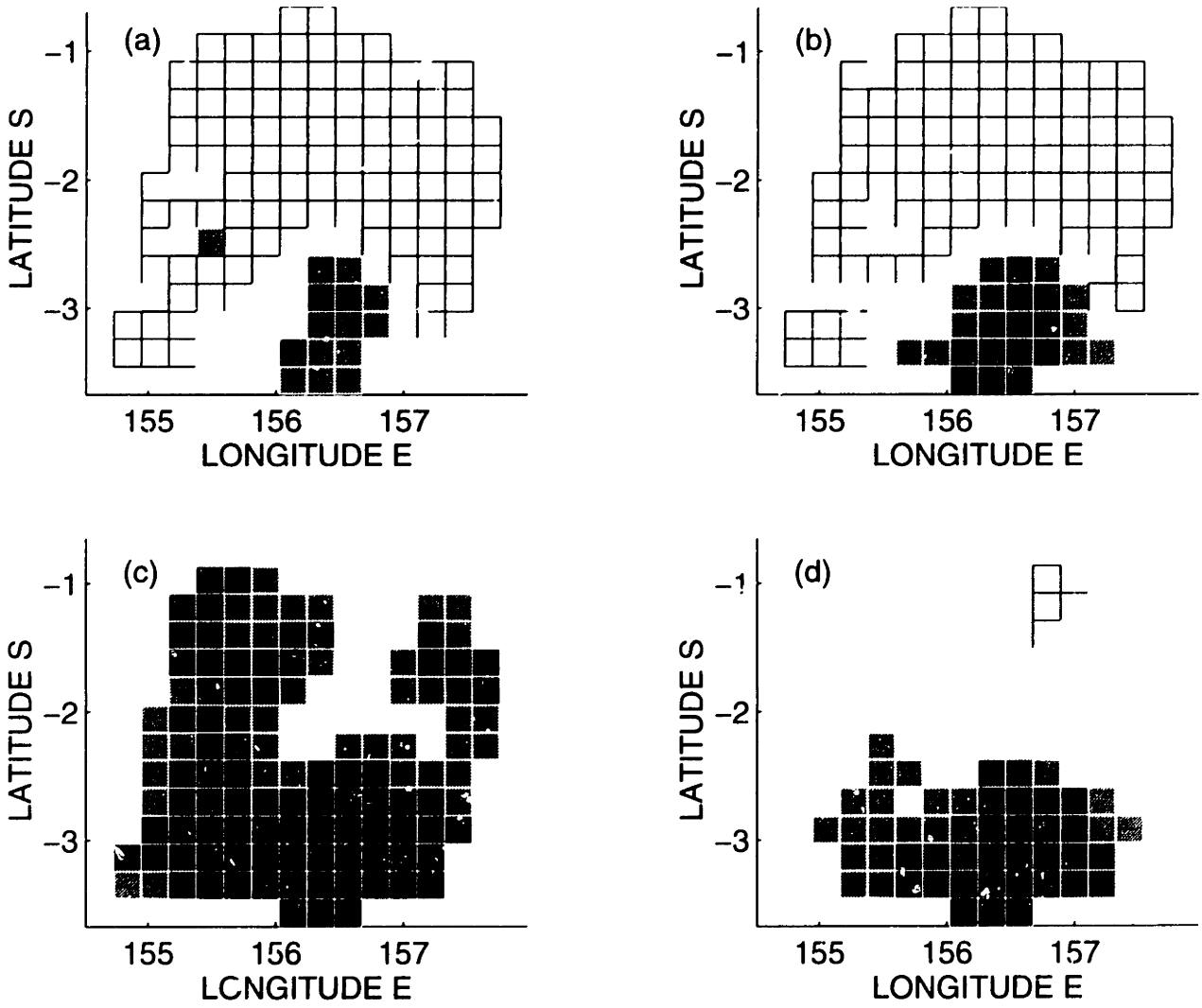

Figure 5-24: Comparison between spatial rainfall patterns obtained by radar and algorithms, 12/21/92, TOGA-COARE. (a) Radar; (b) this model; (c) Prabhakara model; (d) Wilheit Model. See Figure 5-22 for legend.

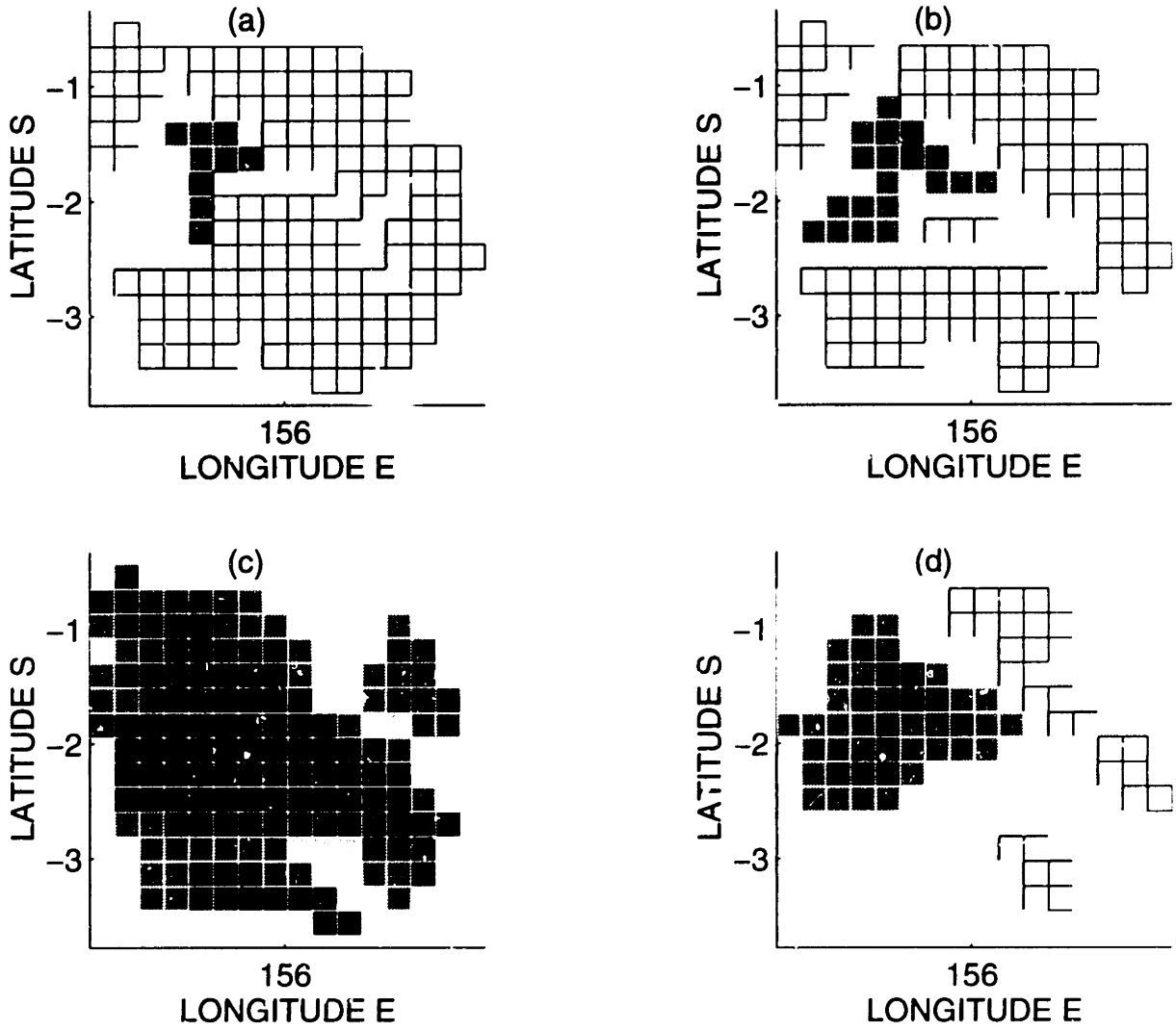

Figure 5-25: Comparison between spatial rainfall patterns obtained by radar and algorithms, 12/25/92, TOGA-COARE. (a) Radar; (b) this model; (c) Prabhakara model; (d) Wilheit Model. See Figure 5-22 for legend.

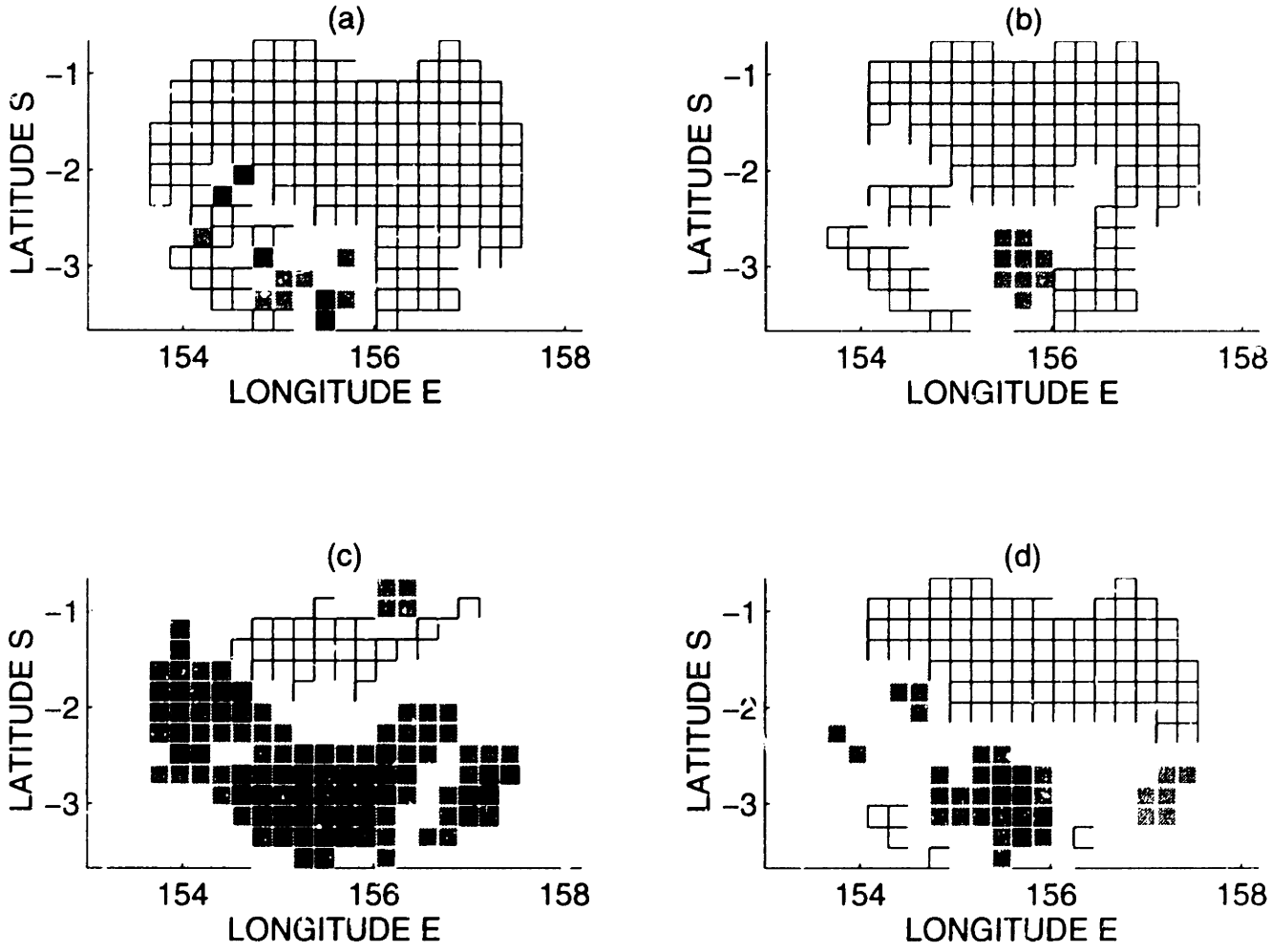

Figure 5-26: Comparison between spatial rainfall patterns obtained by radar and algorithms, 12/26/92, TOGA-COARE. (a) Radar; (b) this model; (c) Prabhakara model; (d) Wilheit Model. See Figure 5-22 for legend.

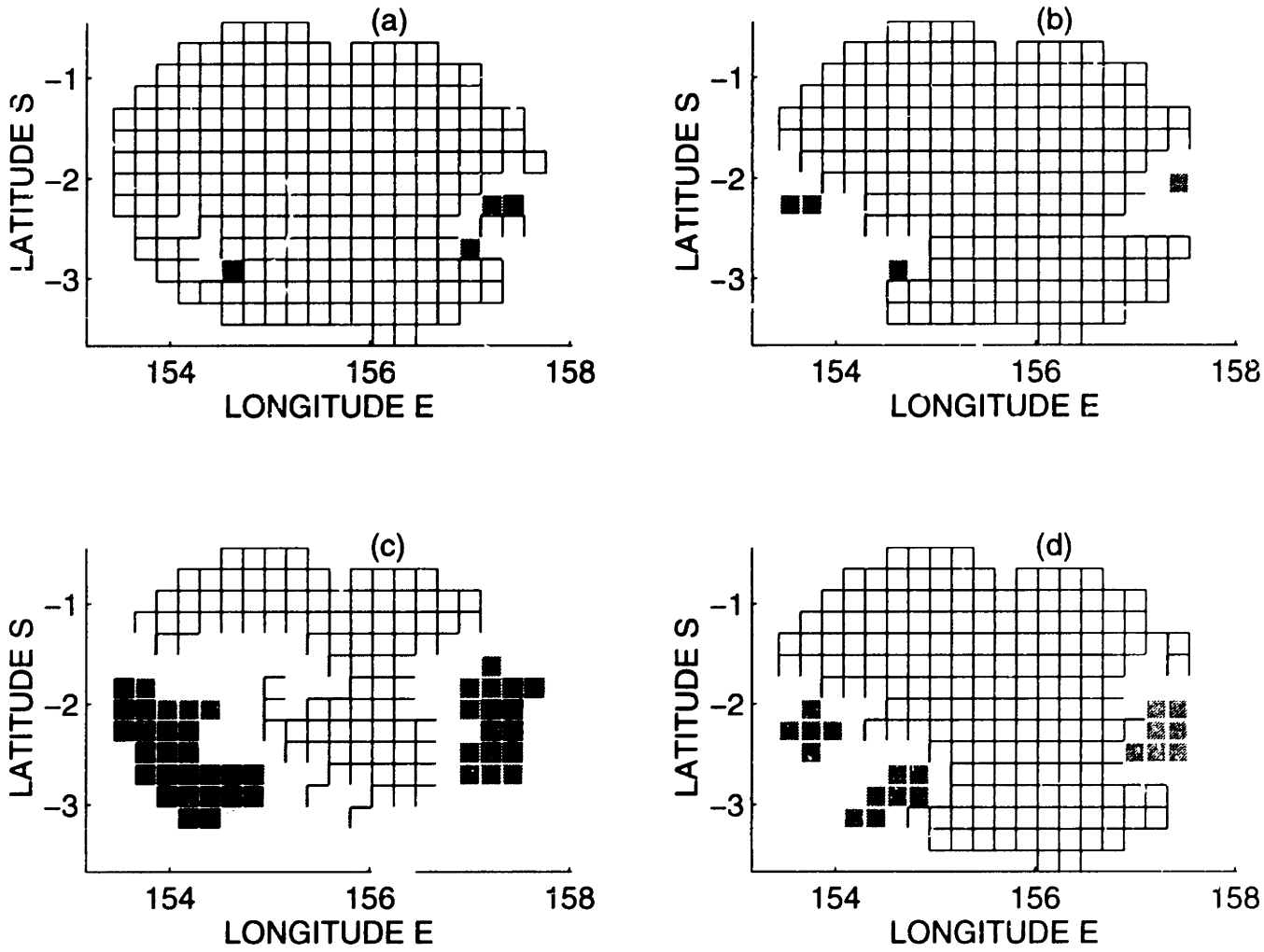

Figure 5-27: Comparison between spatial rainfall patterns obtained by radar and algorithms, 12/28/92, TOGA-COARE. (a) Radar; (b) this model; (c) Prabhakara model; (d) Wilheit Model. See Figure 5-22 for legend.

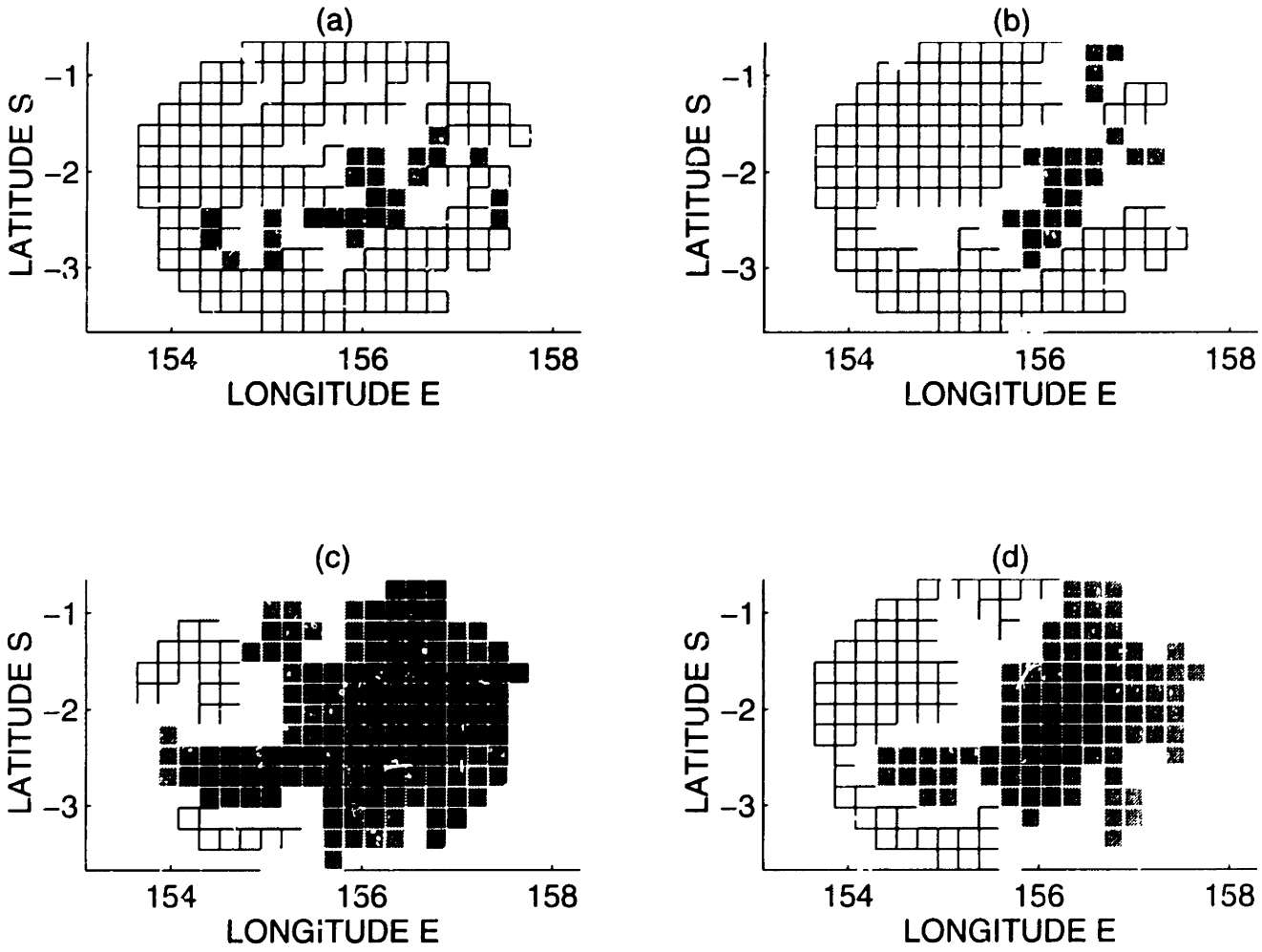

Figure 5-28: Comparison between spatial rainfall patterns obtained by radar and algorithms, 01/03/93, TOGA-COARE. (a) Radar; (b) this model; (c) Prabhakara model; (d) Wilheit Model. See Figure 5-22 for legend.

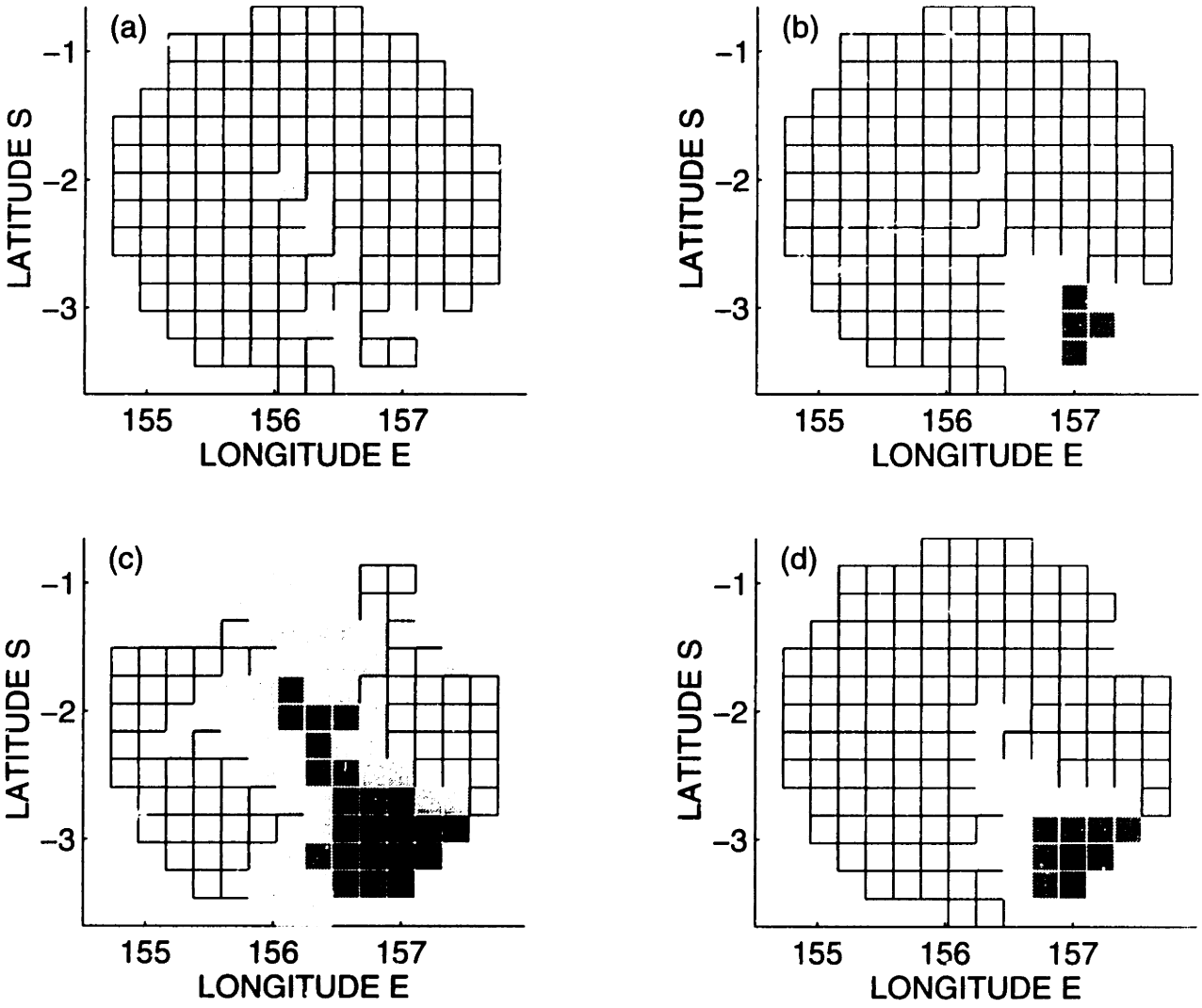

Figure 5-29: Comparison between spatial rainfall patterns obtained by radar and algorithms, 01/18/93, TOGA-COARE. (a) Radar; (b) this model; (c) Prabhakara model; (d) Wilheit Model. See Figure 5-22 for legend.

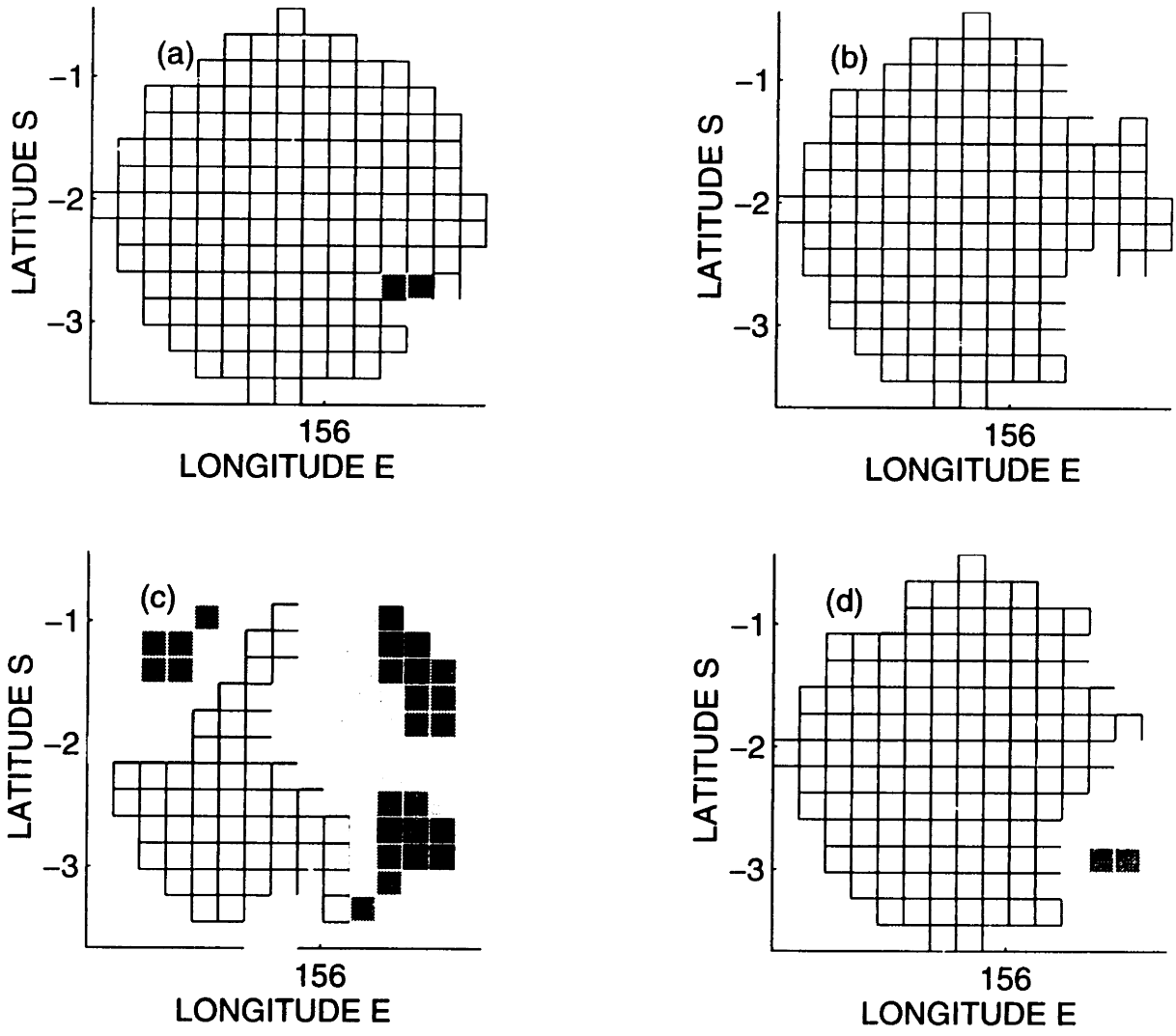

Figure 5-30: Comparison between spatial rainfall patterns obtained by radar and algorithms, 01/28/93, TOGA-COARE. (a) Radar; (b) this model; (c) Prabhakara model; (d) Wilheit Model. See Figure 5-22 for legend.

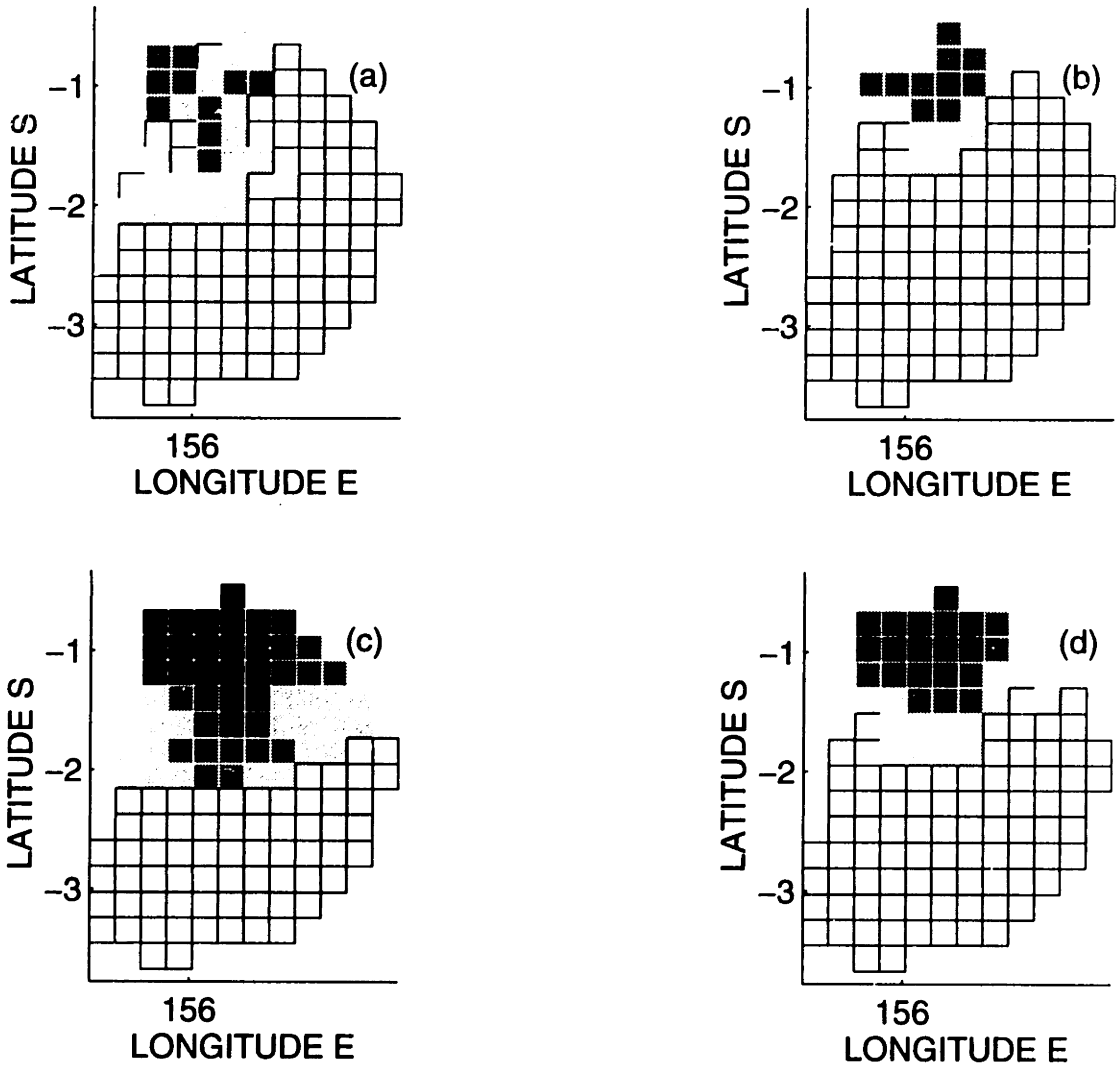

Figure 5-31: Comparison between spatial rainfall patterns obtained by radar and algorithms, 01/29/93, TOGA-COARE. (a) Radar; (b) this model; (c) Prabhakara model; (d) Wilheit Model. See Figure 5-22 for legend.

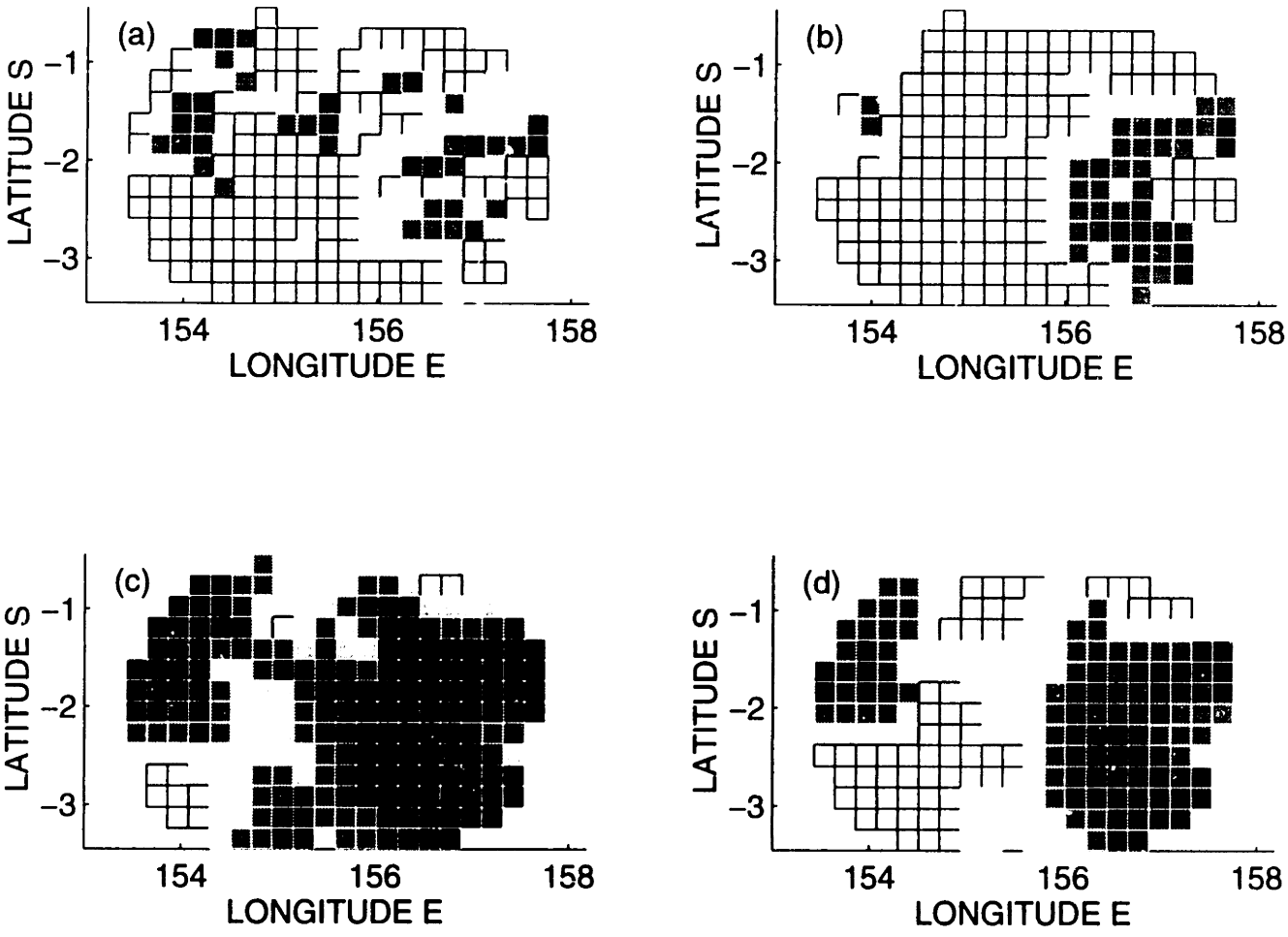

Figure 5-32: Comparison between spatial rainfall patterns obtained by radar and algorithms, 01/31/93, TOGA-COARE. (a) Radar; (b) this model; (c) Prabhakara model; (d) Wilheit Model. See Figure 5-22 for legend.

in TOGA-COARE, i.e., $T_{B,max}$ = 255 °K, $\triangle T = T_{B,max} - T_{B,min}$, and α = 0.5, the observed brightness temperatures were converted to the fractional rainfall coverage (f) according to (5.3). Then f was converted into the FOV mean rain rate (R) using the $f \sim R$ relationship derived from the TOGA-COARE radar data (Figure 5-3).

The spatial distributions of the instantaneous FOV mean rain rate resulting from our model and the other two models, together with the radar-observed rain which serves as the ground truth, are shown in Figure 5-33 and 5-34. Compared with radar, our model produces much better result than the other two models. The Prabhakara model and the Wilheit model, the former in particular, grossly overestimate both the intensity and the spatial extent of rain. For example, while the radar shows only light rainfall over a small area for the 13 January event, these two models predict rainfall everywhere. Overestimation is also profound for the 14 January event (Figure 5-34).

Our model also shows some degree of overestimation, especially for the 13 January event. However, this overestimation can be explained by the special layout of land and sea surfaces within the radar coverage. Remember that in our model we need to count the number of FOVs with brightness temperature over 240 °K to compute A_{240}. During the 13 January event, a portion of the rain occurred over the island and the land area. But the FOVs over the island, which if over water would have high brightness temperature, could not be counted towards A_{240}. This means that the presence of the island results in a lower estimate of frac[TB>240] if a portion of the rainfall occurs over the island. A lower frac[TB>240] leads to a lower $T_{B.min}$ and hence an overestimation of rainfall. Compared with the 13 January event, the 14 January event has a smaller portion of its rainfall over the island and the land. Thus its estimation

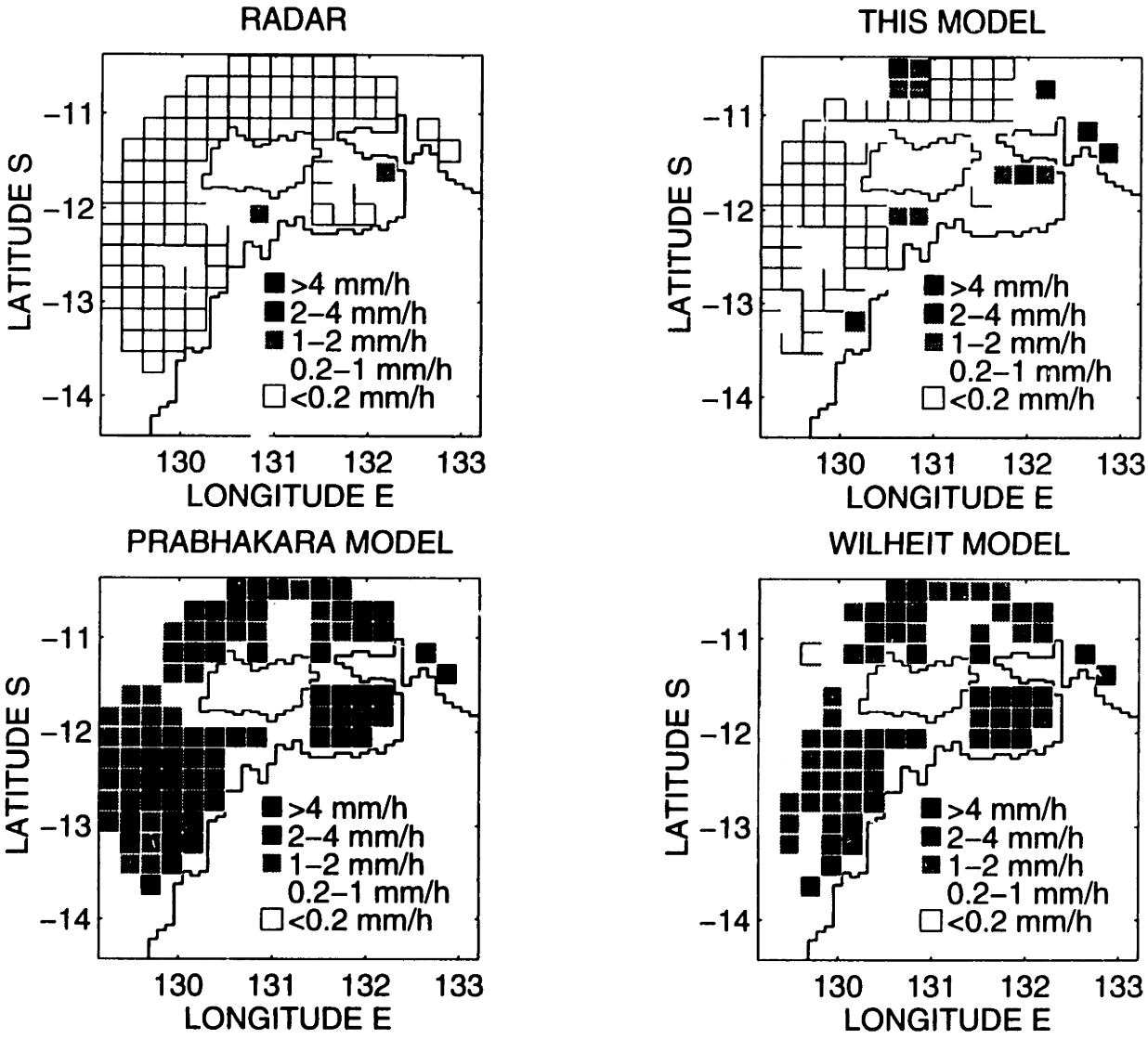

Figure 5-33: Comparison between spatial rainfall patterns obtained by radar and algorithms, 01/13/90, Darwin area.

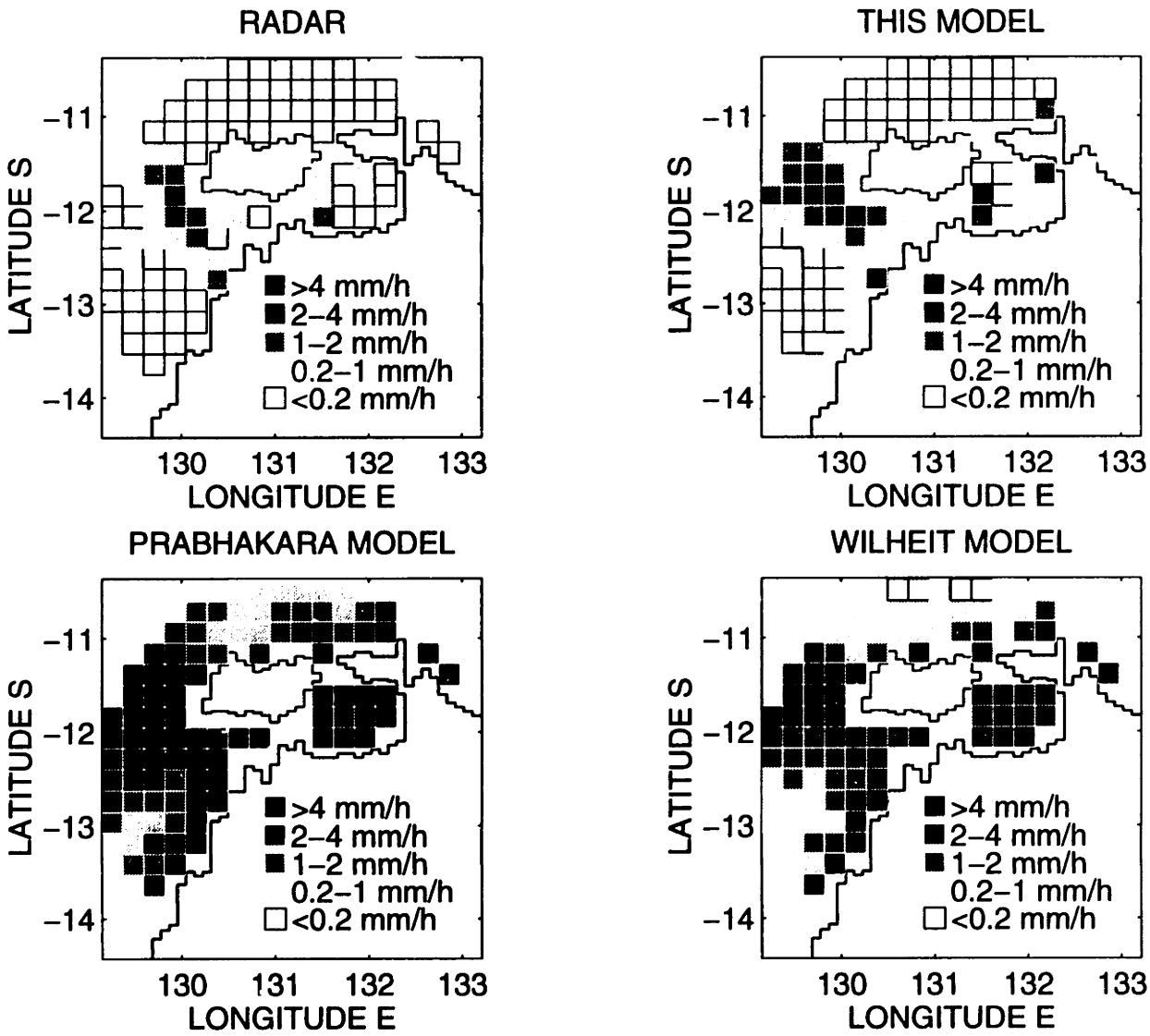

Figure 5-34: Comparison between spatial rainfall patterns obtained by radar and algorithms, 01/14/90, Darwin area.

of frac[TB>240] should be more accurate and should lead to a more accurate estimation of rainfall. This is evident in Figure 5-34 where we see that the rainfall map based on our model compares well with the radar observation.

One thing that should be noted about Figure 5-33 is that all models have predicted rainfall near the top of the figure, while the radar observation shows no rainfall around that area. Rain has been predicted by all three models because the brightness temperatures there are quite high (see Figure 4-5). We speculate that these high brightness temperatures might have been caused by an intense storm further north, which is outside of the radar coverage.

Quantitative comparisons of algorithm-based and radar-observed FOV mean rain rates for the two events are shown in Figure 5-35 and 5-36, respectively. It is clear that the Prabhakara model and the Wilheit model predict much higher rain rate than the observed values. From Figure 5-9 and 5-10 one can see that, at about 250 °K, the Wilheit model predicts a rain rate of about 15 mm h^{-1} and the Prabhakara model predicts nearly 30 mm h^{-1}. Our model, although calibrated only to the TOGA-COARE data, compares pretty well with the radar observation. The moderate overestimation seen in our model is mainly caused by the underestimation of frac[TB>240] as described before.

5.8 Model's Sensitivity to the Value of $T_{B,min}$ in the Retrieval of Areal Rain

To apply our model, one has to determine the value of $T_{B,min}$ for every (250 km–300 km) mesoscale area. A few interesting question are: how sensitive is the retrieved rain to the value of $T_{B,min}$? Is there a simpler way to determine $T_{B,min}$? To answer this question we have applied the model to the same storms

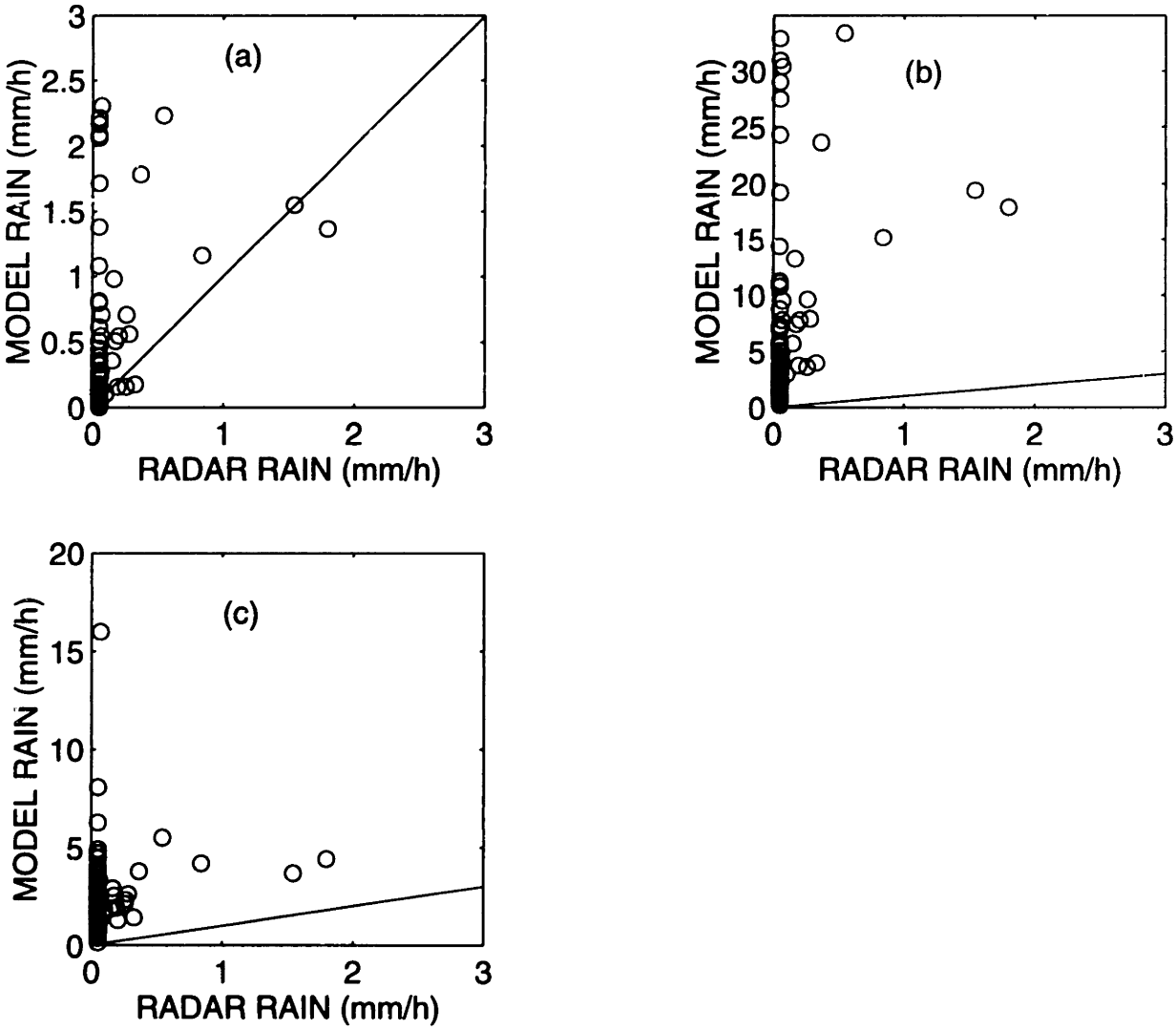

Figure 5-35: Comparison of model-based and radar-observed FOV mean rain rates, 01/13/90, Darwin area. (a) This model; (b) Prabhakara model; (c) Wilheit model.

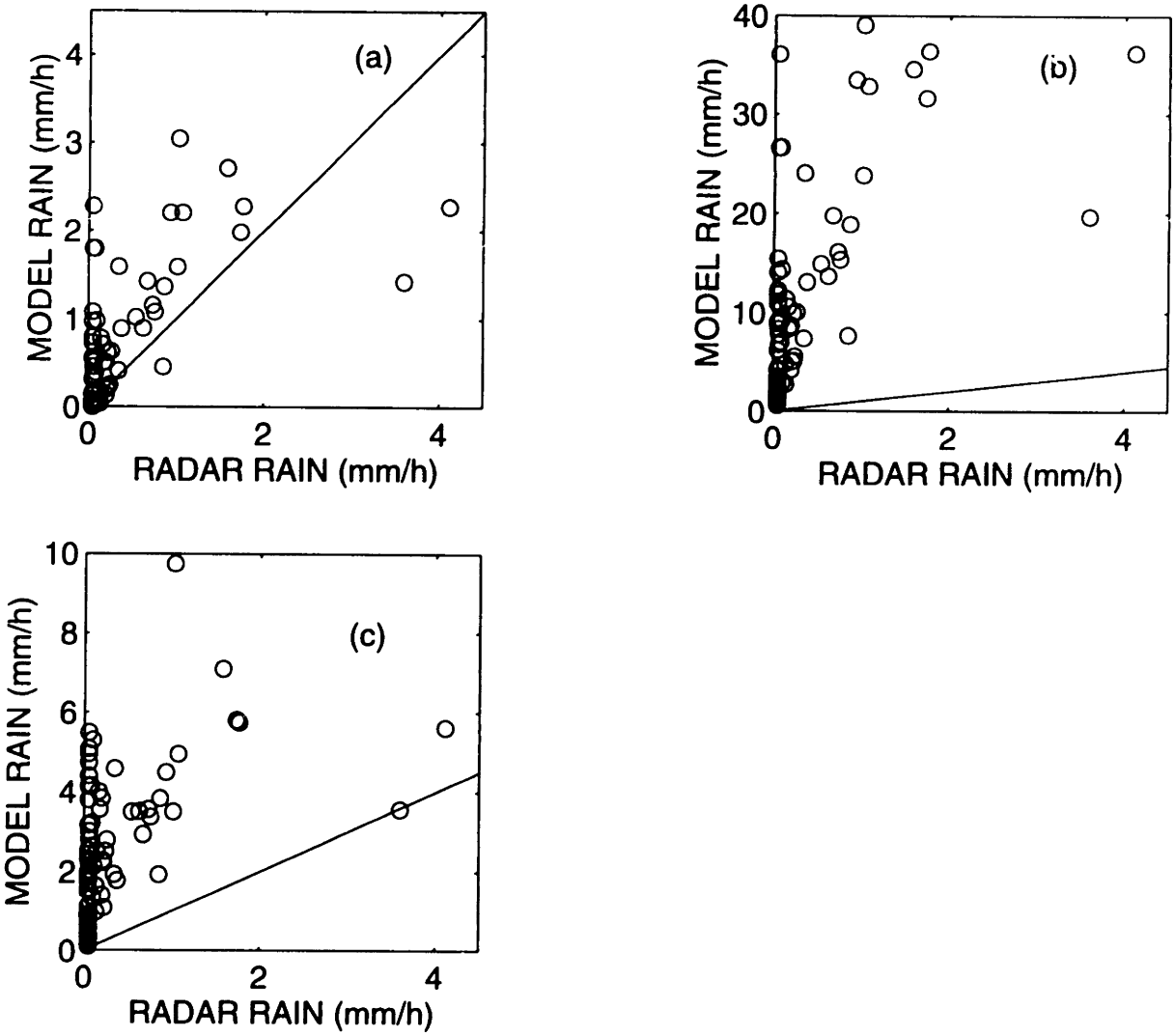

Figure 5-36: Comparison of model-based and radar-observed FOV mean rain rates, 01/14/90, Darwin area. (a) This model; (b) Prabhakara model; (c) Wilheit model.

with the following different values of $T_{B,min}$: one optimal value based on the parameter frac[TB>240] which is shown as **TB,min** in Table 5.5, one value which is equal to the lowest observed brightness temperature (denoted as T_{B0} here) found within the radar scan and is shown as **TB0** in Table 5.5, one value which is equal to T_{B0} + 10, and six fixed values at 160, 170, 180, 190, 200, 210 °K. The areal rain rates for individual cases are shown in Table 5.6 and Figure 5-37. In Table 5.6, the second column indicates the radar-observed average rain rate (mm h^{-1}) over the entire radar scan for each of the 11 storms; case A (third column) indicates the model-calculated areal rain rate using the optimal values of $T_{B,min}$; case B through case G are model-calculated areal rain rate with values of $T_{B,min}$ being 160, 170, 180, 190, 200, and 210 °K; case H is for the situation where $T_{B,min}$ is simply determined as the lowest brightness temperature (T_{B0}) found within the radar scan; case I uses $T_{B,min} = T_{B0}+10$. We want to compare the individual cases with the radar and among themselves. In principle case A should perform best, while case B ($T_{B,min}$ = 160 °K) should tend to overestimate rain and case G ($T_{B,min}$ = 210 °K) should tend to underestimate rain. This is evident in Figure 5-37, where the areal rain for case A and each of the fixed-$T_{B,min}$ is compared with the radar observation. The number printed in each plot indicates the value of $T_{B,min}$; the circle is for case A and the star is for the fixed-$T_{B,min}$ cases. One can see that the cases with $T_{B.min}$ equal to 160 °K and 170 °K have many star symbols far above the 45° line; and the cases with $T_{B,min}$ equal to 200 °K and 210 °K have many star symbols far below the 45° line, compared with the circle symbols. And somewhere in between the stars and circles have similar performance, indicating that at this $T_{B,min}$ range the use of a fixed $T_{B,min}$ for all storms could potentially result in areal rain estimates that are similar to that obtained using variable $T_{B,min}$. Three

measures have been used to compare the performance of the fixed-$T_{B,min}$ versus variable-$T_{B,min}$ cases. One is the mean of the areal rain rate of the 11 storms, which is equivalent to the long-term rain; another is the root-mean-square difference between the radar-observed and the model-calculated areal rain for each case; a third measure is the correlation between model-calculated and radar-observed areal rain rates. A good model should produce a mean that is close to the radar-observed value, a high correlation, and a small rms error. The last few rows in Table 5.6 show the mean, the rms error, and the correlation. The standard deviation is also shown. The radar-observed mean is 0.3 mm h^{-1} and the mean for case A (variable $T_{B,min}$) is 0.32 mm h^{-1}. The mean for case B through case G is decreasing, with case B ($T_{B,min}$ = 160 °K) overestimating the mean at 0.51 mm h^{-1} and case G ($T_{B,min}$ = 210 °K) underestimating at 0.19 mm h^{-1}. The mean obtained in case E ($T_{B,min}$ = 190 °K) is 0.29 mm h^{-1}, which is very close to the radar-observed value of 0.30 mm h^{-1}. Looking at the rms error, one finds that case A has the smallest rms of 0.11 mm h^{-1} among all cases. The rms errors for the fixed-$T_{B,min}$ cases range from 0.14 to 0.28 mm h^{-1}, with case E having the minimum of 0.14 mm h^{-1}.

The performance of case H, where the lowest brightness temperature is taken as $T_{B,min}$, is comparable to case E in terms of rms error but has a somewhat larger error in the retrieval of the mean rain rate of all the 11 storms. A look at Table 5.5 shows that the lowest brightness temperature (T_{B0}) found within the area is often lower than the value of $T_{B,min}$ based on frac[TB>240] for intense events such as #2 and #11, while it is slightly higher for light events. The low T_{B0} for the intense events is responsible for the overestimation of areal rain in case H. To take this fact into account, case I uses $T_{B,min} = T_{B0} + 10$. This results in a mean of 0.30, which is the same as the radar-observed value, and a

reduced rms error of 0.12.

The last row in Table 5.6 shows the correlation between the model-calculated and radar-observed areal rain rates. The three cases with event-specific $T_{B,min}$ (i.e., case A, H, and I) exhibit higher correlation than the fixed-$T_{B,min}$ cases (case B–G). It is interesting to note that the correlation for cases H and I is even higher than that for case A.

Although the above analysis has been based on data from 11 storms only, it nonetheless shows that using event-specific $T_{B,min}$ produces better results than using a fixed $T_{B,min}$, and determining the value of $T_{B,min}$ in a simpler way (case I) does not necessarily compromise the accuracy of the rainfall estimate. Future efforts should be directed towards improved estimation of model parameters, in particular to account for their dependence on the nature of the storm. Until then, however, simpler methods (e.g., case I) can be very useful in routine use of the rainfall retrieval algorithm.

NO.	radar	A	B	C	D	E	F	G	H	I
1	0.44	0.26	0.35	0.27	0.20	0.15	0.10	0.07	0.26	0.19
2	0.84	0.98	1.40	1.31	1.22	1.12	1.02	0.92	1.17	1.07
3	0.29	0.42	0.70	0.60	0.50	0.42	0.35	0.32	0.48	0.40
4	0.23	0.39	0.70	0.58	0.47	0.36	0.26	0.18	0.48	0.37
5	0.22	0.26	0.34	0.24	0.16	0.10	0.06	0.03	0.20	0.14
6	0.10	0.12	0.18	0.11	0.07	0.04	0.02	0.01	0.10	0.06
7	0.40	0.35	0.61	0.51	0.41	0.33	0.25	0.17	0.45	0.36
8	0.03	0.11	0.18	0.10	0.06	0.04	0.03	0.02	0.07	0.05
9	0.02	0.06	0.13	0.06	0.02	0.01	0.004	0.001	0.04	0.01
10	0.20	0.19	0.32	0.24	0.19	0.16	0.12	0.09	0.22	0.18
11	0.56	0.42	0.74	0.64	0.54	0.46	0.38	0.31	0.59	0.50
MEAN	0.30	0.32	0.51	0.42	0.35	0.29	0.24	0.19	0.37	0.30
STD	0.25	0.25	0.37	0.36	0.34	0.32	0.29	0.27	0.32	0.3
RMS	0	0.11	0.28	0.21	0.17	0.14	0.15	0.17	0.14	0.12
CORR	1	0.902	0.886	0.891	0.886	0.888	0.878	0.861	0.916	0.912

Table 5.6: Areal rain rate (mm h^{-1}) for the 11 storms obtained by models with variable and fixed $T_{B,min}$.

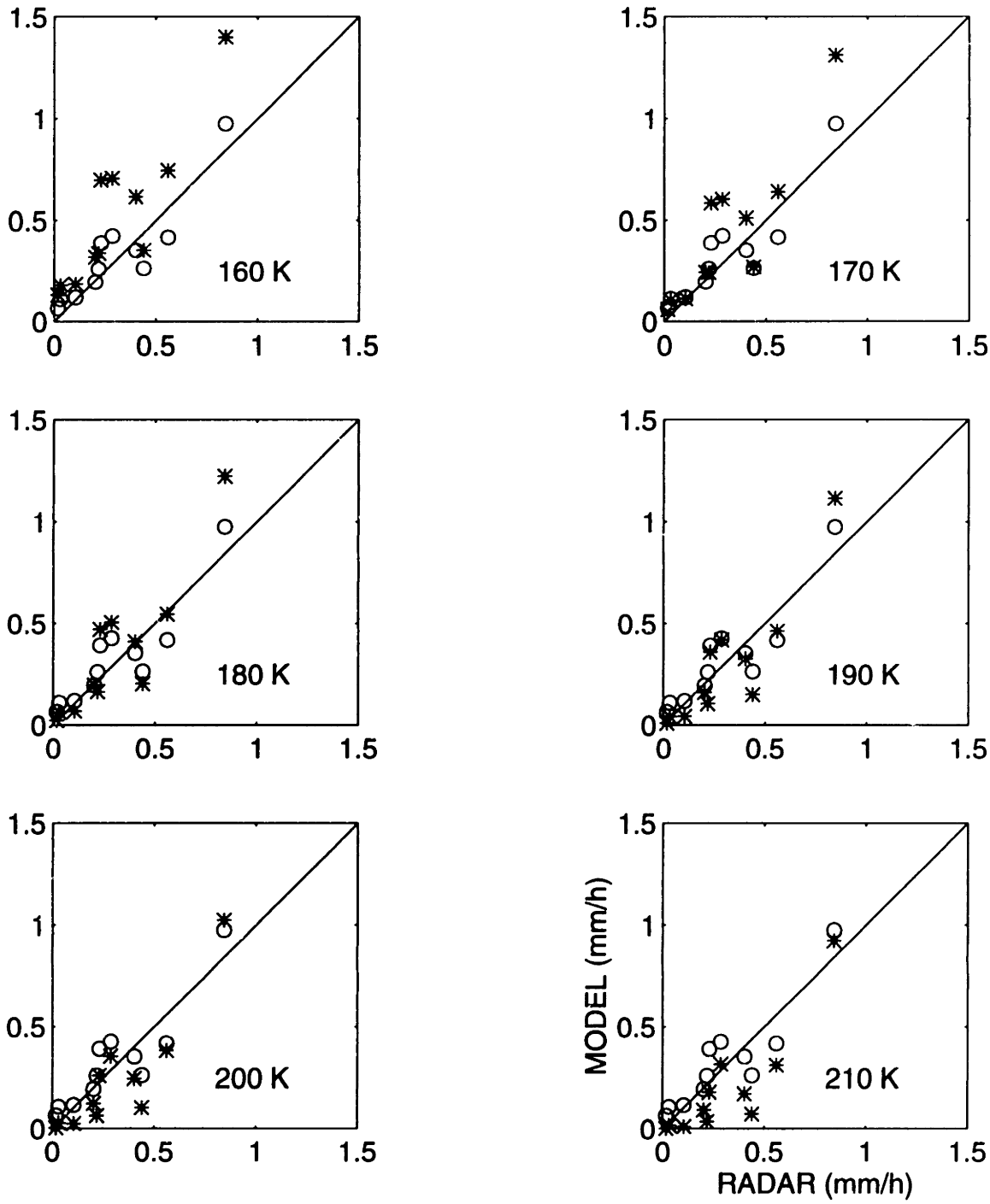

Figure 5-37: Comparison between model-calculated and radar-observed areal rain rate. Circles are for the variable $T_{B,min}$ case and stars are for fixed $T_{B,min}$ cases. The value of the fixed $T_{B,min}$ is written in each plot.

Chapter 6

Conclusions and Future Research

In this study, we have explored two important issues in passive microwave remote sensing of rainfall from space. The first issue is the sampling error associated with the discrete visit of a satellite to a given region on the Earth's surface. The second issue is the effects of environmental noises (wind and non-precipitating clouds) on the estimation of oceanic rainfall by space-borne radiometers.

On the sampling error issue, we first developed the analytical formulation for the quantification of sampling errors associated with the discrete measurements of both stationary and non-stationary rainfall processes. The motivation for the formulation of errors associated with a non-stationary rainfall process is the need to understand the effect of diurnal cycle of rainfall on sampling errors, which has been largely ignored in previous studies. In contrast to most previous studies that use GATE data, which exhibits no significant diurnal cycle, we have used rainfall data collected near Darwin, Australia which shows strong diurnal variations. Our rainfall data have been downloaded from the

original tapes that contain the instantaneous reflectivity data. Using this data set, we have studied the mean, variance, diurnal cycle, and autocorrelation of the area-averaged rain rate. We have also studied the variation of these quantities with the size of the area over which rainfall is averaged. Based on these statistics, the stationary and non-stationary models have been used to quantify the sampling error as a function of sampling frequency, starting sampling time, and the area size.

On the environmental noise issue, we started by reviewing the literature on microwave remote sensing from space, with emphasis on papers that deal with the theoretical (modeling) aspects of radiative transfer through raining clouds. Existing models have failed to take appropriate account of the fact that wind and non-precipitating clouds can cause significant increase in upwelling brightness temperature. We presented observations over two different regions which demonstrate that high brightness temperatures can be caused by factors other than rain. We then proceeded to explain such high brightness temperature in terms of non-precipitating clouds and wind. Non-precipitating clouds increase the upwelling brightness temperature through absorption and emission. A theoretical relationship has been derived which relates the increase in the brightness temperature to the columnar cloud water content. This leads to the conclusion that the presence of non-precipitating clouds can cause about 10 °K increase in the brightness temperature at 37 GHz. Wind influences the emissivity by roughening the sea surface and generating foam. A rough sea surface has higher microwave emissivity relative to a smooth surface, particularly in the horizontal polarization. The foam, which is a mixture of water and air, has a very high emissivity at the microwave frequencies. The presence of foam on the sea surface can cause the brightness temperature to increase, inde-

pendent of polarization. As a result, the strong wind associated with mesoscale cloud clusters will cause the brightness temperature to increase in both polarizations, with more increase in the horizontal polarization than in the vertical polarization for a given wind speed. Consequently, wind can also reduce the polarization difference as a raining cloud, the later having been well-recognized in existing algorithms. We have argued that at the intermediate T_B range, the increase in T_B (and the corresponding reduction in polarization difference) can be and is mainly caused by wind, since wind affects an area much larger than rain cells. We have also argued that ignoring the wind effects can result in overestimation of the raining area and, consequently, the rain amount, as the high T_B caused by the wind is misinterpreted as rain.

A major effort has been devoted to developing a rainfall retrieval model that considers the effects of wind and non-precipitating clouds. The model is based on the concept of partial rainfall coverage within a FOV. Based on the fact that the T_B from intense rain cells saturates rapidly and that the T_B from the sea surface is affected by wind and non-precipitating clouds, we developed a relationship between the upwelling T_B of a FOV and the fractional rainfall coverage (f) within that FOV. This model is semi-physical and semi-statistical in the sense that its structure is physically based, but its parameters have to be determined using data. We have calibrated this model using simultaneous radar/satellite data over TOGA-COARE region. Using this model, one can obtain the fractional rainfall coverage within a FOV based on the observed T_B. To obtain the FOV average rain rate R, we have proposed to use an empirical relationship between R and f, which can be derived from radar data. We have analyzed the TOGA-COARE radar rainfall data and obtained an empirical f–R relationship for a 24 km by 24 km box. The f–R relationship for large areas

($\sim 10^5$ km^2) has been studied extensively by other researchers (e.g., Atlas et al. 1990, Chiu 1988 a,b, Rosenfeld et al. 1990), while it is still not well understood at the scale of a satellite FOV and needs further research to quantify its space-time variability.

Based on the T_B–f and f–R relationships, we have proposed a simple algorithm for rainfall retrieval which considers the noise effects and which relies on the satellite data only. This algorithm has been compared with two existing algorithms by applying them to retrieve the spatial distribution of the instantaneous rain rate in several storms. The radar observations serve as ground truth. The results showed that, without proper consideration of the noises, the other two algorithms overestimate rainfall, particularly for intense storms where the noises are generally expected to be strong.

Our model has focused on the surface conditions and treated the cloud structure crudely (we have assumed a saturation T_B for all raining areas). In contrast, existing models possess sophisticated cloud structures but have treated the surface crudely (they assume constant emissivity or random wind effects). In this sense our model and the existing models complement each other. One area of future research would be to combine these two types of models. Our model can be used to estimate, on a physical basis, the fractional rainy area within a FOV and the sea surface emissivity, which serve as input to algorithms with more realistic cloud structures. This can lead to a more accurate T_B–R relationship.

We have chosen a mesoscale of 250–300 km as the unit area in which to quantify the wind effects. With more data sensitivity analysis could be performed to identify the optimal size of the area.Also, we have used a single $T_{B,min}$ for the whole mesoscale cloud cluster, which may be too low for FOVs

close to major rain cells and too high for FOVs far away from the rain cells. Adjustment of the $T_{B,min}$ for individual FOVs could be achieved by considering the distance between the FOV and nearby major rain cells, where the location of major rain cells can be identified by areas of high brightness temperature.

We can further explore the method for determining $T_{B,min}$. Different approaches may be taken for different purposes. For example, determining the value of $T_{B,min}$ based on the lowest brightness temperature found in a mesoscale area will result in areal rain rate estimates that are as accurate as that obtained by relating $T_{B,min}$ to frac[TB>240].

Our T_B–f relationship still needs to be further validated using more simultaneous radar/satellite data, preferably from different regions of the tropical oceans. The f–R relationship at the FOV scale needs further study. The various mechanisms for rainfall development in different regions and seasons dictate that the f–R relationship should have space-time variability. In addition, the accuracy of the f–R model can be improved if the storm height can be determined by, say, infrared data.

Our model assumes a constant $T_{B,min}$ of about 170 °K when frac[TB>240] is zero. This could lead to some overestimation of rain when dense non-precipitating clouds are present and raise the brightness temperature significantly above 170 °K. A sub-algorithm for the case of zero frac[TB>240] could be added. If frac[TB>240] is zero, we are sure that there is no significant rain in the mesoscale area. Further, if there are moderate high brightness temperatures (say 180 °K) over an extensive area, and at the same time infrared imagery shows low temperature, we are sure that there are wide-spread non-precipitating clouds over the mesoscale area. Overestimation of rain can be avoided if non-precipitating clouds are taken into account in this way.

Since our model can remove the bias caused by the noises, it is important to apply it to obtain the climatology of rainfall over the tropical oceans and compare with those obtained by other algorithms. The difference should stimulate future research.

REFERENCES

Adler, R. F., and I. M. Hakkarinen, 1991: Aircraft multifrequency passive microwave observations of light precipitation over the ocean. *J. Atmo. Ocean. Tech.*,**8**, 201–220.

Adler, R. F., H. Y. M. Yeh, N. Prasad, W. K. Tao, and J. Simpson, 1991: Microwave simulations of a tropical rainfall system with a three-dimensional cloud model. *J. Appl. Meteor.*, **30**, 924–953.

Akvilonava, A. B., M. S. Krylova, B, G. Kutuza, and L. M. Mitnik, 1971: SHF radiometric characteristics of frontal cloudiness as measured from Cosmos-243, *Advances in Satellite Meteorology*, Wiley and Sons, New York.

Allison, L. J., E. B. Rodgers, T. T. Wilheit, and R. W. Fett, 1974: Tropical cyclone rainfall as measured by the Nimbus 5 electrically scanning microwave radiometer. *Buli. Amer. Meteo. Soc.*,**55**, 1074–1089.

Atlas, D., 1994: Footprints of storms on the sea: A view from spaceborne synthetic aperture radar. *J. Geophys. Res.*, **99, C4**, 7961–7969.

Atlas, D., D. Rosenfeld, and D. Short, 1990: The estimation of convective rainfall by areal integrals 1. The theoretical and empirical basis. *J. Geophys. Res.*, **95, D3**, 2153–2160.

Bell, T. L., A. Abdullah, R. L. Martin, and G. R. North, 1990: Sampling errors for satellite-derived tropical rainfall: Monte Carlo study using a space-time stochastic model. *J. Geophys. Res.*, **95, D3**, 2195–2205.

Bras, R.L., and I. Rodriguez-Iturbe, 1985: Random Functions and Hydrology. Addison-Wesley, 559 pp.

Chiu, L. S., 1988a: Rain estimation from satellites: Areal rainfall-rain area relation, paper presented at the 3rd Conference on Satellite Meteorology and Oceanography, Am. Meteor. Soc., Anaheim, Calif., Feb. 1–5.

Chiu, L. S., 1988b: Estimating areal rainfall from rain area, in *Tropical Rainfall Measurements*, edited by J. S. Theon and N. Fugono, pp. 361–367, A. Deepak, Hampton, Va.

Chiu, L. S., G. R. North, D. A. short, and A. McConnell, 1990: Rain estimation from satellite: effect of finite field of view. *J. Geophys. Res.*, **95, D3**, 2177–2185.

Cox, C., and W. Munk, 1955: Some problems in optical oceanography. *J. Marine Res.*, **4**, 63–78.

Dorman, C.E., and R.H. Bourke, 1979: Precipitation over the Pacific Ocean, 30°S to 60°N. *Mon. Wea. Rev.*, **107**, 896–910.

Dorman, C.E., and R.H. Bourke, 1981: Precipitation over the Atlantic Ocean, 30°S to 70°N. *Mon. Wea. Rev.*, **109**, 554–563.

Droppleman, J. D., 1970: Apparent microwave emissivity of sea foam. *J. Geophys. Res.*, **75, NO. 27**, 696–698.

Garcia, O., 1981: A comparison of two satellite estimates for GATE. *J. Appl. Meteor.*, **20**, 430–438.

Goff, R. C., 1976: Vertical structure of thunderstorm outflows. *Mon. Wea. Rev.*,**104**, 1429–1440.

Gunn, K. L. S., and T. W. R. East, 1955: The microwave properties of precipitation particles. *Quart. J. Roy. Meteor. Soc.*,**80**, 522–545.

Hakkarinen, I.M., and R.F. Adler, 1988: Observations of precipitating convective systems at 92 and 183 GHz: Aircraft results. *Meteor. Atmos. Phys.*, **38**, 164–182.

Hollinger, J. P., 1970: Passive microwave measurements of the sea surface. *J. Geophys. Res.*, **75, NO. 27**, 5209–5213.

Intrieri J. M., A. J. Bedard, and R. M. Hardesty, 1990: Details of colliding thunderstorm outflows as observed by doppler lidar. *J. Atmo. Sci.*,**47**, 1081–1097.

Kedem,B., L. S. Chiu, and G. R. North, 1990: Estimation of mean rain rate: Application to satellite observations. *J. Geophys. Res.*, **95**, 1965–1972.

Kilonsky, B.J., and C.S. Ramage, 1976: A technique for estimating tropical open-ocean rainfall from satellite observations. *J. Appl. Meteor.*, **15**, 972–975.

Kummerow, C., R. A. Mack, and I. M. Hakkarinen, 1989: A self-consistency approach to improve microwave rainfall rate estimation from space. *J. Appl. Meteor.*, **28**, 869–884.

Kummerow, C., and J. A. Weinman, 1988: Determining microwave brightness temperatures from horizontally finite and vertically structured clouds. *J. Geophys. Res.*, **93, C4**, 3720–3728.

Lane, J. A., and J. A. Saxton, 1952: Dielectric dispersion in pure polar liquids at very high radio frequencies. *Proc. Roy. Soc. London*, **A312**, 400-408.

Lovejoy, S., and G. L. Austin, 1980: The estimation of rain from satellite-borne radiometers. *Quart. J. Roy. Meteor. Soc.*,**106**, 255–276.

McConnell, A., and G. R. North, 1987: Sampling errors in satellite estimates of tropical rain, *J. Geophys. Res.*, **92**, 9567–9570.

Mahoney, W. P., 1988: Gust front characteristics and the kinematics associated with interacting thunderstorm outflows. *Mon. Wea. Rev.*,**116**, 1474–1091.

Mueller, C. K., and R. E. Carbone, 1987: Dynamics of a thunderstorm outflow. *J. Atmo. Sci.*,**44**, 1879–1898.

Mugnai, A., and E. A. Smith, 1988: Radiative transfer to space through a precipitating cloud at multiple microwave frequencies. Part I: Model description. *J. Appl. Meteor.*, **27**, 1055–1073.

Nordberg, W., J. Conaway, D. B. Ross, and T. Wilheit, 1971: Measurements of microwave emission from a foam-covered, wind-driven sea. *J. Atmo. Sci.*,**28**, 429–435.

North G.R., S.S.P. Shen, and R. Upson, 1993: Sampling errors in rainfall estimates by multiple satellites. *J. Appl. Meteor.*, **32**, 399–410.

North, G.R., and S Nakamoto, 1989: Formalism for comparing rain estimation designs. *J. Atmos. Oceanic Technol.*, **6**, 985–992.

Oki R., and A. Sumi, 1994: Sampling simulation of TRMM rainfall estimation using radar-AMeDAS composites. *J. Appl. Meteor.*, **33**, 1597–1608.

Olson, W. S., 1989: Physical retrieval of rainfall rates over the ocean by multispectral microwave radiometry: Application to tropical cyclones. *J. Geophys. Res.*, **94, D2**, 2267–2280.

Petty, G. W., and K. B. Katsaros, 1990: Precipitation observed over the South China Sea by the Nimbus-7 scanning multichannel microwave radiometer during winter MONEX. *J. Appl. Meteor.*, **29**, 273–287.

Petty, G. W., and K. B. Katsaros, 1992: Nimbus-7 SMMR precipitation observations calibrated against surface radar during TAMEX. *J. Appl. Meteor.*, **31**, 489–505.

Prabhakara, C., G. Dalu, G. L. Liberti, J. J. Nucciarone, and R. Suhasini, 1992: Rainfall estimation over ocean from SMMR and SSM/I microwave data. *J. Appl. Meteor.*, **31**, 532–552.

Reed, R.K., and W.P. Elliott, 1973: Precipitation at ocean weather stations in the North Pacific. *J. Geophys. Res.*, **78**, 7087–7091.

Rosenfeld, D., D. Atlas, and D. Short, 1990: The estimation of convective rainfall by areal integrals 2. The height-area rainfall threshold (HART) method. *J. Geophys. Res.*, **95, D3**, 2161–2176.

Rosenkranz, P. W., D. H. Staelin, and N. C. Grody, 1978: Typhoon June (1975) viewed by a scanning microwave spectrometer. *J. Geophys. Res.*, **83, C4**, 1857–1868.

Rutledge, S. A., E. R. Williams, and T. D. Keenan, 1992: The Down Under Doppler and Electricity Experiment (DUNDEE): Overview and preliminary results, *Bull. Amer. Meteo. Soc.*,**73**, 3–16.

Sawyer, J.S., 1952: The estimation of rainfall amounts from observations of present weather. Meteor. Office Orders c5/1952, London.

Seed, A., and G.L. Austin, 1990: Variability of summer Florida rainfall and its significance for the estimation of rainfall by gages, radar and satellite. *J. Geophys. Res.*, **95**, 2207–2216.

Shin, K.-S., and R. R. North, 1988: Sampling error study for rainfall estimate by satellite using a stochastic model. *J. Appl. Meteor.*, **27**, 1218–1231.

Short, D. A., and G. R. North, 1990: The beam filling error in the Nimbus 5 electronically scanning microwave radiometer observations of Global Atlantic Tropical Experiment rainfall. *J. Geophys. Res.*, **95, D3**, 2187–2193.

Simpson, J., G. R. North, and R. F. Adler, 1988: A proposed Tropical Rainfall Measuring Mission (TRMM) satellite, *Bull. Am. Meteor. Soc.*, **69**, 278–295.

Singer, S. F., and G. F. Williams, 1968: Microwave detection of precipitation over the surface of the ocean. *J. Geophys. Res.*, **73, NO. 10**, 3324–3327.

Spencer, R.W., B.B. Hinton and W.S. Olson, 1983a: Nimbus-7 37 GHz radiances correlated with radar rain rates over the Gulf of Mexico. *J. Climate Appl. Meteor.*, **22**, 2095–2099.

Spencer, R.W., W.S. Olson, Wu Rongzhang, D.W. Martin, J.A. Weinman and D.A. Santek, 1983b: Heavy thunderstorms observed over land by Nimbus-7 Scanning Multichannel Microwave Radiometer, *J. Climate Appl. Meteor.*, **22**, 1041–1046.

Spencer, R.W., H.M. Goodman, and R.E. Hood, 1989: Precipitation retrieval over land and ocean with the SSM/I: Identification and characteristics of the scattering signal. *J. Atmos. Oceanic Technol.*, **6**, 245–263.

Tucker, G.G., 1961: Precipitation over the North Atlantic Ocean. *Quart. J. Roy. Meteor. Soc.*, **87**, 147–158.

Savage, R. C., 1976: The transfer of thermal microwaves through hydrometeors. Ph.D. thesis, University of Wisconsin, Madison, 147 pp.
Stogryn, A., 1967: The apparent temperature of the sea at microwave frequencies. *IEEE Trans. Antennas Propat.*, **15**, 278–286.

Wakimoto,R. M., 1982: The life cycle of thunderstorm gust fronts as viewed with doppler radar and rawinsonde data. *Mon. Wea. Rev.*,**110**, 1060–1082.

Webster, P. J., and R. Lukas, 1992: TOGA COARE: The Coupled Ocean-Atmosphere Response Experiment, *Bull. Amer. Meteo. Soc.*,**73**, 1377–1416.

Webster, W. J., T. T. Wilheit, D. B. Ross, and P. Gloersen, 1976: Spectral characteristics of the microwave emission from a wind-driven foam-covered sea. *J. Geophys. Res.*, **81, NO. 18**, 3095–3099.

Weinman, J. A., and R. Davies, 1978: Thermal microwave radiances from horizontally finite clouds of hydrometeors. *J. Geophys. Res.*, **83, C6**, 3099–3107.

Wentz, F. J., 1983: A model function for microwave brightness temperatures. *J. Geophys. Res.*, **88**, 1892–1908.

Wentz, F. J., 1991: User's manual, SSM/I antenna temperature tapes, revision 1. Prepared by Remote Sensing Systems, Inc.

Wilheit, T. T., 1979: A model for the microwave emissivity of the ocean's surface as a function of wind speed. *IEEE Trans. Geosci. Electron.*,**16**, 138–143.

Wilheit, T.T., 1986: Some comments on passive microwave measurement of rain. *Bull. Amer. Meteor. Soc.*, **67**, 1226–1232.

Wilheit, T. T., A. T. C. Chang, M. S. V. Rao, E. B. Rodgers, and J. S. Theon, 1977: A satellite technique for quantitatively mapping rainfall rates over the oceans. *J. Appl. Meteor.*, **16**, 551–560.

Wilheit, T.T., A.T.C. Chang, J.L. King, E.B. Rodgers, R.A. Nieman, B.M. Krupp, A.S. Milman, J.S. Stratigos and H. Siddalinbaiah, 1982: Microwave radiometric observations near 19.35, 92, and 183 GHz of precipitation in Tropical Storm Cora. *J. Appl. Meteor.*, **21**, 1137–1145.

Wilheit, T. T., A. T. C. Chang, and L. S. Chiu, 1991: Retrieval of monthly rainfall indices from microwave radiometric measurements using probability distribution functions. *J. Atmos. Oceanic Tech.*, **8**, 118–136.

Williams, E. R., S. A. Rutledge, S. G. Geotis, N. Renno, E. Rasmussen, and T. Rickenbach, 1992: A radar and electrical study of tropical "hot towers", *J. Atmos. Sci.*, **49**, 1386–1395.

Williams, G. F., 1969: Microwave radiometry of the ocean and the possibility of marine wind velocity determination from satellite observations. *J. Geophys. Res.*, **74, NO. 18**, 4591–4594.

Woodley, W.L., C.G. Griffith, J.S. Griffin and S.C. Stromatt, 1980: The inference of GATE convective rainfall from SMS-1 imagery. *J. Appl. Meteor.*, **19**, 388–408.

Wu, R., and J. A. Weinman, 1984: Microwave radiances from precipitating clouds containing aspherical ice, combined phase and liquid hydrometeors. *J. Geophys. Res.*, **89**, 7170–7178.

Biographic Sketch

Qihang Li was born in Guangxi Zhuang Nationality Autonomous Region of China in 1964. He was admitted into Tsinghua University, Beijing, in September 1979 and obtained his B. S. in water resources engineering in October 1984 with thesis "Mathematical Modeling of Water Quality in Tuojiang River". From October 1984 to September 1988 he was employed by Pearl River Water Resources Commission of the Ministry of Water Resources of China, where he participated in projects involving analysis of storm and flood, characterization of aquifers, experimental study of evaporation from bare soils, water resources survey using aerial photograph, and others. Starting October 1988 he studied at the University of Tokyo and obtained his M. S. in civil engineering in September 1990 with thesis "Annual Rainfall Over Kanto Region Analyzed by Empirical Orthogonal Functions". From September 1990 to August 1991, Li was employed by Nippon Koei Co. Ltd., Tokyo, as a consulting engineer. In that position he implemented a short term rainfall prediction model and developed a rainfall-runoff model for the sewerage network of the city of Yokohama. In September 1991, Li started his doctoral study at MIT under professor Rafael Bras in the area of hydrology and meteorology. His major topics of research at MIT included predictability of mesoscale precipitation, statistical analysis of radar rainfall data, and passive microwave remote sensing of rainfall. He obtained his Ph.D. degree in hydrometeorology in February 1996 with the thesis "Sampling Error and Environmental Noises in Passive Microwave Rainfall Retrieval From Space".

Li is married to Lili Yao and they live happily with their lovely son, Darwin Hanqin, and daughter, Gina Liqi.